Investigating Entrance Channel Effects in Fusion-Fission Dynamics

A thesis submitted for the degree
of Doctor of Philosophy of
The Australian National University

Annette Caroline Berriman

28 November 2001

This thesis contains no material which has been accepted for the award of any other degree or diploma in any university. To the best of the author's knowledge and belief, it contains no material previously published or written by another person, except where due reference is made in the text.

The following publication, directly related to the work described in this thesis, has been published:

- A.C. Berriman, D.J. Hinde, M. Dasgupta, C.R. Morton, R.D. Butt and J.O. Newton, *Unexpected inhibition of fusion in nucleus-nucleus collisions*, Nature **413**, 144-147 (2001)

Annette Berriman
28 November 2001

"If we knew what it was we were doing,
it would not be called research, would it ?"

Albert Einstein
(1879-1955)

Acknowledgements

I would like to thank my supervisor David Hinde for his support and assistance with my PhD project. I am indebted to David for his insight into fusion-fission dynamics, for always being there when I encountered problems, and for being one of the best supervisors on campus.

My thanks also to Nanda Dasgupta for sharing her extensive knowledge of fusion modelling, and for always being a ray of sunshine, even at four o'clock in the morning. Thanks also to Aidan Byrne who helped me view my project from a different perspective, and for his unfailing optimism.

The experiments detailed in this work could not have conducted without the assistance of David Hinde, Nanda Dasgupta, Clyde Morton, John Newton, and Rachel Butt.

I am grateful to the technical, academic, and support staff of the Department of Nuclear Physics for their assistance in a great many ways.

Finally, a big thanks to my husband Dave for his encouragement and selfless support over the years of this project.

Abstract

Fission and evaporation residue (ER) decay have been measured for ^{216}Ra compound nuclei formed in the three reactions ^{12}C + ^{204}Pb, ^{19}F + ^{197}Au and ^{30}Si + ^{186}W. For decreasing mass-asymmetry (heavier projectiles) there was a decrease in yield of ERs, and an increase in the width of the fission fragment mass-distributions. These results show convincing, model-independent evidence both of inhibition of fusion and of the presence of quasi-fission for the heavier projectiles. Quasi-fission is identified for the first time in a reaction involving a projectile as light as ^{19}F on a non-actinide target. These results defy interpretation within the standard picture of nuclear fusion and fission. However, the results can be interpreted assuming quasi-fission occurs for mass-asymmetries less than that for the Businaro-Gallone potential energy maximum [Busi55A, Busi55B, Davi85]. These are also the first experimental data that show convincingly that quasi-fission competes not only with fusion-fission reactions but also, at low angular momentum, with ER production.

Some ^{12}C projectile breakup was evident for the reaction ^{12}C + ^{204}Pb, but not enough to significantly influence the above decay comparison, or conclusions.

A new Monte Carlo statistical model code has been written to compare calculations with experimental data. It included the option to include shell and pairing effects in the level density calculations. Calculations using this option were able to provide limited improvement to the fits to some evaporation residue measurements, but failed to provide an improved reproduction of the full range of experimental ER and fission decay data.

The effect of the $N = 126$ closed shell on compound nucleus decay was investigated following a recent report of a localised effect on fission fragment anisotropies [Shri99]. Fission cross-sections and fission fragment anisotropies were measured for the six reactions, ^{16}O + ^{192,194,196,198}Pt and ^{18}O + ^{196,198}Pt, which lead to the com-

pound nuclei, ^{208,210,212,214,216}Rn (N = 122, 124, 126, 128, and 130). Evaporation residues were determined for the two reactions ^{16}O + ^{194}Pt and ^{18}O + ^{198}Pt. Neither the experimental results, nor model calculations (with or without shell and pairing enhancements) showed localised effects of the N = 126 closed shell on the decay of the compound nuclei.

Contents

CHAPTER 1

Introduction

In the simplest picture of heavy-ion fusion, two nuclei colliding with sufficient energy will be captured by the nuclear potential and fuse to form an excited compound nucleus. The compound nucleus will evolve to a state of equilibrium, and then decay by the evaporation of light particles (neutrons, protons or alpha-particles), and the emission of gamma rays, or by fission. Additional considerations such as angular momentum, excitation energy and a broad range of energies over which the onset of fusion occurs (Coulomb barrier region) adds complexity to the formation-decay processes of the compound nucleus. Underpinning this picture of fusion and decay is Niels Bohr's hypothesis of independence (formulated in 1936 to explain neutron capture) [Bohr36], which states that compound nuclei with the same excitation energy and angular momentum will decay independently of their method of formation.

Increasingly, this picture is being challenged by the observation of processes such as quasi-fission [Back85, Tōke85, Hind95A, Hind95B, Hind99A], where capture takes place but fission occurs without the compound nucleus reaching full equilibrium. While quasi-fission does not occur for all reactions, it has been noted in reactions on actinide targets (e.g. [Hind95A, Mein97]), and in reactions using heavy targets ($A \geq 154$) [Back96, Hind92] together with projectiles of ^{24}Mg or heavier [Back85]. Evidence for quasi-fission in reactions such as ^{32}S + ^{197}Au [Back85] and ^{24}Mg + ^{208}Pb [Back85], but not in the reactions ^{18}O + ^{197}Au [Hind92] and ^{16}O + ^{208}Pb [Back85, Mort95B], supports the idea that the formation and decay of compound nuclei in heavy-ion reactions are not independent processes. They also raise the question as to the threshold for the onset of quasi-fission.

The usually understood definition of the compound nucleus (as introduced by Niels Bohr) is of a combined nucleus in a fully equilibrated state. The term com-

pound nucleus is used in the present work to refer to any combined system of projectile and target where the two nuclei are captured within the potential energy barrier, the kinetic energy of the projectile has been absorbed by the system and the energy of the system is equilibrated. It refers to systems that could be elongated, at the saddle-point, or in a fully equilibrated state.

Reactions leading to the production of super-heavy compound nuclei are greatly inhibited by quasi-fission. Although very recently a handful of super-heavy nuclei have been formed [Nino99, Ogan99A, Ogan99B, Ogan00, Ogan01], most nuclear collisions, after damping of their kinetic energy and mass transfer to the lighter nucleus, lead to re-separation of the two colliding nuclei via quasi-fission. Hope of forming more substantial quantities of super-heavy nuclei has centred on the super-heavy island of stability around the predicted magic numbers $Z = 114$, 120 and 126 and $N = 184$. It is therefore essential that both quasi-fission and the influence of closed shells in capture-decay reactions are thoroughly understood.

This work explores systematically, entrance channel effects and $N = 126$ closed shell effects in heavy-ion capture-decay reactions. To help understand the processes at work a new statistical model code of compound nucleus decay has been written, and the calculations are compared to the experimental results.

Three reactions, $^{12}C + {}^{204}Pb$, $^{19}F + {}^{197}Au$ and $^{30}Si + {}^{186}W$, which following fusion all form the same compound nucleus, ^{216}Ra, were chosen to explore entrance channel effects. These span the expected threshold for quasi-fission and have similar excitation energies and angular momentum distributions. The compound nuclei formed in these reactions were chosen to be in a region where decay would occur by both fission and formation of evaporation residues (ERs). Evaporation residues are formed when the compound nuclei survive fission and shed energy by evaporating neutrons (and sometimes protons and α-particles depending on the mass of the compound nucleus).

The identity and cross-sections of ERs from these three reactions were determined by precise measurements of their subsequent α-decay. Detailed measurements were also made of the properties and cross-sections for fission, which included both fusion-fission and quasi-fission (in which no ERs are produced). Measurements were made for a range of energies from the Coulomb barrier region upwards, at centre-of-mass energy intervals, ΔE, of approximately 3.7 MeV. Thereby, ^{216}Ra compound

nuclei were formed at several excitation energies, which were the same in the three reactions.

Direct comparison of the experimental data from the three reactions was carried out, as well as comparison with model calculations. The presence and extent of entrance channel effects for the ^{216}Ra compound nucleus have been identified. Inhibition of fusion was observed in the two reactions ^{19}F + ^{197}Au and ^{30}Si + ^{186}W, consistent with the presence of quasi-fission. This is believed to be the first observation of quasi-fission for a projectile as light as ^{19}F on a non-actinide target. Quasi-fission was shown conclusively to compete not only with fusion-fission reactions but also with fusion-ER reactions at low angular momentum. Using this information and results from other experiments, a clear threshold for quasi-fission may be predicted.

The effect of the $N = 126$ closed shell on the decay of compound nuclei formed in heavy-ion capture reactions has generally been neglected, the excitation energy of the compound nuclei being sufficiently high as to destroy the shell and pairing effects evident in ground-state nuclei [Sier86]. However recent experimental results by Shrivastava *et al.* [Shri99] were interpreted as showing the presence of shell effects in the angular distribution of fission fragments from the compound nucleus ^{210}Po ($N = 126$), but not from the compound nucleus ^{206}Po ($N = 122$).

Since the compound nucleus ^{216}Ra is only two neutrons away from the $N = 126$ closed shell, this claim was investigated by studying a series of reactions chosen to produce compound nuclei with neutron numbers encompassing $N = 126$. The reactions ^{16}O + ^{192,194,196,198}Pt and ^{18}O + ^{196,198}Pt which lead to the compound nuclei, ^{208,210,212,214,216}Rn ($N = 122$, 124, 126, 128 and 130), were chosen because the compound nuclei were unlikely to exhibit a significant contribution from quasi-fission, would have similar projectiles and targets, and would form compound nuclei similar to the ^{210}Po nucleus. Detailed measurements were made of the fission cross-sections and fission fragment angular distributions for these six reactions. In addition, for two of the reactions, ^{16}O + ^{194}Pt and ^{18}O + ^{198}Pt, ER cross-sections were determined by precise measurements of ER α-decay. Thereby capture cross-section and angular momentum distributions could be obtained. The results from the six O + Pt reactions were compared to models of compound nucleus decay, either with or without shell and pairing enhancements.

All the model calculations in this work were performed using a new Monte Carlo statistical model (SM) code called JO_SHELL, written as part of this work. Like most statistical models, it is based on the formation of a fully equilibrated compound nucleus, and does not take into consideration quasi-fission. The new code is derived in part from codes by Lestone [Lest90, Lest91, Lest93] and Junghans *et al.* [Jung98]. It allows the inclusion of shell and pairing effects on nuclear level densities, with these effects decreasing with increasing excitation energy.

The new SM code was used in conjunction with the Transition State Model (TSM) of fission to provide predictions of both fission and ER characteristics. Accurate angular momentum distributions for each reaction and energy were used in the model codes. Capture angular momentum distributions were obtained by fitting both the experimental capture cross-sections (σ) and the capture barrier distributions ($d^2(E\sigma)/dE^2$) with simplified coupled-channels calculations [Dass83A, Dass83B].

If the decay of compound nuclei are affected by localised effects of closed shells, as claimed by Shrivastava *et al.* [Shri99], it was expected that the use of shell and pairing enhancements in the calculation of the level densities in the SM code would reflect these effects. Both the fission probabilities and the fission fragment angular distributions were examined for such localised shell effects. However, no effects close to the $N = 126$ closed shell were observed in the experimental measurements from the six O + Pt reactions, or in the model calculations either with or without shell and pairing enhancements.

The structure of this thesis is as follows:

Chapter 2: Theory. This chapter details theoretical descriptions of heavy-ion capture and decay processes. It discusses capture reactions including the interaction potential of the projectile and target, the partial wave representation of capture, capture barrier distributions and the coupled-channels methodology. The decay of compound nuclei is described in terms of the various models; liquid drop models, the Transition State Model and the statistical model. This is followed by an outline of other influences on compound nucleus reactions.

Chapter 3: Experimental Methods. A description of how the experimental measurements were made is presented in Chapter Three. It includes details of beam production using the ANU 14UD accelerator, the targets used, and the detection

equipment and procedures. Data extraction methods are described in detail.

Chapter 4: Results and Analysis. Chapter Four presents the results of the experimental measurements made in this work. Results from the six O + Pt reactions studied as part of the closed shell investigation are presented separately from the three ^{216}Ra compound nucleus reactions used to investigate entrance channel effects. Analysis of the results, and comparison with model calculations are presented separately for the two groups of reactions.

Chapter 5: Entrance Channel Effects in the Decay of Compound Nuclei. This chapter discussed the significance of the entrance channel dependent decay found in this work, and provides an interpretation of the physics involved. The results from this work are used together with previous studies to predict thresholds for quasi-fission. The implications for other reactions are outlined.

Chapter 6: Summary and Conclusion. The last chapter summarises the results, analysis and discussion presented in this work, and highlighting its most significant findings.

CHAPTER 2

Theory

Before discussing the current experimental work and results, the theoretical descriptions of heavy-ion capture reactions and the mechanisms by which compound nuclei decay are reviewed. Also discussed are several models which have been developed based on these theoretical descriptions, together with their associated computer codes, and the limitations of these models in describing heavy-ion reactions.

This chapter begins with a discussion of heavy-ion capture reactions, including the Coulomb barrier, the coupled-channels methodology, and capture barrier distributions. Liquid drop models of excited nuclei are covered in Section 2.2. Section 2.3 examines fission, the angular distribution of fission fragments, and the Transition State Model which is used to describe fission. Section 2.4 describes particle evaporation from a hot fused nucleus, and the production of evaporation residues. Decay probabilities for fission and evaporation are detailed in Section 2.5, together with statistical model codes. The last section, 2.6, describes other reaction mechanisms which can lead to incomplete fusion and quasi-fission.

2.1 Capture Reactions

2.1.1 The Interaction Potential

When two nuclei approach one another, whether they fuse or not is determined primarily by their relative kinetic energy and the potential energy between the two nuclei, known as the interaction potential. The interaction potential is the sum of three terms; the repulsive Coulomb potential ($V_{Coulomb}$) which results from the positively charged protons; the attractive nuclear potential ($V_{nuclear}$) resulting from

the short range attraction between nucleons; and a centrifugal potential ($V_{centrifugal}$) which comes from conservation of angular momentum ($l\hbar$) in the collision. For spherical inert nuclei, the interaction potential is dependent only on the distance (r) between their centres, and can be written as

$$V_l(r) = V_{nuclear}(r) + V_{Coulomb}(r) + V_{centrifugal}(r) \tag{2.1}$$

The interaction potential, equation 2.1, is only valid when the overlap between the two nuclei is not significant. Below this distance the Coulomb potential cannot be considered as a two body function, and also other effects such as friction and loss of projectile and target identity become important.

2.1.1.1 Nuclear Potential

The nuclear potential (in MeV) is taken in the present work to have a Woods-Saxon form [Brog81]:

$$V_{nuclear}(r) = \frac{-V_0}{1 + \exp[(r - R_N)/a_0]} \tag{2.2}$$

where V_0 is the potential depth (in MeV), a_0 is the surface diffuseness parameter (in fm), R_N is the nuclear radius $R_N = r_N(A_1^{1/3} + A_2^{1/3})$ fm, A_1 and A_2 are the mass numbers of the projectile and target respectively, and r_N is the nuclear radius parameter (in fm).

2.1.1.2 Coulomb Potential

The Coulomb potential (in MeV) is given by [Birk79]:

$$V_{Coulomb}(r) = \begin{cases} \dfrac{Z_1 Z_2 e^2}{4\pi\epsilon_0 r} & ; \text{for } r \geq R_C \\ \dfrac{Z_1 Z_2 e^2 (3R_C^2 - r^2)}{8\pi\epsilon_0 R_C^3} & ; \text{for } r < R_C \end{cases} \tag{2.3}$$

where Z_1 and Z_2 are the charge numbers of the projectile and target respectively, R_C is the charge radius ($R_C = 1.2(A_1^{1/3} + A_2^{1/3})$ fm), e is the unit charge, ϵ_0 is the permittivity of free space, and $\frac{e^2}{2\pi\epsilon_0} = 1.44$ fm.

2.1.1.3 Centrifugal Potential

The Centrifugal potential (in MeV) is given by [Brog81];

$$V_{centrifugal}(r) = \frac{l(l+1)\hbar^2}{2\mu r^2} \tag{2.4}$$

where l is the orbital angular momentum quantum number, $\hbar = h/2\pi$, h is Planck's constant, and μ is the reduced mass of the system, $\mu = \frac{A_1 A_2}{A_1+A_2}$, in units of the atomic mass.

The angular momentum, $l\hbar$, is equal to the product of the initial relative momentum of the projectile and target, p_∞, and the impact parameter, b.

$$l\hbar = bp_\infty \tag{2.5}$$

The impact parameter is the perpendicular distance between the projectile's initial trajectory and the centre of the target nucleus. The initial relative momentum is related to the reduced de-Broglie wavelength λ by $p_\infty = \hbar/\lambda$.

2.1.2 The Coulomb Barrier

When a projectile nucleus collides head-on with a target nucleus, the impact parameter, b, and the angular momentum $l\hbar$ in the collision are both zero. In this case it can be seen that the interaction potential (equation 2.1) is dependent only on the nuclear ($V_{nuclear}$) and Coulomb ($V_{Coulomb}$) potentials. The interaction potential forms a maximum known as the Coulomb barrier (or fusion barrier), of height B_0, at radius R_0 (see Figure 2.1). Classically, for capture to take place in a head-on collision, the centre-of-mass kinetic energy must be greater than the height of the Coulomb barrier. Once the nuclear densities overlap, nucleon-nucleon interactions cause a loss of kinetic energy, and the two nuclei can get trapped in the potential pocket inside the Coulomb barrier to form a compound nucleus. The term compound nucleus is used in this work to refer to any combined system of projectile and target where the kinetic energy of the projectile is fully damped. This is broader than the usual definition of compound nucleus, which refers to a combined system which is fully equilibrated, and is thus at its equilibrium deformation.

For collisions with impact parameters greater than zero, ($b > 0$, $l > 0$), the centrifugal potential ($V_{centrifugal}$) is non-zero. As l increases, the height of the

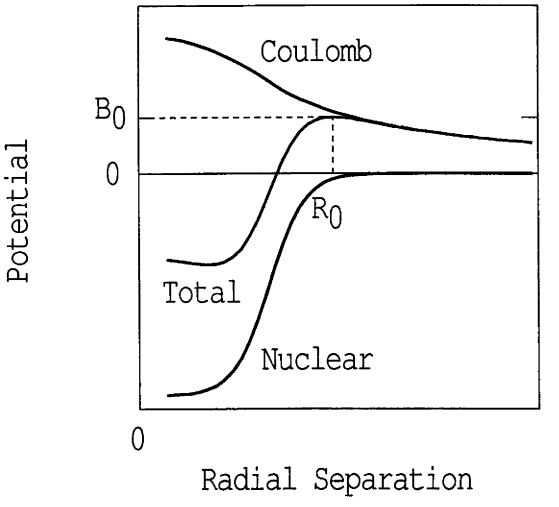

Figure 2.1: The $l = 0$ interaction potential (red line), as a function of nuclear separation, forms a maximum known as the Coulomb barrier, with height B_0, located at radial separation R_0.

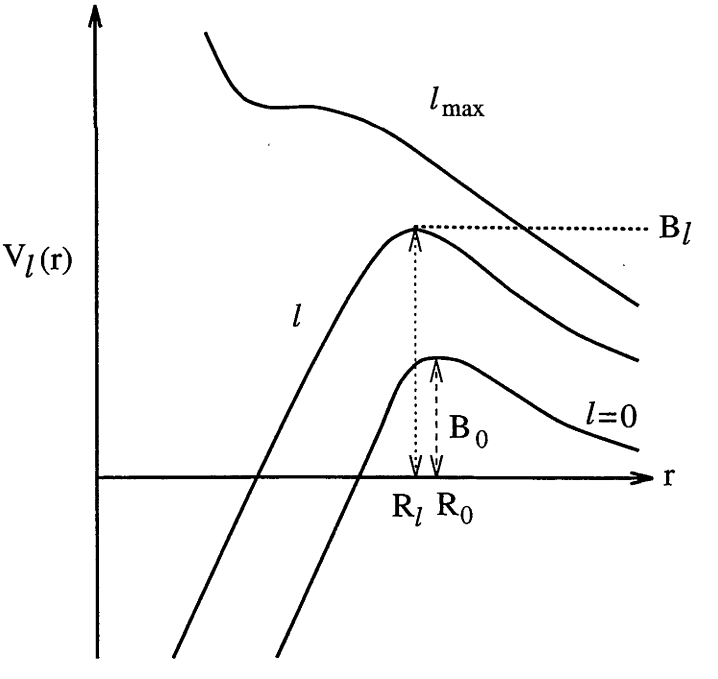

Figure 2.2: The interaction potential $V_l(r)$, as a function of the angular momentum quantum number l. For $l = 0$ the Coulomb barrier occurs at R_0 and has height B_0. As l increases the barrier height increases and occurs at a smaller separation, R_l. At $l = l_{max}$ the interaction potential does not have a potential pocket but continues to increase with decreasing separation. [Rowl89]

barrier B_l increases, and occurs at a smaller separation R_l (see Figure 2.2). At a critical angular momentum l_{max}, the interaction potential no longer exhibits a peak with a potential pocket inside. At this angular momentum capture is no longer possible, within this simple model.

Although classically the interaction potential forms an impenetrable barrier, quantum mechanically, tunnelling through the barrier and reflection above the barrier occur.

2.1.3 Partial Wave Representation

Due to the importance of angular momentum in capture reactions, capture cross-sections are usually described in terms of partial waves. The simplest partial wave description is the one-dimensional barrier penetration model (so named because the potential depends only on one variable, the separation r). Here the capture cross-section $\sigma(E)$ is given by the summation over partial waves,

$$\sigma(E) = \frac{\pi\hbar^2}{2\mu E}\sum_{l=0}^{\infty}(2l+1)\mathcal{T}_l(E) \tag{2.6}$$

where E is the centre-of-mass energy and $\mathcal{T}_l(E)$ is the capture (or transmission) probability.

2.1.3.1 Reduced Cross-sections

By removing the projectile and target dependent terms from equation 2.6, the reduced capture cross-section can be defined as:

$$\overline{\sigma}(E) = \sigma(E)\frac{2\mu E}{\pi\hbar^2} = \sum_{l=0}^{\infty}(2l+1)\mathcal{T}_l(E) \tag{2.7}$$

If the decay of a compound nucleus is independent of the reaction entrance channel, then for a given angular momentum distribution, the reduced cross-sections for two different reactions should show no entrance channel dependence. The concept of the reduced cross-section is used throughout this work to compare compound nucleus decay.

2.1.3.2 Sharp Cut-Off Model

In the classical case, also known as the sharp cut-off model, the capture probability is a function only of the barrier height B_l,

$$\mathcal{T}_l(E) = \begin{cases} 1 & ; \text{for } E \geq B_l \\ 0 & ; \text{for } E < B_l \end{cases} \tag{2.8}$$

and the maximum angular momentum is $l_{max}\hbar$.

In this case, it is assumed that the barrier radius is independent of angular momentum, $R_l = R_0$. Therefore combining equations 2.6 and 2.8 the capture cross-section for $E \geq B_0$ and $l \gg 1$ can be expressed as:

$$\sigma(E) = \frac{\pi\hbar^2}{2\mu E}\sum_{l=0}^{l_{max}}(2l+1) \tag{2.9}$$

$$\approx \frac{\pi\hbar^2}{2\mu E} l_{max}^2 \tag{2.10}$$

Combining equations 2.1, 2.4, and 2.10 leads to,

$$\sigma(E) = \frac{\pi\hbar^2}{2\mu E}\left[\frac{\{2\mu(E-B_0)\}^{1/2}R_0}{\hbar}\right]^2 \tag{2.11}$$

$$E\sigma(E) = \pi R_0^2(E - B_0) \tag{2.12}$$

Equation 2.12 gives a linear relationship between $E\sigma(E)$ and E, which approximates experimental data above the Coulomb barrier. However it can be seen in Figure 2.3 that the classical model (equation 2.12) does not reproduce the data representation below, or near, the Coulomb barrier, nor at energies high above the Coulomb barrier. Quantum tunnelling through the barrier and reflection above the barrier result in discrepancies between equation 2.12 and experimental data around the Coulomb barrier region, particularly at below-barrier energies. At higher energies, well above the barrier region, the assumption that the barrier radius $R_l = R_0$ becomes increasingly poor, as the barrier radius shifts to smaller r (see Figure 2.2) leading to an over-estimation of the capture cross-section.

2.1.3.3 One-Dimensional Barrier Penetration Model

The inclusion of quantum tunnelling can be achieved approximately by using the Hill-Wheeler [Hill53] expression for the tunnelling probability. This uses a parabolic

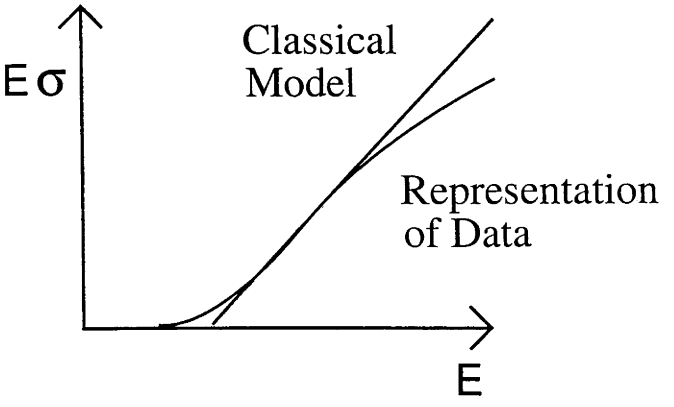

Figure 2.3: Capture excitation function showing $E\sigma$ as a function of E. The blue line shows the classical relationship in equation 2.12, while the red line shows a realistic representation of reaction data.

approximation to the Coulomb barrier of the interaction potential (equation 2.1), giving the capture probabilities as:

$$\mathcal{T}_l = \frac{1}{1 + \exp\left[\frac{2\pi}{\hbar\omega}(B_l(R_0) - E)\right]} \tag{2.13}$$

The product $\hbar\omega$ is the curvature of the parabola, and $B_l(R_0)$ is the l-dependent barrier height, which is sometimes assumed to be at a fixed separation R_0. Using the Hill-Wheeler capture probability (equation 2.13) in equation 2.6, and replacing the sum over l with an integral, gives the relationship often referred to as the Wong cross-section [Wong73]:

$$E\sigma(E) = \frac{\hbar\omega R_0^2}{2} \ln\left[1 + \exp\left\{\frac{2\pi}{\hbar\omega}(E - B_0)\right\}\right] \tag{2.14}$$

$$\equiv \frac{\hbar\omega R_0^2}{2} \ln(1 + e^x) \quad ; \quad x = \left\{\frac{2\pi}{\hbar\omega}(E - B_0)\right\} \tag{2.15}$$

At below- and near-barrier energies, the one-dimensional barrier penetration model gives a good fit to experimental capture cross-sections for reactions of light nuclei, where the participants behave much like inert spherical nuclei. However, for reactions of heavy nuclei, where other degrees of freedom become important, this model does not adequately fit the experimental data.

2.1.3.4 Degrees of Freedom

Several degrees of freedom can influence the capture reaction. Take for example, the case of a spherical projectile and a deformed target. The distance between the centres of the nuclei, r, is no longer the only dimension of interest. When compared to collisions of two spherical nuclei, collisions with the tips of the deformed nucleus encounter a lower potential barrier, at a larger separation r, while those with the flattened sides of the deformed nuclei encounter a higher barrier, at a smaller separation. Figure 2.4 demonstrates the effect of deformation on the excitation functions for $^{16}O+^{A}Sm$ reactions [Stok78, Dasg98], where the isotopes of samarium make a transition from spherical (^{144}Sm) to prolate deformed (^{154}Sm).

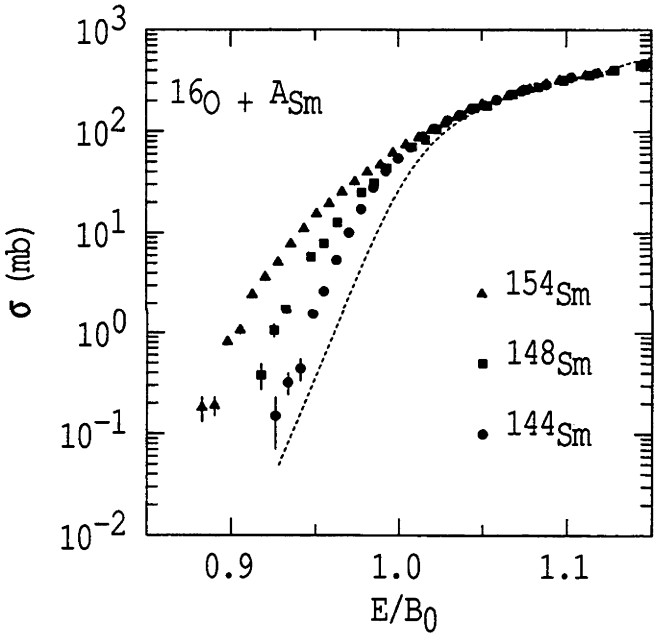

Figure 2.4: Capture excitation functions for $^{16}O+^{A}Sm$ reactions for various samarium isotopes. The isotopes of samarium become progressively more deformed with increasing A [Dasg98]. The dashed line shows calculated cross-sections assuming a single barrier at energy B_0.

In addition to deformation, capture can be influenced by other physical processes such as nuclear surface vibrations, and the transfer of nucleons between the target and projectile. The effect of coupling to these other degrees of freedom is to replace [Stea86, Beck88, Dass83A, Dass83B] the single Coulomb barrier with a distribution of barrier energies.

2.1.4 Capture Barrier Distributions

In order to understand capture barrier distributions, and their usefulness in interpreting experimental data, it is helpful to take a further look at the one-dimensional barrier penetration model. The first and second derivatives, with respect to E, of equation 2.15 are [Rowl91, Dasg98]:

$$\frac{1}{\pi R_0^2}\frac{d(E\sigma)}{dE} = \frac{1}{(1+e^x)} \tag{2.16}$$

$$\frac{1}{\pi R_0^2}\frac{d^2(E\sigma)}{dE^2} = \frac{2\pi}{\hbar\omega}\frac{e^x}{(1+e^x)^2} \tag{2.17}$$

$$\equiv G(E-B_0) \tag{2.18}$$

Looking again at the classical case, by taking the limit $\hbar \to 0$, equations 2.15, 2.16, and 2.18 become:

$$E\sigma = \begin{cases} 0 & ;\text{ for } E < B_0 \\ \pi R_0^2(E-B_0) & ;\text{ for } E \geq B_0 \end{cases} \tag{2.19}$$

$$\frac{d(E\sigma)}{dE} = \begin{cases} 0 & ;\text{ for } E < B_0 \\ \pi R_0^2 & ;\text{ for } E \geq B_0 \end{cases} \tag{2.20}$$

$$\frac{1}{\pi R_0^2}\frac{d^2(E\sigma)}{dE^2} = \delta(E-B_0) \tag{2.21}$$

It can be seen that the classical limit of the one-dimensional barrier penetration model (equation 2.19) is the same as in the sharp cut-off model (equation 2.12). Of more interest is the result that the function on the left-hand side of equation 2.21 neatly returns the barrier energy B_0.

Now, instead of a single barrier B_0, take a continuous distribution of barriers with energy B, and probability $D(B)$. The total capture cross-section is then given by [Stel88, Rowl91]:

$$\sigma(E) = \int_0^\infty \sigma(E,B)D(B)dB \tag{2.22}$$

where $\sigma(E,B)$ is the capture cross-section measured at energy E, involving the sum over all l for the barrier B, and $D(B)$ is normalised as $\int D(B)dB = 1$.

The equivalent of equation 2.18 then becomes [Rowl91, Dasg98]:

$$\frac{1}{\pi R_0^2}\frac{d^2(E\sigma)}{dE^2} = \int_0^\infty G(E-B)D(B)dB \tag{2.23}$$

and taking the classical limit gives:

$$\frac{1}{\pi R_0^2}\frac{d^2(E\sigma)}{dE^2} = D(E) \tag{2.24}$$

Thus the quantity on the left-hand side simply returns the capture barrier distribution $D(E)$. Using this technique it was shown by Rowley *et al.* [Rowl91] that the capture barrier distribution can be extracted directly from experimental data. In the quantum mechanical treatment (equation 2.23), the capture barrier distribution is similar to the classical case, but smeared out by the Gaussian function $G(E-B)$, which is symmetric about its peak at $E = B$, and has unit area. The peak width has a full-width-half-maximum (FWHM) $\approx 0.56\hbar\omega$, typically 2-3 MeV for the reactions studied here.

Figure 2.5 demonstrates the capture barrier distribution concept. It includes an illustrative capture barrier distribution (2.5a), the resultant function $E\sigma$ (2.5b), and the first (2.5c), and second (2.5d) derivatives of $E\sigma$. The classical case is shown by the thick broken lines, while the quantum mechanical result is shown by the thick blue curves.

2.1.5 Capture Barrier Distributions and Experimental Data

As mentioned previously, Rowley *et al.* [Rowl91] showed that experimental data could be used to extract capture barrier distributions, and illustrated that the second derivative of the discrete experimental data could be determined by a point-difference method. For experimental cross-sections σ_1, σ_2, and σ_3 measured respectively at centre-of-mass energies E_1, E_2, and E_3, the second derivative of $E\sigma$ at energy $(E_1 + 2E_2 + E_3)/4$ is approximately given by the point-difference formula [Dasg98]:

$$\frac{d^2(E\sigma)}{dE^2} = 2\left(\frac{E_3\sigma_3 - E_2\sigma_2}{E_3 - E_2} - \frac{E_2\sigma_2 - E_1\sigma_1}{E_2 - E_1}\right)\left(\frac{1}{E_3 - E_1}\right) \tag{2.25}$$

For experimental data recorded at equal energy steps, $\Delta E = (E_2 - E_1) = (E_3 - E_2)$, equation 2.25 becomes:

$$\frac{d^2(E\sigma)}{dE^2} = \left(\frac{E_3\sigma_3 - 2E_2\sigma_2 + E_1\sigma_1}{\Delta E^2}\right) \tag{2.26}$$

As the point-difference formula produces a smoothing of the capture barrier distribution, when comparing capture barrier distributions from experimental data and

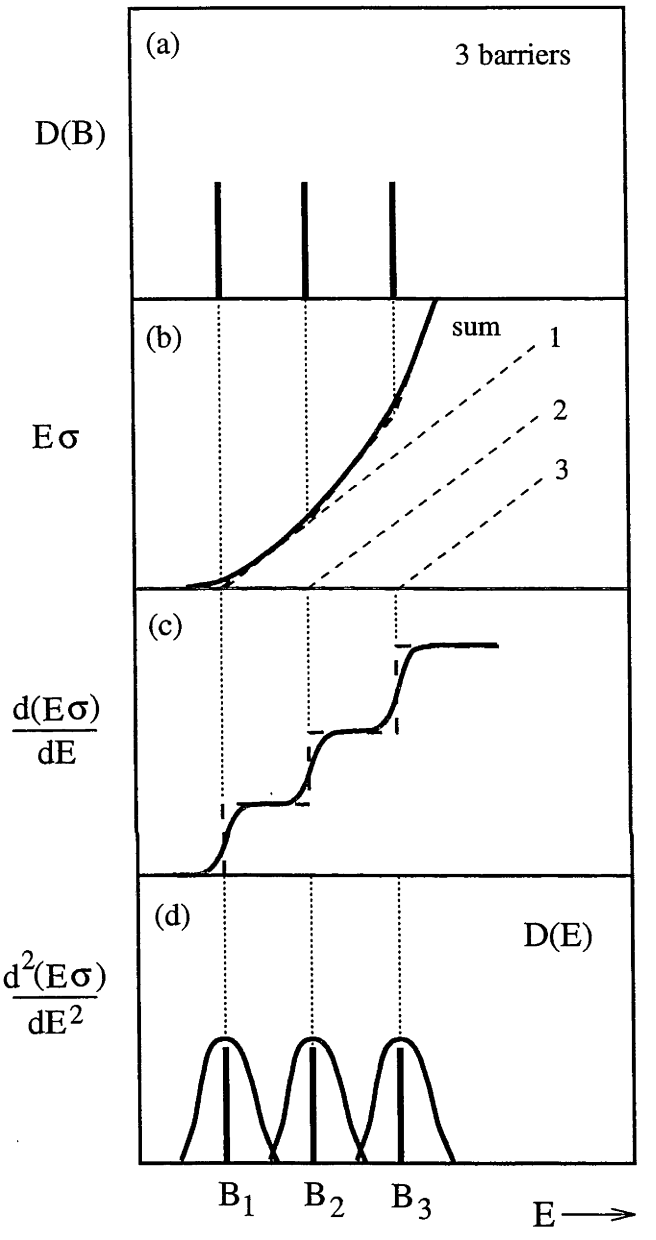

Figure 2.5: Illustrative capture barrier distribution [Mort95A]. (a) In this example the barrier distribution $D(B)$ is represented by three barriers having the same separation in energy and the same weight. The thick vertical lines represent the positions and weights of the barriers. (b) The thin broken lines marked 1, 2, and 3 are the quantities $E\sigma_B$ calculated from the classical cross-sections for the respective barriers B_1, B_2, and B_3. The thick broken line is the quantity $E\sigma$ for all the barriers. (c) The first derivative of $E\sigma$ is a series of steps (thick broken line). (d) The second derivative of $E\sigma$ returns the original discrete distribution of barriers $D(E)$ as given in equation 2.24. When the effects of quantum tunnelling are included, $E\sigma$ and its derivatives are a smooth function of E (thick blue curves). Equation 2.23 is shown by the thick blue curve in frame (d).

theory it is necessary to process the theoretical excitation function using the same energy step. The statistical uncertainty δ_c of the point-difference capture barrier function 2.26 at energy E is given by [Wei91]:

$$\delta_c \simeq \left(\frac{E}{\Delta E^2}\right)\left[(\delta\sigma_1)^2 + 4(\delta\sigma_2)^2 + (\delta\sigma_3)^2\right]^{1/2} \tag{2.27}$$

where $\delta\sigma_i$ is the absolute error in the cross-section σ_i.

Thus the uncertainty δ_c will increase with increasing energy E and decrease with increasing energy step ΔE.

2.1.6 Coupled-Channels Calculations

For capture reactions which include coupling to various channels, theoretical calculations of capture excitation functions, and subsequently capture barrier distributions, are usually handled using coupled-channels equations. A brief description of this formalism is given here.

Based on the time independent Schrödinger equation, capture can be modeled by solving a set of coupled-channels equations [Dass83A]:

$$\left[-\frac{\hbar^2}{2\mu}\frac{d^2}{dr^2} + V_l(r) - E\right]\chi_\alpha(r) = -\sum_\beta \langle\alpha|\mathbf{H}_0 + V_{cpl}(r,\xi)|\beta\rangle\chi_\beta(r) \tag{2.28}$$

where $\mathbf{H}_0$ is the intrinsic Hamiltonian, and $|\alpha\rangle$ and $|\beta\rangle$ are the associated eigenvectors for the initial α and final β configurations of the system. $V_l(r)$ is the interaction potential (equation 2.1) for two nuclei at centre-of-mass separation distance r, and $\chi_\alpha(r)$ and $\chi_\beta(r)$ are the relative motion wave-functions. The coupling interaction is given by $V_{cpl}(r,\xi)$, ξ being an internal structure variable.

The reflection and transmission functions in each channel are denoted by r_α and t_α respectively, and δ is the Kronecker function of the orthogonality property of the internal wave-function. Equations 2.28 are to be solved for the following boundary conditions:

$$\chi(r) \to \begin{cases} \delta_{\alpha 0}e^{-ik_\alpha r} + r_\alpha e^{ik_\alpha r} & r \to +\infty \\ t_\alpha e^{-ik_\alpha r} & r \to -\infty \end{cases} \tag{2.29}$$

Here $\hbar^2 k_\alpha^2/2\mu = E - \varepsilon_\alpha$, and ε_α is the sum of the eigenvalues of the non-interacting system.

2.1.6.1 Decoupling the Equations

In order to simplify the above set of equations, the coupling interaction $V_{cpl}(r,\xi)$ is factored into a relative-motion part, $F(r)$, and an intrinsic part, $G(\xi)$ [Dass83B]. The coupling matrix $\mathbf{M}_{\alpha\beta}$ can then be written:

$$\mathbf{M}_{\alpha\beta} = \langle\alpha|\mathbf{H}_0 + V_{cpl}|\beta\rangle = \delta_{\alpha\beta}\varepsilon_\alpha + F(r)\langle\alpha|G(\xi)|\beta\rangle \tag{2.30}$$

In a further approximation, known as the constant coupling approximation, it is assumed that the relative-motion function is spatially constant in the region of the barrier, $F(r) = F_0$. The coupled equations can then be decoupled and give:

$$\left[-\frac{\hbar^2}{2\mu}\frac{d^2}{dr^2} + V_l(r) + \lambda_\beta(r) - E\right]\sum_\alpha \mathbf{U}_{\beta\alpha}(r)\chi_\alpha(r) = 0 \tag{2.31}$$

where $\mathbf{U}_{\beta\alpha}(r)$ is a unitary matrix which diagonalises the coupling matrix $\mathbf{M}_{\alpha\beta}$ to give a set of eigenvalues $\lambda_\beta(r)$.

The capture excitation function can then be calculated using the one-dimensional barrier penetration model (equation 2.6) where the capture probability is given by:

$$\mathcal{T}_l(E) = \sum_\beta |\mathbf{U}_{\beta 0}(r)|^2 \mathcal{T}_l[E, V_l(r) + \lambda_\beta(r)] \tag{2.32}$$

The effect of the coupling is to replace the single barrier $V_l(r)$ with a set of barriers $V_l(r) + \lambda_\beta(r)$. The capture probability then becomes a weighted average of the capture probabilities for each effective barrier.

2.1.6.2 Coupled-Channels Computer Code

In principle, there are an infinite number of equations to be solved. However, practically it is necessary to truncate the number of equations down to a few potentially important channels. Several computer codes solve the decoupled equations by diagonalising the coupling matrix, and include CCFUS [Dass87], and its developments CCDEF [Fern89], and CCMOD/CCMPH [Dasg92, Dasg97]. Alternatively, exact coupled-channels codes solve equations 2.28 exactly for a given set of wavefunctions, as in the code CCFULL [Hagi97, Hagi99].

In this work the computer code CCMPH (which can handle multiphonon excitations) using couplings expected for a given reaction, was used to calculate capture

cross-section and capture barrier distributions, in order to reproduce the experimental data. Although the CCPMH code was unable to handle properly, high energy excited states, such as the first excited state of the ^{12}C nucleus, it has been shown [Taki94, Hagi97] that couplings to states with high excitation energy only leads to a shift in energy of the barrier distribution without affecting the shape of the barrier distribution. For the $^{30}Si+^{186}W$ reaction, calculations using the CCMPH code were compared to those from the CCFULL code which, unlike the CCMPH code, could include both target and projectile couplings realistically.

2.1.7 Angular Momentum Distributions

It has been shown [Rowl93, Bala96] that for a capture reaction, the partial cross-sections for each l-wave, known as the angular momentum distribution (or just l-distribution), can be obtained from the capture excitation function. In fact, a model that reproduces both the capture excitation function and the barrier distribution is expected to give an accurate prediction of the angular momentum distribution [Dasg98]. Similarly, from an accurately measured angular momentum distribution, the capture barrier distribution should in principle be obtainable.

Figure 2.6 shows angular momentum distributions for calculations made with the sharp cut-off model, the one-dimensional barrier penetration model, and for a coupled-channels calculation with several channels leading to a distribution of barriers. The shape of the sharp cut-off distribution (solid line) is the same as for classical collisions. When the quantum effects are taken into consideration, as in the one-dimensional barrier penetration model (dashed line), the distribution is smoothed around the classical maximum. Coupling to a large number of channels, such as for target deformation, leads to a further broadening of the angular momentum distribution (dotted line).

The angular momentum distribution can have a strong influence on compound nucleus decay. Thus, it is important to use accurate angular momentum distributions, in particular for modelling fission and particle evaporation probabilities, and fission fragment angular distributions.

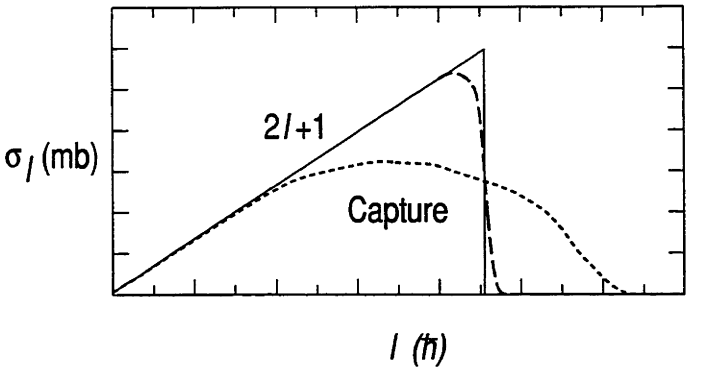

Figure 2.6: Angular Momentum Distributions: shown are l-distributions calculated using the sharp cut-off model (solid line), the one-dimensional barrier penetration model (dashed line), and for a coupled-channels calculation with a wide capture barrier distribution (dotted line).

2.2 Liquid Drop Models of the Nucleus

This section describes the formalisms for discussing the energy of excited or 'hot' nuclei formed in capture reactions. To determine the excitation energy E_x, of 'hot' nuclei, an energy 'base-line' must be established. The most obvious 'base-line' is the ground-state energy of the non-rotating nucleus. However, for excited nuclei formed in capture reactions this is not always appropriate. High excitation energy and angular momenta will destroy shell effects, and the nucleus will behave as though the smoothed liquid drop ground-state energy is the base-line.

2.2.1 The Charged Liquid Drop Model

The first model that attempted to describe the binding energy or ground-state energy of a nucleus, is the charged liquid drop model (LDM). This model gives a good description of the average trends in measured ground-state nuclear masses for nuclei with $A \geq 10$. For a nucleus with charge Z and mass A, the liquid drop ground-state mass $M_{LDM}(Z, A)$ is given by the expression;

$$M_{LDM}(A, Z) = M_N N + M_P Z + E_v + E_s + E_C \tag{2.33}$$

where the neutron mass is $M_N = 1.008665$ amu (atomic mass units), the proton mass is $M_N = 1.00727$ amu, and N is the number of neutrons $N = A - Z$. The volume E_v, surface E_s, and Coulomb E_C energies, with associated constants C_v, C_s, and C_C are given by:

$$E_v = -C_v A \tag{2.34}$$

$$E_s = f(shape)E_s^{(0)} = f(shape)C_s A^{2/3} \tag{2.35}$$

$$E_C = g(shape)E_C^{(0)} = g(shape)C_C \frac{Z^2}{A^{1/3}} \tag{2.36}$$

where the superscript (0) denotes sphericity.

Due to the saturation of nucleon density, each nucleon inside the nucleus is on average surrounded by the same number of neighbours, and E_v is proportional to A, with proportionality constant C_v. For the nucleons near the surface of the nucleus, E_s is analogous to the surface tension of a liquid drop, and is proportional to the nuclear surface area. The quantity $f(shape)$ is the ratio of the surface area of the desired nuclear shape to that of a sphere of the same volume. This surface term has the associated constant C_s.

The Coulomb energy E_C is due to the repulsion of the positively charged protons in the nucleus. The quantity $g(shape)$ is the ratio of the electrostatic energy of the desired nuclear shape to that of a sphere of the same Z and A, and C_C is a constant.

In addition, a symmetry term reflecting the observed tendency of nuclei to be most stable for $Z = N$, is usually incorporated into the nuclear terms (equations 2.34 and 2.35) by assuming:

$$C_v = a_v \left[1 - \kappa \left(\frac{N-Z}{A}\right)^2\right] \tag{2.37}$$

$$C_s = a_s \left[1 - \kappa \left(\frac{N-Z}{A}\right)^2\right] \tag{2.38}$$

where a_v, a_s, κ are constants. Using parameters from Green, [Gree54], and Myers and Swiatecki [Myer66, Myer67] the expressions for the energy terms (in MeV) for spherical nuclei become:

$$E_v = -15.494 \left[1 - 1.783 \left(\frac{N-Z}{A}\right)^2\right] A \tag{2.39}$$

$$E_s^{(0)} = +17.944 \left[1 - 1.783 \left(\frac{N-Z}{A}\right)^2\right] A^{2/3} \tag{2.40}$$

$$E_C^{(0)} = +0.7053\frac{Z^2}{A^{1/3}} - 1.1529\frac{Z^2}{A} \tag{2.41}$$

The last term in Equation 2.41 corrects for the diffuseness of the charge distribution near the nuclear surface.

The difference between the LDM ground-state binding energies and the measured ground-state binding energies for a range of atomic masses A can be seen in Figure 2.7. The general trend of the measured energies is well reproduced by the LDM, except for where shell effects are significant around the nuclear magic numbers.

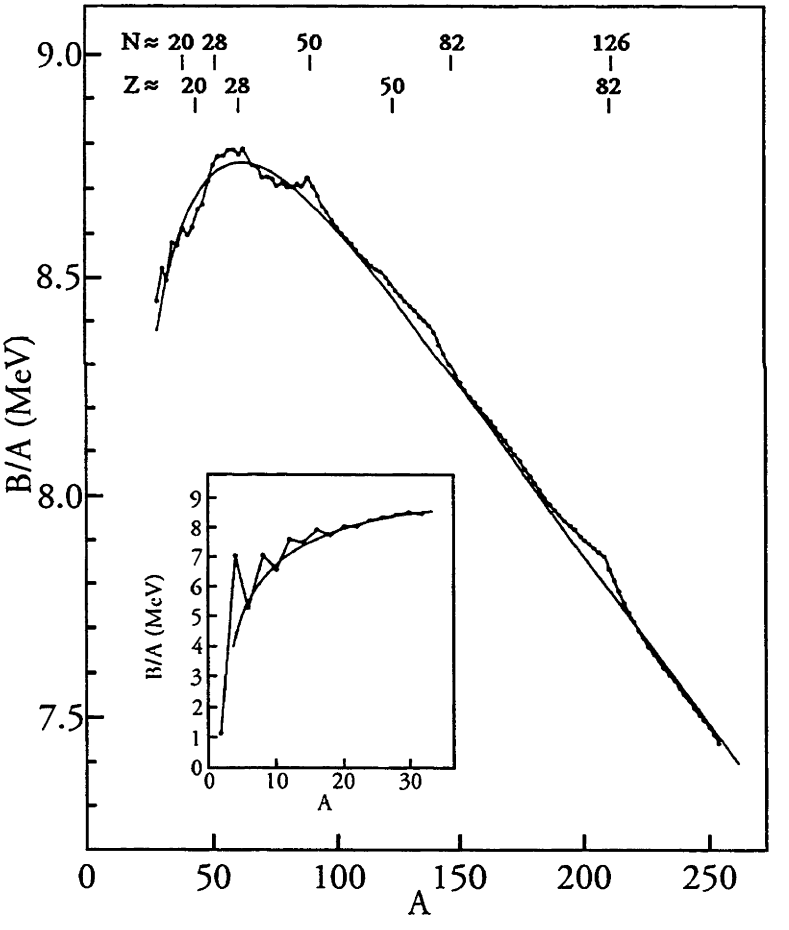

Figure 2.7: Ground-state binding energies as a function of mass number, A. The smooth curved line shows the liquid drop model calculated ground-state binding energies in comparison with the measured ground-state binding energies. Discrepancies occur around the nuclear closed shells.

2.2.2 The Liquid Drop Model and Fission

The LDM in Figure 2.7 is based on a spherical nucleus. However, if nuclear deformation is taken into account, then the LDM can be used to describe the binding energy of a nucleus as its shape evolves during the fission process.

As shown in Equations 2.35 and 2.36, both the surface energy E_s and the Coulomb energy E_C are shape dependent. For a small change in shape from spherical, where the ellipsoidal deformation is specified by the parameter d, the radius for the deformed shape R_d along the elongated axis can be assigned as:

$$R_d = R^{(0)}(1+d) \tag{2.42}$$

where $R^{(0)}$ is the radius for the spherical nucleus.

The surface and Coulomb energies can then be expressed in terms of the changes in surface energy ΔE_s and Coulomb energy ΔE_C [Bohr39] for small values of d:

$$E_s = E_s^{(0)} + \Delta E_s \tag{2.43}$$

$$E_C = E_C^{(0)} + \Delta E_C \tag{2.44}$$

where for small d,

$$\Delta E_s = +2/5 E_s^{(0)} d^2 \tag{2.45}$$

$$\Delta E_C = -1/5 E_C^{(0)} d^2 \tag{2.46}$$

This shows that when the nuclear shape deviates from sphericity, the decrease in Coulomb energy is initially less than the increase in surface energy, and the potential energy of the nucleus increases. However, as the deformation grows, ΔE_s and ΔE_C no longer follow equations 2.45 and 2.46, and the potential energy ceases to increase. This potential energy peak is known as the saddle-point, and its height above the nucleus equilibrium potential is known as the fission barrier. Further deformation leads to a decrease in the potential energy, accelerating the nuclei to separate into two fission fragments, known as scission.

In this picture, for increasing deformation, there must be an initial increase in potential. For the nucleus to be stable against fission decay [Vand73]:

$$-\frac{\Delta E_s}{\Delta E_C} < 1 \tag{2.47}$$

or using equations 2.45 and 2.46

$$\frac{E_s^{(0)}}{2E_C^{(0)}} = x < 1 \tag{2.48}$$

The quantity x is the fissility parameter. From the nuclear surface energy (equation 2.40) and the Coulomb energy (equation 2.41) the fissility parameter can be written as:

$$x = \frac{Z^2}{A} \frac{1}{50.883 \left[1 - 1.783 \left(\frac{N-Z}{A}\right)^2\right]} \tag{2.49}$$

The fissility parameter is a measure of nuclear stability against fission. Equation 2.49 predicts that nuclei with $Z \geq 120$ do not have a fission barrier, and therefore cannot be stable against fission decay, without an additional stabilising mechanism.

2.2.3 The Rotating Liquid Drop Model

In heavy-ion reactions, where l is large, the effect of nuclear rotation needs to be included in the LDM, giving the rotating liquid drop model (RLDM). The rotational energy is given by:

$$E_{rot}(J) = \frac{J(J+1)\hbar^2}{2\mathcal{J}} \tag{2.50}$$

where $J\hbar$ is the angular momentum, and $\mathcal{J}$ is the moment of inertia. A spherical nucleus of mass M, radius R and moment of inertia $\mathcal{J}^{(0)} = \frac{2}{5}MR^2$ has rotational energy:

$$E_{rot}^{(0)}(J) = \frac{J(J+1)\hbar^2}{2\mathcal{J}^{(0)}} \tag{2.51}$$

The angular momentum dependent fission barrier $B_f(J)$ is defined as the difference between the rotational energy at the saddle-point $E_{rot}^{(sp)}(J)$ and the rotational energy at the equilibrium deformation. For nuclei with equilibrium deformations that are spherical, the barrier is given by:

$$B_f(J) = E_{rot}^{(sp)}(J) - E_{rot}^{(0)}(J) \tag{2.52}$$

This is shown graphically in Figure 2.8, where with increasing angular momentum, the rotational energy of the equilibrium deformation increases more rapidly than that of the saddle-point. The height of the fission barrier falls as J^2, so for sufficiently large angular momentum, $B_f(J)$ goes to zero and there is no barrier to fission.

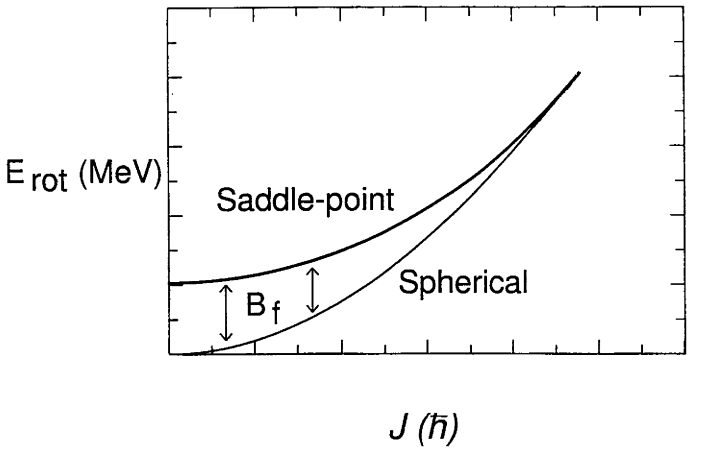

Figure 2.8: The fission barrier, $B_f(J)$, as a function of angular momentum for a nucleus with a spherical equilibrium deformation. The fission barrier is the difference between the rotational energies at the saddle-point and spherical equilibrium deformations.

Analysis of many experimental fission and evaporation residue cross-sections for compound nuclei with $A \approx 200$ using statistical model codes have been performed (e.g. [Leig82]). This analysis indicated that the RLDM fission barriers needed to be scaled by a barrier scaling factor k_f (taken to be independent of J) of between 0.5 and 0.9 [Beck78, Ande79, Plas80, Oert80, Blan82A, Siko82, Hind82, Hind83, Blan82B, Becc83, Plic83, Plas84] in order to fit the experimental data. This reduction was needed to compensate for the RLDM not taking into account the finite range of the nuclear force. Sierk [Sier86] incorporated this effect into the finite range rotating liquid drop model (FRLDM), which predicted lower fission barriers, more consistent with experimental data.

2.2.4 Shell and Pairing Corrections

As shown in Figure 2.7, the LDM discussed above (equation 2.33) does not reproduce the measured ground-state energies around the neutron and proton closed shells. For the measurements mentioned above, interpreted using the standard statistical model codes, it was assumed that the nuclei produced in the heavy-ion fusion reactions have excitation energies high enough to destroy shell effects.

However, the reactions covered by this work lie near or on the $N = 126$ neutron closed shell, and the excitation energy of nuclei facing last chance decay may not be sufficient to negate these effects, and it may be inappropriate to ignore them. In this work, shell and pairing effects, as a function of excitation energy, have been taken into account following the work of Junghans *et al.* [Jung98]. These have been included in a new version of the statistical model code JOANNE [Lest90, Lest91, Lest93], named JO_SHELL (see Section 2.5.4.2).

The shell correction comes from Möller, Nix, Myers and Swiatecki [Möll95], who have calculated and tabulated shell corrections to the FRLDM. The shell energy correction $E_{shell}(Z, N, shape)$ is given by the sum of the proton and neutron shell corrections [Möll95]:

$$E_{shell}(Z, N, shape) = E_{shell}^{proton}(Z, shape) + E_{shell}^{neuton}(N, shape) \tag{2.53}$$

Both terms can be evaluated from a set of calculated single-particle levels using Strutinsky's method [Stru67, Stru68]. The neutron shell correction is given by

$$E_{shell}^{neuton}(N, shape) = \sum_{i=1}^{N} e_i - \tilde{E}^{neutron}(N, shape) \tag{2.54}$$

where e_i are calculated single particle energies and $\tilde{E}^{neutron}(N, shape)$ is the smooth single-particle energy sum [Stru67, Stru68]. An analogous expression holds for protons.

The factor k, a parameter representing the washing out of this shell effect as a function of the effective excitation energy, E_x^*, is given by the relationship [Jung98]:

$$k(E_x^*) = 1 - e^{-\gamma E_x^*} \tag{2.55}$$

with

$$\frac{1}{\gamma} = 0.4\frac{A^{4/3}}{a} \tag{2.56}$$

where a is the level density parameter (see Section 2.5.1).

With an average ground-state pairing gap (MeV) of

$$\Delta = 12B_s/\sqrt{A} \tag{2.57}$$

where B_s is a deformation parameter (see level densities, Section 2.5.1), the microscopic pairing energy correction, in MeV, is given by [Jung98]:

$$E_{pair} = -\frac{1}{4}\Delta^2\frac{6a}{\pi^2} + 2\Delta \tag{2.58}$$

The factor h, which relates to the progressive washing out of the pairing correction as a function of the effective excitation energy E_x^*, with a critical energy $E_{crit} = 10$ MeV, is given by [Jung98]:

$$h(E_x^*) = \begin{cases} 1 - (1 - \frac{E_x^*}{E_{crit}})^2 & ; \text{for } E_x^* < E_{crit} \\ 1 & ; \text{for } E_x^* \geq E_{crit} \end{cases} \tag{2.59}$$

In addition to the microscopic pairing correction above, the effective excitation energy E_x^* is shifted with respect to the excitation energy E_x to accommodate the average pairing energies of even-even, odd mass, and odd-odd nuclei:

$$\begin{aligned} E_x^* &= E_x & ; \text{odd-odd} \\ E_x^* &= E_x - \Delta & ; \text{odd mass} \\ E_x^* &= E_x - 2\Delta & ; \text{even-even} \end{aligned} \tag{2.60}$$

As functions of the excitation energy, these shell and pairing corrections will vary the calculated binding energy between the limits of the measured ground-state energy and the FRLDM ground state energy. The correction to the binding energy is given by:

$$E_{corr} = E_x - [E_x^* + k(E_x^*)E_{shell}(Z, N, shape) + h(E_x^*)E_{pair}] \tag{2.61}$$

2.3 Fission

When a heavy compound nucleus in the actinide region is formed by a capture reaction of two heavy nuclei, it decays either by fissioning, or by evaporating light particles (neutrons, protons and alpha particles), giving either two fission fragments or an evaporation residue (ER). Any remaining energy is then lost through the emission of gamma rays. This work does not discuss the emission of gamma rays, as its focus is on the nuclear mass evolution. This section deals with the fission decay of excited ('hot') compound nuclei. The next Section 2.4 examines light particle evaporation and the formation of evaporation residues. Section 2.5 then describes the relative decay probabilities for fission and evaporation, and computer codes for predicting compound nuclei decay.

When hot nuclei fission, the resultant fission fragments separate with characteristic angular and mass-distributions. By understanding these observables, insight can be achieved into the fission process.

2.3.1 Angular Distribution of Fission Fragments

During fission the compound nucleus separates into two fission fragments and several light particles. In the centre-of-mass frame the fission fragments separate at an angle of 180° to each other. The standard model of fission [Bohr56], known as the Transition State Model (TSM), assumes that the fission fragments are emitted along the direction of the nuclear symmetry axis at scission, and that this direction does not change between the saddle-point (the transition state) and scission. The angular distribution of fission fragments depends on the angular momentum of the nucleus and the orientation of the symmetry axis with respect to the beam direction.

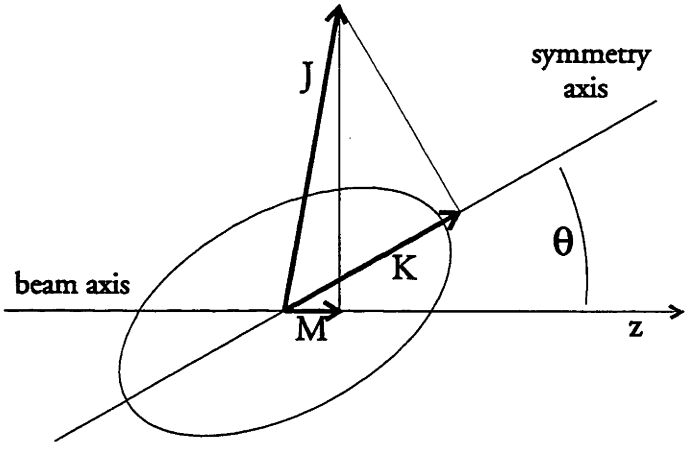

Figure 2.9: Schematic of the angular momentum vectors used to describe fission fragment angular distributions. For a deformed nucleus with symmetry axis at an angle θ to the beam axis z, and total angular momentum quantum number J, the projection of J onto the symmetry axis is given by K and the projection of J onto the beam axis is given by M.

Figure 2.9 gives a schematic picture of the angular momentum vectors used in describing fission fragment angular distributions. For a nucleus with total angular momentum $J\hbar$ and angle θ between the symmetry axis and the beam axis, K is the projection of J onto the symmetry axis and M is the projection of J onto the beam axis. The TSM assumes that the value of K does not change between the saddle-point and scission [Vand73].

2.3.1.1 Transition State Model

For nuclei with large enough excitation energy, the statistical model together with the TSM can be used to describe decay probabilities. Together with the two assumptions above, one further assumes that the excited nuclei have been formed through complete fusion reactions, where the compound nucleus reaches an equilibrated state. Given these assumptions, the fission fragment angular distributions are given by the symmetric-top wave-functions as follows [Back85]:

$$W^J_{MK}(\theta) = \frac{(2J+1)}{4\pi}|\mathcal{D}^J_{MK}(\phi,\theta,\psi)|^2 \tag{2.62}$$

where ϕ, θ and ψ are the Euler angles.

For the case of spin zero nuclei for which the angular momentum vector, $J\hbar$, is perpendicular to the beam axis ($M = 0$), and the two Euler angles ϕ and ψ disappear by taking the absolute square, equation 2.62 reduces to [Back85]:

$$W^J_{0K}(\theta) = \frac{(2J+1)}{4\pi}|d^J_{0K}(\theta)|^2 \tag{2.63}$$

where

$$d^J_{0K}(\theta) = J!\sqrt{(J-K)!(J+K)!}\sum_{x=K}^{J}(-1)^x\frac{(\sin\frac{\theta}{2})^{2x-K}(\cos\frac{\theta}{2})^{2J+K-2x}}{(J-x)!(J+K-x)!(x-K)!x!} \tag{2.64}$$

For a fixed excitation energy E_x and total angular momentum $J\hbar$, the expression of Halpern and Strutinski [Halp58] gives the statistical distribution of K states at the saddle-point:

$$\rho(K) = \begin{cases} \dfrac{\exp\left(\dfrac{-K^2}{2K_0^2}\right)}{\sum_{K=-J}^{J}\exp\left(\dfrac{-K^2}{2K_0^2}\right)} & ; \text{for } K \leq J \qquad (2.65) \\ 0 & ; \text{for } K > J \qquad (2.66) \end{cases}$$

where

$$K_0^2 = \frac{\mathcal{J}_{eff}}{\hbar^2}T \tag{2.67}$$

The distribution of K values is therefore Gaussian with a standard deviation of K_0, and a variance K_0^2. It is related to the nuclear temperature, T, and the effective

moment of inertia, $\mathcal{J}_{eff}$. The effective moment of inertia is a function of the saddle-point moments of inertia ,$\mathcal{J}_{\|}$ and $\mathcal{J}_{\perp}$, respectively about the symmetry axis and an axis perpendicular to the symmetry axis.

$$\mathcal{J}_{eff}^{-1} = \mathcal{J}_{\|}^{-1} - \mathcal{J}_{\perp}^{-1} \tag{2.68}$$

By summing over all values of J and K, the fission fragment angular distributions are given by [Back85]

$$W(\theta) = \sum_{J=0}^{\infty}(2J+1)\mathcal{T}_J \frac{\sum_{K=-J}^{J} \frac{1}{2}(2J+1)|d_{0K}^{J}(\theta)|^2 \exp[-K^2/2K_0^2]}{\sum_{K=-J}^{J} \exp[-K^2/2K_0^2]} \tag{2.69}$$

In this expression, $\mathcal{T}_J$ is the capture probability for fusion of the Jth partial wave and $K_0(J)$ is the standard deviation of the K distribution at angular momentum J.

In the classical case, where the symmetry axis is parallel to the beam axis and $K = 0$, the fragments are emitted in a plane which includes the beam axis and the angular distribution behaves as $1/\sin\theta_{c.m.}$, where $\theta_{c.m.}$ is the centre-of-mass angle between the fragments' flight direction and the incident beam direction. More generally the angular distributions are sensitive to the ratio of J/K_0. Figure 2.10 [Mort95A] shows fission fragment angular distributions for a range of J/K_0 values calculated using the expressions given in Appendix A of Back *et al.* [Back85]. As can be seen, for a given value of J, the smaller the value of K_0 the more forward peaked is the angular distributions.

2.3.1.2 Fission Fragment Anisotropies

The fission fragment anisotropy, A, is defined as the ratio of the fission fragment yield parallel to the beam axis ($\theta_{c.m.} = 0°$ or $180°$) to that perpendicular ($\theta_{c.m.} = 90°$). In the TSM [Vand73] the anisotropy is approximately given by the expression:

$$A = \frac{W(180°)}{W(90°)} \approx 1 + \frac{\langle J^2\rangle \hbar^2}{4\mathcal{J}_{eff}T} = 1 + \frac{\langle J^2\rangle}{4K_0^2} \tag{2.70}$$

where $\langle J^2\rangle$ is the mean square angular momentum of the compound nucleus. The quantity K_0^2 can be determined by either model calculation of $\mathcal{J}_{eff}$ and T, or from experimental calibration reactions [Vand92]. The anisotropy is very sensitive to $\langle J^2\rangle$, as well as to properties of the fission process. In equation 2.70 if A and K_0^2 are

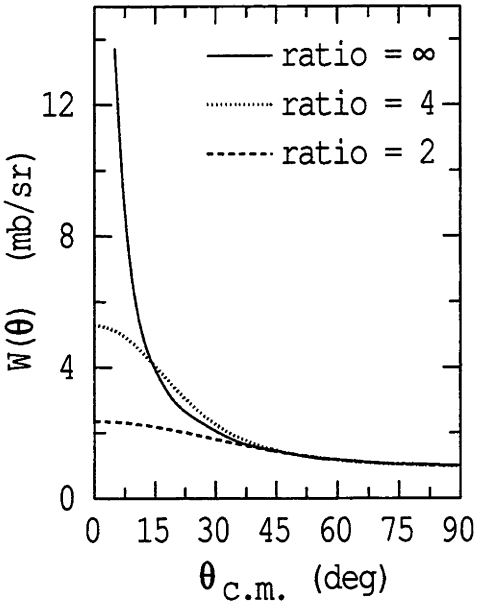

Figure 2.10: Fission fragment angular distributions as a function of angle $\theta_{c.m.}$ for several ratios of J/K_0. Where the ratio $J/K_0 = \infty$, the angular distributions is $1/sin\theta_{c.m.}$, as in the classical case.

known then $\langle J^2 \rangle$ for fission can be determined. As $\langle J^2 \rangle$ for fission is closely related to $\langle l^2 \rangle$ for capture, the anisotropies provide a consistency check for the fusion models.

Before the compound nucleus scissions it may emit one or more neutrons, or with a lower probability, protons and α-particles. This pre-scission emission lowers the temperature T of the nucleus, causing an increase in anisotropy (see equation 2.70)). Fission before particle emission is referred to as first-chance fission, while last-chance fission refers to those fission events which occur before further emission makes fission energetically impossible. The observed experimental anisotropy is a composite of the anisotropies for all chances of fission. Because the temperature of last-chance fission is much lower than for the other chance fission, its larger anisotropy may have a significant effect on the total or experimentally observed anisotropies.

While the effect of the different chances of fission is included in the TSM, the model assumes that the compound nucleus is in an equilibrated state, having been formed through a complete fusion reaction. Fission reactions without complete fusion (see Section 2.6) are therefore not expected to be correctly described by the TSM.

2.3.2 Mass-Distribution of Fission Fragments

When fusion-fission takes place fission fragments are emitted with a mass-distribution which is a function of excitation energy. Studies have shown that the characteristics of fission fragment mass-distributions are dependent on the particular fissioning nuclei [Mura86, Rusa97, Schm00], and are a useful tool for investigating fission before formation of an equilibrated compound nucleus [Hind95B, Hind96].

Here the mass-distribution is quantified in terms of the mass-ratio of the fragment mass, m_1, to the summed masses of the two fragments, $m_1 + m_2$, and is given by:

$$M = \frac{m_1}{m_1 + m_2} \tag{2.71}$$

The fission fragment mass-width, σ_M^2, is given by the normalised variance of the mass-ratio distribution.

Although the width of fission fragment mass-distributions depends principally on excitation energy, it may also depend slightly on angular momentum.

2.4 Particle Evaporation

Particle evaporation following fusion competes with fission. Particle evaporation from heavy nuclei is dominantly by emission of neutrons, protons or α-particles. Evaporation can only occur when the excitation energy of the fully equilibrated compound nucleus, $E_x(C.N.)$, less the rotational energy, E_{rot} (equation 2.50), is larger that the binding energy, B, of the particle. The binding energy for the different particle emissions is given by:

$$B_{n,p,\alpha} = M_{GS}^{D}(A - \Delta A, Z - \Delta Z) + M_{n,p,\alpha}(\Delta A, \Delta Z) - M_{GS}^{P}(A, Z) \tag{2.72}$$

Here $M_{GS}^{P}(A, Z)$ and $M_{GS}^{D}(A - \Delta A, Z - \Delta Z)$ are the measured ground-state binding energies respectively of the parent and daughter compound nuclei, and $M_{n,p,\alpha}(\Delta A, \Delta Z)$ is the energy of the emitted neutron, proton or α-particle with mass ΔA and charge ΔZ.

The energy removed as a result of the evaporation of a particle is the sum of the particle binding energy and the kinetic energy $\varepsilon_{n,p,\alpha}$ of the emitted particle:

$$\Delta E_{n,p,\alpha} = B_{n,p,\alpha} + \varepsilon_{n,p,\alpha} \tag{2.73}$$

As noted above, the emission of particles is not only a function of excitation energy, but also of the angular momentum dependent rotational energy. Figure 2.11 shows schematically the relationship between angular momentum, excitation energy and neutron emission, for a simple example of neutron evaporation [Bass80]. Neutrons that are emitted remove excitation energy ΔE_n from the compound nucleus, but remove little angular momentum. Neutrons continue to be emitted until the excitation energy falls below the line B_n. The rotational energy or yrast line

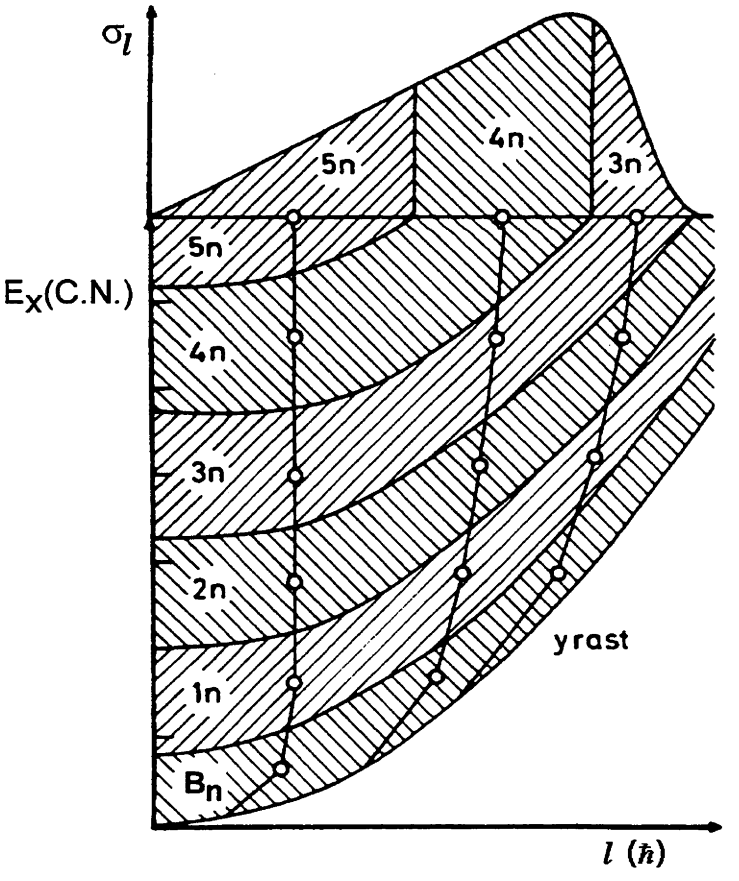

Figure 2.11: Schematic of the decay of a highly excited compound nucleus by neutron and gamma emission. The top shows the l-distribution of the initial compound nucleus. The bottom shows typical decay paths in the l-$E_x(C.N.)$ plane. [Bass80]

represents the lowest energy where nuclear states can be found for a given angular momentum $l\hbar$. The line marked B_n is one neutron binding energy above the yrast line, and represents the lowest excitation energy $E_x(C.N.)(l)$ where neutron emission is possible. Below B_n gamma emission takes over. It can be seen that the number of neutrons emitted, xn, is a function of both excitation energy and angular momentum, and that for a given l-distribution there will be statistically several multiplicities, x.

Proton and α-particle evaporation is inhibited as both are positively charged and have to surmount a Coulomb barrier before being emitted from the compound nucleus. Therefore, emission of low energy charged particles from the compound nuclei will be strongly inhibited relative to the emission of neutrons. As the excitation energy of the compound nucleus increases charged particle evaporation becomes more significant.

The range of angular momenta which result in particle evaporation is limited by fission decay. As angular momentum increases the fission barrier decreases and the fission probability increases exponentially.

This is demonstrated in Figure 2.12, which gives a schematic diagram of an angular momentum distribution showing the contributions of evaporation and fission decay. At low angular momenta ER production is dominant, while the probability of fission increases rapidly with increased angular momenta. The result is an angular momentum limit to the production of ERs, l_{lim}^{ER}.

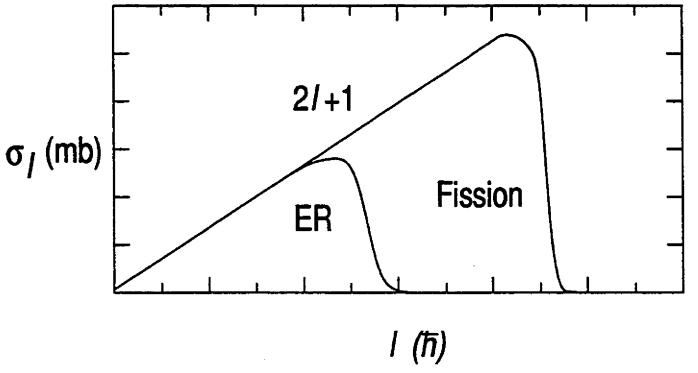

Figure 2.12: Schematic of the contributions made to particle evaporation and fission decay as a function of l.

2.4.1 Reduced Evaporation Residue Cross-Sections

To assist in comparing cross-sections for evaporation residue decay from different reactions, and using the reduced cross-sections as defined in equation 2.7, the reduced ER cross-section is given by:

$$\overline{\sigma}_{ER}(E) = \sigma_{ER}(E)\frac{2\mu E}{\pi\hbar^2} = \sum_{l=0}^{\infty}(2l+1)\mathcal{T}_l(E)[1 - P_{fis}(E,l)] \tag{2.74}$$

where $P_{fis}(E,l)$ is the fission probability. Then, for a limiting particle evaporation angular momentum l_{lim}^{ER}, $\overline{\sigma}_{ER}(E)$ will saturate when the capture coefficient $\mathcal{T}_l(E)$ is at a maximum for $l \leq l_{lim}^{ER}$. At beam energies sufficiently high above the Coulomb barrier region, all capture models predict $\mathcal{T}_l(E) \cong 1$ for all l which lead to ERs. Therefore at these energies, if $P_{fis}(E,l)$ is independent of the entrance channel, then the saturated value of $\overline{\sigma}_{ER}(E)$ should also be independent of the reaction entrance channel.

2.5 Decay Probabilities

As discussed in the previous sections, excited compound nuclei can decay by fission or particle evaporation. Due to the high excitation energy the number of states available for decay is huge, and therefore a statistical approach, usually just referred to as *the statistical model* (SM), is appropriate to analyse compound nucleus decay. The SM describes decay of a nucleus with given excitation energy, $E_x(C.N.)$, and angular momentum, J, from a fully equilibrated compound nucleus formed through complete fusion of the target and projectile.

The statistical model calculations are usually based on the following assumptions:

1. The compound nucleus is formed by complete fusion of the projectile and target (e.g. no projectile breakup).

2. The compound nucleus is at its equilibrated deformation.

3. The decay of the nucleus is independent of the formation except for conservation of energy, angular momentum and parity.

4. All decay channels have an equal probability of being populated - except where the probability is reduced by the appropriate capture probability.

The rate of decay for a particular decay channel is usually denoted by the decay width, Γ. Decay widths are primarily functions of the level densities, ρ, of the initial and final states.

2.5.1 Level Densities

As nuclei become excited, the number of levels available in the nucleus increases. At the energies involved in capture reactions, the number of levels available is so high that they cannot be individually counted. Instead, energy levels can be considered as a continuum, with a level density measured in units of energy levels per MeV. For compound nucleus decay, the level densities of the daughter nuclei determine how many decay states are available, and therefore the probability of a particular decay channel.

For temperatures, T, that are small compared to the Fermi energy, the level density, $\rho(E_x)$, can be given by:

$$\rho(E_x) \propto \exp(2\sqrt{aE_x}) \tag{2.75}$$

The parameter, a, is the level density parameter and is defined as:

$$a = \frac{\pi^2 g_0}{6} \tag{2.76}$$

where g_0 is the single-particle level density at the Fermi energy, representing the sum of the proton and neutron level densities. Of the several parameterisations available [Tōke81, Igna75], the following values of a, from Tōke and Swiatecki [Tōke81], have been used in this work.

$$a = 0.0684A + 0.213B_sA^{2/3} + 0.385B_kA^{1/3} + ... \tag{2.77}$$

In equation 2.77, A is the atomic mass number, and B_s and B_k are respectively the surface area and integrated curvature of the nuclear surface in units of their values for the spherical shape (i.e. for spherical nuclei $B_s = B_k = 1$). For most practical purposes the first three terms in equation 2.77 are sufficient, and additional terms make little difference to the value of a.

In compound nuclei with high angular momentum, some of the excitation energy is tied up in the rotational energy E_{rot}, as given in equation 2.50. This energy is unavailable to excite the nucleus in any other manner, and is not used in calculating the angular momentum dependent level density [Bohr69]. The thermal energy, U, is therefore defined as the excitation energy, E_x, less the rotational energy, E_{rot}.

$$U = E_x - E_{rot} \tag{2.78}$$

The angular momentum dependent level density is then given by [Bohr69]:

$$\rho(E_x, J) = \frac{(2J+1)}{12}\frac{\sqrt{a}}{U^2}\left(\frac{\hbar^2}{2\mathcal{J}}\right)^{3/2}\exp\left(2\sqrt{aU}\right) \tag{2.79}$$

The level density is strongly dependent on the excitation energy, E_x, used. The use of shell and pairing corrections to the excitation energy, as described in Section 2.2.4, has a significant effect on the calculated decay probabilities for the compound nucleus [Jung98].

2.5.2 Decay Widths

The decay width for a compound nucleus with initial excitation energy, E_i, and angular momentum quantum number, J_i, is a function of the level density of the parent nucleus, $\rho(E_i, J_i)$, the capture probability, $\mathcal{T}_l(\varepsilon)$, and the level density of the final configuration. The final configuration is considered to be either the daughter nucleus (for particle evaporation) or the saddle-point configuration (for fission). The parameter ε is the kinetic energy of the final configuration.

2.5.2.1 Particle Evaporation

For particle evaporation, the decay width is a sum of all possible daughter angular momentum quantum numbers, J_f, and an integral over all allowable particle energies, ε, giving [Thom64, Zebe74, Dela77, Lest90]:

$$\Gamma_{n,p,\alpha} = \frac{1}{2\pi\rho(E_i, J_i)}\sum_{l=0}^{\infty}\sum_{S=|l-s|}^{l+s}\sum_{J_f=|J_i-S|}^{J_i+S}\int_0^{\varepsilon_{max}}\mathcal{T}_l(\varepsilon)\rho(E_i - \Delta E_{n,p,\alpha}, J_f)d\varepsilon \tag{2.80}$$

where $\Delta E_{n,p,\alpha}$ is the energy removed by the evaporating particle (see equation 2.73), l and s are respectively the particle orbital angular momentum quantum number,

and intrinsic spin, and the maximum particle energy is:

$$\varepsilon_{max} = E_i - E_{rot}(J_f) - B_{n,p,\alpha} \tag{2.81}$$

where $B_{n,p,\alpha}$ is the particle binding energy (see equation 2.72).

In SM calculations, the capture probabilities, $\mathcal{T}_l(\varepsilon)$, are usually approximated by optical model transmission probabilities, which are based on global fits to elastic scattering data. Assuming $s \ll J_i$, the level density (equation 2.79) can be incorporated into equation 2.80, giving the particle decay width as:

$$\Gamma_{n,p,\alpha} = \frac{(2s+1)(2J_f+1)}{2\pi(2J_i+1)\dfrac{\exp(2\sqrt{a_{part}U_i})}{U_i^2}} \sqrt{\frac{a^*_{part}}{a_{part}}} \sum_{l=0}^{\infty} \sum_{J_f=|J_i-l|}^{J_i+l} \int_0^{\varepsilon_{max}} \mathcal{T}_l(\varepsilon) \frac{\exp(2\sqrt{a^*_{part}U_f})}{U_f^2} d\varepsilon \tag{2.82}$$

where a_{part} and a^*_{part} are respectively the level density parameters for the equilibrated parent and daughter nuclei, the thermal energy of the parent is $U_i = E_i - E_{rot}(J_i)$, and the thermal energy of the daughter is $U_f = E_i - E_{rot}(J_f) - \Delta E_{n,p,\alpha}$.

2.5.2.2 Fission

The decay width for fission is similar to that for particle emission, except the saddle-point is taken as the determining configuration within the transition state model. The fission barrier height, B_f, is analogous to the particle binding energy, and the saddle-point kinetic energy, ε_{sp}, is analogous to the particle kinetic energy. The fission decay width is given by [Bohr69, Lest90]:

$$\Gamma_{fis} = \frac{1}{2\pi\rho(E_i, J_i)} \int_0^{E_i - k_f B_f} \mathcal{T}_l(\varepsilon_{sp}) \rho(E_i - k_f B_f - \varepsilon_{sp}, J_i) d\varepsilon_{sp} \tag{2.83}$$

here the fission barrier scaling factor k_f (see Section 2.2.3) has also been included. For fission, $\mathcal{T}_l(\varepsilon_{sp})$ is usually taken to be unity above the barrier and zero below the barrier:

$$\mathcal{T}_l(\varepsilon_{sp}) = \begin{cases} 1 & ; \text{for } \varepsilon_{sp} \geq B_l \\ 0 & ; \text{for } \varepsilon_{sp} < B_l \end{cases} \tag{2.84}$$

Inserting the level densities for equation 2.79 and $\mathcal{T}_l(\varepsilon_{sp})$ from equation 2.84 into equation 2.83 gives:

$$\Gamma_{fis} = \frac{1}{2\pi\dfrac{\exp(2\sqrt{a_{part}U_i})}{U_i^2}} \sqrt{\frac{a_f}{a_{part}}} \int_0^{E_i - k_f B_f} \frac{\exp(2\sqrt{a_f U_{sp}})}{U_{sp}^2} d\varepsilon_{sp} \tag{2.85}$$

where a_f is the fission saddle-point level density parameter, and the thermal energy at the saddle-point is $U_{sp} = E_i - \varepsilon_{sp} - k_f B_f$.

2.5.3 Relative Decay Widths

The total decay width is the sum of the particle emission and fission decay widths:

$$\Gamma_{total} = \Gamma_n + \Gamma_p + \Gamma_\alpha + \Gamma_{fis} \tag{2.86}$$

The fission probability is therefore:

$$P_{fis} = \frac{\Gamma_{fis}}{\Gamma_{total}} \tag{2.87}$$

while the survival probability is:

$$P_{part} = \frac{\Gamma_n + \Gamma_p + \Gamma_\alpha}{\Gamma_{total}} \tag{2.88}$$

For lower excitation energies, where the Coulomb barrier inhibits charged particle emission, the decay of the compound nucleus is largely dependent on the ratio of the fission and neutron decay widths. This can be written as [Ward83]:

$$\frac{\Gamma_{fis}}{\Gamma_n}(J) \propto \exp\left[2\sqrt{a_f(E_i - k_f B_f(J))} - 2\sqrt{a^*_{part}(E_i - B_n)}\right] \tag{2.89}$$

where a^*_{part} in this case is the daughter level density parameter after neutron emission. For increasing angular momentum the fission barrier height $B_f(J)$ decreases, and when $k_f B_f(J) > B_n$, fission becomes dominant over neutron emission.

2.5.4 Statistical Model Codes

Using the statistical model decay widths outlined above, several computer codes have been developed. These fall into two main categories [Bass80], the codes that solve the problem in a grid (e.g. ALICE [Blan66, Blan72, Plas78], MBII [Beck78], ALERT1 [Blan82A], and CASCADE [Pühl77]), and those that use the Monte Carlo method (e.g. PACE [Gavr80] and JOANNE [Lest90, Lest91, Lest93]). All of the codes above, except JOANNE, originally used RLDM fission barriers.

For this work a modified version of JOANNE, call JO_SHELL, was written which incorporates shell effects into the level densities and decay widths. Before discussing JO_SHELL, a brief description of the JOANNE code is given.

2.5.4.1 Computer Code - 'JOANNE'

JOANNE uses $\mathcal{T}_l(\varepsilon)$ determined using the optical model potentials of Perey and Perey [Pere76] for neutron and proton emission, and Huizenga and Igo [Huiz62] for α-particle emission. The yrast energies and fission barriers used are those of the FRLDM of Sierk [Sier86]. The binding energies are derived from the LDM equations 2.33, 2.39, 2.40, and 2.41. JOANNE calculates the distribution of fission events in a matrix of T and J, in order to evaluate the fission fragment angular distributions.

The fission decay width in Section 2.5.2.2, assumes that there is only a small coupling between the thermal energy and the nuclear collective degrees of freedom. It further assumes that the nucleus will fission if it passes the saddle-point configuration. However, if a nucleus has passed over the saddle-point configuration, fluctuations in its collective energy could return it to its equilibrium deformation, assuming the viscosity of the nucleus is large enough [Lest90]. Kramers [Kram40] developed a diffusion model applicable to nuclear fission and showed that the fission decay width varies as a function of the frequency of the inverse harmonic-oscillator potential of the fission barrier at the saddle-point and a reduced frictional constant. Based on Kramers diffusion model, Grange and Weidenmuller [Gran80, Gran86] found that the full fission decay width takes a finite time to become established. The time required for the fission decay width to reach 90% of its quasi-stationary value is usually referred to as the transient time. In the JOANNE code, it is assumed [Lest91] that the fission width varies with time according to:

$$\Gamma_{fis}(t) = \Gamma_{fis}\left[1 - \exp\left(\frac{-t}{\tau_f}\right)\right] \tag{2.90}$$

given that t is the lifetime of a particular decay, and τ_f is the fission transient delay time.

To allow investigation of the time dependence of fission, JOANNE includes two variables, τ_f which restricts how quickly fission can take place, and a factor, called the Kramers factor K_r, which scales the fission decay width:

$$\Gamma^*_{fis} = \Gamma_{fis}/K_r \tag{2.91}$$

The Q-values used in JOANNE were evaluated relative to the liquid-drop ground-state using:

$$Q_{LDM} = M_{GS}(A_{proj}, Z_{proj}) + M_{GS}(A_{targ}, Z_{targ}) - M_{LDM}(A_{C.N.}, Z_{C.N.}) - 3\delta \tag{2.92}$$

where $M_{GS}(A_{proj}, Z_{proj})$, and $M_{GS}(A_{targ}, Z_{targ})$ are the projectile and target true ground-state binding energies [LUND], $M_{LDM}(A_{C.N.}, Z_{C.N.})$ is the compound nucleus liquid drop binding energy from equation 2.33, and δ is the pairing energy ($\delta = 11/\sqrt{A_{C.N.}}$) [Char86].

Evaporated particle binding energies are calculated using the liquid drop masses of the parent and daughter nuclei, together with the energy of the evaporated particle.

$$B_{n,p,\alpha} = M^{D}_{LDM}(A - \Delta A, Z - \Delta Z) + M_{n,p,\alpha}(\Delta A, \Delta Z) - M^{P}_{LDM}(A, Z) \quad (2.93)$$

All level densities are calculated for a compound nucleus excitation energy:

$$E_x(C.N.) = E_{c.m.} - Q_{LDM} \quad (2.94)$$

2.5.4.2 Computer Code - 'JO_SHELL'

The code JO_SHELL is a modified version of JOANNE. It incorporates the option to include shell and pairing effects into the level density calculation. The shell and pairing effects are as outlined in Section 2.2.4, and are included by using formulae from Junghans *et al.* [Jung98, Jung00]. In the JO_SHELL code the excitation energy of the compound nucleus is taken to be:

$$E_x(C.N.) = E_{c.m.} - Q_{GS} \quad (2.95)$$

for

$$Q_{GS} = M_{GS}(A_{proj}, Z_{proj}) + M_{GS}(A_{targ}, Z_{targ}) - M_{GS}(A_{C.N.}, Z_{C.N.}) \quad (2.96)$$

where $M_{GS}(A_{C.N.}, Z_{C.N.})$ is the measured ground-state binding energy of the compound nucleus [LUND].

Level densities are calculation for an energy of $E_x(C.N.) - E_{corr}$ where the energy correction, E_{corr}, is given by equation 2.61. The particle evaporation level densities are calculated at the equilibrium deformation, either by; incorporating shell and pairing effects, which wash out with increasing excitation energy $E_x(C.N.)$ (SM-SP option); or without such effects, using the FRLDM ground-state energies calculated with E_{corr} at a maximum (SM-FRLDM option). The particle binding energies are calculated using equation 2.72 with the modification that the parent and daughter binding energies are first corrected for appropriate shell and pairing effects.

The fission level densities are calculated for excitation energies modified to reflect the loss of shell effects at the saddle-point. This is accomplished by using the FRLDM ground-state energies with E_{corr} at a maximum. The average ground-state pairing gap, Δ from equation 2.57, was used in the JO_SHELL code, with Δ being larger at the saddle-point deformation than at the equilibrium deformation.

The effect of the different level density calculations are presented in a series of figures (Figures 2.13 to 2.18) showing calculations for the $^{12}C + ^{204}Pb$ reaction. A typical and identical angular momentum distribution is used for all the calculations.

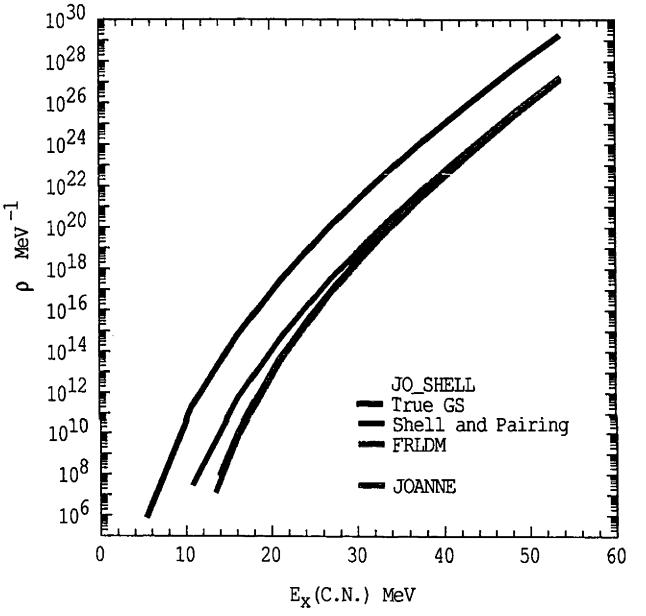

Figure 2.13: Parent compound nucleus level densities as a function of initial excitation above the parent true ground-state. Shown are level densities calculated by JO_SHELL based on the FRLDM ground-state (green line), energy dependent shell and pairing effects (red line), and true ground-state energies (black line). Also shown are level densities calculated using JOANNE (blue line).

Figures 2.13, 2.14 and 2.15 respectively show the parent, daughter (after a single neutron emission), and saddle-point level densities, plotted against initial compound nucleus excitation energy above the parent true ground-state, $E_x(C.N.) = E_{c.m.} - Q_{GS}$.

In these figures the green lines are JO_SHELL level density calculations based on the FRLDM ground-state energies, representing a total washing out of shell

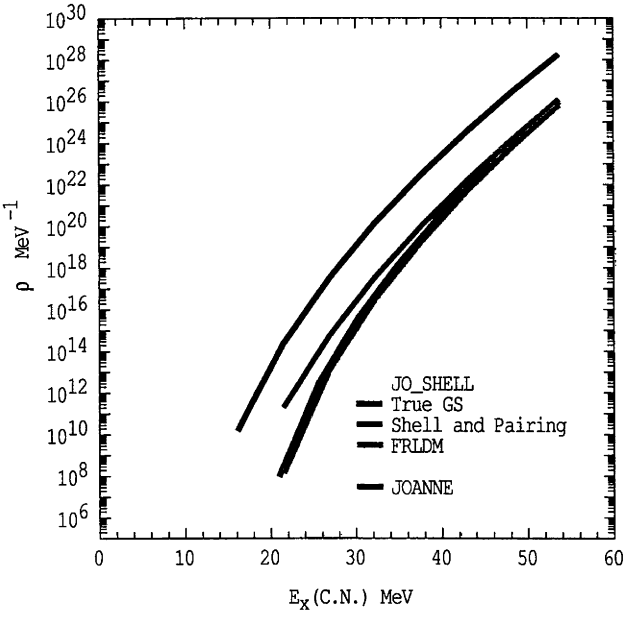

Figure 2.14: Daughter compound nucleus level densities following a single neutron evaporation, as a function of initial excitation above the measured ground-state of the parent. The lines are the same as for Figure 2.13.

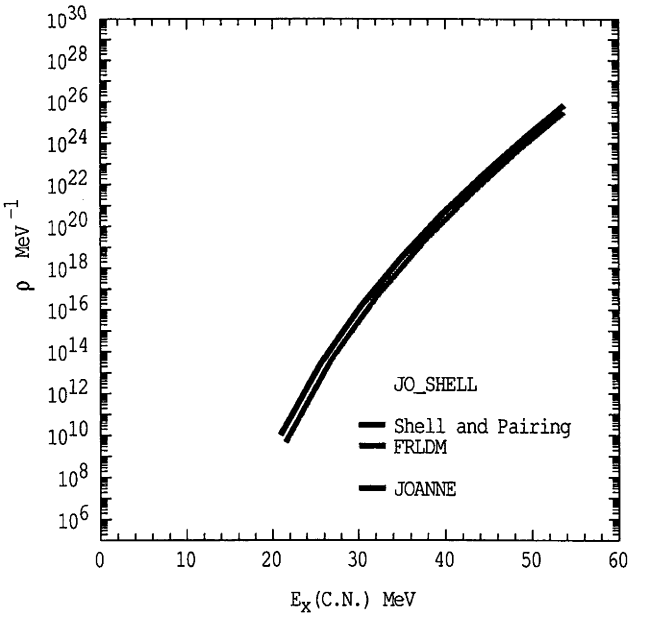

Figure 2.15: Fission saddle-point level densities as a function of initial excitation above the parent measured ground-state. The calculations with JO_SHELL assume complete washing out of the shell and pairing effects at the saddle-point. The red and green lines are therefore identical.

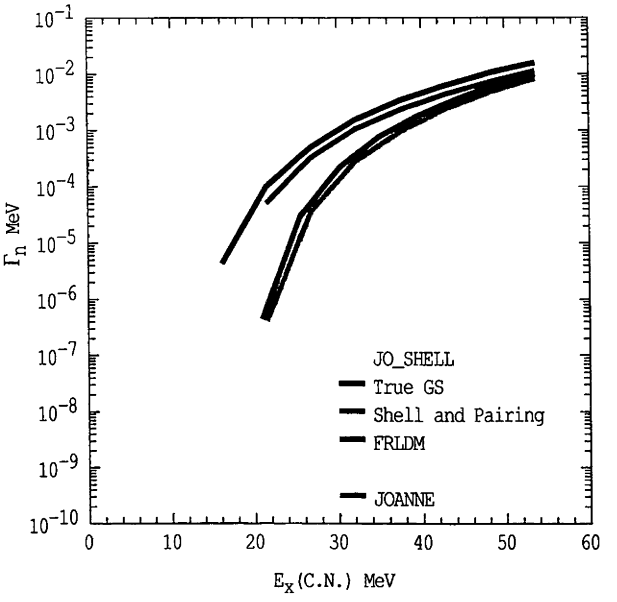

Figure 2.16: Decay widths for neutron evaporation, as a function of initial excitation above the parent measured ground-state. Shown are decay widths calculated by JO_SHELL based on; the FRLDM ground-state (green line); energy dependent shell and pairing effects (red line); and true ground-state energies (black line). Also shown are decay widths calculated using JOANNE (blue line).

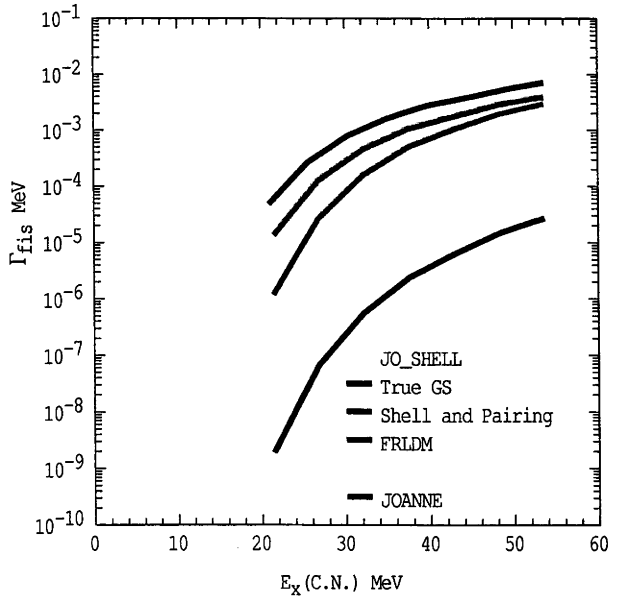

Figure 2.17: Fission decay widths, as a function of initial excitation above the parent measured ground-state. The lines are the same as for Figure 2.16. Because of the negative shell ground-state correction, the "True GS" calculation sees a higher fission barrier, resulting in a low fission width.

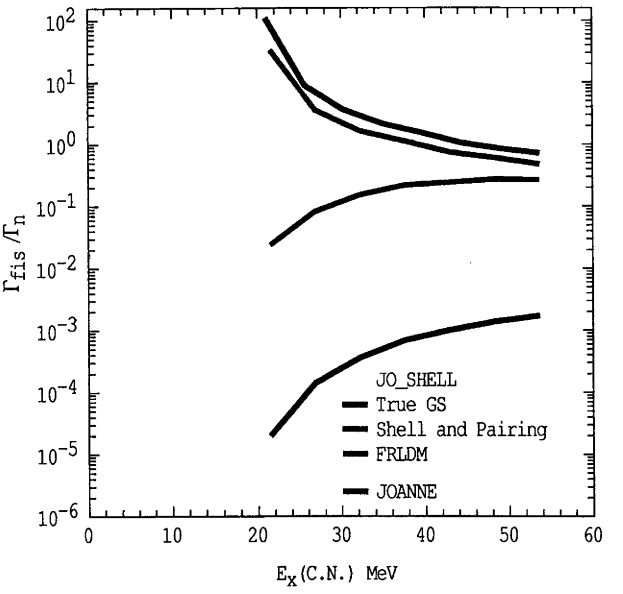

Figure 2.18: Ratio of fission to neutron decay widths, as a function of initial excitation above the parent measured ground-state. The lines are the same as for Figure 2.16.

effects. As expected, they are very similar to the JOANNE calculation shown by the blue lines. The difference between the two calculations being the difference in the way the average pairing gap is calculated. The black lines represent level densities calculated using JO_SHELL, based on the true ground-state energies, and are shown only for illustrative purposes.

The red lines correspond to JO_SHELL calculations using excitation energy dependent shell and pairing corrections to the level densities. At high excitation energies, where shell effects are washed out, these calculations correspond to the FRLDM calculation (green lines) for the parent (2.13) and daughter (2.14) level densities. As the excitation energy drops there is an increasing enhancement of these level densities (red lines), which approach those from the true ground state calculations (black lines) as the excitation energy falls to zero.

The saddle-point level densities (Figure 2.15) using the JO_SHELL code were all calculated assuming the complete washing out of the shell effects. The shell and pairing (red) and FRLDM (green) JO_SHELL saddle-point level densities calculations are therefore identical. Again the difference between the JO_SHELL and

JOANNE the calculations is due to how the average pairing gap is calculated.

The compound nucleus decay widths are functions of the ratio of the level density of the daughter or saddle-point to the level density of the parent nucleus (see Sections 2.5.2 and 2.5.3). Therefore the decay widths will reflect the differences in the level density calculations shown in Figures 2.13, 2.14 and 2.15.

The decay widths for neutron emission are shown in Figure 2.16. Calculation using the level densities with energy dependent shell and pairing effects (red line) approach the decay widths based on the FRLDM ground-states (green line) at the largest excitation energies. However, at lower energies it rapidly starts to approach and follow the trend of the decay widths using the true ground-state energies (black lines). This reflects the larger level density enhancement of the daughter nucleus, resulting from its reduced excitation energy following emission of a neutron.

Unlike the neutron decay widths, the fission decay widths (Figure 2.17) show only the effect of modified parent level densities. The energy dependent shell and pairing calculation (red line), change from being like the FRLDM decay widths (green line) at higher energies to approaching the true ground-state calculations as the energy decreases - the latter gives very low fission widths because using the true ground-state as a baseline results in a much higher fission barrier.

For the decay of a compound nucleus, the competition between fission and formation of evaporation residues, and thus the fission and survival decay probabilities, is largely dependent on the relative decay widths of the fission saddle-point and of neutron emission (assuming in this case little or no charged particle evaporation). The calculated relative fission to neutron decay widths (equation 2.89) are shown in Figure 2.18. The effect of the energy dependent shell enhancements (red lines) is to decrease the probability of fission at lower excitation energies, with this effect becoming less significant as the energy increases. Thus the probability of the later chances of fission (once some energy has been removed through particles evaporation) is decreased, when shell and pairing effects are considered in the level density calculations. This will not only give a reduction in fission probability when compared to calculations based on a complete washing out of such effects, but will also decrease the fission fragment anisotropies.

2.6 Other Influences on Compound Nucleus Reactions

The models presented in the previous sections are usually applied assuming that the projectile and target are completely fused to form an equilibrated compound nucleus. However, there is experimental evidence that this does not always occur.

For loosely bound light projectiles, the Coulomb potential can be sufficient to break apart the projectile before capture occurs [Sign97, Dasg99]. Even for reactions where projectile breakup does not occur, fission may take place before an equilibrated compound nucleus can be formed [Back85, Hind95B, Hind96, Hind99A].

In these cases the standard models of fusion and fission do not accurately reproduce experimental results. This section explores the conditions of projectile breakup and fission from a non-equilibrated nucleus. The term 'complete fusion' will be used to denote fusion of the entire projectile and target.

2.6.1 Projectile Breakup

With the recent availability of radioactive beams, there has been increasing interest in capture reactions involving nuclei which are loosely bound. Experiments involving nuclei ^{6,7,9,11}Li [Taka97, Petr97, Dasg00], and ^{9,10,11}Be [Feko95, Yosh95, Sign98, Dasg99] on heavy targets have show substantial fractions of incomplete fusion due to projectile breakup. For the reaction ^{9}Be + ^{208}Pb, the measured complete fusion cross-sections are only 68% of those predicted [Dasg99]. Even for the reaction ^{12}C + ^{197}Au, there are experimental [Bimb72, Park91, Verg93] indications of a small amount of ^{12}C breakup. Incomplete fusion with the projectile breakup products can be measured to reconstruct the reaction dynamics and the total capture cross-sections.

2.6.2 Quasi-Fission

Several experiments have shown that fission can occur before the compound nucleus reaches full equilibrium [Back85, Tōke85, Hind95A, Hind95B, Hind99A], and that although the capture cross-sections can be reproduced precisely using coupled-channels models, the fission fragment angular distributions for these reactions are not well described by the TSM. These reactions are characterised by having either

(or both), a heavy projectile ($A \geq 24$) incident on a heavy target, or a reaction with a deformed actinide target nucleus.

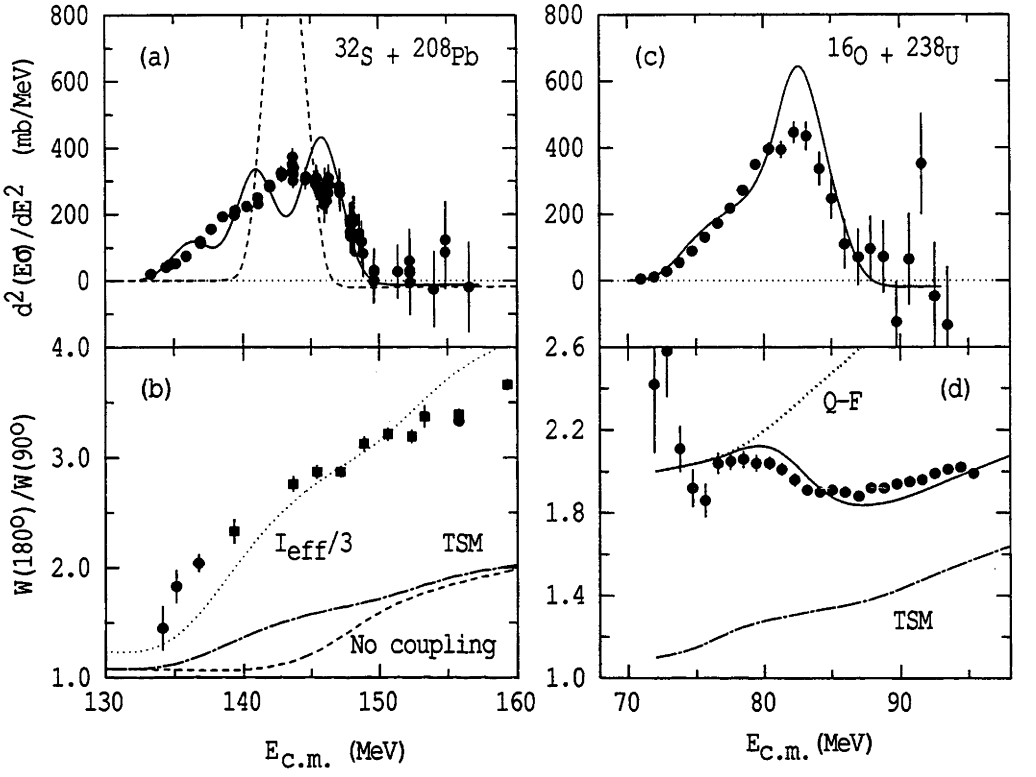

Figure 2.19: (a) Capture barrier distributions for the reaction $^{32}S + ^{208}Pb$, together with a single barrier calculation (no coupling) and a coupled-channels calculation (solid line). The fission fragment anisotropies are shown in (b), with corresponding calculations based on the TSM shown by the dashed and dot-dashed lines respectively. A factor of 3 change in $\mathcal{J}_{eff}$ (dotted line) gives a good reproduction of the data [Hind99A]. (c) and (d) show the same comparison for $^{16}O + ^{238}U$. The dotted and solid lines in frame (d) are respectively the assumed quasi-fission anisotropy, and a model calculation for quasi-fission together with fusion-fission, from Hinde et al. [Hind99A]

An example of a reaction with a large projectile incident on a heavy target is the reaction $^{32}S + ^{208}Pb$ [Hind99A]. Figure 2.19(a) shows the experimental capture barrier distribution together with a single barrier calculation (no coupling, dashed line) and an empirical fit using the coupled-channels formalism (solid line). The measured anisotropies for this reaction (Figure 2.19(b)) are consistently higher by a factor of around three, than either of the TSM predictions, which are based on the angular momentum distribution for the coupled-channels calculations (dot-dash line,

annotated TSM) or the single barrier calculation angular momentum distribution (no coupling, dashed line). The decrease in anisotropy with decreasing beam energy indicates that for this reaction the mechanisms do not change substantially as a function of beam energy.

Figures 2.19(c) and (d) show the results for the reaction $^{16}O + ^{238}U$ [Hind96]. The anisotropies are again higher than the TSM calculations, but here the anisotropies increase substantially as the beam energy decreases through the Coulomb barrier region. This suggests that there is a correlation between the relative orientation of the projectile and the deformed target (which will affect the potential barrier height), and the anisotropy.

Explanations for non-equilibrium fission fall into two main categories:

The first we call the 'Non-Equilibrated K' (N.E.K.) Models [Rama85, Vork95, Lest97], which postulate that the combined system is formed inside the true fission saddle-point, and is equilibrated in all degrees of freedom except K, the projection of J onto the symmetry axis (see Section 2.3.1). The system fissions before a 'K-equilibration time', favouring the deformation axis of the target nucleus, leading to an enhanced anisotropy as observed in some reactions. This implies that the system does not have time to change shape to become elongated perpendicular to the direction of the angular momentum vector, as is assumed in the TSM. The N.E.K. model is able to explain the observed large anisotropies for most of the reactions studied.

The second category involves the Quasi-Fission (QF) process [Back85, Tōke85], where an equilibrated compound nucleus is not formed inside the unconditional fission saddle-point. Instead, the combined nucleus forms an elongated nucleus, which is initially trapped inside the conditional saddle-point, evolves over the potential energy surface, and scissions before reaching mass-symmetry [Hind96]. As demonstrated in Figure 2.19(b), the anisotropies for the $^{32}S + ^{208}Pb$ reaction can be well reproduced, when the effective moment of inertia, $\mathcal{J}_{eff}$ (see equation 2.68) is decreased by a factor of three (dotted line), indicating the more elongated shape of the fissioning system. In principle there is some memory of the projectile and target involved in the initial collision.

The QF model explains the high anisotropies in reactions on actinide targets, at beam energies around the Coulomb barrier, in terms of target orientation. The

lowest barriers (at the lower beam energies) correspond to the projectile reacting with only the tips of the deformed target, resulting in elongated combined system. These elongated configurations are more likely to result in quasi-fission than the more compact configuration that result from projectile collisions with the equatorial regions of the target, which occur at higher energies. When QF is considered in conjunction with fusion-fission, the anisotropies for the $^{16}O + ^{238}U$ reaction in Figure 2.19(d) can be well reproduced (solid line). Since quasi-fission occurs from shapes more elongated than the fission saddle-point, the presence of quasi-fission should be correlated with a reduction in the ER yield. The QF explanation for non-equilibrium fission will be able to explain, at least qualitatively, the results in this work.

2.6.3 Businaro-Gallone Criterion

The threshold for QF in non-actinide reactions is a function of the potential energy of the combined system. Davies and Sierk [Davi85] have calculated saddle-point potential energy surfaces for dinuclear systems as a function of the fissility, x (equation 2.49), and mass-asymmetry, $\alpha = \frac{M_R - M_L}{M_R + M_L}$. The parameters M_R and M_L are the partial nuclear masses respectively to the right and left of a plane passing through the neck of the dinuclear system. A mass-asymmetry of $\alpha = 0$ corresponds to half of the nuclear mass in both the right and left portions, while a mass-asymmetry of $\alpha = 1$ corresponds to a sphere containing all the nuclear mass on the right, with an infinitesimally small sphere on the left. The energy of this latter configuration, for all fissility values, is exactly equal to that of the ground-state.

The calculations of Davies and Sierk are shown in Figure 2.20. Shown are saddle-point energies, in units of $E_s^{(0)}$, as a function of constrained mass-asymmetry, α, for various values of the LDM fissility, x. For fissility values less than a critical value, $x < x_{BG}$ (called the Businaro-Gallone (BG) value [Busi55A, Busi55B], $x_{BG} \approx 0.396$ [Sobo84]) the potential energy always decreases as α increases from 0 to 1, encouraging the nucleus into a more asymmetric shape. For higher fissility values, $x > x_{BG}$, the potential energy forms a maximum. As α increases from 0, the potential energy rises until it reaches the maximum, then decreases as α approaches 1. For α less that the maximum it is energetically more favourable for the nucleus to change into a more symmetrical shape, which is more likely to proceed by quasi-fission.

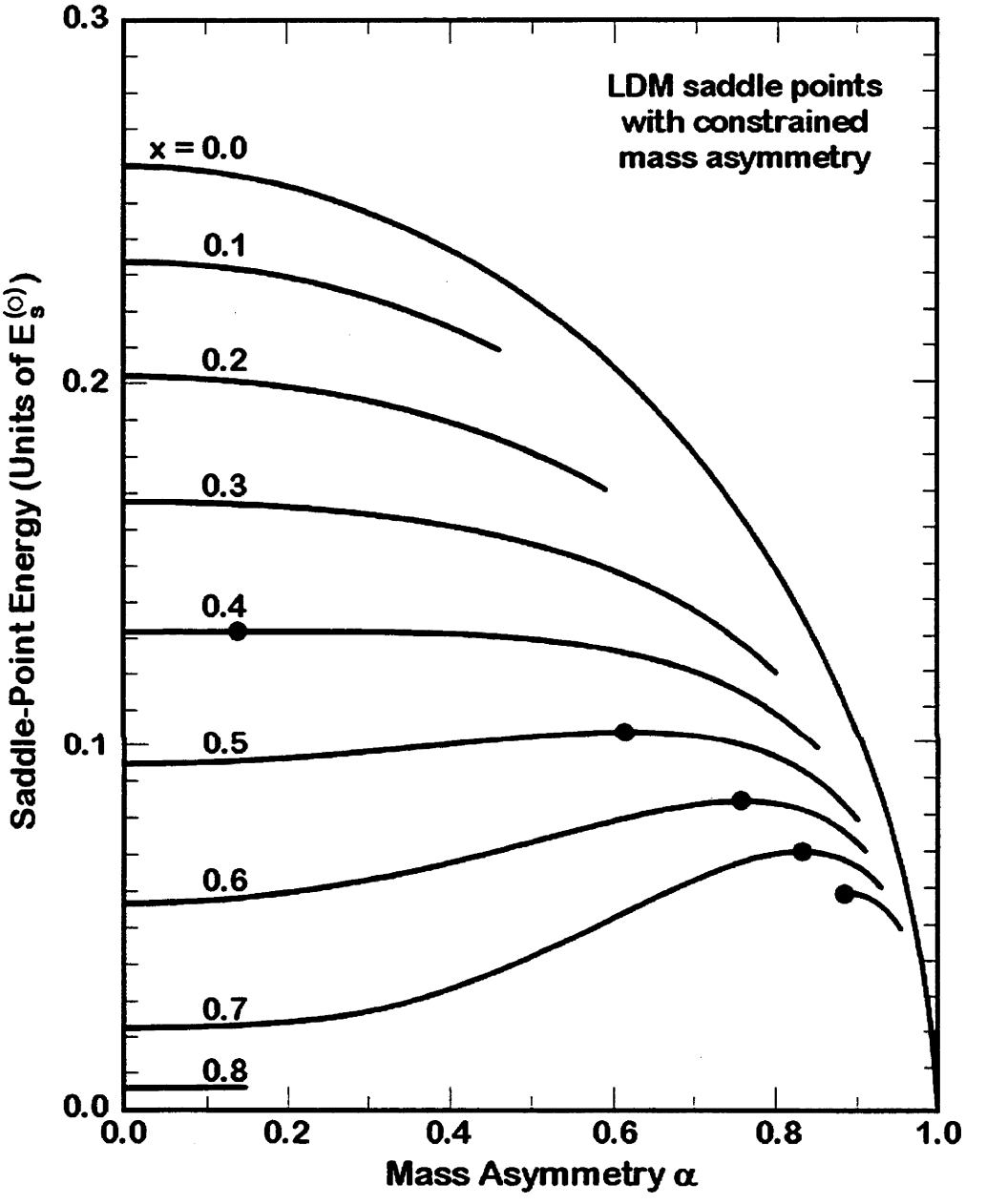

Figure 2.20: Saddle-point energies as a function of constrained mass-asymmetry, α, for various values of the LDM fissility, x, and $J = 0$ (calculated by Davies and Sierk [Davi85]). The solid points correspond to the Businaro-Gallone potential energy maxima. The $x = 0.8$ curve is not complete due to the limitations of the calculations.

The calculated potential energy heights of the mass-asymmetry fission barriers have similarities to the potential energy landscape determining evolution of the system after capture, and for which detailed calculations are not available. As the time for energy equilibration is shorter than the time for QF or mass-equilibration, the mass-asymmetry at the saddle-point may be comparable to the initial mass-asymmetry. Therefore, where the initial mass-asymmetry lies with respect to the Businaro-Gallone saddle-point potential energy maxima, may be expected to be reflected in the amount of QF that will occur. In turn, this will manifest itself in differences from TSM prediction for the fission and ER decay probabilities, fission fragment anisotropies and fission fragment mass-distributions.

CHAPTER 3

Experimental Methods

Experiments were performed for three reactions which, if fusion occurs, all form the compound nucleus ^{216}Ra, and for six O + Pt reactions leading to $^{208-216}$Rn compound nuclei which span the $N = 126$ neutron closed shell (see Table 3.1).

$$
\begin{aligned}
^{12}\mathrm{C} + {}^{204}\mathrm{Pb} &\rightarrow {}^{216}\mathrm{Ra} \\
^{19}\mathrm{F} + {}^{197}\mathrm{Au} &\rightarrow {}^{216}\mathrm{Ra} \\
^{30}\mathrm{Si} + {}^{186}\mathrm{W} &\rightarrow {}^{216}\mathrm{Ra}
\end{aligned}
$$

$$
\begin{aligned}
^{16}\mathrm{O} + {}^{192}\mathrm{Pt} &\rightarrow {}^{208}\mathrm{Rn} \\
^{16}\mathrm{O} + {}^{194}\mathrm{Pt} &\rightarrow {}^{210}\mathrm{Rn} \\
^{16}\mathrm{O} + {}^{196}\mathrm{Pt} &\rightarrow {}^{212}\mathrm{Rn} \\
^{16}\mathrm{O} + {}^{198}\mathrm{Pt} &\rightarrow {}^{214}\mathrm{Rn} \\
^{18}\mathrm{O} + {}^{196}\mathrm{Pt} &\rightarrow {}^{214}\mathrm{Rn} \\
^{18}\mathrm{O} + {}^{198}\mathrm{Pt} &\rightarrow {}^{216}\mathrm{Rn}
\end{aligned}
$$

Table 3.1: Experimental Reactions

Measurements were made using the Australian National University (ANU) 14UD Accelerator, for both capture-fission (which includes both fusion-fission and quasi-fission) and fusion-ER (evaporation residue) reactions. Two different detection systems were used, to measure fission fragments, and α-decay from ERs. Particular emphasis was put on obtaining precise data over the range of beam energies used.

This chapter describes how these experimental measurements were made, including details of the beam production, the targets, detection equipment and procedures,

and data extraction methods. The experimental results themselves, together with analysis of the results, are given in Chapter 4.

3.1 The ANU 14UD Accelerator

The beams were produced by the 14UD Pelletron Accelerator at the ANU. Ions from a negative ion source were mass-selected by a 90° magnet before being accelerated through the machine. A further 90° analysing magnet allowed the beam energy to be precisely defined. By measuring the magnetic field of the 90° analysing magnet with a nuclear magnetic resonance (NMR) probe, the energy of the beam was determined using the relativistic expression:

$$E = CB^2 \left(\frac{Z_{eff}^2}{m}\right) \left(1 + \frac{E}{2Mc^2}\right)^{-1} \tag{3.1}$$

where C is the magnet constant, B is the magnetic field strength, Z_{eff} is the effective charge of the particle and M is its mass. Based on a calibration of the accelerator in 1999, which occurred during the period of the experiments discussed in this work, and previous calibrations [Spea77, Mort94], the energy of the beam was found to be accurate to better than 0.04%. Thus for beam energies in the order of 100 MeV, the absolute beam energy is defined to ±40 keV. The relative accuracy of several beam energies measured in series, was found to be better than ±5 keV.

Pulsed beams were used for each of the measurements. The pulsing was obtained by one of two methods. The first was by bunching the beam before acceleration into 1 ns width packets separated by 106.7 ns, and chopping the beam after acceleration, to remove any background ions between the pulses [Weis88]. The second method was to use a slow chopper to obtain pulse widths and pulse intervals in multiples of 106.7 ns.

3.2 Projectiles

The projectile species used, together with their beam energies E_{beam}, and characteristic pulsing rates are shown in Table 3.2. Low beam pulsing rates were used when measuring α-particle decay (with various lifetimes) from the ERs formed in the fusion-ER reactions. For the reaction ^{30}Si + ^{186}W, two ER measurements were

Beam Species	Energy Range E_{beam} (MeV)	Pulsing	Measurement
^{12}C	56.0 to 94.6	1 ns on/106.7 ns off	Fission
		106.7 ns on/533.5 ns off	ER
^{19}F	82.0 to 134.0	1 ns on/106.7 ns off	Fission
		106.7 ns on/533.5 ns off	ER
^{30}Si	126.8 to 177.7	1 ns on/106.7 ns off	Fission
		106.7 ns on/533.5 ns off	ER (A)
		1 s on/1 s off	ER (B)
^{16}O	74.0 to 95.0	1 ns on/106.7 ns off	Fission
	73.0 to 95.0	10 ms on/20 ms off	ER
^{18}O	74.0 to 95.0	1 ns on/106.7 ns off	Fission
	72.0 to 95.0	10 ms on/20 ms off	ER

Table 3.2: Beam species, energy range, and characteristic pulsing rates for each measurement type.

performed, denoted (A) and (B) in Table 3.2. In order to obtain the average energy of the projectiles during the reaction, E_{lab}, the beam energy was corrected for losses in the target. For the reactions leading to the ^{216}Ra compound nucleus, beam energies were chosen such that the compound nuclei were formed at the same excitation energies in the three reactions. The subscripts *lab* and *c.m.* are used in this work to denote respectively the laboratory and centre-of-mass frames of reference.

3.3 Targets

Details of the targets used are outlined in Table 3.3. Targets were prepared by evaporating the target material onto either a backing material, or in the cases of ^{197}Au and ^{196}Pt onto glass plates coated with release agent. The ^{197}Au and ^{196}Pt material was then floated off the glass, forming self-supporting targets. All targets were mounted in a target frame, with the backing material located downstream relative to the beam direction. Two exceptions were the $^{186}WO_3$ target arrangements, which consisted of two adjacent foils of tungsten oxide on carbon backings. These were arranged in two configurations, either with the two tungsten oxide ele-

Target	Measurement	Composition	Thickness ($\mu g/cm^2$)	Function
^{204}Pb	fission	$^{204}PbCl_2$ 99.7%	35	target material
		C	20	backing material
	ER	$^{204}PbCl_2$ 99.7%	50	target material
		Al	10	backing material
		Al	550	catcher
^{197}Au	fission	^{197}Au 100%	320	target material
	ER	^{197}Au 100%	250	target material
		Al	800	catcher
^{186}W	fission	$^{186}WO_3$ 97.1% $^{184}WO_3$ 2.2%	85	target material
		C	20	backing material
	ER	$^{186}WO_3$ 97.1% $^{184}WO_3$ 2.2%	2 × 50	target material
		C	2 × 20	backing material
		Al	1600 (run A)	catcher
			1800 (run B)	
^{192}Pt	fission	^{192}Pt 57.0% ^{194}Pt 26.2% ^{195}Pt 1.2% ^{196}Pt 4.7%	15	target material
		C	15	backing material
^{194}Pt	fission/ER	^{194}Pt 95.1% ^{195}Pt 3.8% ^{196}Pt 1.0%	50	target material
		C	20	backing material
	ER	Al	550	catcher
^{196}Pt	fission	^{195}Pt 2.4% ^{196}Pt 96.5% ^{198}Pt 0.3%	200	target material
^{198}Pt	fission/ER	^{195}Pt 1.2% ^{196}Pt 2.2% ^{198}Pt 95.8%	50	target material
		C	20	backing material
	ER	Al	550	catcher

Table 3.3: Composition and thickness of targets: Composition fractions of less than 1% are not shown. Non self-supporting target material was placed on a backing material. To measure decay from the ERs, they were first stopped in a catcher foil, which was located immediately downstream of the target.

ments facing each other (run A), or with both the tungsten oxide elements facing upstream (run B). For fusion-ER experiments, a catcher foil was placed adjacent to, and downstream from, the targets. It was important that the catcher foils were sufficiently thick to capture all recoiling ERs produced, to allow accurate determination of the ER cross-sections. The catcher foil thicknesses were 1.5 to 2.5 times the mean ER recoil range for each reaction. The repeat measurements for the ^{30}Si + ^{186}W reaction with a thicker catcher gave the same cross-sections, confirming that all ERs were stopped.

3.4 Evaporation Residue Experiments

The aim of the evaporation residue (ER) experiments was to determine, over a range of beam energies, the distribution and cross-sections of the residue nuclei formed in fusion-evaporation reactions. There are both direct and indirect methods that can be used to identify ER. Direct methods include the use of velocity filters and time-of flight techniques. Indirect methods involve the measurement of particles or radiation emitted during the decay of the ERs, such as α-particles and γ-rays. The decay of the ER should not be confused with the prompt evaporation of particles and γ-rays from the hot compound nucleus just after capture has occurred. The ERs generally decay from their ground-states. In most cases their decay has previously been measured and reported, including half-lives, branching ratios, decay modes and energies.

In this work an indirect method of measuring ER was used, through detecting the energies and decay times of α-particles emitted by the ERs. The emission of α-particles is the prominent decay mode for most of the ERs of interest in this work, together with a substantial number of their daughter nuclei. Measurements were performed for the reactions ^{12}C + ^{204}Pb, ^{19}F + ^{197}Au, ^{30}Si + ^{186}W, ^{16}O + ^{194}Pt, and ^{18}O + ^{198}Pt.

In the next section, the known half-lives, α-particle energies, and branching ratios for the possible ERs, and their daughter nuclei, formed in the above reactions are tabulated. Section 3.4.2 details the experimental equipment used to detect the α-particles. The process of correlating the α-decay and the emitting nuclei then follows (Section 3.4.3), together with extraction of cross-sections for each ER

channel (Section 3.4.4), and the total reaction ER cross-sections for each reaction (Section 3.4.4.3).

3.4.1 Alpha Particle Decay from Evaporation Residues

For each reaction and beam energy, there will be a statistical distribution of ER channels that may occur. For each ER channel, in addition to the ER itself there may be a number of daughter nuclei, all of which may emit one or more α-particles. Tables 3.4, 3.5, 3.6, and 3.7 list each ER channel, the nuclei involved in that channel, their half-lives, $t_{1/2}$, α-decay branching ratios and α-particle energies, E_α. Nuclear data in these tables has been extracted from Firestone, *Table of Isotopes 8th Edition* [Fire96]. Nuclei with half-lives of more than one day or with less than a 1% branching ratio have either been excluded or placed within parentheses. Evaporation residues formed by only the evaporation of neutrons are denoted as xn ERs, where x is the number of neutrons. The notation αxn, and pxn, are used respectively for ERs formed by the evaporation of an α-particle or proton, together with x neutrons.

The xn ER α-decay data for the compound nucleus ^{216}Ra formed in the reactions ^{12}C + ^{204}Pb, ^{19}F + ^{197}Au, ^{30}Si + ^{186}W are listed in Table 3.4, whereas αxn, and pxn ER channels for these reactions are listed in Table 3.5. The daughter nuclei for most of the xn channels were the same as primary nuclei for either αxn or pxn channels, although the branching ratios differed. In these cases, the observed decay from the common nuclei was separated into ER channels by calculating the xn daughter nuclei contribution from the decay of the xn parent nuclei, and then subtracting this from the total decay from the common nucleus. For some channels the electron capture process let to isobars of the parent (e.g. ^{212}Fr and ^{212}Rn nuclei from the ^{212}Ra parent), which subsequently α-decayed.

Table 3.6 shows α-particle decay data for ER channels for the compound nucleus ^{210}Rn formed in the reaction ^{16}O + ^{194}Pt. Several of the charged particle channels, $\alpha 2n$, $\alpha 3n$ and $p3n$, have low α-decay branching ratios, which lead to yields insufficient to determine the αxn and pxn ERs cross-sections for these channels. This resulted in a significant deficiency in the total ER cross-sections. In all other cases, α-decay allows all channels to be measured.

Data for xn ER channel α-decay for the compound nucleus ^{216}Rn formed in the

ER	Nucleus	$t_{1/2}$	α-decay branching ratio	E_α (MeV)
$2n$	^{214}Ra	2.46s	99.94%	7.137
	^{210}Rn	2.4h	96.0%	6.040
$3n$	^{213}Ra	2.74m	36%	6.731
			40%	6.624
			4.8%	6.522
	^{209}Rn	28.5m	14%	6.039
	^{213}Fr	34.6s	18%	6.775
	^{209}At	5.41h	3.5%	5.647
$4n$	^{212}Ra	13.0s	≈90%	6.899
	^{208}Rn	24.35m	≈60%	6.144
	^{212}Fr	20.0m	≈1%	6.406
			≈1%	6.383
			≈2%	6.262
	^{212}Rn	23.9m	≈6%	6.264
$5n$	^{211}Ra	13s	>93%	6.910
	^{207}Rn	9.25m	>19%	6.131
	^{211}Fr	3.10m	≈5.6%	6.534
	^{207}At	1.80h	≈6.8%	5.758
$6n$	^{210}Ra	3.7s	≈96%	7.019
	^{206}Rn	5.67m	≈60%	6.258
	^{202}Po	44.7m	≈1%	5.587
	^{210}Fr	3.18m	≈2%	6.543
	^{210}Rn	2.4h	≈2%	6.040
$7n$	^{209}Ra	4.6s	≈90%	7.008
	^{205}Rn	2.8m	≈21%	6.262
	^{209}Fr	50.0s	≈9%	6.646
	^{205}At	26.2m	≈8%	5.902
$8n$	^{208}Ra	1.3s	≈95%	7.133
	^{204}Rn	1.24m	≈69%	7.031
	^{200}Po	11.5m	≈7.7%	5.863
	^{208}Fr	59.1s	≈4.5%	6.641
	^{204}At	9.2m	≈1.2%	5.951

Table 3.4: Summary of xn particle ER channels, ER and daughter nuclei, α-decay branching ratios and α-particle energies [Fire96] for the compound nucleus ^{216}Ra. Nuclei with half-lives of more than one day or with less than a 1% branching ratio have been excluded.

ER	Nucleus	$t_{1/2}$	α-decay branching ratio	E_α (MeV)
$\alpha 2n$	^{210}Rn	2.4h	96.1%	6.040
$\alpha 3n$	^{209}Rn	28.5m	17%	6.039
	^{209}At	5.41h	3.4%	5.647
$\alpha 4n$	^{208}Rn	24.35m	62%	6.144
$\alpha 5n$	^{207}Rn	9.25m	21%	6.131
	^{207}At	1.80h	6.8%	5.758
$\alpha 6n$	^{206}Rn	5.67m	62%	6.258
	^{202}Po	44.7m	1.2%	5.587
$\alpha 7n$	^{205}Rn	2.8m	23%	6.262
	^{205}At	26.2m	7.7%	5.902
$p2n$	^{213}Fr	34.6s	99.45%	6.775
	^{209}At	5.41h	4.1%	5.647
$p3n$	^{212}Fr	20.0m	9.46%	6.406
			10.3%	6.383
			1.33%	6.342
			4.39%	6.335
			16.1%	6.262
	^{212}Rn	23.9m	5.7%	6.264
$p4n$	^{211}Fr	3.10m	>80%	6.534
	^{207}At	1.80h	>6.8%	5.758
	^{211}Rn	14.6h	<2%	5.852
			<3.5%	5.784
	^{211}At	7.214h	<6%	5.870
	^{211}Po	0.516s	<8.5%	7.450
$p5n$	^{210}Fr	3.18m	60%	6.543
	^{210}Rn	2.4h	0.38%	6.040
$p6n$	^{209}Fr	50.0s	89%	6.646
	^{205}At	26.2m	8.9%	5.902
	^{209}Rn	28.5m	1.9%	6.039
	^{209}At	5.41h	3.4%	5.647
$p7n$	^{208}Fr	59.1s	90%	6.641
	^{204}At	9.2m	3.4%	5.951
	^{208}Rn	24.35m	6.2%	6.144

Table 3.5: Summary of charged particle ER channels, ER and daughter nuclei, α-decay branching ratios and α-particle energies [Fire96] for the compound nucleus ^{216}Ra. Nuclei with half-lives of more than one day or with less than a 1% branching ratio have been excluded.

ER	Nucleus	$t_{1/2}$	α-decay branching ratio	E_α (MeV)
$3n$	^{207}Rn	9.25m	21%	6.131
	^{207}At	1.8h	6.8%	5.758
$4n$	^{206}Rn	5.67m	62%	6.258
	^{202}Po	44.7m	1.2%	5.587
$5n$	^{205}Rn	2.8m	23%	6.262
	^{205}At	26.2m	7.7%	5.902
$\alpha 2n$	^{204}Po	3.53h	(0.66%)	5.377
$\alpha 3n$	^{203}Po	36.7m	(0.11%)	5.383
$\alpha 4n$	^{202}Po	44.7m	2.0%	5.587
$p2n$	^{207}At	1.80h	8.6%	5.758
$p3n$	^{206}At	30.0m	(0.85%)	5.703
$p4n$	^{205}At	26.2m	10.0%	5.902

Table 3.6: Summary of ER channels, ER and daughter nuclei, α-decay branching ratios and α-particle energies [Fire96] for the compound nucleus ^{210}Rn. Nuclei with half-lives of more than one day have been excluded. Branching ratios of less then 1% are shown in parentheses.

ER	Nucleus	$t_{1/2}$	α-decay branching ratio	E_α (MeV)
$3n$	^{213}Rn	25ms	99%	8.088
			1%	7.553
$4n$	^{212}Rn	23.9m	100%	6.264
$5n$	^{211}Rn	14.6h	9.3%	5.852
			17.3%	5.784
	^{211}At	7.214h	30.3%	5.870
	^{211}Po	0.516s	41.8%	7.450
$6n$	^{210}Rn	2.4h	96.1%	6.040
$7n$	^{209}Rn	28.5m	17%	6.039
	^{209}At	5.41h	3.4%	5.647

Table 3.7: Summary of xn ER channels, ER and daughter nuclei, α-decay branching ratios and α-particle energies [Fire96] for the compound nucleus ^{216}Rn. Nuclei with half-lives of more than one day or branching ratios of less then 1% have been excluded.

reaction $^{18}O + ^{198}Pt$ is displayed in Table 3.7. Unlike the earlier tables, only data for xn channels are shown, as the probability of charged particle ER channels is very low. This expectation was corroborated by the experimental α-energy spectra, which showed no signs of charged particle ER channels.

3.4.2 The Detection Equipment

In order to detect the α-particles emitted by the ERs, the ERs first needed to be captured. Catcher foils (see Table 3.3) were located immediately downstream of the targets. To ensure all ERs were captured, for each reaction, the thickness of the catcher foils was between 1.5 to 2.5 times the mean ER recoil range, as calculated using a program based on the range calculations of Ziegler [Zieg80]. Alpha-particles emitted from the captured ERs were detected in an annular silicon surface barrier (SSB) detector and a circular SSB detector (front detector), as shown in Figure 3.1. The annular detector was located at an average angle of 174.8° to the beam

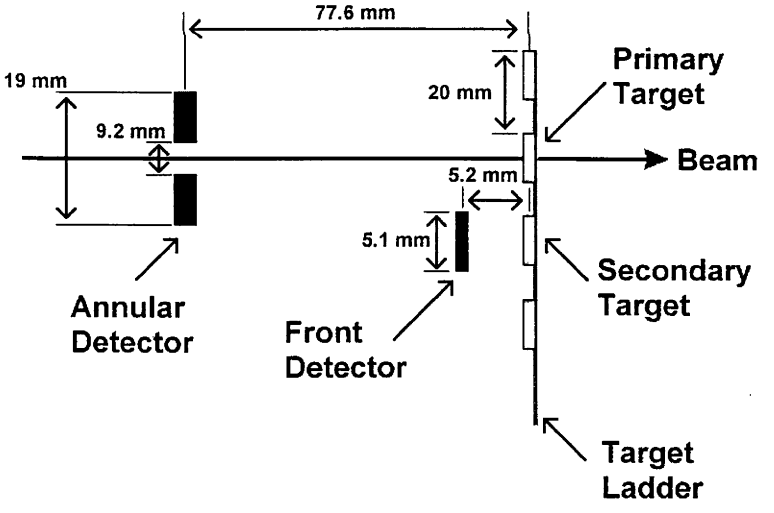

Figure 3.1: Relationship of the annular and front detectors to the target.

direction. Its solid angle of $d\Omega = 35.6$ millisteradians was determined precisely using calibration reactions (see Section 3.4.2.2). The annular detector had an outer diameter of 19mm and an inner diameter of 9.2mm, and was located 77.6 mm away

from the primary target. Up to seven targets were positioned at 20mm intervals on a target ladder, which moved vertically. The front detector was located 5.2mm away from the secondary target, positioned 20mm below the primary target.

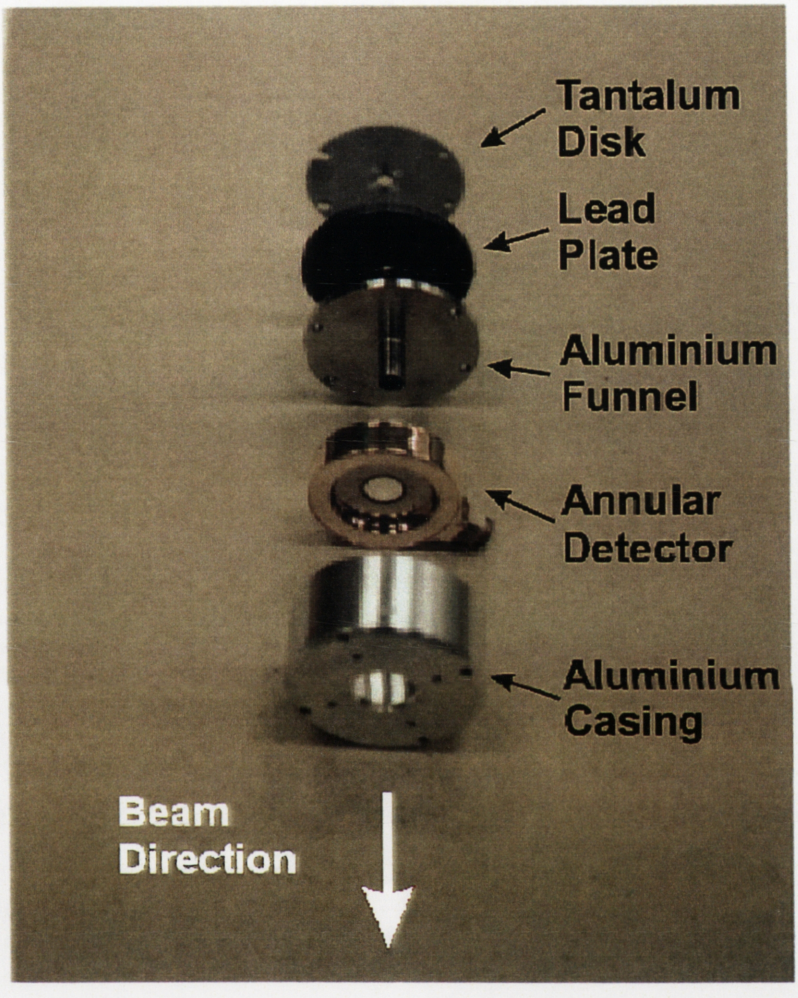

Figure 3.2: Photograph of the annular detector components.

The annular detector was shielded (see Figure 3.2) to protect it from the beam and stop unwanted radiation being detected. Starting at the upstream end, there was a tantalum disk to stop incoming beam particles hitting the back of the detector. Next was a lead plate to shield the detector from X-rays. The annular detector was located between a machined aluminium funnel and an aluminium casing. This, in conjunction with the front detector, limited the acceptance of the detector to only activity from the primary target, excluding activity from the other targets on the

target ladder.

Two types of measurements were made, those while the target was being bombarded by the beam (on-line) and those after bombardment (off-line). For each on-line measurement, elastically scattered beam particles were detected in two silicon surface-barrier (SSB) detectors (monitors) located at $\pm 22.5°$ from the beam direction. These data were used to normalise the absolute ER differential cross-sections. Elastically scattered beam particles, fission and other prompt emissions from the target were vetoed from the annular and front detector signals, resulting in clean energy spectra. The cycle time between pulses (see Section 3.2) is shown schematically in Figure 3.3. The veto was synchronised to the beam pulse, having a width slightly wider than the beam pulse. The ratio of the recording time, t_r to the cycle time t_c varied for each run. The ratio t_r/t_c was determined for each run using a free running pulser. For post-bombardment measurements, the veto was removed, resulting in $t_r/t_c = 1$.

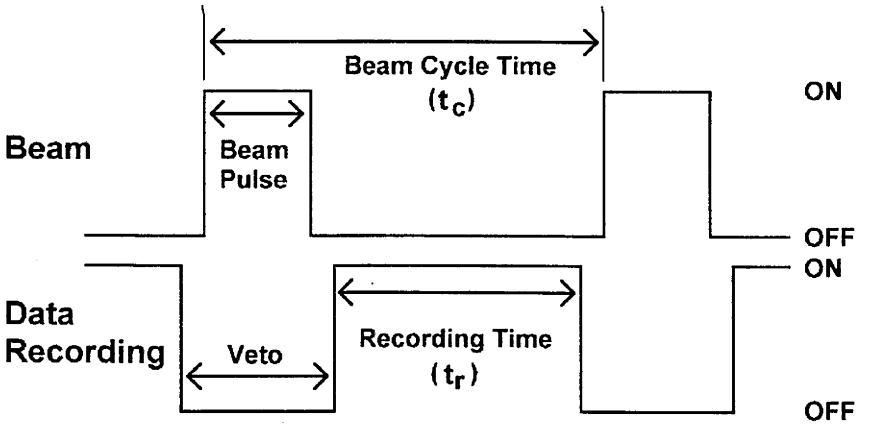

Figure 3.3: Relationship between beam pulsing and data recording.

Up to seven parameters were recorded digitally on computer files for later analysis; the energy and time from both the annular and the front detectors, energy from both the monitors, and a pulser trigger signal. The front detector was not used for

the $^{19}F + ^{197}Au$ measurements, and time information from the two detectors was not recorded for the O + Pt reactions. Scalers were used to determine losses in the analog to digital converters (ADCs) and data acquisition system. Losses in the electronics were also checked by passing pulser signals through the detector electronics, and comparing the resultant number of recorded pulser events in the detectors, to the number of recorded events in the pulser, and the number of pulser scaler events.

3.4.2.1 Normalisation

As stated above, for each run, data from the annular detector were normalised using elastically scattered beam particles detected in two silicon surface-barrier (SSB) detectors (monitors M_L and M_R). The monitors were positioned at angles of $\pm 22.5°$ relative to the beam axis. At this angle the elastic scattering differential cross-sections may safely be assumed to be equal to the Rutherford cross-sections, $d\sigma_R/d\Omega$. Figure 3.4 shows the ratio of elastic scattering cross-sections to Ruther-

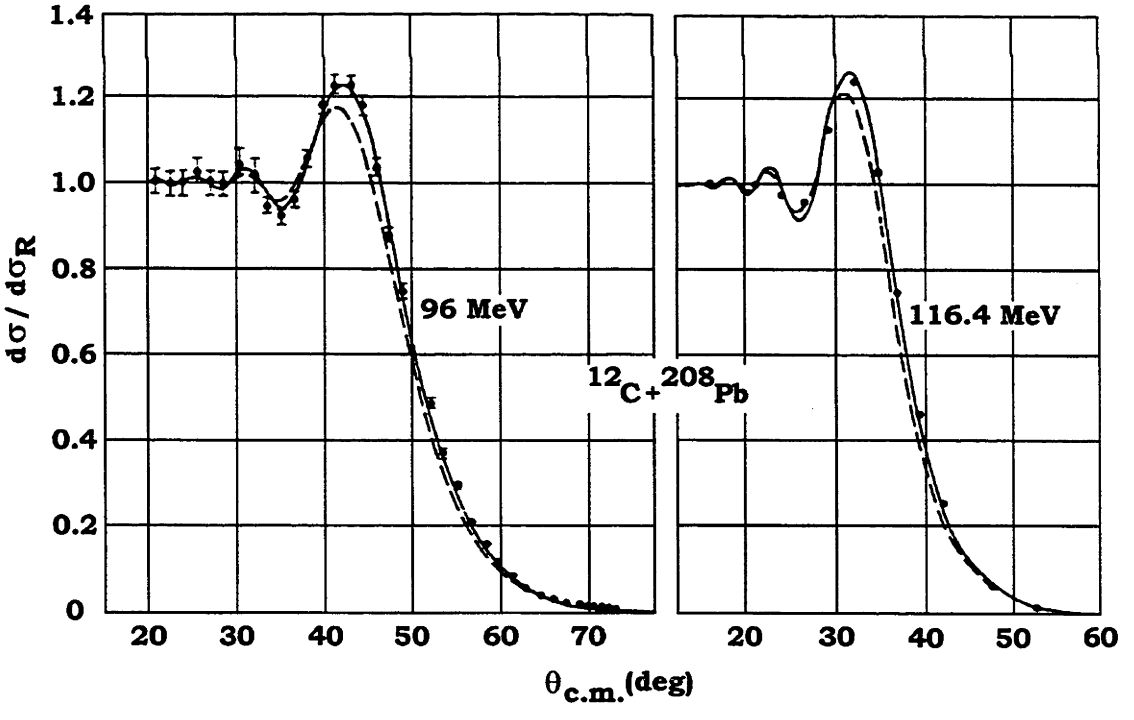

Figure 3.4: Elastic scattering data and two optical model fits for the reaction $^{12}C + ^{208}Pb$ at $E_{lab} = 96$ and 116.4 MeV shown against centre-of-mass scattering angle, from Ball *et al.* [Ball75].

ford scattering cross-sections for the reaction $^{12}C + ^{208}Pb$ at $E_{lab} = 96$ MeV [Ball75] and 116.4 MeV [Lars72]. As this reaction is very similar to the $^{12}C + ^{204}Pb$ reaction used in this work, the angular dependence of the elastic scattering ratios is expected to be similar. Therefore, at the monitor angle of $\theta_{lab} = 22.5°$ ($\theta_{c.m.} = 23.8°$) and with beam energies all less than 100 MeV, the elastic scattering cross-sections are expected to be within a few percent of the Rutherford cross-sections. For the other reactions in this work, at $\theta_{lab} = 22.5°$, the difference between the elastic scattering and Rutherford cross-sections is expected to be less than for the $^{12}C + ^{204}Pb$ reaction.

3.4.2.2 Calibration Reactions

Several calibration measurements, shown in Table 3.8, were conducted to simultaneously measure elastic scattering in the monitors and the annular detector. With this information the relative solid angles of the annular detector and monitors were calculated. The solid angle of the front detector was determined by comparing the relative activity detected in the front and annular detectors, from a very long lifetime ER from the same target. The front detector solid angle was found to be 18 $\pm$ 1 times larger than the solid angle of the annular detector, from a large number of determinations.

Calibrating Reaction	Beam Energy	Detector Calibrated
$^{19}F + ^{197}Au$	68.00 MeV	Annular (^{216}Ra runs)
$^{30}Si + ^{197}Au$	100.00 MeV	Annular (^{216}Ra runs)
$^{16}O + ^{194}Pt$	60.00 MeV	Annular (O + Pt runs)
$^{29}Si + ^{197}Au$	118.00 MeV	Annular (O + Pt runs)
Time Calibrator (80ns)	-	Annular (Time)

Table 3.8: Elastic scattering reactions used to calibration the Annular detector when used for measuring α-decay from fusion-ER reactions. Also included is the time calibration of the time spectrum.

The time spectrum was calibrated, without signals from the detectors, using a time calibrator generating a pulse every 80ns. During measurements, a pulser signal was injected into the detector preamplifier pulse inputs, at a pulse rate of

6.845 pulses/sec (O + Pt reactions) or 9.05 pulses/sec (^{216}Ra compound nucleus reactions). This achieved two purposes; firstly to provide a check of the losses in the electronics and data collection system, and secondly to provide time signals at a known interval by which long lifetimes could be measured.

The energy spectra for both detectors were calibrated over the experimental range of energies, using the position of well known α-particle decay energies, taking into consideration the implantation depth of the compound nuclei and the energy loss of the emitted α-particle as it transverses the backing and target material to reach the detectors. The dependence of implantation depth with beam energy was an important ingredient in identifying individual xn, pxn, and αxn channels.

3.4.3 Using Alpha-Particle Decay to Identify Nuclei

Since at each bombarding energy there were up to ten ER channels (including daughters) present, the correct identification of the α-decay spectra was crucial in determining the individual ER cross-sections. The process used to separate the individual components involved correlating α-decay energies and half-lives. In most instances only activity from ER parent and daughter nuclei was required for identification and calculation of ER cross-sections.

3.4.3.1 Alpha-Particle Energies

For each reaction and beam energy several spectra were obtained. On-line data were collected in the annular detector, whereas one or more off-line measurements were done using either or both the annular and front detectors. The delay between bombardment and off-line collection was chosen based on the half-lives of the decays to be measured. The energy spectra were fitted to determine and quantify individual ER α-decays. Background counts were first subtracted from some on-line spectra, based on counts in energy regions where no ER α-decay was expected. Off-line measurements proved to be very clean, with little or no background counts. The presence of background in some off-line measurements occurred because they were collected using the front detector with the target in the secondary position, while another target in the primary position was being bombarded. Although a signal veto was in place, scattered beam particles were sometimes recorded by the annular and front detectors. Counts above background were fitted with Gaussian peaks at

energies of known ER α-decays. When two known α-decay energies were very close to one another, only a single peak was fitted, and further separation was conducted using the decay lifetimes. Figure 3.5 illustrates three typical energy spectra and their Gaussian fits. The blue lines are fits to individual peaks and the red lines are the total fits. Relative intensities of lines were tied together where appropriate, in the peak-fitting routine used.

For the reactions leading to the compound nucleus ^{216}Ra most of the half-lives of interest were in the order of seconds to a few hours (see Tables 3.4, and 3.5). On-line measurements were taken for periods between one and two hours, while off-line measurements were in the order of a half to one hour with delays of 2 to 30 minutes. Figure 3.5(a) is a typical on-line spectrum. It is characterised by three major features. At the higher energies ($E_\alpha \approx 7.0$ MeV) are the shorter half-life Radium nuclei α-decays, from xn parent channels. Lower in energy, around $E_\alpha \approx 6.6$ MeV, are the Francinium nuclei α-decays, from the pxn parent and xn daughter (after electron capture) channels. At energies around $E_\alpha \approx 6.1$ MeV, are Radon nuclei α-decays, from αxn parent and xn daughter (after one α-decay) channels.

The reaction ^{16}O + ^{194}Pt resulted in ERs with half-lives between 2.8 minutes and a few hours (see Table 3.6). On-line recordings were for an average duration of 30 minutes, while off-line measurements ranged from 5 to 90 minutes with delays of 2 to 105 minutes. For the charged particle ER channels $\alpha 2n$, $\alpha 3n$, and $p3n$ virtually no α-particle decay could be measured, as the α-decay branching ratios for these channels were less than 1%.

For the reaction ^{18}O + ^{198}Pt, the ERs of interest had half-lives ranging from 25 ms to 14.6 hours (see Table 3.7). As well as on-line measurements of around one hour, off-line measurements of 10 to 102 minutes were made at delays ranging from 1.3 minutes to 27 hours. The longer delay times were due to an added complication in measuring the decay from the $5n$ ER channel. The half-life of the parent nucleus formed following $5n$ evaporation, ^{211}Ra, is 14.6 hours, while the half-life of the daughter, ^{211}At, is shorter at 7.214 hours and the half-life of the grand-daughter, ^{211}Po, is only 0.516 seconds. Further, the single α-decay energy from the ^{211}At ($E_\alpha = 5.8695$ MeV) is very close to the energy of the higher of the two α-particles from the ^{211}Rn nucleus (E_α=5.7839 & 5.8522 MeV) . In order to determine the

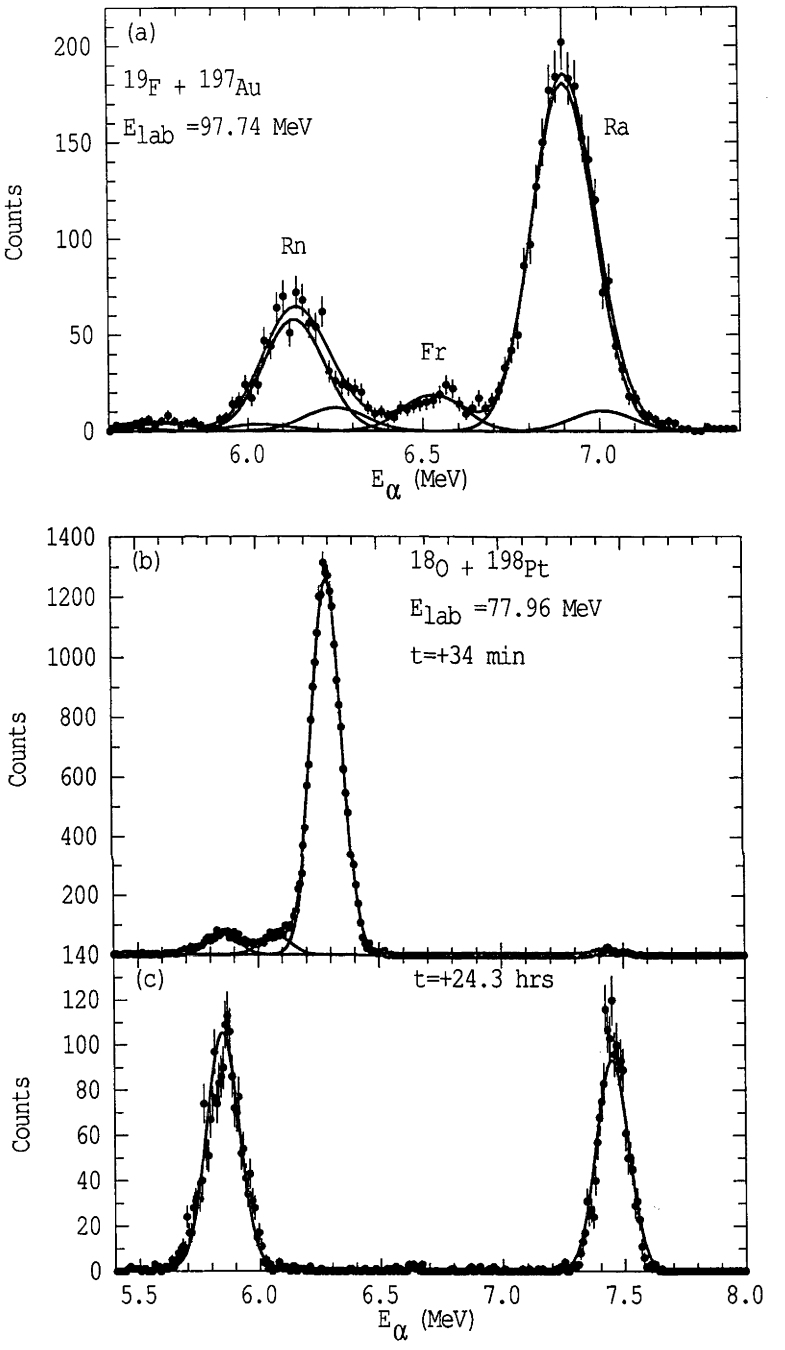

Figure 3.5: Alpha spectra shown as activity (in counts) against α-particle energy. For all spectra, the background has been subtracted and the remaining activity fitted with Gaussian peaks corresponding to known α-decay energies (blue lines). The red lines are the total fits. Frame (a) shows an on-line spectrum from the annular detector for the reaction $^{19}F + ^{197}Au$ at $E_{lab} = 97.74$ MeV. Frames (b) and (c) show spectra from the front detector for the reaction $^{18}O + ^{198}Pt$ at an energy of $E_{lab} = 77.96$ MeV, 34 min and 24.3 hours after bombardment respectively.

amount of direct production of the ^{211}Rn nucleus, activity was measured after a few minutes and also after 20+ hours. By comparing the two spectra, and in particular the activity from the ^{211}Po decay (E_α = 7.450 MeV), the production rate for the $5n$ ER channel was deduced.

Figures 3.5(b) and 3.5(c) are from off-line measurements with delays of 34 min and 24.3 hours respectively for the reaction ^{18}O + ^{198}Pt at E_{lab} = 77.96 MeV. Frame (b) shows the 23.9 minute half-life α-decay from ^{212}Rn as the large peak at E_α = 6.264 MeV. To the immediate left of the large peak is a small peak from the α-decay of ^{210}Rn (E_α = 6.040 MeV) which has a half-life of 2.4 hours. The left-most peak is from ^{211}Rn and ^{211}At α-decay. After 24.3 hours the remaining activity is shown in Frame (c). The activity from the ^{211}Po α-decay is visible on the right of the spectrum while the overlapping activity on the left of the frames is from the ^{211}Rn and ^{211}At nuclei, with longer lifetimes.

3.4.3.2 Decay Lifetimes

Together with fitting the α-particle energy spectrum, α-decay channels were identified using measured lifetimes. Decay lifetime spectra were constructed by use of the constant rate pulser. The decay events were separated into segments, using a set number of pulser events corresponding to 60 seconds. The methodology of determining lifetimes is demonstrated in Figure 3.6. Frame 3.6(a) shows the off-line α-particle energy spectrum for the reaction ^{16}O + ^{194}Pt at E_{lab} = 94.96 MeV, including the pulser events on the left of the frame. The corresponding time against energy plot is shown in frame 3.6(b) for the same energy range. The pulser events on the left remain constant as a function of time, while the α-particle decay events decrease from bottom to top. The small area at the bottom of the plot with no events corresponds to the delay time of 2.08 minutes between the end of bombardment and the start of the off-line recording. For a constant cut in energy, represented by the boxes in frames 3.6(b) and 3.6(c) the time spectrum is displayed in frame 3.6(c). The lines represent the individual (blue) and combined (red) decay fits to the data. In this case there are two lifetimes of approximately 8 minutes and 4 minutes, corresponding to the ^{206}Rn 6.258 MeV ($t_{1/2}$ = 5.7 min) and ^{205}Rn 6.262 MeV ($t_{1/2} \doteq$ 2.8 min) α-particle decays.

Half-lives of less than a few hours could be determined from the data. The

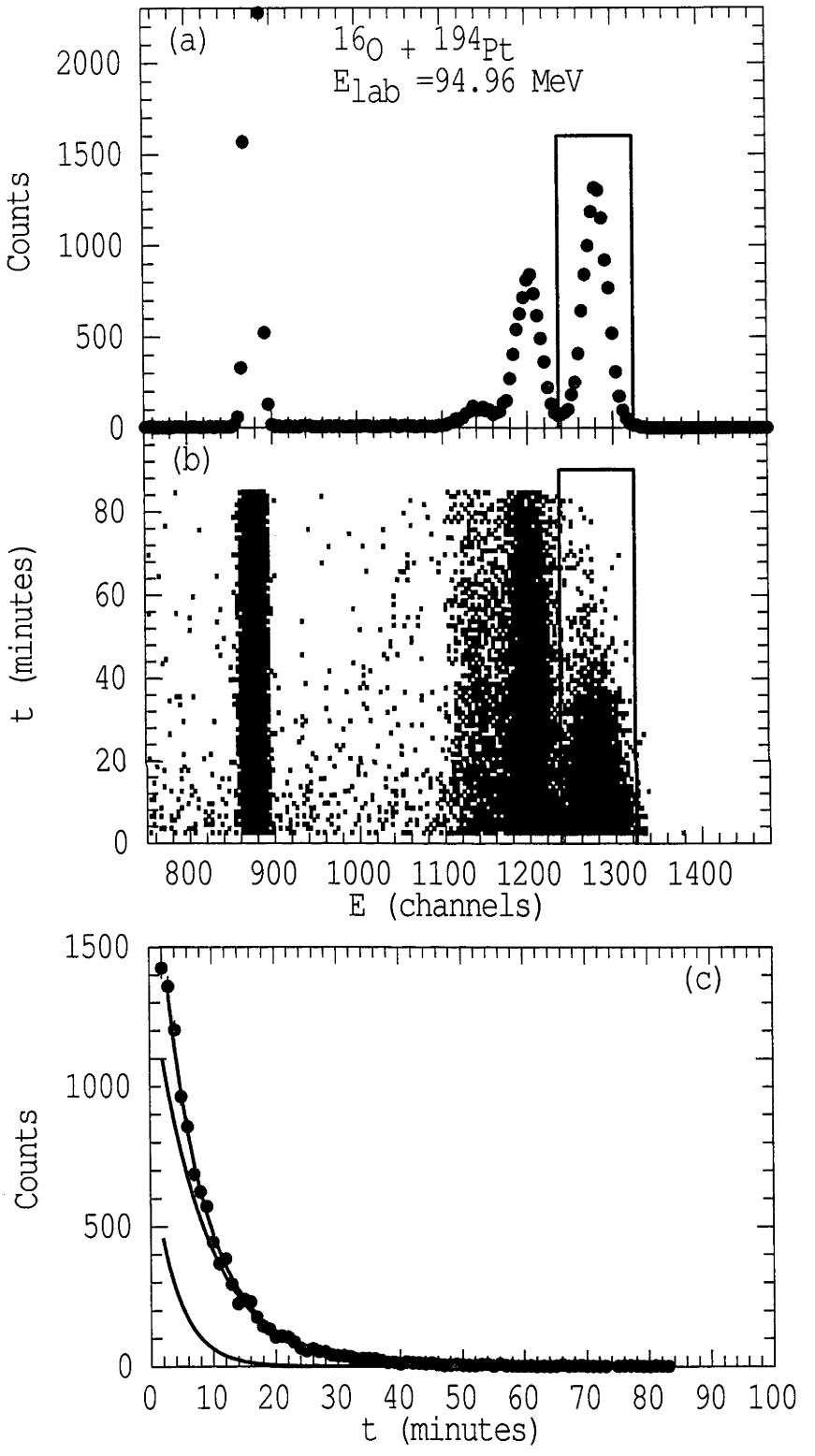

Figure 3.6: Alpha-decay spectra from the reaction $^{16}O + ^{194}Pt$ at $E_{lab} = 94.96$ MeV. (a) The α-particle energy spectrum, (b) the energy versus time plot, and (c) the time spectrum for the area shown by the boxes in frames (a) and (b).

identity of each of the α-decays was determined from the combined information of α-energy and half-life by comparing the measured quantities with those given in Tables 3.4 to 3.7. For the case of nuclei with similar α-energies, but with different lifetimes, the relative populations was obtained by refitting the time spectra with exact lifetimes corresponding to each decay.

3.4.3.3 Activity

The activity A, in terms of number of counts for each particular ER α-particle decay, was taken from the fits to the α-particle energy spectrum. For α-decays with energies close to each other, the activities were weighted iteratively such that the calculated relative populations of emitting nuclei corresponded to the relative populations determined from the lifetime spectra.

3.4.4 Evaporation Residue Cross-Sections

3.4.4.1 ER Decay and Production Rates

To calculate the number of ERs produced in the fusion reaction, their relationship with the measured α-particle activities, A, must be established. The general expression for the number of radioactive nuclei, $N(t)$, at a given time, t, is given by;

$$N(t) = \frac{R}{\lambda}(1 - e^{-\lambda t}) \tag{3.2}$$

where R is the rate at which new nuclei are being produced, and λ is the decay constant. For a given time interval $\Delta t = t_2 - t_1$, the number of nuclei will change by $\Delta N = N(t_2) - N(t_1)$ giving

$$\Delta N = \frac{R}{\lambda}(e^{-\lambda t_1} - e^{-\lambda t_2}) \tag{3.3}$$

For an α-decay branching ratio, B, (see Tables 3.4 to 3.7) the total number of decaying nuclei, A/B, in time Δt, is the number of nuclei produced, $R\Delta t$, less the difference between the final number of nuclei at time t_2 and the initial number of nuclei at time t_1;

$$\frac{A}{B} = R\Delta t - \Delta N \tag{3.4}$$

For a known activity A (the measured α-particle decay), the rate of production becomes

$$R = \frac{A}{B(\Delta t - \frac{1}{\lambda}(e^{-\lambda t_1} - e^{-\lambda t_2}))} \tag{3.5}$$

and the number of ER produced in time, Δt, is given by;

$$dN_{Ann}^{ER} = R\Delta t \tag{3.6}$$

The method used above is valid for parent ERs decaying to daughter nuclei. For the subsequent decay of the daughter nuclei to a grand-daughter nuclei, the equation for the number of daughter nuclei, $N_2(t)$, is;

$$N_2(t) = R\left(\frac{1}{(\lambda_1 - \lambda_2)}e^{-\lambda_1 t} - \frac{\lambda_1}{\lambda_2(\lambda_1 - \lambda_2)}e^{-\lambda_2 t} - \frac{1}{\lambda_2}\right) \tag{3.7}$$

where λ_1 and λ_2 are respectively the decay constants for the parent and daughter nuclei. Equation 3.7 was used to calculate ER production rates from daughter activity, when the daughter half-life was shorter or approximately the same as the parent (for example the $5n$ channel for the $^{18}O + ^{198}Pt$ reaction). However, when the daughter has a significantly greater half-life than the parent, $\lambda_1 \gg \lambda_2$, then the number of daughter nuclei was approximated by:

$$N_2(t) \approx \frac{R}{\lambda_2}(1 - e^{-\lambda_2 t}) \tag{3.8}$$

which is similar to equation 3.2.

Therefore for those ERs where the daughter nuclei had half-lives substantially longer than the ER parent nuclei (which was the case for the majority of ERs), equations 3.5 and 3.6 were used with $\lambda = \lambda_2$, to determine the number of ERs produced from the measured daughter activity.

3.4.4.2 Individual ER Channel Cross-Sections

The differential cross-section, $d\sigma/d\Omega$, for a reaction can be calculated using the relationship;

$$dN = In\frac{d\sigma}{d\Omega}d\Omega \tag{3.9}$$

where dN is the number of events detected in the solid angle $d\Omega$, I is the number of incident particles in the beam, n is the number of nuclei/cm^2 in the target, and $d\Omega$ is the solid angle. For a given experimental run the product In is a constant.

Using equation 3.9 and the data from the elastic calibration reactions (Table 3.8), the relative solid angles of the monitors, $\sum d\Omega_{mon}$, and annular detector, $d\Omega_{ann}$, was calculated using;

$$\frac{\sum d\Omega_{mon}}{d\Omega_{Ann}} = \frac{\sum dN_{mon}^{el-calib}}{dN_{Ann}^{el-calib}} \frac{\frac{d\sigma}{d\Omega}_{Ann}^{Ruth-calib}}{\frac{d\sigma}{d\Omega}_{mon}^{Ruth-calib}} \tag{3.10}$$

where $\sum dN_{mon}^{el-calib}$ is the number of elastic events in the monitors, and $dN_{Ann}^{el-calib}$ is the number of elastic events in the annular detector during the calibration run. The Rutherford differential cross-sections, for the calibration run, at the angles corresponding to the annular detector and monitors are given respectively by $\frac{d\sigma}{d\Omega}_{Ann}^{Ruth-calib}$ and $\frac{d\sigma}{d\Omega}_{mon}^{Ruth-calib}$.

The relative solid angles were then used in calculating the differential cross-sections for each ER channel using;

$$\frac{d\sigma}{d\Omega}_{Ann}^{ER} = \frac{t_r}{t_c} \frac{d\sigma}{d\Omega}_{mon}^{Ruth} \frac{dN_{Ann}^{ER}}{\sum dN_{mon}^{el}} \left[\frac{\sum d\Omega_{mon}}{d\Omega_{Ann}} \right] \tag{3.11}$$

where dN_{Ann}^{ER} comes from equation 3.6, $\sum dN_{mon}^{el}$ is the number of elastic events in the monitors scaled when necessary by the fraction of the desired isotope in the target (from Table 3.3), $\frac{d\sigma}{d\Omega}_{mon}^{Ruth}$ is the Rutherford differential cross-sections at the monitor angle, and t_r/t_c is the ratio of the recording time to the pulsing cycle time (see Section 3.4.2).

The general equation for a reaction cross-section, σ, is given by;

$$\sigma = \int \frac{d\sigma}{d\Omega} d\Omega \tag{3.12}$$

If the solid angle, $d\Omega$, is defined in terms of the centre-of-mass scattering angle $\theta_{c.m.}$ and the centre-of-mass azimuthal angle $\phi_{c.m.}$, as $d\Omega = \sin\theta_{c.m.} d\theta_{c.m.} d\phi_{c.m.}$, then the cross-section becomes;

$$\sigma = \int_0^{\pi} \sin\theta_{c.m.} d\theta_{c.m.} \int_0^{2\pi} d\phi_{c.m.} \frac{d\sigma}{d\Omega} \tag{3.13}$$

For isotropic emission, as in the case of α-decay from ERs, the cross-section simplifies to:

$$\sigma = 4\pi \frac{d\sigma}{d\Omega} \tag{3.14}$$

The cross-sections for each ER channel, $\sigma_{ER}^{channel}$, were calculated using equation 3.14 where the differential cross-section was given by equation 3.11.

The uncertainty in the individual ER cross-sections was taken to be the higher of the statistical errors on the peak fits, the parent percentage error (when looking at daughter nuclei), or a combination of both these for nuclei formed in more than one ER channel.

Individual xn ER cross-sections for the reaction $^{19}F + ^{197}Au$ (Figure 3.7) show the characteristic distribution of channels as a function of energy. Only 2-3 xn evaporation channels are present at any given energy. Chapter 4 discusses in detail the individual ER cross-sections.

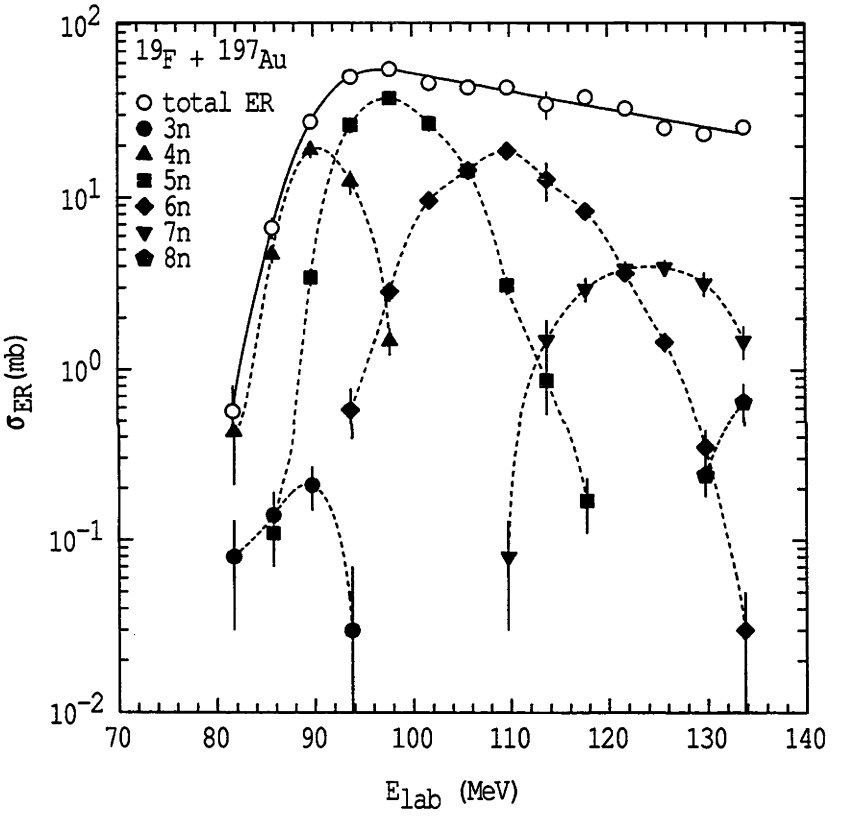

Figure 3.7: Cross-sections for xn ER channels for the reaction $^{19}F + ^{197}Au$ as a function of laboratory energy, E_{lab}. Experimental uncertainties are in several cases smaller than the size of the points. The lines guide the eye.

The ER cross-sections for the $^{12}C + ^{204}Pb$ reaction were also consistent with expectations with no evidence of ERs formed by reaction of ^{12}C with the 0.17% ^{206}Pb contaminant in the ^{204}Pb target.

No ERs were observed from the reaction of ^{30}Si with the 2% ^{184}W contaminant

in the ^{186}W target. However, if ^{30}Si + ^{184}W capture reactions occurred and did not proceed to fission, the actual ^{30}Si + ^{186}W ER cross-sections could be up to 2% lower than measured. This additional uncertainty was not considered significant for this reaction.

For both the ^{16}O + ^{194}Pt and ^{18}O + ^{198}Pt reactions the presence of other isotopes in the targets produced spurious effects in the cross-sections. For the ^{18}O + ^{198}Pt reaction in Figure 3.8, fusion of ^{16}O with the 2.2% ^{196}Pt in the target produced unexpectedly high ^{210}Rn ($6n$) ER cross-sections at approximately 20 MeV less than the maximum of the ^{210}Rn cross-section. This was because the $4n$ ER for the reaction ^{18}O + ^{196}Pt reaction is the ^{210}Rn nucleus, the same as the $6n$ ER for the reaction ^{18}O + ^{198}Pt. The magnitude of the ^{196}Pt $4n$ cross-section was calculated

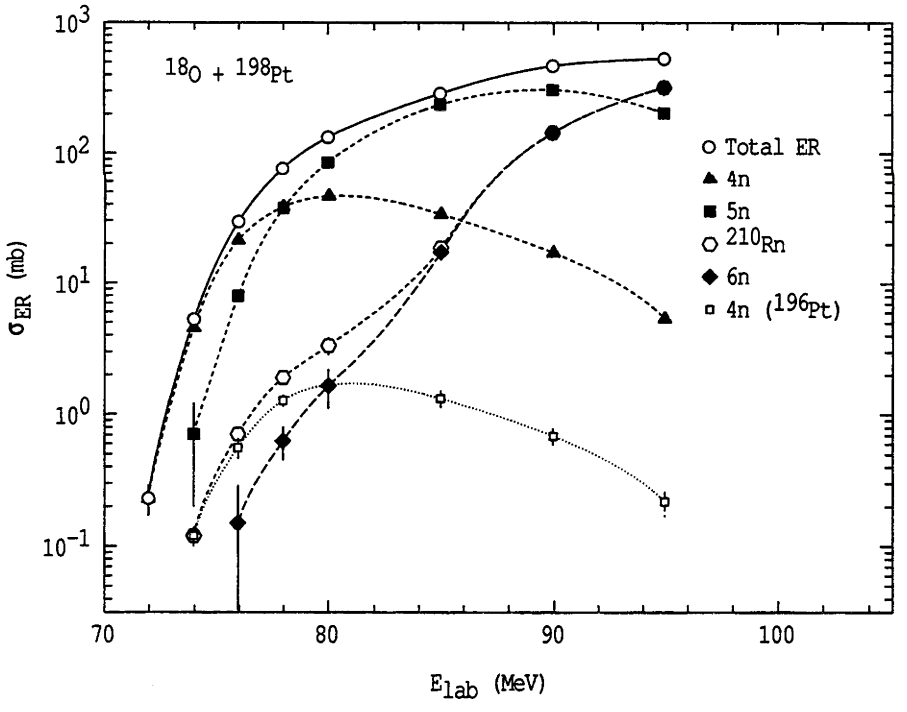

Figure 3.8: Cross-sections for ER channels from the reaction ^{18}O + ^{198}Pt as a function of bombarding energy E_{lab}. The measured cross-sections for ^{210}Rn decay is shown by the open hexagons. The calculated effect of the 2.2% ^{196}Pt in the target is shown by the open squares. The corrected ^{18}O + ^{198}Pt $6n$ ER cross-section is shown by the solid diamonds. Experimental uncertainties are in mose cases smaller than the size of the points. The lines guide the eye.

by scaling the $^{18}O + ^{198}Pt$ $4n$ ER cross-section by 0.022 (the ^{196}Pt fraction in target) and shifting its energy by 0.26 MeV (corresponding to the difference in reaction Q-values). The calculated contaminant cross-section, shown in Figure 3.8 by the open squares, was then subtracted from the measured ^{210}Rn cross-section to obtain the corrected $^{18}O + ^{198}Pt$ $6n$ ER cross-section (solid diamonds). No charged particle ER channels were detected for the $^{18}O + ^{198}Pt$ reaction.

For the $^{16}O + ^{194}Pt$ reaction, a 3.8% ^{195}Pt content in the target meant that measurements for this reaction had similar problems to the $^{18}O + ^{198}Pt$ reaction. The effect of this contaminant was handled in the same way as for the $^{18}O + ^{198}Pt$ reaction, and the resulting ER cross-sections are shown in Figure 3.9. In addition,

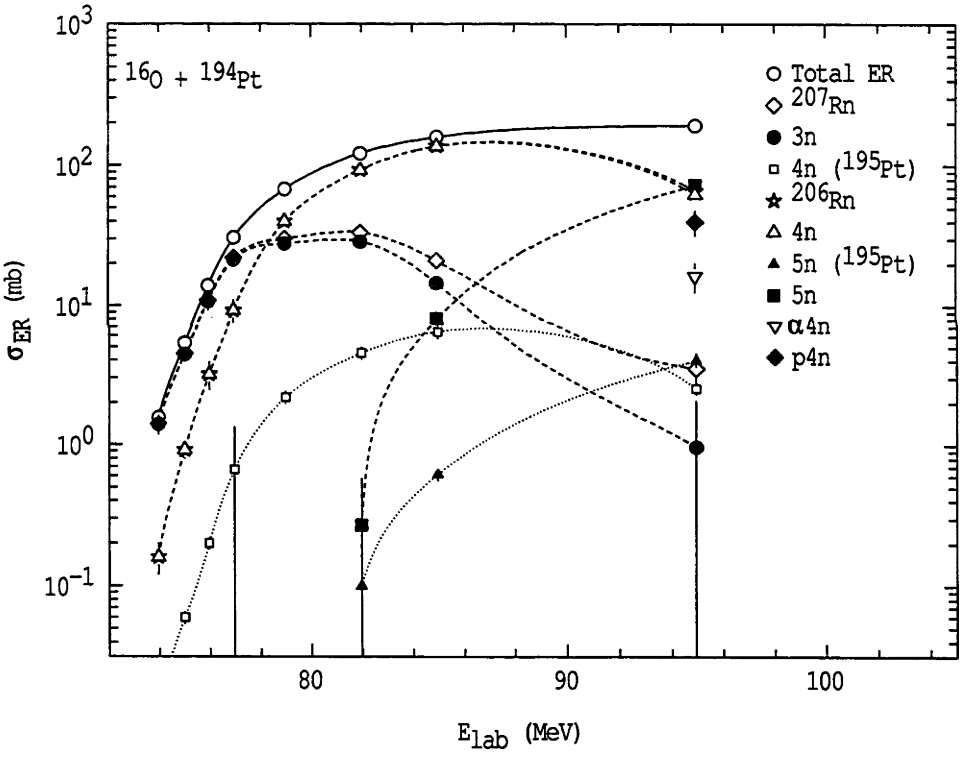

Figure 3.9: Cross-sections for ER channels from the reaction $^{16}O + ^{194}Pt$ as a function of bombarding energy E_{lab}. The measured cross-sections for ^{207}Rn decay are shown by the open diamonds. The $^{16}O + ^{194}Pt$ $3n$ cross-sections (solid circles) were determined after subtracting the effect of the $^{16}O + ^{195}Pt$ $4n$ component (open squares). Similarly the ^{206}Rn decay is shown by the stars, with the corrected cross-sections for the $^{16}O + ^{194}Pt$ $4n$ being shown by the open upward-pointing triangles (partially obscuring the stars), and the solid triangles being the cross-sections for the $^{16}O + ^{195}Pt$ $5n$ reaction. Experimental uncertainties are typically smaller than the size of the points.

the extremely low α-decay branching ratios for some charged particle ER channels resulted in no cross-sections being measured for the channels $\alpha 2n$, $\alpha 3n$ and $p3n$.

3.4.4.3 Total Evaporation Residue Cross-Sections

The total ER cross-section for each reaction, at each energy, is the sum of the cross-sections for all possible ER channels.

$$\sigma_{ER} = \sum_{channels} \sigma_{ER}^{channel} \tag{3.15}$$

Using this equation and the individual experimental channel cross-sections, total ER cross-sections were obtained for the reactions $^{18}O + {}^{198}Pt$, $^{12}C + {}^{204}Pb$, $^{19}F + {}^{197}Au$, and $^{30}Si + {}^{186}W$. Only partial ER cross-sections were obtained for the reaction $^{16}O + {}^{194}Pt$, due to a lack of measurements for some charged particle channels. At lower beam energies where charged particle emission from the fused nuclei is not expected to be significant, the partial ER cross-sections should approximately equal the total ER cross-sections. However at higher beam energies, a significant discrepancy is expected between the measured partial and the actual total ER cross-sections.

The total ER cross-section uncertainties were taken as the larger of either those calculated from the individual cross-section uncertainties (which were purely statistical), or $\pm 5\%$, to reflect system uncertainties such as target thickness, beam current uniformity, reported α-decay energies and branching ratios, background estimations and residual long-lifetime activity in multiple use targets.

3.5 Fission Fragment Experiments

The fission fragment experiments involved directly measuring one or both of the fission fragments produced in capture-fission reactions, which includes both fusion-fission and QF. Measurements of fission fragments were performed using the CUBE detector system shown in Figure 3.10. When in use the CUBE was covered by a vacuum chamber, the operational pressure being around 2 x 10^{-6} Torr.

Details of the spectrometer and the process of recording data are outlined in Section 3.5.1, while post-experimental fission fragment identification and extraction of results are discussed in Sections 3.5.2 and 3.5.3 respectively.

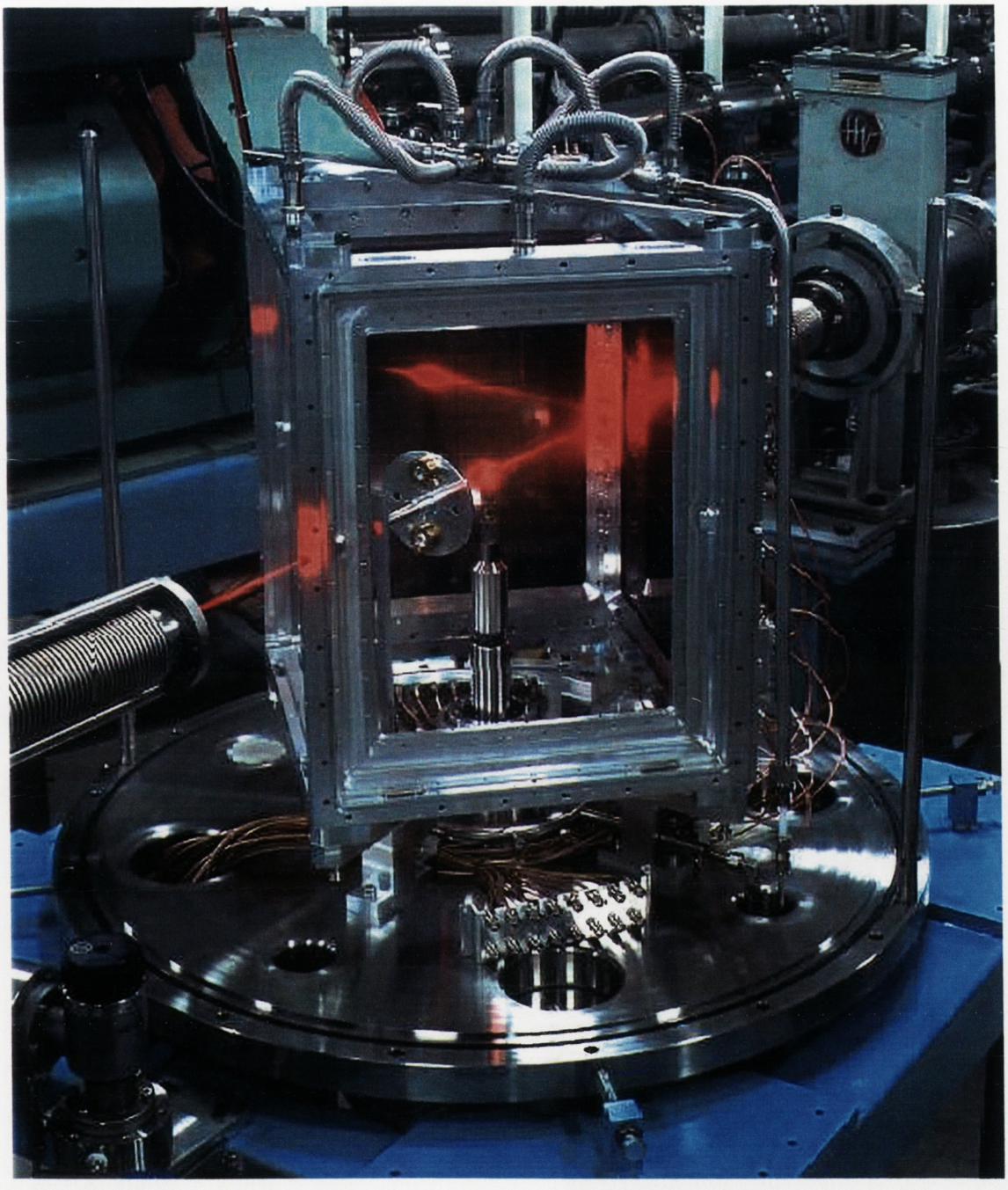

Figure 3.10: The CUBE detector system used to measure fission fragments.

3.5.1 The Detection Equipment

The CUBE consisted of two large-area position-sensitive multi-wire proportional counters (MWPCs). The active dimensions of each MWPC were 284 mm in width and 357 mm in height, consisting of 284 vertical and 357 horizontal gold coated tungsten wires spaced at intervals of 1mm [Mort95A]. The vertical and horizontal wires were positioned in two parallel planes 6 mm apart. A section through the MWPCs is shown in Figure 3.11. In order to obtain position information, signals generated in the wires as a result of incident particles were passed through delay lines with 1 ns delay between each wire. This resulted in a position resolution for each MWPC of approximately 1mm.

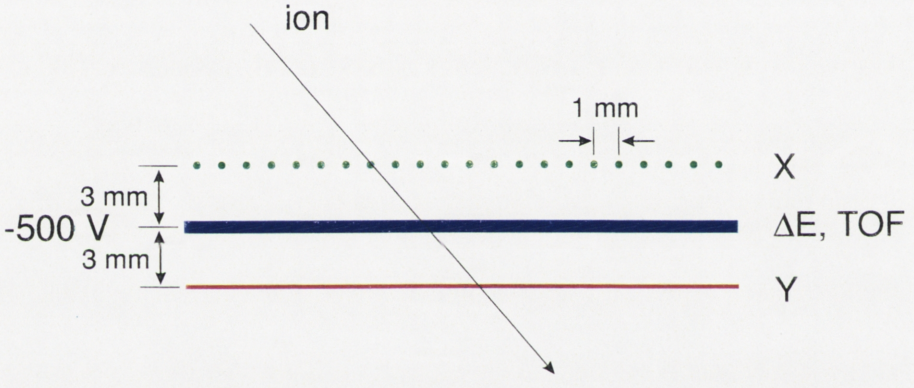

Figure 3.11: Schematic section through the MWPCs in the CUBE. The central cathode is flanked by two planes of position sensitive wires.

Each MWPC had a central foil cathode located between, and 3mm away from, the two planes of position sensitive wires (see Figure 3.11). The foil cathodes were made from approximately 40 $\mu g/cm^2$ of gold, coating each side of a 0.9 μm thick polyethylene terephthalete (PET) foil. They were each divided into four quadrants in order to reduce the capacitance of each quadrant. The voltage applied to the cathode was around -500 V. The region between the electrodes was filled with propane gas and maintained at a pressure of 4 Torr by a gas-flow system. The signal from the central cathode was used to obtain energy loss (ΔE) and time-of-flight (TOF) information for each particle. The entrance windows in each of the MWPCs, which separated the gas filled region from the vacuum chamber, was

made by coating 0.9 μm thick PET foil with copper. The copper reduced diffusion through the window, and also acted to dissipate undesirable charge build-up on the inside of the detector windows.

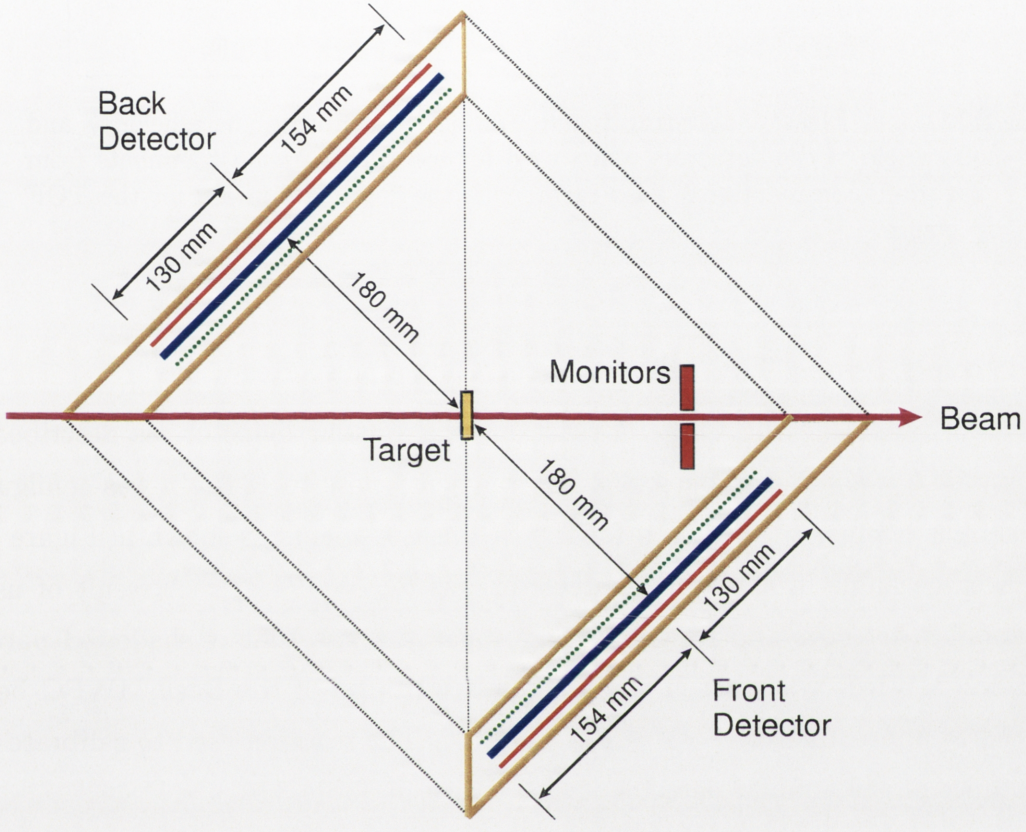

Figure 3.12: Plan view of the CUBE spectrometer.

The two MWPCs were each positioned 180 mm away from the target at angles of $\theta_{lab} = 45°$ and $\theta_{lab} = -135°$, as shown in Figure 3.12. The angles covered by the MWPCs were $5° \leq \theta_{lab} \leq 80°$ for the Front (downstream) MWPC, and $-95° \leq \theta_{lab} \leq -170°$ for the Back (upstream) MWPC. The efficiency and solid angles of the MWPCs were calibrated using both a californium source in the target position, and several elastic scattering reactions as shown in Table 3.9. Heavy beams were used, for which the backscattered ions has a large energy loss, to obtain the same 100% detection efficiency as for fission fragments. The elastic scattering reactions were each performed at energies well below the Coulomb barriers.

The TOF spectra from the two MWPCs were calibrated, without signals from

Calibrating Reaction	Beam Energy	Detector Calibrated
^{58}Ni + ^{197}Au	122.05 MeV	MWPC (^{216}Ra runs)
^{32}S + ^{198}Pt	74.00 MeV	MWPC (O + Pt runs)
^{32}S + ^{197}Au	74.00 MeV	Annular (O + Pt runs)
TAC(10ns)		MWPC (TOF)

Table 3.9: Elastic scattering reactions used to calibrate the efficiency and solid angle of the detectors when used for measuring fission fragments from capture-fission reactions. Also included is the TAC calibration for the TOF spectrum.

the detectors, using a TAC calibrator generating a pulse every 10ns.

When measuring the O + Pt reactions the annular detector, as described in Section 3.4.2, was used to detect fission fragments close to 180°. In was configured in a similar manner to that used for the ER measurements as shown in Figure 3.1. The average angle of the annular detector was $\theta_{lab} = 174.72°$. A result of using the annular detector and its supporting apparatus was that it shadowed part of the Back MWPC, resulting in the angular acceptance of the Back MWPC being reduced to approximately $-95° \leq \theta_{lab} \lesssim -164°$. The reaction used to calibrate the acceptance of the annular detector is also shown in Table 3.9.

For each run, data from the MWPCs and the annular detector were normalised using elastically scattered beam particles detected in two silicon surface-barrier (SSB) detectors (monitors M_L and M_R). The monitors were positioned at angles of ±22.5° relative to the beam axis, as in the case of the ER measurements. By normalising the data, absolute differential cross-sections were obtained (see Section 3.4.2.1).

Up to thirteen parameters were recorded for each fission fragment measurement; x and y position, energy loss (ΔE), and time-of-flight (TOF) from both of the MWPCs; the energy spectrum from the two monitors (M_L and M_R), TOF and energy from the annular detector (O + Pt reactions only) and a generated pulser signal. To minimise the number of elastic events being recorded in the Front MWPC, only events in the Front MWPC which were coincident with events in the Back MWPC were accepted. All events in the Back MWPC were accepted. All parameters were recorded digitally on computer file for off-line analysis. Like the ER measurements,

scalers were used to determine losses in the analog to digital converters (ADCs) and data acquisition system, in conjunction with the pulser signals in all the fission ADCs.

3.5.2 Identifying Fission Events

From the data parameters recorded, and using the calibration information, a number of derived parameters were obtained. These derived parameters included; Front and Back MWPC positions x and y in mm; scattering angle θ_{lab}; azimuthal angle ϕ_{lab}; and laboratory and centre-of-mass frame velocities v and V respectively. Using the recorded and derived parameters, fission events were cleanly identified, and their angular distribution extracted.

3.5.2.1 Position

Figure 3.13 gives an example of the position and angular information from the Back MWPC when the annular detector was not present. The coverage of the Back MWPC is shown both in terms of experimental x and y channel numbers, frame (a), and angles θ_{lab} and ϕ_{lab}, frame (b). The azimuthal angle of $\phi_{lab} = 90°$ corresponds to the middle of the MWPC, which was perpendicular to the target. Each MWPC gave a similar fan shaped angular acceptance, with the narrower range of ϕ_{lab} occurring at angles closest to $\theta_{lab} = \pm 90°$. The combined solid angle of the two MWPC was about 4.3 steradians, or 34% or 4π.

3.5.2.2 TOF vs ΔE

The MWPCs detected not only fission fragments but also elastically scattered beam particles. As the elastically scattered particles have shorter TOF and lower ΔE, they could usually be distinguished using these two measured data parameters. In Figure 3.14(a), the elastically scattered events and fission fragment events are clearly identifiable.

For some reactions it was insufficient to use only the single detector to identify fission events. This was due to either low fission rates in comparison with elastic scattering (as occurred at low beam energies), or scattering of the beam in the upstream beamline or from other objects within the experimental chamber. This

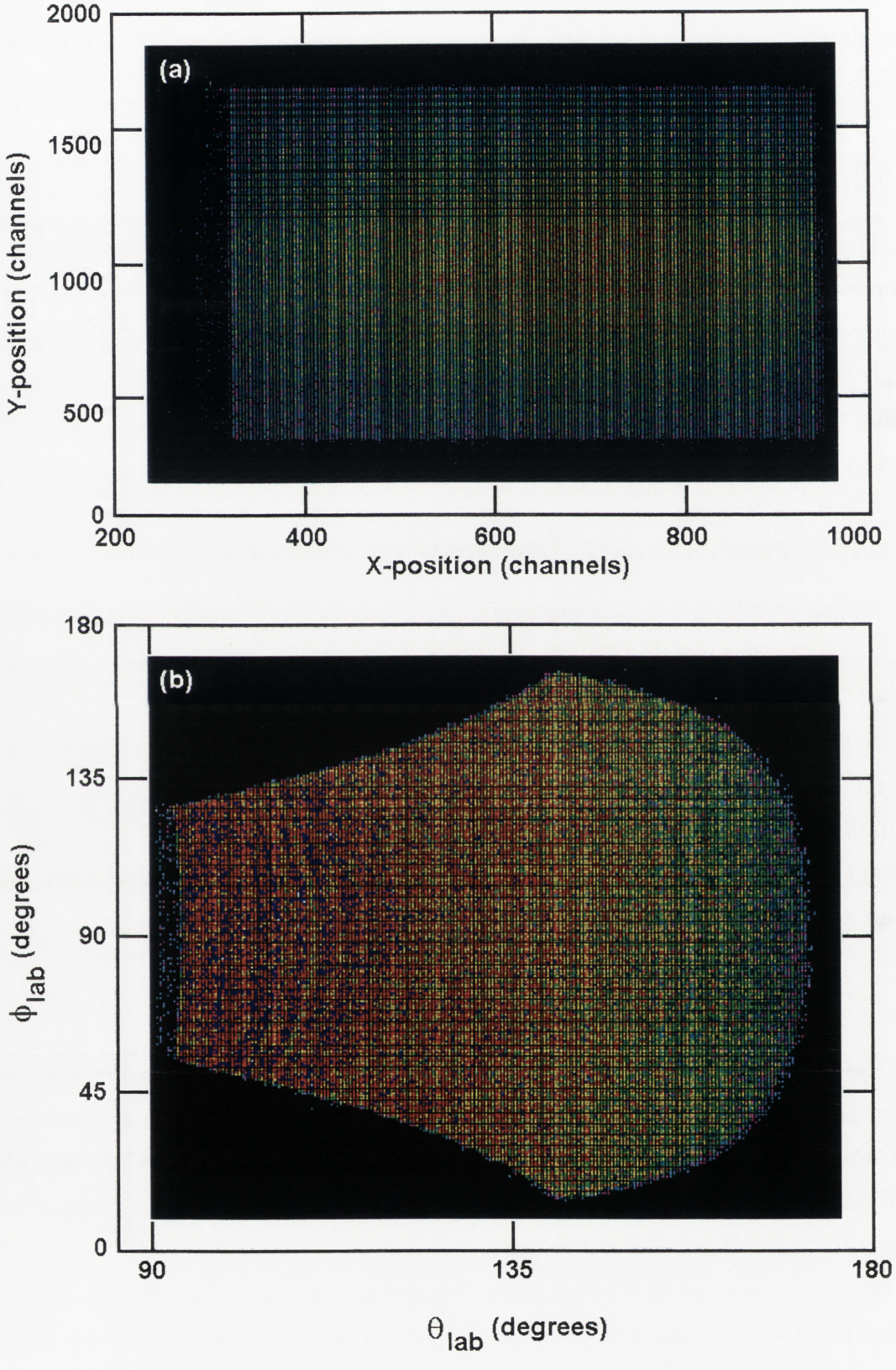

Figure 3.13: Back MWPC position information in (a) channels, and (b) derived angular coordinates θ_{lab} and ϕ_{lab}.

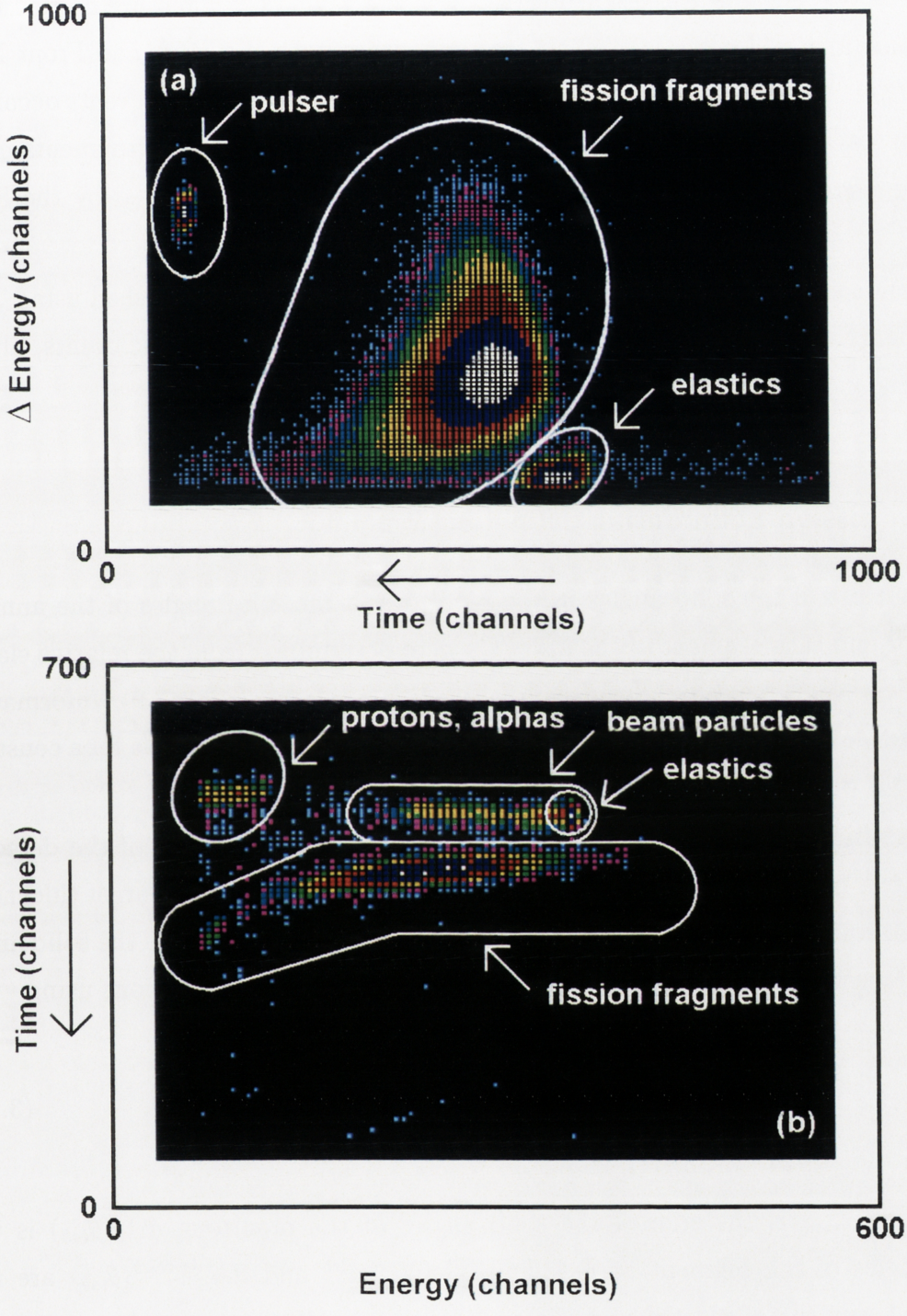

Figure 3.14: (a) TOF vs ΔE from the Back MWPC and (b) energy vs TOF from the annular detector. Elastically scattered events and fission fragment events are shown. The scales are in channel numbers. Note that TOF increases right to left in frame (a) and top to bottom in frame (b).

problem was significant at the lower angles accepted by the Back MWPC, where elastic scattering was greatest. In these cases the TOF vs ΔE picture needed to be supplemented by looking at coincidence data from both the Back and Front MWPCs. Coincidence measurements could not be performed for fission events occurring with angles greater than $\theta_{lab} \gtrsim -155°$, as the corresponding fission fragments in the front detector occurred at $\theta_{lab} \lesssim 5°$ and therefore were not captured by the Front MWPC.

Fission events measured by the annular detector, were distinguished using TOF and energy as shown in figure 3.14(b). As well as fission and elastic events, alpha-particles and protons can also be distinguished.

3.5.3 Fission Differential Cross-Sections

The ratio of the solid angles in the monitors to the solid angles of the annular detector and each segment of the MWPCs were determined from the relative elastic scattering events measured during the calibration reactions (Table 3.9). Information from the MWPCs was segmented by taking $\Delta\theta_{lab} = 5°$ cuts in the data for a constant cut of $\phi_{lab} = 70°$ ($55° \leq \phi_{lab} \leq 125°$).

The ratio of the solid angles of the monitors to the solid angle of the detector segments is independent of the number of incident particles and the target thickness. By using equation 3.9, the ratio of the solid angles of the monitors to the solid angle of the detecting segment was determined from the calibration reactions using:

$$\frac{\sum d\Omega_{mon}}{d\Omega_S(\theta_{lab})} = \frac{\sum dN_{mon}^{el-calib}}{dN_S^{el-calib}(\theta_{lab})} \frac{\frac{d\sigma}{d\Omega_S}^{Ruth-calib}(\theta_{lab})}{\frac{d\sigma}{d\Omega_{mon}}^{Ruth-calib}} \tag{3.16}$$

where $\sum d\Omega_{mon}$ is the sum of the solid angles of the monitors, $d\Omega_S(\theta_{lab})$ is the solid angles of the segment at θ_{lab}, and $\sum dN_{mon}^{el-calib}$ and $dN_S^{el-calib}(\theta_{lab})$ are the corrected number of elastic events counted respectively in the monitors and the segment, during the calibration measurement. The number of events counted were corrected for losses in the ADCs and data acquisition system using the scalers. The Rutherford differential cross-section at the angle θ_{lab} and the monitor angle, for the calibration reaction, are given by $\frac{d\sigma}{d\Omega_S}^{Ruth-calib}(\theta_{lab})$ and $\frac{d\sigma}{d\Omega_{mon}}^{Ruth-calib}$ respectively.

Fission differential cross-sections were obtained using the expression:

$$\frac{d\sigma}{d\Omega_S}^{fis}(\theta_{lab}) = \frac{d\sigma}{d\Omega_{mon}}^{Ruth} \frac{dN_S^{fis}(\theta_{lab})}{\sum dN_{mon}^{el}} \left[\frac{\sum d\Omega_{mon}}{d\Omega_S(\theta_{lab})}\right] \tag{3.17}$$

given the Rutherford differential cross-section at the monitor angle, $\frac{d\sigma}{d\Omega_{mon}}^{Ruth}$, the number of elastics counted by the monitors, $\sum dN_{mon}^{el}$, and the number of fission events counted in the segment $dN_S^{fis}(\theta_{lab})$.

Two typical sets of fission differential cross-sections are shown in Figure 3.15 for the reactions indicated. The angles have been converted from the laboratory

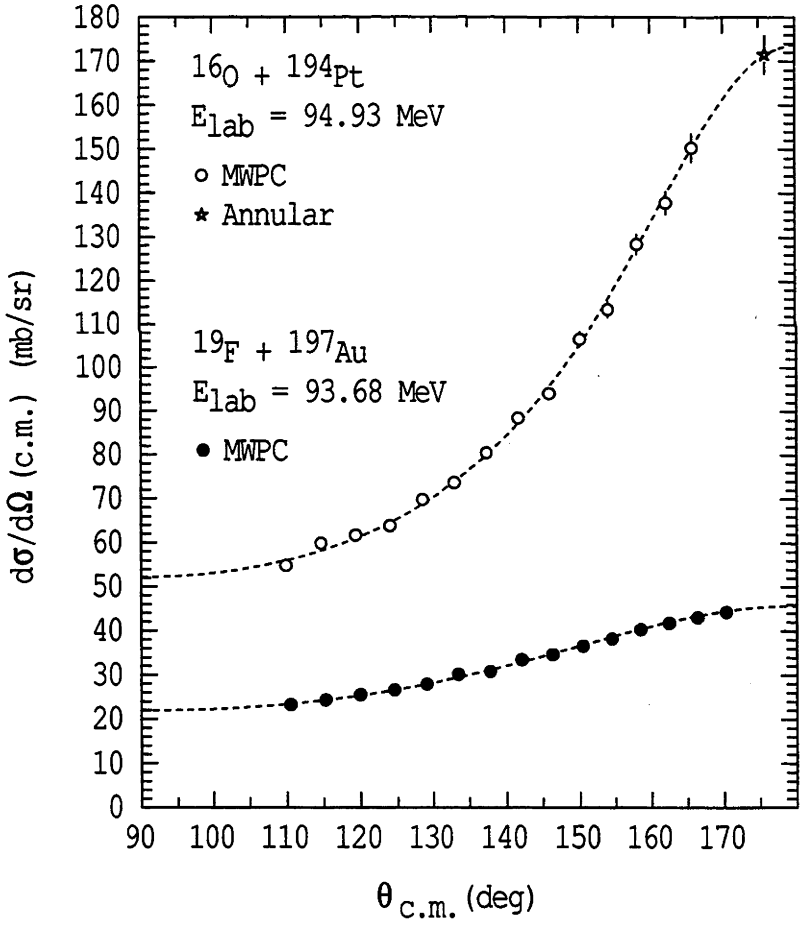

Figure 3.15: Fission differential cross-sections. The top group are from the reaction $^{16}O + ^{194}Pt$ at $E_{lab} = 94.93$ MeV. The bottom group are from the reaction $^{19}F + ^{197}Au$ at $E_{lab} = 93.68$ MeV. Experimental uncertainties are typically smaller than the size of the points.

frame, θ_{lab}, to the centre-of-mass frame, $\theta_{c.m.}$, using total kinetic energy (TKE) systematics from Viola *et al.* [Viol85] (the negative signs on the angles for the back quadrant have been dropped). For the $^{16}O + ^{194}Pt$ system the fourteen points up to $\theta_{c.m.} \approx 165°$ are from segments in the Back MWPC, while the point at $\theta_{c.m.} \approx 176°$ is from the annular Si detector. The bottom group are from the reaction $^{19}F + ^{197}Au$ at $E_{lab} = 93.68$ MeV and contain fifteen points all from the Back MWPC. The lines are fits to the data using a Transition State Model [Back85] calculation extrapolated to $\theta_{c.m.} = 90°$ and $\theta_{c.m.} = 180°$. The fits were done in two stages, first with an average angular momentum, and later with a angular momentum distribution obtained from fits to the capture cross-sections. The latter fits are shown in Figure 3.15. The fitting of capture cross-sections with coupled-channels calculations is covered in Chapter 4.

3.5.4 Total Fission Cross-Sections

The total fission cross-sections were obtained by multiplying the fits to the differential cross-sections by $2\pi \sin\theta_{c.m.}$ and integrating over $90° \leq \theta_{c.m.} \leq 180°$ as there are two fission fragments.

For the reaction $^{16}O + ^{192}Pt$, the low isotopic purity of the ^{192}Pt target (57% ^{192}Pt) necessitated that the fission cross-sections and anisotropies were corrected to exclude the influence of the other isotopes in the target. As cross-sections were also measured for reactions of ^{16}O with most of these other platinum isotopes, $^{194,195,196}Pt$, in this target, the adjusted cross-sections for $^{16}O + ^{192}Pt$, σ^*_{fis}, were calculated using:

$$\sigma^*_{fis}(^{16}O + ^{192}Pt) = \frac{\sigma_{fis}(^{16}O + ^{192}Pt) - \sum \sigma_{fis}(^{16}O + ^{A}Pt) n(^{A}Pt)}{n(^{192}Pt)} \qquad (3.18)$$

Here $\sigma_{fis}(^{16}O + ^{A}Pt)$ are the measured cross-sections for the various ^{A}Pt targets, and $n(^{A}Pt)$ are the isotopic fractions in the ^{192}Pt target. The cross-sections for the reaction $^{16}O + ^{195}Pt$ were estimated from the neighbouring reactions.

The uncertainty in the fission cross-sections was taken as the higher of the statistical error or $\pm 0.5\%$.

3.5.5 Fission Fragment Anisotropies

The fission fragment anisotropies were obtained by taking the ratio of the extrapolated differential cross-section at $\theta_{c.m.} = 180°$ to that at $\theta_{c.m.} = 90°$. In Figure 3.15 the anisotropy, A, for the $^{16}O + ^{194}Pt$ reaction is $A = 3.30 \pm 0.06$, while the anisotropy for the $^{19}F + ^{197}Au$ reaction is $A = 2.08 \pm 0.02$.

3.5.6 Fission Fragment Mass-Distributions

In order to determine fission mass-distributions and mass-ratios a kinematic coincidence method was used [Tōke85, Hind96]. The first step was to determine the velocities of the two fission fragment.

3.5.6.1 Velocity

In the laboratory frame the two fragments have velocity v_i, while in the centre-of-mass frame they have velocity V_i. The velocity of the centre-of-mass frame with respect to the laboratory frame is given by $v_{c.m.}$.

The two fragments are emitted opposite to each other in the centre-of-mass frame. Figure 3.16 shows the fragment velocity vectors and the beam axis as

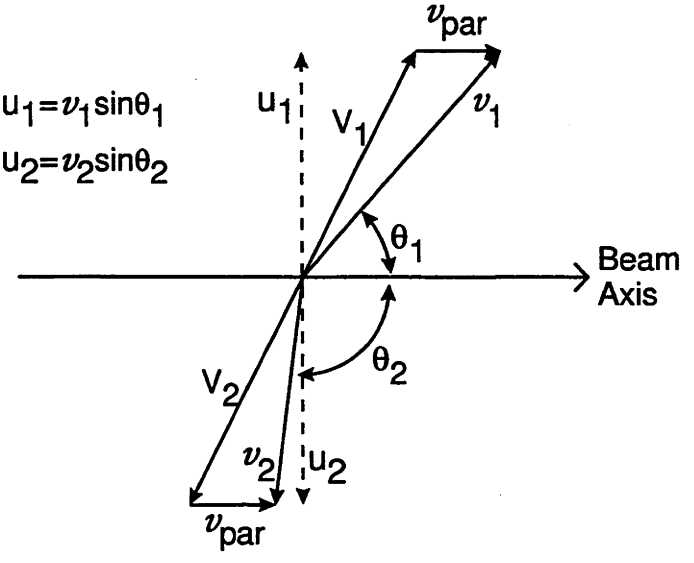

Figure 3.16: Diagram of the relevant fission fragment velocity components in the plane including the fission fragment velocity vectors and the beam axis.

co-planar. The velocity v_{par} represents the component of $v_{c.m.}$ parallel to the beam direction, and can be determined in terms of the parallel, w_i, and perpendicular, u_i, components of v_i, where $w_i = v_i \cos\theta_{lab,i}$ and $u_i = v_i \sin\theta_{lab,i}$, giving;

$$v_{par} = \frac{u_1 w_2 + u_2 w_1}{u_1 + u_2} \tag{3.19}$$

The mass-ratio, M, can in principle be deduced from u_1 and u_2 using the conservation of momentum equation:

$$A_1 u_1 = A_2 u_2 \tag{3.20}$$

leading to

$$M = \frac{u_1}{u_1 + u_2} \tag{3.21}$$

where A_i are the masses of the two fragments. However, in practice, the emission of light particles significantly perturbs the fragment vectors, u_1 and u_2 for values of θ close to the beam axis, which significantly affects the deduced mass-ratio, M.

To avoid this problem the fragment velocities V_i were evaluated defining v_{par} to be equal at the value expected for complete fusion, $v_{c.m.}$. This is a valid assumption for the full momentum transfer (FMT) reactions using in this work. The mass-split was then determined using;

$$M = \frac{V_1}{V_1 + V_2} \tag{3.22}$$

where the fragment velocities were derived from the experimentally detected positions and TOFs of the fission fragments in the MWPCs.

3.5.6.2 Mass

A typical scatter plot for the reaction $^{19}F + ^{197}Au$ at $E_{lab} = 105.75$ Mev is shown in Figure 3.17, where v_{par} is plotted against M for the Back MWPC. The data are symmetric and peaked about $M = 0.5$, as expected for fusion-fission. They also show symmetric distributions about $v_{par} = v_{c.m.}$, consistent with the assumption made in deriving M using equation 3.22. From scatter plots such as Figure 3.17 the mass-distributions for each energy were acquired, for a fixed cut in the deduced fission centre-of-mass angle of $130° \lesssim \theta_{c.m.} \lesssim 165°$.

The mass-distributions for the three reactions leading to the compound nucleus ^{216}Ra are shown in Figure 3.18 for approximately the same excitation energy, $E_x(C.N.) \approx 60$ MeV. The area under the three peaks has been normalised to the

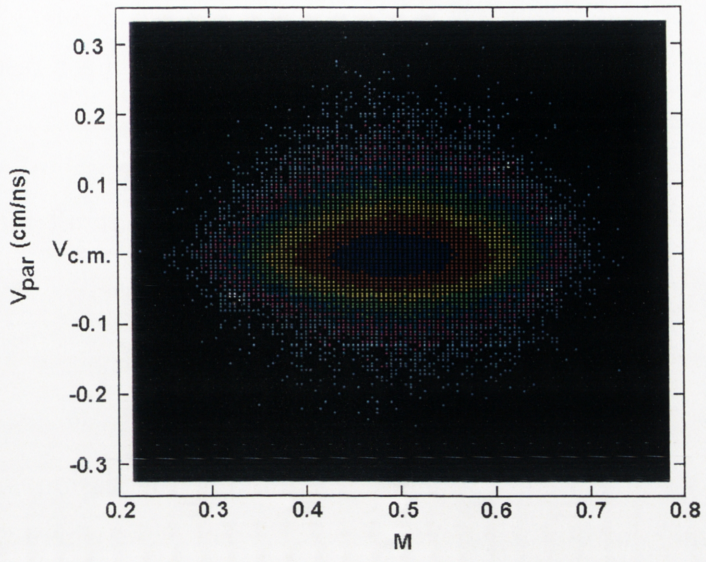

Figure 3.17: Scatter plot of the parallel velocity component of the fissioning nuclei, v_{par}, against the deduced mass-ratio, M.

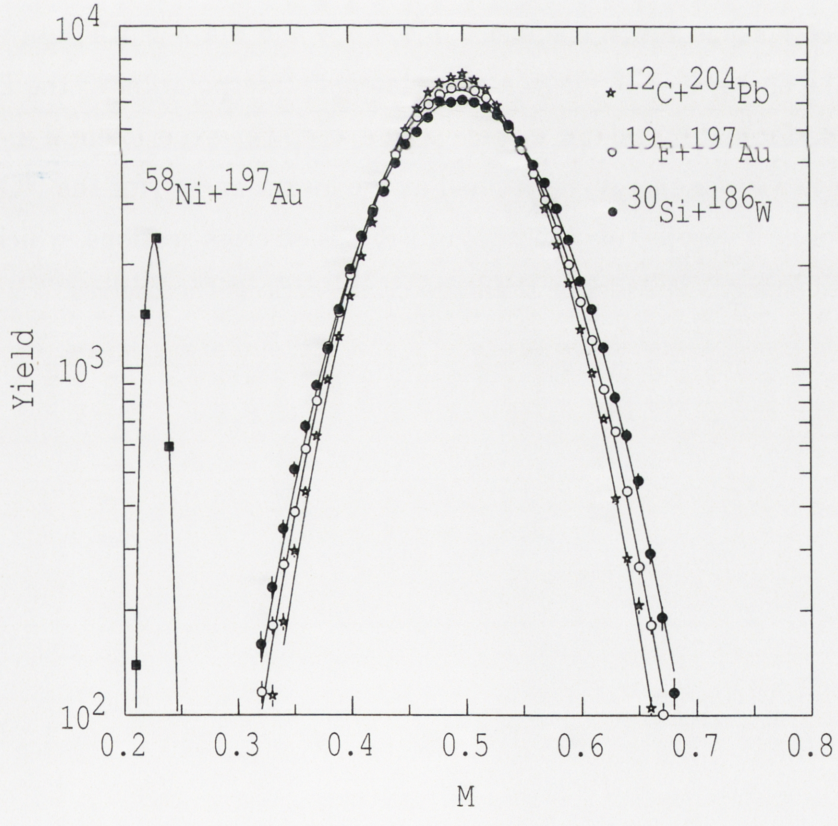

Figure 3.18: Normalised mass-distribution at $E_x(C.N.) \approx 60$ MeV for the three reactions leading to the compound nucleus ^{216}Ra shown in terms of M, the ratio of the fragment mass in the Back MWPC to the summed masses of the two fragments. The mass-distribution for the elastic scattering of ^{58}Ni from ^{197}Au is shown on the left.

same value. The mass-distribution for the elastic scattering of ^{58}Ni from ^{197}Au is shown on the left of the figure to demonstrate the good mass resolution of the measuring technique, even for a less favourable case than fission.

The mass-width, σ_M^2 (the normalised variance of the Gaussian) was extracted from the mass-distributions for the three ^{216}Ra reactions at all measured beam energies.

3.6 Capture Cross-Sections

Capture cross-sections were obtained by summing the fission and ER cross-sections for the same centre-of-mass energies, $E_{c.m.}$. For cases where the fission and ER cross-sections were not measured at the same $E_{c.m.}$ ($\Delta E_{c.m.} \lesssim 0.05$ MeV), the ER cross-sections were extrapolated or interpolated to correspond the the energies for the fission cross-sections. The ER cross-sections were scaled rather than the fission cross-sections, as fission fragment anisotropy and mass-width data were only available at the energies of the fission experiments. Interpolation of the ER cross-sections was performed by taking a cubic spline fit to the experimental data, while extrapolation to a lower energy, performed at the lowest energy for the ^{12}C + ^{204}Pb reaction, was done by projecting the ratio of ER/fission cross-sections, which showed a much weaker energy dependence than the cross-sections themselves.

CHAPTER 4

Results and Analysis

This chapter presents the results of the experimental measurements undertaken in this work, together with analysis of the results, and comparison with model calculations. The O + Pt reactions are presented first, followed by the three reactions ^{12}C + ^{204}Pb, ^{19}F + ^{197}Au and ^{30}Si + ^{186}W which, following fusion, all form the compound nucleus ^{216}Ra.

The evaporation residue (ER) and fission data are discussed separately, before obtaining the capture excitation functions. The capture excitation functions for each reaction are fitted using coupled-channels calculations, from which angular momentum distributions are obtained. The angular momentum distributions are then used in statistical model (SM)/Transitions State Model (TSM) calculation in an attempt to simultaneously reproduce the fission and ER measurements.

4.1 O + Pt Reactions

Shrivastava *et al.* [Shri99] reported that model calculations using shell corrected level densities were able to reproduce anisotropies for the reaction ^{12}C + ^{194}Pt which leads to the compound nucleus ^{206}Po (with $N = 122$), but that the model underestimated the measured anisotropies for the reaction ^{12}C + ^{198}Pt leading to the closed shell compound nucleus ^{210}Po (with $N = 126$). The underestimation of the latter anisotropies decreased with increasing excitation energy. Shrivastava *et al.* suggested that a substantial and localised effect of the $N = 126$ closed shell was responsible for the observed larger anisotropies from the decay of the ^{210}Po compound nucleus.

In this work the effect of the $N = 126$ closed shell on fission probabilities

and anisotropies was investigated through a systematic study of six reactions, ^{16}O + $^{192,194,196,198}Pt$ and ^{18}O + $^{196,198}Pt$, which lead to the compound nuclei, $^{208,210,212,214,216}Rn$. These compound nuclei span the $N = 126$ neutron closed shell.

The initial excitation energy of a compound nucleus formed in a heavy-ion reaction is expected to be sufficiently high as to substantially wash out shell and pairing effects. Only once some energy is lost by the emission of particles, will the decaying nucleus be in the energy realm where these effects are expected to be significant. By using a systematic study of the O + Pt reactions, forming compound nuclei which span both above and below the closed shell, any localised shell effects should be apparent.

In this work evaporation residue cross-sections have been extracted for the reactions ^{16}O + ^{194}Pt and ^{18}O + ^{198}Pt from their measured α-decay, and fission fragments measurement were made for all reactions, allowing determination of fission cross-sections and fission fragment anisotropies.

The capture cross-sections for the two reactions ^{16}O + ^{194}Pt and ^{18}O + ^{198}Pt were derived from the experimental fission and ER cross-sections. These were fitted with coupled-channels calculations using the same bare potential. This bare potential was subsequently used in calculating the capture cross-sections for the other four reactions, where only fission cross-sections were measured. Derived angular momentum distributions from the coupled-channels calculations were used in model calculations.

Statistical model calculations of compound nucleus decay and Transition State Model calculation of fission, were compared to the experimental data to investigate the effect of the $N = 126$ closed shell on the fission fragment anisotropies and fission probabilities for the six reactions.

4.1.1 Cross-Sections

4.1.1.1 Evaporation Residue Cross-Sections

For the reaction ^{16}O + ^{194}Pt, the cross-sections for individual evaporation channel, and total ER cross-sections (sum of the individual cross-sections) are listed in Table 4.1. As discussed in the previous chapter, cross-sections for ERs formed by just the emission of neutrons (xn) have been extracted for all neutron multiplicities,

E_{lab} (MeV)	$E_{c.m.}$ (MeV)	σ_{3n} (mb)	σ_{4n} (mb)	σ_{5n} (mb)	σ_{ER} (mb)
73.96	68.32	1.40 ± 0.22	0.16 ± 0.04		1.56 ± 0.22
75.00	69.29	4.42 ± 0.32	0.92 ± 0.12		5.34 ± 0.34
75.96	70.17	10.7 ± 0.8	3.18 ± 0.72		13.9 ± 1.1
76.96	71.10	21.3 ± 2.4	9.2 ± 1.7		30.5 ± 2.9
78.98	72.96	27.8 ± 2.2	39.9 ± 1.9		67.7 ± 2.8
81.96	75.72	28.6 ± 1.6	92.5 ± 1.7	0.27 ± 0.31	121 ± 2
84.96	78.49	14.4 ± 1.4	136 ± 2	8.02 ± 0.95	159 ± 2
94.96	87.72	1.0 ± 1.1	62.4 ± 1.5	72.5 ± 7.5	
		$\sigma_{\alpha 4n}$ (mb)	σ_{p4n} (mb)		
94.96	87.72	16.4 ± 3.8	39.8 ± 8.1		192 ± 12

Table 4.1: ER cross-sections for the reaction $^{16}O + ^{194}Pt$.

x. However, cross-sections for charged particle emission ER channels (pxn and αxn) could not be completely determined as several of the channels have very low ($< 1\%$) α-decay branching ratios.

The total ER cross-sections, obtained by summing the xn yields, except at $E_{lab} = 94.96$ MeV where $p4n$ and $\alpha 4n$ yields have also been included, are shown in Figure 4.1 by the open circles, together with the individual ER channel cross-sections. Also shown are unpublished total ER cross-sections for the same reaction by Scarlassara *et al.* [Scar95] (small solid diamonds), which were measured by direct detection of the ERs using an E-TOF telescope after rejection of beam particles by an electrostatic deflector. The beam used in this experiment was monitored using four surface-barrier silicon detectors. Because of the technique used, the Scarlassara data would not have suffered from the problem of ERs having low α-branching ratios. However, these data did suffer from some minor problems [Scar99], such as poor transmission of the electrostatic deflector, large cross-section uncertainties, low efficiency of the Si detectors, and beam energies being shifted to lower values. Despite these problems the experiment was assessed as giving reasonable results [Scar99]. The Scarlassara data and the data from this work are not in agreement. However, by energy shifting the Scarlassara cross-sections by a constant $\Delta E_{lab} = 1.1$

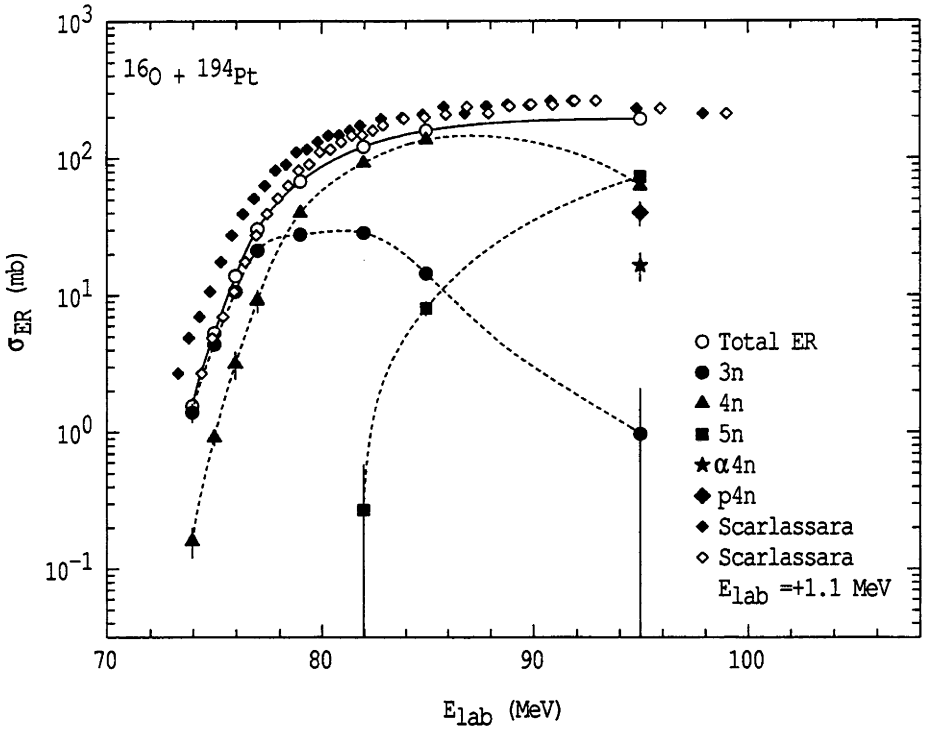

Figure 4.1: Evaporation residue cross-sections for the reaction $^{16}O + ^{194}Pt$ as a function of laboratory energy. The small solid diamonds are total ER cross-sections from Scarlassara *et al.* [Scar95]. Energy shifted (E_{lab} = +1.1 MeV) Scarlassara data is shown by the open diamonds. The lines guide the eye. For most points the uncertainties are less than the size of the points.

MeV (open diamonds in Figure 4.1), good agreement can be achieved at lower energies with the ER cross-sections from this work. At higher energies, the divergence in cross-sections is likely to be due to the inability to determine some charged particle ER channels using the α-decay method used in the present work. For this reason the energy shifted Scarlassara cross-sections are expected to be more accurate at energies above $E_{lab} \gtrsim 78.0$ MeV. They are used later in the $^{16}O + ^{194}Pt$ analysis, although due to the problems associated with the data, the uncertainties are increased to $\pm 10\%$.

For the reaction $^{18}O + ^{198}Pt$, the individual ER channel cross-sections are listed in Table 4.2 and shown in Figure 4.2. Although the α-branching ratios for the charged particle emission ER are large, no α-decay from pxn and αxn ERs was detected, consistent with SM calculations for decay of the neutron-rich ^{216}Rn.

E_{lab} (MeV)	$E_{c.m.}$ (MeV)	σ_{4n} (mb)	σ_{5n} (mb)	σ_{6n} (mb)	σ_{ER} (mb)
71.96	65.96	0.23 ± 0.06			0.23 ± 0.06
73.96	67.80	4.57 ± 0.28	0.71 ± 0.51		5.28 ± 0.58
75.96	69.63	21.3 ± 1.3	7.98 ± 0.57	0.15 ± 0.14	29.4 ± 1.4
77.96	71.46	38.3 ± 2.2	37.5 ± 2.5	0.63 ± 0.18	76.4 ± 3.3
80.00	73.33	46.3 ± 2.8	85.3 ± 5.7	1.66 ± 0.55	133 ± 6
84.96	77.88	33.7 ± 1.8	237 ± 14	17.3 ± 1.1	288 ± 14
89.96	82.46	17.1 ± 1.0	307 ± 18	144 ± 8	468 ± 20
94.96	87.05	5.43 ± 0.41	205 ± 14	321 ± 17	532 ± 22

Table 4.2: ER cross-sections for the reaction $^{18}O + ^{198}Pt$.

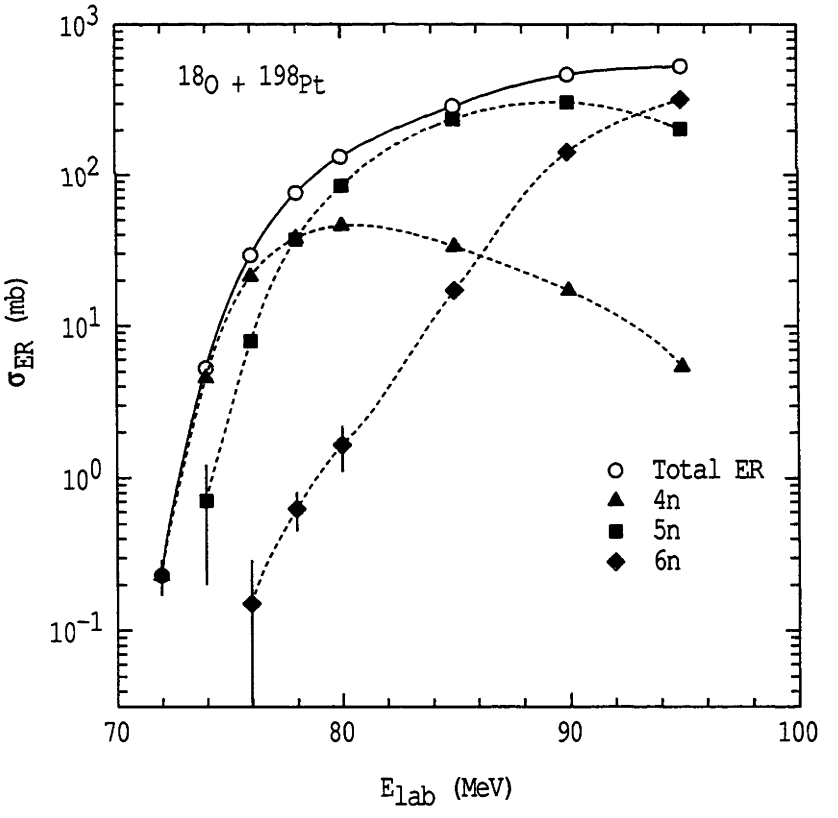

Figure 4.2: Evaporation residue cross-sections for the reaction $^{18}O + ^{198}Pt$ as a function of laboratory energy. The lines guide the eye. For most points the uncertainties are less than the size of the points.

Although the ER cross-sections for both reactions increase with increasing energy, the rate of increase is sharply reduced above a limiting energy. This is consistent with the higher angular momenta leading to fission, and there being a limiting angular momentum beyond which no ERs are produced.

4.1.1.2 Fission Cross-Sections

Fission fragment measurements were made for the six reactions ^{16}O + $^{192,194,196,198}Pt$ and ^{18}O + $^{196,198}Pt$. As detailed in the previous chapter, the fission fragment angular distribution data were fitted with Transition State Model (TSM) calculations, in order to extract the fission cross-sections. This was done in two stages, first with a single average angular momentum, and secondly with a distribution of angular momenta obtained by fitting the capture cross-sections with coupled-channels calculations (as described in Section 4.1.2). The fission cross-sections from the second of these fits are shown as a function of centre-of-mass energy in Figure 4.3, and listed in Table 4.3. The use of an angular momentum distribution only made a small change in the cross-sections obtained.

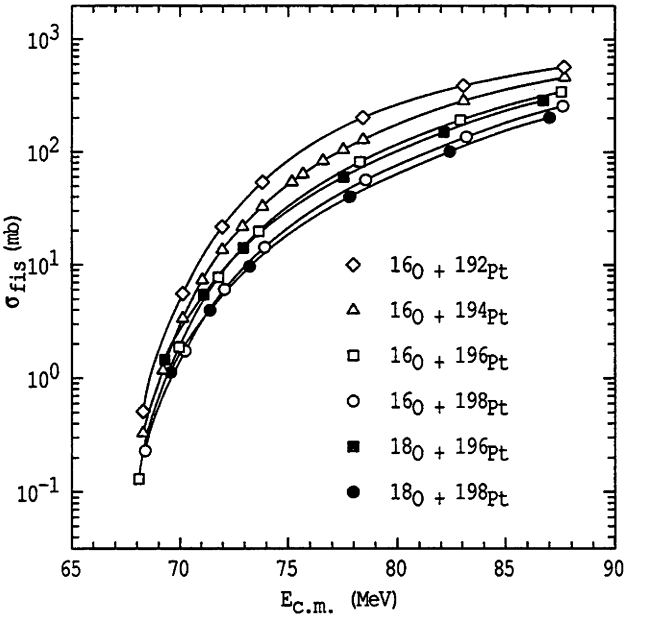

Figure 4.3: Fission cross-sections as a function of centre-of-mass energy for the reactions ^{16}O + $^{192,194,196,198}Pt$ and ^{18}O + $^{196,198}Pt$. The uncertainties are less than the size of the points. The lines guide the eye.

$^{16}O + {}^{192}Pt$

E_{lab} (MeV)	$E_{c.m.}$ (MeV)	σ_{fis} (mb)
73.98	68.29	0.51 ± 0.01
75.99	70.14	5.56 ± 0.07
77.98	71.98	21.65 ± 0.11
79.98	73.83	53.82 ± 0.27
84.98	78.44	201.9 ± 1.0
89.98	83.06	388.3 ± 1.9
94.98	87.67	570.8 ± 2.9

$^{16}O + {}^{198}Pt$

E_{lab} (MeV)	$E_{c.m.}$ (MeV)	σ_{fis} (mb)
73.92	68.39	0.23 ± 0.01
75.93	70.25	1.74 ± 0.01
77.92	72.09	6.08 ± 0.03
79.91	73.94	14.29 ± 0.07
84.92	78.57	56.49 ± 0.28
89.92	83.20	136.3 ± 0.7
94.70	87.62	256.7 ± 1.3

$^{16}O + {}^{194}Pt$

E_{lab} (MeV)	$E_{c.m.}$ (MeV)	σ_{fis} (mb)
73.92	68.29	0.33 ± 0.01
74.92	69.21	1.18 ± 0.02
75.92	70.14	3.37 ± 0.02
76.92	71.06	7.36 ± 0.05
77.92	71.98	13.61 ± 0.07
78.92	72.91	21.78 ± 0.11
79.92	73.83	32.82 ± 0.16
81.38	75.18	54.19 ± 0.27
81.92	75.68	63.45 ± 0.32
82.92	76.60	83.48 ± 0.42
83.94	77.54	105.1 ± 0.5
84.92	78.45	128.6 ± 0.6
89.92	83.07	285.3 ± 1.4
94.93	87.70	461.3 ± 2.3

$^{18}O + {}^{196}Pt$

E_{lab} (MeV)	$E_{c.m.}$ (MeV)	σ_{fis} (mb)
75.65	69.29	1.46 ± 0.01
77.66	71.13	5.44 ± 0.04
79.66	72.96	14.11 ± 0.09
84.67	77.55	60.19 ± 0.30
89.68	82.14	150.5 ± 0.7
94.70	86.73	288.0 ± 1.4

$^{16}O + {}^{196}Pt$

E_{lab} (MeV)	$E_{c.m.}$ (MeV)	σ_{fis} (mb)
73.66	68.10	0.13 ± 0.01
75.68	69.97	1.88 ± 0.01
77.67	71.81	7.77 ± 0.04
79.68	73.67	19.83 ± 0.10
84.69	78.30	81.56 ± 0.41
89.69	82.92	192.4 ± 1.0
94.70	87.55	343.3 ± 1.7

$^{18}O + {}^{198}Pt$

E_{lab} (MeV)	$E_{c.m.}$ (MeV)	σ_{fis} (mb)
75.91	69.58	1.13 ± 0.01
77.91	71.42	3.98 ± 0.03
79.91	73.25	9.66 ± 0.05
84.92	77.84	40.15 ± 0.20
89.92	82.43	101.0 ± 0.5
94.92	87.01	202.8 ± 1.0

Table 4.3: Fission cross-sections for the reactions $^{16}O + {}^{192,194,196,198}Pt$ and $^{18}O + {}^{196,198}Pt$.

4.1.1.3 Capture Excitation Functions

The capture cross-sections for the reaction $^{18}O + ^{198}Pt$ (Table 4.4) were obtained by adding the experimental fission cross-sections and interpolated ER cross-sections from this work. At the lowest energies the fission cross-sections were less than 3% of the capture yield and were not measured; here the capture cross-sections have been taken as approximately equal to the ER cross-sections.

$E_{c.m.}$ (MeV)	σ_{fis} (mb)	σ_{ER} (mb)	σ_{ER} interpolated (mb)	σ (mb)
65.96		0.23 ± 0.06		$\approx 0.23 \pm 0.06$
67.80		5.28 ± 0.58		$\approx 5.28 \pm 0.58$
69.58	1.13 ± 0.01		28.5 ± 1.5	29.6 ± 1.5
69.63		29.4 ± 1.4		
71.42	3.98 ± 0.03		75.1 ± 3.5	79.0 ± 3.5
71.46		76.4 ± 3.3		
73.25	9.66 ± 0.05		131 ± 7	140 ± 7
73.33		133 ± 6		
77.84	40.15 ± 0.20		287 ± 14	327 ± 15
77.88		288 ± 14		
82.43	101.0 ± 0.5		467 ± 20	568 ± 20
82.46		468 ± 20		
87.01	202.8 ± 1.0		531 ± 22	734 ± 22
87.05		532 ± 22		

Table 4.4: Capture cross-sections for the reaction $^{18}O + ^{198}Pt$.

The capture cross-sections for the reaction $^{16}O + ^{194}Pt$ were calculated by adding the experimental fission cross-sections to interpolated ER cross-sections, where the ER cross-sections were taken from the experimental results in this work for $E_{lab} < 78$ MeV and from the energy shifted Scarlassara *et al.* [Scar95] data for $E_{lab} \gtrsim 78$ MeV. The fission, ER and resulting capture cross-sections, σ, are listed in Table 4.5, where the energy shifted Scarlassara cross-sections are denoted (S). As mentioned before the uncertainties on the interpolated Scarlassara data were set to $\pm 10\%$.

$E_{c.m.}$ (MeV)	σ_{fis} (mb)	σ_{ER} (mb)	σ_{ER} interpolated (mb)	σ (mb)
68.29	0.33 ± 0.01		1.48 ± 0.30	1.81 ± 0.30
68.32		1.56 ± 0.22		
69.21	1.18 ± 0.02		4.90 ± 0.50	6.08 ± 0.50
69.29		5.34 ± 0.34		
70.14	3.37 ± 0.02		13.5 ± 1.4	16.9 ± 1.4
70.17		13.9 ± 1.1		
71.06	7.36 ± 0.05		29.8 ± 3.0	37.2 ± 3.0
71.10		30.5 ± 2.9		
71.98	13.61 ± 0.07		48.1 ± 4.9	61.7 ± 4.9
72.96		67.7 ± 2.8		
72.89		81.5 ± 1.5 (S)		
72.91	21.78 ± 0.11		81.7 ± 8.2 (S)	104 ± 8
73.81		110.8 ± 2.1 (S)		
73.83	32.82 ± 0.16		111 ± 11 (S)	144 ± 11
75.18	54.19 ± 0.27		146 ± 15 (S)	200 ± 15
75.20		146.3 ± 2.0 (S)		
75.68	63.45 ± 0.32		147 ± 15 (S)	211 ± 15
75.66		147.2 ± 2.1 (S)		
76.58		173.3 ± 2.2 (S)		
76.60	83.48 ± 0.42		174 ± 17 (S)	257 ± 17
77.51		193.5 ± 2.3 (S)		
77.54	105.1 ± 0.5		194 ± 19 (S)	299 ± 19
78.43		197.9 ± 5.1 (S)		
78.45	128.6 ± 0.6		198 ± 20 (S)	327 ± 20
83.05		246.2 ± 3.9 (S)		
83.07	285.3 ± 1.4		246 ± 25 (S)	532 ± 25
87.70	461.3 ± 2.3		239 ± 24 (S)	700 ± 24
88.59		228.3 ± 2.6 (S)		

Table 4.5: Capture cross-sections for the reaction $^{16}O + ^{194}Pt$. The interpolated ER cross-sections were taken from the experimental results in this work for $E_{lab} < 78$ MeV and from the energy shifted Scarlassara *et al.* [Scar95] data for $E_{lab} \gtrsim 78$ MeV (denoted (S)).

4.1.2 Coupled-Channels Calculations

To model the six O + Pt reactions with the statistical model, capture angular momentum distributions for each reaction at each energy were required. The angular momentum distributions for the two reactions $^{16}O + ^{194}Pt$ and $^{18}O + ^{198}Pt$ were obtained by fitting the experimental capture cross-sections with coupled-channels calculations. In order to provide a basis from which to calculate the capture cross-sections for the other four reactions, a common bare potential was used in the calculations.

The first step in the fitting process, was to fit the capture cross-sections above the Coulomb barrier for the two reactions $^{16}O + ^{194}Pt$ and $^{18}O + ^{198}Pt$ with one-dimensional barrier penetration model calculations. This fit was based on a bare potential which utilised a Woods-Saxon form of the nuclear potential (equation 2.2). The potential depth, V_0, the surface diffuseness parameter, a_0, and the nucleus radius parameter, r_N, were varied to give the best fit to the above-barrier capture excitation functions (the lowest average χ^2) for the two reactions. The resulting values were $V_0 = 66.0$ MeV, $a_0 = 0.925$ fm, and $r_N = 1.131$ fm. One-dimensional barrier penetration model calculations made with just the bare potential underpredicted the experimental capture cross-sections at lower energies for these reactions, as shown by the dashed lines in Figure 4.4. Better agreement was achieved by including the deformation of the Pt targets and couplings to transfer channels, as shown by the solid lines in the Figure 4.4. At higher energies, $E_{c.m.} \gtrsim 75$ MeV the additional coupled-channels do not significantly affect the calculated capture cross-sections.

The couplings expected and included for each reaction are listed in Table 4.6. The target has been treated as statically deformed with quadrupole, β_2, and hexadecapole, β_4 deformations [Rama87, NDS]. The strengths, β_3, and energies, E_{β_3}, of octupole vibrational couplings in the targets [Cott88, Spea89], and transfer reaction with Q-values, Q_t, and coupling strengths, S_t, were included in the coupling matrix. The transfer channels denoted p, 2p, n and 2n, refer to the transfer of one or two protons or neutrons from the projectile to the target.

While the channels used in the calculations represent reasonable physical conditions, the inclusion of any or all of these channels are not meant to suggest that these are indeed the physical dynamics at work during the capture process. These

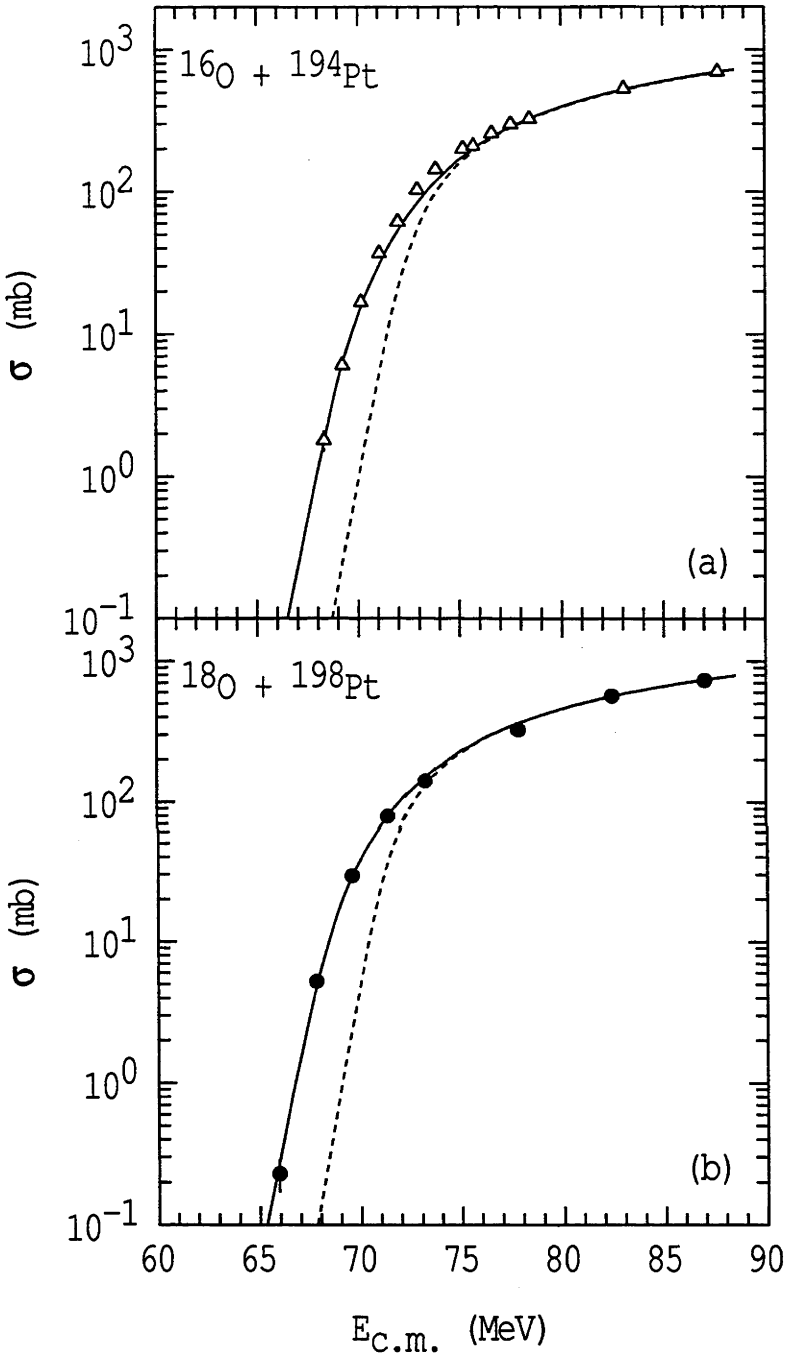

Figure 4.4: Experimental (points) and calculated (lines) capture cross-sections, for the reactions (a) $^{16}O + ^{194}Pt$, where the experimental data is taken from Table 4.5, and (b) $^{18}O + ^{198}Pt$. The solid lines are the coupled-channels calculations using the parameters in Table 4.6, while the dashed lines are calculated using just the bare potential. Experimental uncertainties are typically smaller than the size of the points.

Reaction	Static Deformation		Octupole couplings		Transfer		
	β_2	β_4	β_3	E_{β_3} (MeV)	Q_t (MeV)	S_t (MeV)	Channel
$^{16}O + ^{192}Pt$	-0.1549	-0.047	0.102	1.378	0.801	1.4	p
$^{16}O + ^{194}Pt$	-0.1434	-0.045	0.086	1.432	1.50	1.2	p
			0.030	2.154			
			0.017	2.246			
			0.068	2.543			
$^{16}O + ^{196}Pt$	-0.1308	-0.042	0.073	1.447	2.18	1.2	p
			0.061	2.431			
			0.042	2.608			
			0.061	2.638			
			0.052	2.707			
$^{16}O + ^{198}Pt$	-0.113	-0.039	0.073	1.681	2.854	1.2	p
			0.054	2.441			
			0.029	2.513			
			0.073	2.604			
			0.054	2.796			
			0.059	2.826			
$^{18}O + ^{196}Pt$	-0.1308	-0.042	0.073	1.447	0.914	1.4	2p
			0.061	2.431	1.214	0.6	2n
			0.042	2.608			
			0.061	2.638			
			0.052	2.707			
$^{18}O + ^{198}Pt$	-0.113	-0.039	0.073	1.681	0.65	1.4	2n
			0.054	2.441	2.165	0.6	2p
			0.029	2.513			
			0.073	2.604			
			0.054	2.796			
			0.059	2.826			

Table 4.6: Parameters used in coupled-channels calculations for the O + Pt reactions. Shown are quadrupole, β_2, and hexadecapole, β_4, deformations of the targets; strengths, β_3, and energies, E_{β_3}, of octupole states in the targets; and transfer reaction Q-values, Q_t, coupling strengths, S_t, and number of protons or neutrons transferred from the projectile to the target.

channels are included in order to reproduce the measured capture cross-sections, and to obtain angular momentum distributions. A different set of channels that gives an equally good reproduction of the capture excitation functions, would give similar angular momentum distributions [Dasg98].

To predict the capture excitation functions and angular momentum distributions for the other four reactions, the methodology used in fitting the $^{16}O + ^{194}Pt$ and $^{18}O + ^{198}Pt$ reactions was followed. The same bare potential was used, and the couplings for the other reactions included β_2, β_4, β_3 and transfer components. The β_2, β_4, and β_3 values were reasonably constrained by existing published values [Rama87, NDS, Cott88, Spea89]. However, the inclusion of the particular transfer channels, and particularly their coupling strengths, was based on similar transfer reactions being needed to fit the experimental data for the $^{16}O + ^{194}Pt$ and $^{18}O + ^{198}Pt$ reactions. While this may cause some uncertainty at lower energies, their effect at energies above the average barrier ($E_{c.m.} \gtrsim 75$ MeV) will be very small.

4.1.3 Fission Probabilities

The fission probability, the ratio of the fission to capture cross-sections, is one experimental result which can be easily compared to model calculations, and which provides a sensitive measure of compound nucleus decay. The fission probabilities for the O + Pt reactions are given in Figure 4.5. The uncertainties in the fission probabilities are small for the two reactions where the capture cross-sections are known from experimental data. However, for the other four reactions much larger uncertainties have been assigned ($\pm 100\%$ below the barrier and $\pm 50\%$ in the barrier region) due to the dependence of the capture cross-sections on the couplings used in the coupled-channels calculations. Above the average barrier, where the outcome is less dependent on the couplings than on the bare potential, the uncertainties in the fission probabilities were set at $\pm 10\%$. The lowest energy fission probabilities for the reactions $^{16}O + ^{192}Pt$, $^{16}O + ^{196}Pt$, $^{16}O + ^{198}Pt$ and $^{18}O + ^{196}Pt$ are not shown in Figure 4.5 due to their large uncertainties.

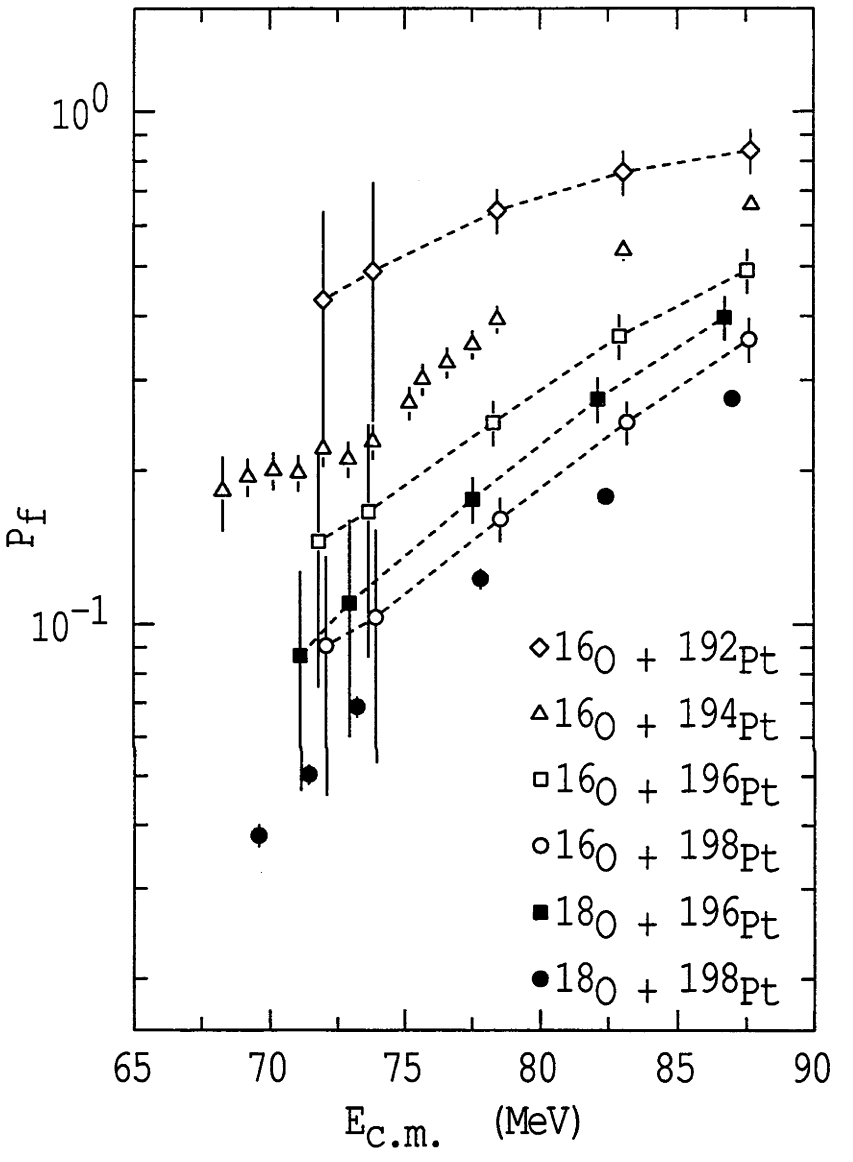

Figure 4.5: Fission probabilities for the six O + Pt reactions as a function of centre-of-mass energy. The open triangles are the experimental fission probabilities for the reaction $^{16}O + ^{194}Pt$, where the experimental data are taken from Table 4.5. The solid circles are the experimental fission probabilities for the reaction $^{18}O + ^{198}Pt$. The other points are fission probabilities calculated from coupled-channels capture cross-sections and experimental fission cross-sections. The dashed lines guide the eye.

4.1.4 Fission Fragment Anisotropies

The fission fragment anisotropies comprise the second measure of compound nucleus decay which is compared to model calculations (Section 4.1.5). The experimental anisotropies were obtained by fitting the fission fragment angular distributions with a Transition State Model calculation allowing K_0 to vary freely, and using the angular momentum distributions from the coupled-channels calculations. The anisotropies are shown in Figure 4.6 for the six O + Pt reactions as a function of centre-of-mass energy, and are listed in Table 4.7.

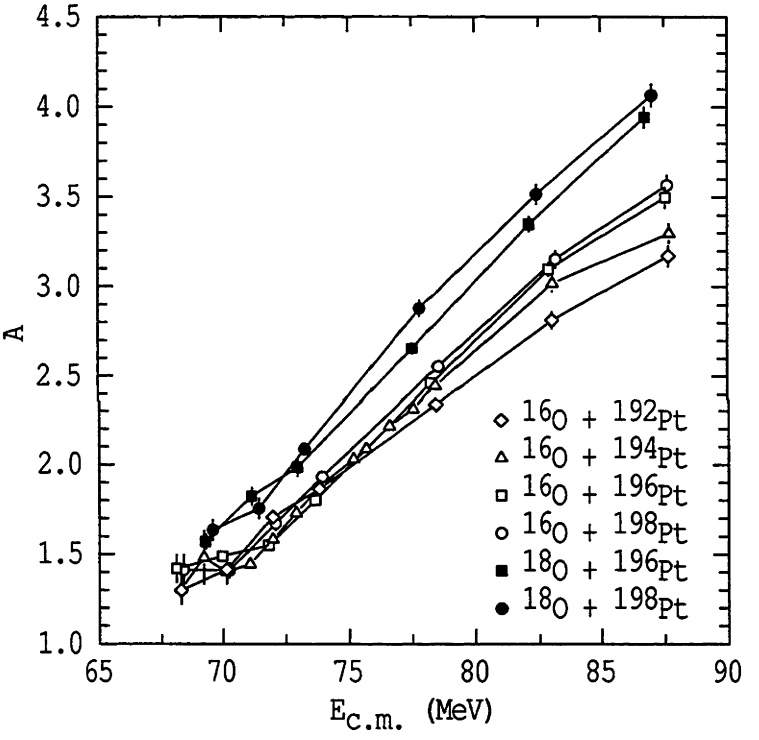

Figure 4.6: Fission fragment anisotropies for the six O + Pt reactions as a function of centre-of-mass energy. The lines guide to eye.

As was the case for determining the fission cross-sections, the use of an angular momentum distribution in TSM calculated fits to the differential fission cross-sections only resulted in a small change in anisotropies when compared to calculations using a single average angular momentum. Therefore, the larger uncertainties in the calculated coupled-channels capture cross-sections at lower energies, did not have a significant effect on the anisotropies.

$^{16}O + ^{192}Pt$

$E_{c.m.}$ (MeV)	A
68.29	1.30 ± 0.08
70.14	1.41 ± 0.08
71.98	1.71 ± 0.03
73.83	1.86 ± 0.03
78.44	2.34 ± 0.04
83.06	2.81 ± 0.05
87.67	3.17 ± 0.06

$^{16}O + ^{198}Pt$

$E_{c.m.}$ (MeV)	A
68.39	1.41 ± 0.09
70.25	1.41 ± 0.05
72.09	1.67 ± 0.04
73.94	1.93 ± 0.03
78.57	2.55 ± 0.04
83.20	3.16 ± 0.05
87.62	3.57 ± 0.06

$^{16}O + ^{194}Pt$

$E_{c.m.}$ (MeV)	A
68.29	1.30 ± 0.08
69.21	1.48 ± 0.15
70.14	1.40 ± 0.04
71.06	1.44 ± 0.04
71.98	1.58 ± 0.03
72.91	1.73 ± 0.03
73.83	1.88 ± 0.03
75.18	1.03 ± 0.03
75.68	2.09 ± 0.03
76.60	2.22 ± 0.03
77.54	2.31 ± 0.03
78.45	2.45 ± 0.04
83.07	3.02 ± 0.05
87.70	3.30 ± 0.06

$^{18}O + ^{196}Pt$

$E_{c.m.}$ (MeV)	A
69.29	1.57 ± 0.04
71.13	1.82 ± 0.05
72.96	1.99 ± 0.05
77.55	2.65 ± 0.03
82.14	3.35 ± 0.05
86.73	3.94 ± 0.06

$^{16}O + ^{196}Pt$

$E_{c.m.}$ (MeV)	A
68.10	1.42 ± 0.08
69.97	1.49 ± 0.04
71.81	1.55 ± 0.03
73.67	1.80 ± 0.02
78.30	2.46 ± 0.03
82.92	3.10 ± 0.04
87.55	3.50 ± 0.06

$^{18}O + ^{198}Pt$

$E_{c.m.}$ (MeV)	A
69.58	1.63 ± 0.06
71.42	1.76 ± 0.06
73.25	2.09 ± 0.04
77.84	2.88 ± 0.05
82.43	3.52 ± 0.06
87.01	4.07 ± 0.07

Table 4.7: Fission fragment anisotropies for the reactions $^{16}O + ^{192,194,196,198}Pt$ and $^{18}O + ^{196,198}Pt$.

4.1.5 Statistical Model and Transition State Model Calculations

The statistical model (SM) of compound nucleus decay (Section 2.5) was used in conjunction with the Transition State Model (TSM) of fission [Bohr56], to provide model calculations with which to compare to the experimental data.

The SM code JO_SHELL uses l-distributions from the coupled-channels calculations, together with a number of input parameters (outlined below) to model the decay of the compound nucleus as described in Section 2.5. The SM code outputs the number of fission events as a matrix of their saddle-point angular momentum quantum number, J, and temperatures, $T(J)$, where for each event;

$$[T(J)]^2 = \frac{E_x(C.N.) - k_f B_f(J) - E_{rot}(J) - \Delta E_{total}}{a_f} \tag{4.1}$$

here $E_x(C.N.)$ is the excitation energy of the compound nucleus above the FRLDM ground-state at the saddle-point deformation, k_f is the fission barrier scaling factor, $B_f(J)$ is the Sierk fission barrier [Sier86], $E_{rot}(J)$ is the rotational energy at the equilibrium deformation (equation 2.50) [Sier86], ΔE_{total} is the reduction in energy due to the evaporation of light particles (for each individual evaporated particle ΔE is given by equation 2.73), and a_f is the level density parameter at the saddle-point.

The TSM code JO_A_SHELL uses equations 2.64 and 2.69, the SM $J-T$ fission matrix, and moments of inertia for the fissioning system, to calculate the fission fragment angular distributions. The angular momentum dependent moments of inertia, perpendicular and parallel to the symmetry axis, were determined using the parameterisation by Lestone [Lest95] of the Sierk [Sier86] rotating finite range model.

Comparisons of model calculations with experimental data were made by looking simultaneously at the anisotropies and fission probabilities for the six reactions. In an attempt to provide a close fit between the calculations and the experimental data, the calculations were performed for a range of inputs. A Monte Carlo ensemble of 50,000 cascades per reaction per energy was performed for each calculation.

The primary option in the SM inputs determines how the level densities are calculated. As outlined in Section 2.5.4, the level densities were computed for excitation energies determined by either the energy of the nucleus above the finite range liquid drop model (FRLDM) ground-state (SM-FRLDM option), or the modified energy of the nucleus above the true ground-state (SM-SP option). The first ap-

proach is based on the premise that the compound nucleus, formed in a heavy-ion collision, has an excitation energy sufficiently high that the shell and pairing effects are washed out. The second approach includes energy dependent shell and pairing effects, and is based in part on codes by Junghans [Jung00] and Lestone [Lest91]. If the decay of compound nuclei are affected by the $N = 126$ closed shell, the use of shell and pairing effects in calculating the level densities, may reflect these effects. For both options the level densities were calculated using equation 2.79 [Bohr69], using level density parameters at the equilibrium deformation and at the saddle-point determined using equation 2.77.

The probability of fission was modified through the fission barrier scaling factor, k_f, although a similar effect could have been achieved by varying the Kramers factor, which was set as a constant ($K_r = 1$). Also set as a constant was the fission transient delay time, $\tau_f = 20 \times 10^{-21}$ sec, reflecting the time range needed for the large mass compound nuclei to change shape. For the excitation energies here, this does not significantly affect the calculated results.

Figure 4.7 shows calculated SM fission probabilities and TSM anisotropies in comparison to experimental data (triangles) for the reaction $^{16}O + ^{194}Pt$. Looking firstly at calculations based on the FRLDM excitation energies, the green lines correspond to the SM-FRLDM option with fission barrier scaling factors of $k_f = 1.02$ (solid line), $k_f = 1.00$ (dashed line) and $k_f = 0.98$ (dot-dashed line). Of these, the calculations with $k_f = 0.98$ gave the best reproduction of both the experimental fission probabilities, Figure 4.7(a), and anisotropies, Figure 4.7(b).

Inclusion of shell and pairing effects are shown by the red lines in Figure 4.7. The solid, dashed and dot-dashed lines correspond to the SM-SP option with $k_f = 1.00$, $k_f = 0.75$ and $k_f = 0.72$ respectively. The use of the SM-SP option and $k_f = 0.72$, while providing a good reproduction of the fission probabilities, did not reproduce the anisotropies as well as the SM-FRLDM option ($k_f = 0.98$).

The two calculations corresponding to the SM-FRLDM option ($k_f = 1.02$) and SM-SP option ($k_f = 0.75$) are shown in Figure 4.7 as these parameters gave the best reproduction of the fission probabilities over the six reactions.

Figure 4.8 compares model calculations to the experimental results for all six O + Pt reactions, where common SM inputs were used for each reactions. The fission probabilities are shown as a ratio of calculated to experimental probabilities.

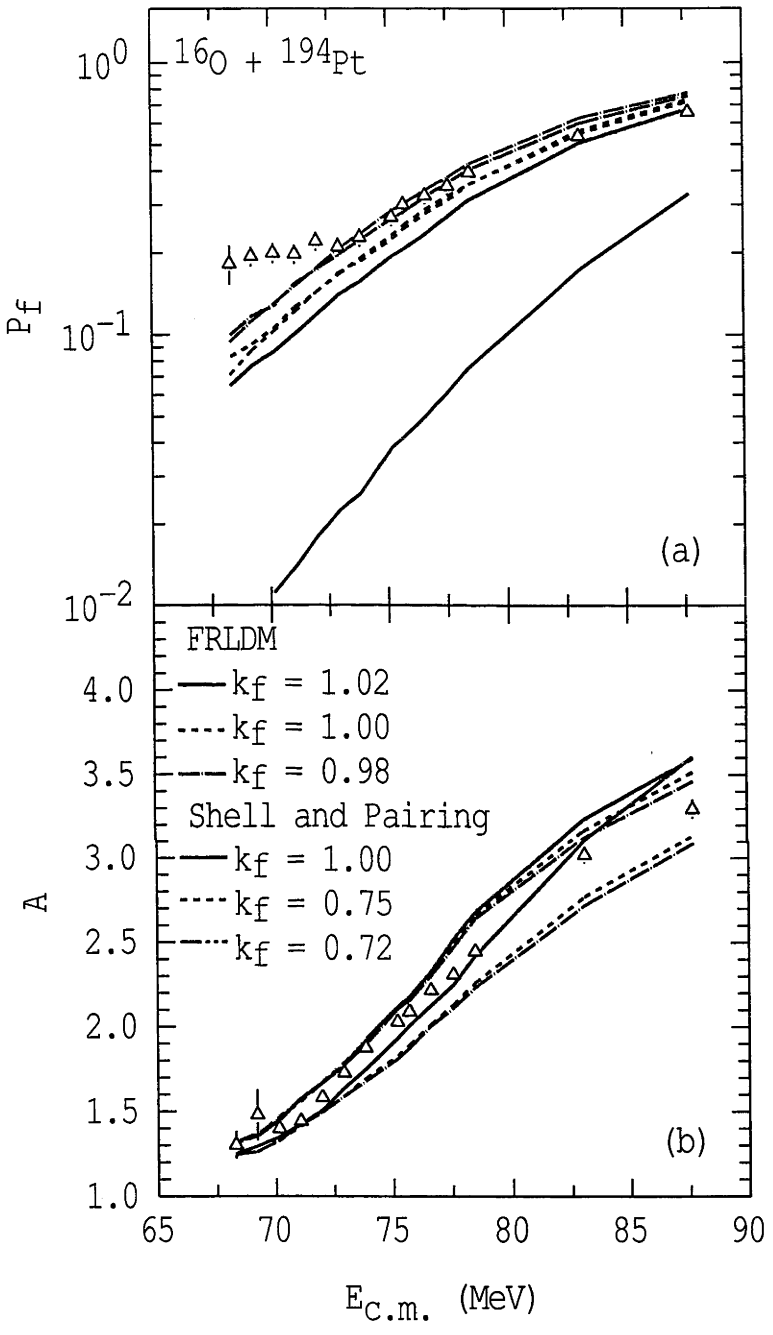

Figure 4.7: Fission probabilities (a) and fission fragment anisotropies (b) for the reaction ^{16}O + ^{194}Pt as a function of centre-of-mass energy. The points show the experimental data, the lines represent model calculation for six model inputs; (green lines) SM-FRLDM option k_f = 1.02 (solid lines), k_f = 1.00 (dashed lines) and k_f = 0.98 (dot-dashed lines); (red lines) SM-SP option k_f = 1.00 (solid lines), k_f = 0.75 (dashed lines) and k_f = 0.72 (dot-dashed lines).

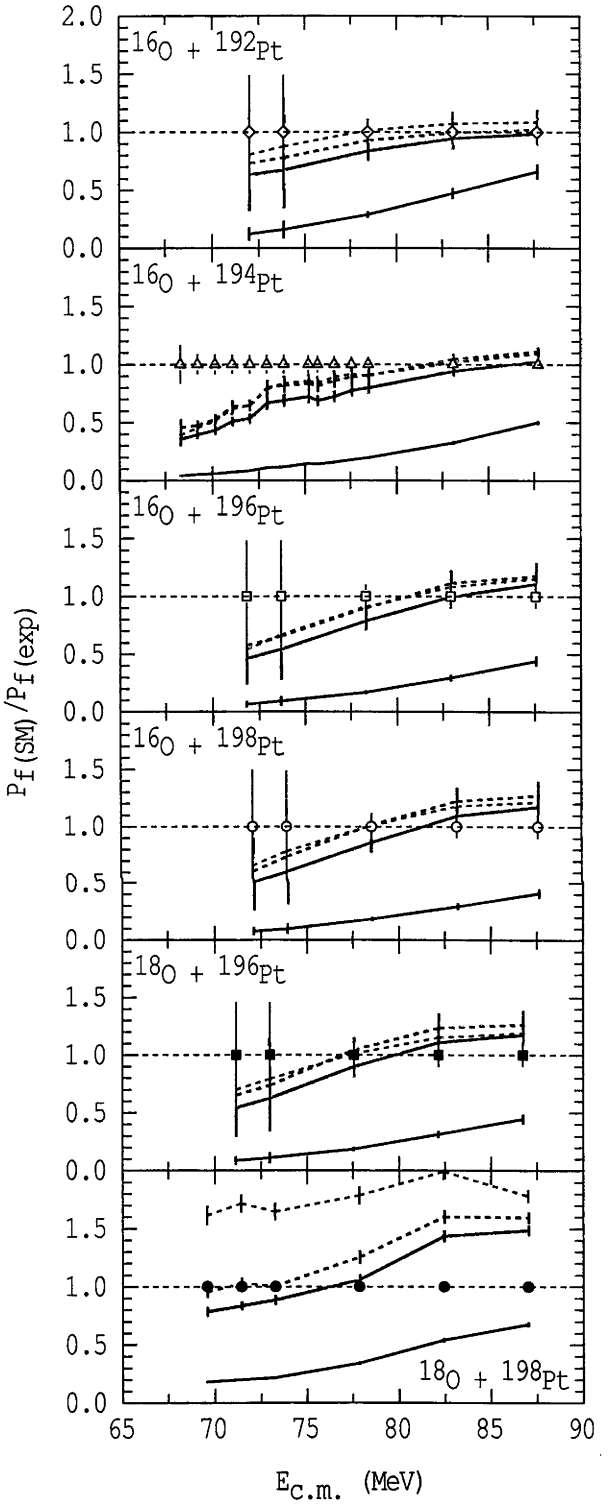

Figure 4.8: Comparison of calculated and experimental fission probabilities for the six O + Pt reactions as a function of centre-of-mass energy. The ratio of the Statistical Model calculation to the experimental results are shown for four model inputs; (green lines) SM-FRLDM option $k_f = 1.02$ (solid lines) and $k_f = 1.00$ (dashed lines); (red lines) SM-SP option $k_f = 1.00$ (solid lines) and $k_f = 0.75$ (dashed lines).

Calculations with four parameter sets are shown. The green solid and dashed lines correspond to the SM-FRLDM option with fission barrier scaling factors of $k_f = 1.02$ and $k_f = 1.00$ respectively. The red solid and dashed lines correspond to the SM-SP option with $k_f = 1.00$ and $k_f = 0.75$ respectively. Regardless of the parameters used, the calculations overestimate the slope of the fission probabilities with increasing energy, a pattern which is consistent for all six reactions.

Calculations of the fission probabilities using the SM-FRLDM option gives a good reproduction of the experimental results for realistic values of the fission barrier scaling factors. However, in order to reproduce the experimental results using the SM-SP option, an unrealistically low value for the fission barrier scaling factor ($k_f = 0.75$) was required. Even with this value, the SM-SP option failed to predict the fission probabilities for the $^{18}O + ^{198}Pt$ reaction.

A comparison of the model predictions and experimental reduced anisotropies $(A - 1)$, for the six reactions, is shown in Figure 4.9. The TSM calculations are based on the same four SM calculations as use in Figure 4.8. In a similar fashion to the fission probabilities, the model calculations generally overestimate the slope of the anisotropies with energy. The parameter sets which reproduce the fission probabilities in Figure 4.8, do not reproduce the anisotropies in Figure 4.9.

It can be seen that no series of model calculations with a single input set, fully reproduce the experimental fission probabilities and anisotropies for the six reactions simultaneously. Nevertheless, the calculations using level densities based on FRLDM ground-states (SM-FRLDM option) gives a more reasonable reproductions of the data than those using level densities based on the modified energy of the nucleus above the true ground-state taking into account shell and pairing effects (SM-SP option).

To distinguish any closed shell behaviour, fission probability ratios and reduced anisotropy ratios for the six reactions are shown in Figure 4.10 for an energy slice of $77.55 \leq E_{c.m.} \leq 78.57$ MeV. The points are plotted as a function of the average neutron number of the fissioning system, being the number of neutrons in the compound nucleus less the average number of neutrons emitted before fission occurs. The average neutron number varies slightly for each calculation. The calculations are the same as in Figures 4.8 and 4.9. Within this energy slice, all the calculated ratios vary with neutron number in a similar fashion, although none give a good

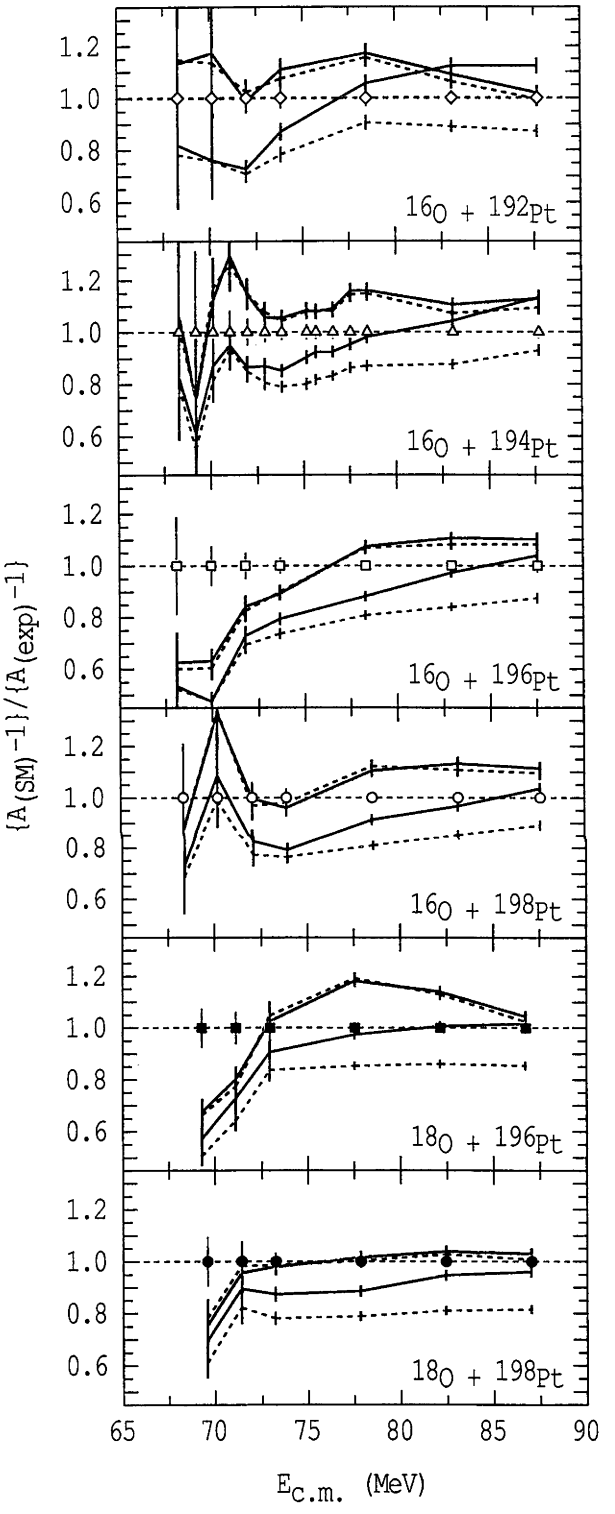

Figure 4.9: Ratio of reduced $(A-1)$ TSM calculations to experimental fission fragment anisotropies as a function of centre-of-mass energy, for the six O + Pt reactions. The calculations are based on SM calculations using the same inputs as Figure 4.8.

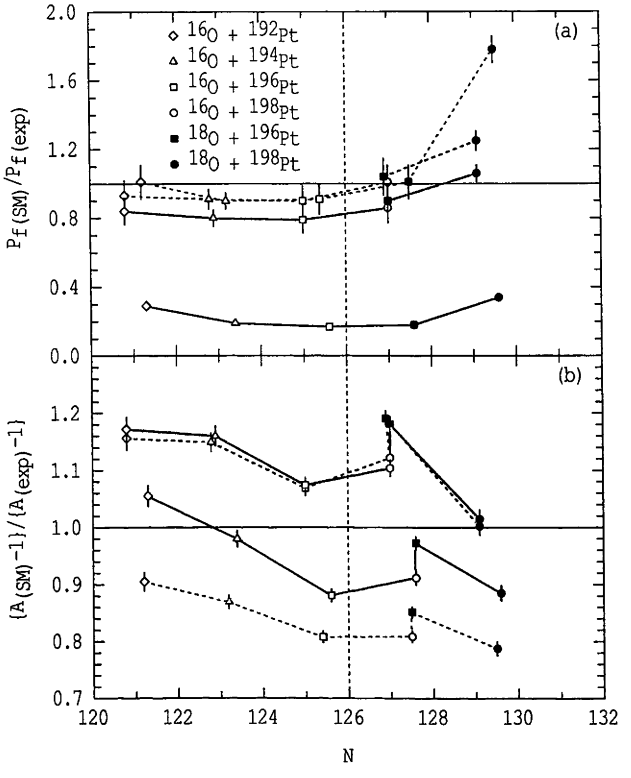

Figure 4.10: Ratio of model calculations and experimental data, as a function of the average neutron number of the fissioning systems for the energy range $77.55 \leq E_{c.m.} \leq 78.57$ MeV. Frame (a) shows the fission probabilities, while frame (b) shows the reduced fission fragment anisotropies. Each series of points represent calculations for the same set of inputs as used in Figures 4.8 and 4.9. The lines guide the eye.

fit to the data. Looking at the anisotropy ratios, they exhibit a step feature at neutron number, $N \approx 127.5$, where the two reactions ^{16}O + ^{198}Pt and ^{18}O + ^{196}Pt both form the compound nucleus ^{214}Rn. In each case the points with the higher anisotropy ratio comes from the ^{18}O + ^{196}Pt reaction.

The initial justification for including the shell and pairing effects was to produce a model that would better reproduce measurements near the closed shell. However the inclusion of these effects in the model does not provide a better fit to the experimental results. Junghans *et al.* [Jung98] reported that their experimental data could not be described using just shell and pairing effects in SM level densities calculations, but could be described when other collective modes were included. These observations are further discussed in Chapter 6.

4.1.6 The $N = 126$ closed shell

In this work, no evidence has been found to support a localised effect of the $N = 126$ closed shell on the fission fragment anisotropies as claimed by Shrivastava *et al.* [Shri99]. Regardless of the inputs used in the model calculations, the general trend of all the calculations in comparison to the experimental data was similar. For the anisotropies, there were fluctuations across the range of neutron numbers but no dramatic features that could be attributed to the $N = 126$ closed shell. The most noticeable feature was due to the projectile and target combination for the two reactions leading to the ^{214}Rn. The fission probabilities showed even less change across the closed shell than do the anisotropies. The experimental data could be reasonably described by the SM calculations using the FRLDM excitation energies.

This result contradicts observations by Shrivastava *et al.* [Shri99] of an increase in anisotropies for reactions leading to nuclei on the $N = 126$ closed shell. Anisotropies from the compound nucleus ^{210}Po (with $N = 126$) formed in the reaction ^{12}C + ^{198}Pt were compared to those from the compound nucleus ^{206}Po (with $N = 122$) formed in the reaction ^{12}C + ^{194}Pt. When evaluated against model calculations, larger anisotropies were reported for the ^{210}Po nucleus. This discrepancy decreased with increasing energy. Shrivastava *et al.* attributed this result to shell effects due to the $N = 126$ closed shell, despite the use of shell corrected level densities in the model calculations.

Pre-fission neutron multiplicities, ν_{pre}, for the same compound nucleus ^{210}Po, have been measured using the reaction ^{18}O + ^{192}Os [Hind86, Newt88]. Extrapolation of the ^{18}O + ^{192}Os data gives $1 < \nu_{pre} < 3$ for the energy range used by Shrivastava *et al.*. This assumes that the ^{210}Po compound nuclei formed in the two reactions will have similar decay properties at the same excitation energies. Based on this assumption the neutron number of the fissioning system will be less than $N = 126$ for the energy range used by Shrivastava. In order for the $N = 126$ closed shell to influence the compound nucleus decay, a narrow effect would be required at the initial excitation energy. With the evaporation of neutrons from the compound nucleus the excitation energy of the nucleus would drop to a level where shell effects may be present, but the nucleus is at that stage no longer at the closed shell. Although the last chance fission component has a large influence on the anisotropies, it is also where shell effects would be the least, due to neutron number. As the

discrepancies in the Shrivastava *et al.* anisotropies did not extend to ^{206}Po (with $N = 122$) a narrow shell effect would need to be present to describe the observed anisotropies. No such narrow features were observed for the O + Pt reactions measured in this work, nor for the SM calculation either with or without shell and pairing effects.

Further discussion of the $N = 126$ closed shell effect on compound nucleus decay is given in Chapter 6. However, as there appears to be no local impact of the $N = 126$ closed shell on the decay of compound nuclei near or on the closed shell, it is assumed that, similarly, there will be no influence of the closed shell on the decay of the compound nucleus ^{216}Ra ($N = 128$).

4.2 Reactions leading to the Compound Nucleus ^{216}Ra

Using the three reactions ^{12}C + ^{204}Pb, ^{19}F + ^{197}Au and ^{30}Si + ^{186}W, the formation and decay of the $Z = 88$ and $N = 128$ compound nucleus (^{216}Ra) was studied. By studying the influence of the entrance channel (projectile and target) on the subsequent decay of the compound nucleus, insight was sought into the capture-decay processes. Both fission fragment measurements and ER α-decay measurements were made over a range of energies spanning the Coulomb barriers. A broad spectrum of fission and ER data was obtained. Fission cross-sections, anisotropies, and fission mass-distributions were measured. Total ER and individual ER cross-sections were determined. From the fission and ER data, capture cross-sections were obtained.

Coupled-channels calculations were performed to fit the capture cross-sections and capture barrier distributions for the three reactions. Decay calculations, using angular momentum distributions obtained from the coupled-channels calculations, were then compared to the experimental data.

In this section, where data are plotted as a function of excitation energy, the excitation energy of the compound nucleus was determined using equations 2.95 and 2.96. The Q_{GS} values used for the three reactions were;

$$
\begin{aligned}
^{12}\mathrm{C} + ^{204}\mathrm{Pb} &\rightarrow ^{216}\mathrm{Ra} \quad Q_{GS} = -28.40 \text{ MeV} \\
^{19}\mathrm{F} + ^{197}\mathrm{Au} &\rightarrow ^{216}\mathrm{Ra} \quad Q_{GS} = -35.92 \text{ MeV} \\
^{30}\mathrm{Si} + ^{186}\mathrm{W} &\rightarrow ^{216}\mathrm{Ra} \quad Q_{GS} = -70.22 \text{ MeV}
\end{aligned}
$$

4.2.1 Evaporation Residues

Evaporation residue (ER) cross-sections for the three reactions leading to ^{216}Ra are presented in this section. Firstly the individual ER cross-sections for each reaction are presented. The individual ER cross-sections for the three reactions are then compared. Lastly evidence of ^{12}C and ^{19}F projectile breakup is presented.

4.2.1.1 Evaporation Residue Cross-Sections

Cross-sections were determined for all ER channels for compound nuclei formed in the three reactions, ^{12}C + ^{204}Pb, ^{19}F + ^{197}Au, and ^{30}Si + ^{186}W.

For the ^{12}C + ^{204}Pb reaction, the individual ER cross-sections are shown Figure 4.11, and are listed in Table 4.8. Using the α-energies and lifetimes of the α-

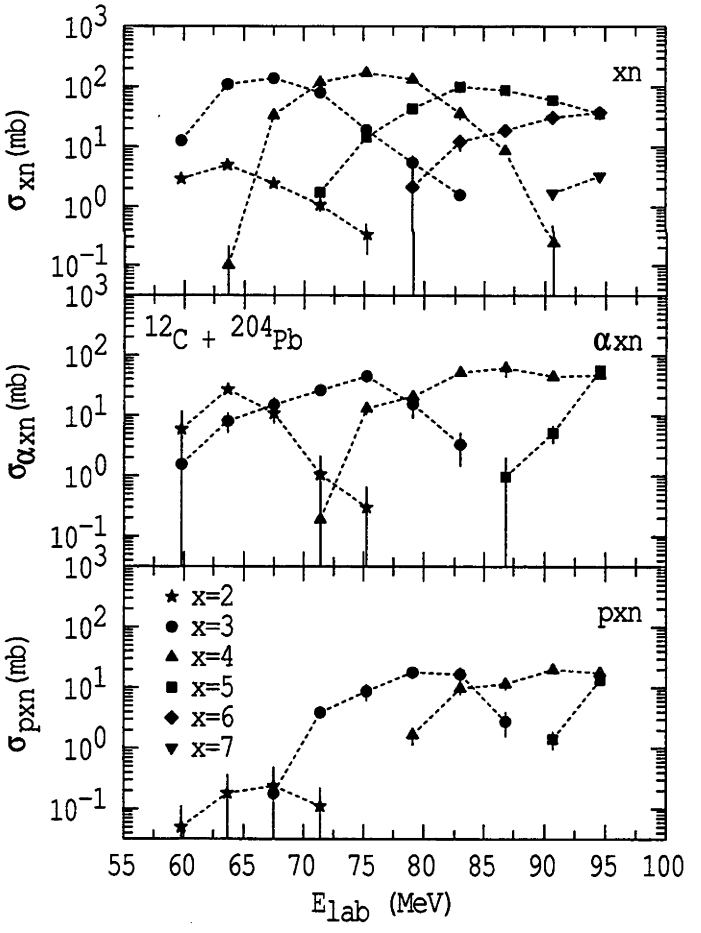

Figure 4.11: Individual xn, αxn, and pxn ER cross-sections for the reaction ^{12}C + ^{204}Pb as a function of E_{lab}. The lines guide the eye.

E_{lab} (MeV)	$E_{c.m.}$ (MeV)	σ_{2n} (mb)	σ_{3n} (mb)	σ_{4n} (mb)	σ_{5n} (mb)
59.80	56.48	2.90 ± 0.29	12.5 ± 0.8		
63.66	60.12	4.94 ± 0.49	109 ± 4	0.10 ± 0.11	
67.52	63.77	2.44 ± 0.35	138 ± 6	33.4 ± 2.1	
71.39	67.42	1.07 ± 0.24	79.7 ± 3	118 ± 6	1.7 ± 0.4
75.25	71.07	0.33 ± 0.18	19.1 ± 1.1	170 ± 4	14.4 ± 1.5
		σ_{6n} (mb)			
79.11	74.72	2.1 ± 2.1	5.4 ± 1.7	132 ± 13	43.2 ± 4.4
82.98	78.37	12.2 ± 3.7	1.58 ± 0.22	35.9 ± 7.2	100 ± 20
86.84	82.02	18.7 ± 2.0	σ_{7n} (mb)	8.55 ± 0.99	87.2 ± 8.9
90.7	85.66	30.9 ± 1.7	1.69 ± 0.24	0.24 ± 0.25	59.6 ± 4.9
94.56	89.31	37.2 ± 1.7	3.27 ± 0.40		35.7 ± 3.7
E_{lab} (MeV)	$E_{c.m.}$ (MeV)	$\sigma_{\alpha 2n}$ (mb)	$\sigma_{\alpha 3n}$ (mb)	$\sigma_{\alpha 4n}$ (mb)	$\sigma_{\alpha 5n}$ (mb)
59.80	56.48	5.9 ± 5.9	1.6 ± 1.6		
63.66	60.12	26.8 ± 3.6	8.0 ± 2.9		
67.52	63.77	10.8 ± 3.4	15.0 ± 4.7		
71.39	67.42	1.1 ± 1.1	26.2 ± 3.3	0.19 ± 0.21	
75.25	71.07	0.30 ± 0.37	45.1 ± 9.6	13.1 ± 2.8	
79.11	74.72		15.5 ± 6.4	20.6 ± 4.2	
82.98	78.37		3.3 ± 1.9	51.8 ± 5.5	
86.84	82.02			62.1 ± 18.9	1.0 ± 1.1
90.7	85.66			44.9 ± 4.8	5.2 ± 1.7
94.56	89.31			47.5 ± 5.0	56.8 ± 6.1
E_{lab} (MeV)	$E_{c.m.}$ (MeV)	σ_{p2n} (mb)	σ_{p3n} (mb)	σ_{p4n} (mb)	σ_{p5n} (mb)
59.80	56.48	0.05 ± 0.06			
63.66	60.12	0.18 ± 0.19			
67.52	63.77	0.24 ± 0.25	0.18 ± 0.12		
71.39	67.42	0.11 ± 0.11	3.89 ± 0.51		
75.25	71.07		8.7 ± 2.7		
79.11	74.72		17.9 ± 3.7	1.66 ± 0.53	
82.98	78.37		16.6 ± 5.0	9.8 ± 2.0	
86.84	82.02		2.8 ± 1.2	11.5 ± 2.4	
90.7	85.66			19.8 ± 2.1	1.4 ± 0.5
94.56	89.31			17.7 ± 1.9	13.5 ± 1.5

Table 4.8: Individual xn, αxn, and pxn ER cross-sections for the reaction $^{12}C + ^{204}Pb$ as a function of E_{lab} and $E_{c.m.}$.

particles emitted from the ERs, good separation of the individual ER channels was achieved. At lower collision energies the formation of xn ERs is dominant, but with increasing energy, αxn and pxn ER production becomes more significant.

The cross-sections for individual ERs formed in the $^{19}F + ^{197}Au$ reaction are shown in Figure 4.12 and listed in Table 4.9. Again the major ER yields at the lower energies result from xn evaporation, while at higher energies, changed particle (αxn and pxn) evaporation becomes dominant.

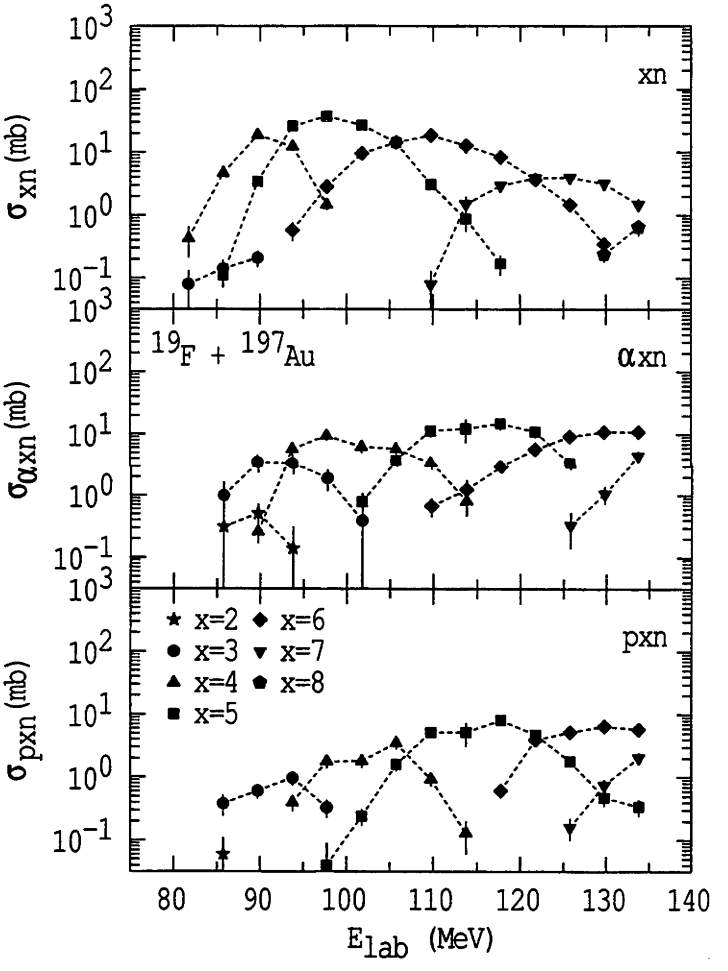

Figure 4.12: Individual xn, αxn, and pxn ER cross-sections for the reaction $^{19}F + ^{197}Au$ as a function of E_{lab}. The lines guide the eye.

The individual ER cross-sections for the $^{30}Si + ^{186}W$ reaction are presented in two parts, corresponding to the two series of measurements, Runs A and B. The first set of measurements (Run A) was acquired with lower α-particle counts than

E_{lab}(MeV)	$E_{c.m.}$(MeV)	σ_{3n} (mb)	σ_{4n} (mb)	σ_{5n} (mb)	σ_{6n} (mb)
81.72	74.53	0.08 ± 0.05	0.43 ± 0.22		
85.74	78.20	0.14 ± 0.05	4.69 ± 0.51	0.11 ± 0.04	
89.73	81.84	0.21 ± 0.06	18.9 ± 1.9	3.44 ± 0.38	
93.78	85.53	0.03 ± 0.04	12.4 ± 1.9	26.2 ± 2.7	0.58 ± 0.19
97.74	89.14		1.47 ± 0.26	37.5 ± 3.1	2.84 ± 0.35
101.75	92.80			26.9 ± 2.7	9.60 ± 0.99
105.75	96.45	σ_{7n} (mb)		14.4 ± 1.5	14.4 ± 1.5
109.76	100.11	0.08 ± 0.05		3.11 ± 0.35	18.6 ± 1.9
113.76	103.75	1.50 ± 0.46		0.87 ± 0.32	12.8 ± 3.2
117.76	107.40	2.97 ± 0.47		0.17 ± 0.06	8.37 ± 0.88
121.77	111.06	3.87 ± 0.41			3.66 ± 0.39
125.77	114.71	3.95 ± 0.43	σ_{8n} (mb)		1.46 ± 0.18
129.77	118.36	3.20 ± 0.51	0.24 ± 0.06		0.35 ± 0.09
133.78	122.01	1.48 ± 0.32	0.65 ± 0.18		0.03 ± 0.02
E_{lab}(MeV)	$E_{c.m.}$(MeV)	$\sigma_{\alpha 2n}$ (mb)	$\sigma_{\alpha 3n}$ (mb)	$\sigma_{\alpha 4n}$ (mb)	$\sigma_{\alpha 5n}$ (mb)
81.72	74.53	0.02 ± 0.03	0.03 ± 0.05		
85.74	78.20	0.31 ± 0.34	0.99 ± 0.66		
89.73	81.84	0.51 ± 0.21	3.5 ± 1.2	0.26 ± 0.09	
93.78	85.53	0.14 ± 0.17	3.4 ± 1.2	5.8 ± 1.2	
97.74	89.14		1.88 ± 0.71	9.4 ± 1.5	
101.75	92.80		0.39 ± 0.43	6.3 ± 1.3	0.79 ± 0.29
105.75	96.45	$\sigma_{\alpha 6n}$ (mb)		5.79 ± 0.94	3.81 ± 0.87
109.76	100.11	0.67 ± 0.22		3.40 ± 0.74	11.4 ± 2.4
113.76	103.75	1.24 ± 0.51		0.81 ± 0.35	12.3 ± 5.0
117.76	107.40	2.96 ± 0.63			15.0 ± 3.1
121.77	111.06	5.67 ± 0.88	$\sigma_{\alpha 7n}$ (mb)		11.0 ± 2.3
125.77	114.71	9.1 ± 1.4	0.33 ± 0.19		3.38 ± 0.77
129.77	118.36	10.9 ± 1.7	1.06 ± 0.33		
133.78	122.01	10.9 ± 1.7	4.45 ± 0.80		
E_{lab}(MeV)	$E_{c.m.}$(MeV)	σ_{p2n} (mb)	σ_{p3n} (mb)	σ_{p4n} (mb)	σ_{p5n} (mb)
81.72	74.53	0.007 ± 0.010	0.005 ± 0.010		
85.74	78.20	0.06 ± 0.05	0.38 ± 0.14		
89.73	81.84	0.02 ± 0.02	0.61 ± 0.15		
93.78	85.53	0.01 ± 0.02	0.98 ± 0.24	0.40 ± 0.11	
97.74	89.14		0.33 ± 0.10	1.78 ± 0.40	0.04 ± 0.05
101.75	92.80			1.80 ± 0.38	0.24 ± 0.07
105.75	96.45			3.52 ± 0.73	1.60 ± 0.35
109.76	100.11			0.93 ± 0.21	5.20 ± 0.82
113.76	103.75	σ_{p6n} (mb)		0.13 ± 0.07	5.2 ± 2.1
117.76	107.40	0.61 ± 0.14			8.1 ± 1.3
121.77	111.06	3.94 ± 0.61	σ_{p7n} (mb)		4.76 ± 0.74
125.77	114.71	5.20 ± 0.81	0.16 ± 0.06		1.79 ± 0.31
129.77	118.36	6.51 ± 1.00	0.75 ± 0.17		0.48 ± 0.13
133.78	122.01	5.75 ± 0.90	2.04 ± 0.43		0.34 ± 0.10

Table 4.9: Individual xn, αxn, and pxn ER cross-sections for the reaction $^{19}F + ^{197}Au$ as a function of E_{lab} and $E_{c.m.}$.

was considered optimal, resulting in too few counts to obtain cross-sections for the weaker channels. The underlying difficulty with these measurement was a combination of low overall ER cross-sections, thin targets and low beam currents, resulting in low α-particle count rates. The second set of measurements (Run B) provided data with higher count rates, but at fewer energies. The total ER cross-sections from the two sets of measurements proved to be in good agreement. However, the individual ER cross-sections from Run B were assessed to be more reliable that those from Run A, particularly at low beam energies. The results for Run A are given in Figure 4.13 and Table 4.10, while results from Run B are given in Figure 4.14 and Table 4.11.

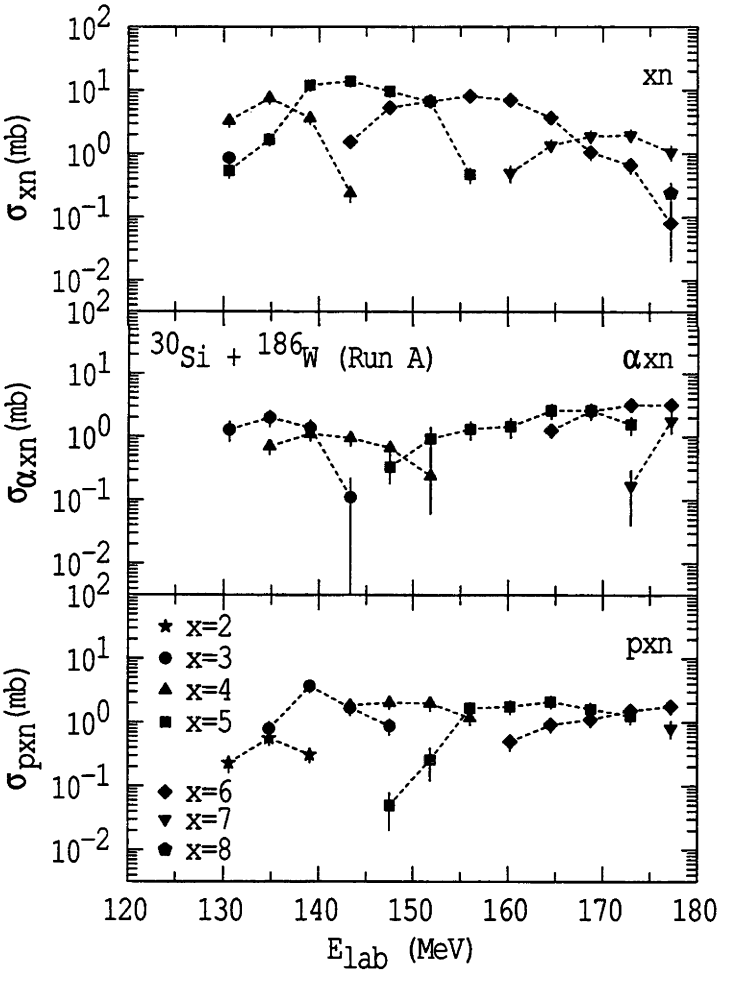

Figure 4.13: Individual xn, αxn, and pxn ER cross-sections for the reaction ^{30}Si + ^{186}W (Run A) as a function of E_{lab}. The lines guide the eye.

E_{lab} (MeV)	$E_{c.m.}$ (MeV)	σ_{3n} (mb)	σ_{4n} (mb)	σ_{5n} (mb)	σ_{6n} (mb)
130.55	112.42	0.86 ± 0.20	3.34 ± 0.70	0.54 ± 0.13	
134.79	116.07		7.6 ± 1.5	1.68 ± 0.36	
139.03	119.72		3.66 ± 0.76	12.1 ± 2.4	
143.28	123.38		0.24 ± 0.07	14.0 ± 2.8	1.54 ± 0.33
147.52	127.03			9.7 ± 2.0	5.4 ± 1.1
151.78	130.70			6.7 ± 1.4	6.7 ± 1.4
156.00	134.33	σ_{7n} (mb)		0.47 ± 0.13	8.2 ± 1.7
160.24	137.98	0.50 ± 0.15			7.0 ± 1.5
164.49	141.64	1.36 ± 0.31			3.71 ± 0.78
168.72	145.29	1.89 ± 0.44			1.06 ± 0.27
172.94	148.92	1.97 ± 0.45	σ_{8n} (mb)		0.66 ± 0.18
177.21	152.60	1.06 ± 0.30	0.24 ± 0.11		0.08 ± 0.06
E_{lab} (MeV)	$E_{c.m.}$ (MeV)	$\sigma_{\alpha 3n}$ (mb)	$\sigma_{\alpha 4n}$ (mb)	$\sigma_{\alpha 5n}$ (mb)	$\sigma_{\alpha 6n}$ (mb)
130.55	112.42	1.28 ± 0.45			
134.79	116.07	1.99 ± 0.58	0.70 ± 0.19		
139.03	119.72	1.37 ± 0.44	1.11 ± 0.27		
143.28	123.38	0.11 ± 0.11	0.95 ± 0.25		
147.52	127.03		0.66 ± 0.19	0.33 ± 0.15	
151.78	130.70		0.24 ± 0.18	0.93 ± 0.50	
156.00	134.33			1.32 ± 0.43	
160.24	137.98			1.46 ± 0.51	
164.49	141.64			2.61 ± 0.71	1.26 ± 0.31
168.72	145.29	$\sigma_{\alpha 7n}$ (mb)		2.62 ± 0.79	2.58 ± 0.62
172.94	148.92	0.17 ± 0.13		1.58 ± 0.51	3.21 ± 0.72
177.21	152.60	1.79 ± 0.67			3.19 ± 0.80
E_{lab} (MeV)	$E_{c.m.}$ (MeV)	σ_{p2n} (mb)	σ_{p3n} (mb)	σ_{p4n} (mb)	σ_{p5n} (mb)
130.55	112.42	0.23 ± 0.07			
134.79	116.07	0.56 ± 0.13	0.79 ± 0.23		
139.03	119.72	0.31 ± 0.08	3.70 ± 0.82		
143.28	123.38		1.69 ± 0.43	1.85 ± 0.40	
147.52	127.03		0.88 ± 0.25	2.04 ± 0.44	0.05 ± 0.03
151.78	130.70			2.00 ± 0.51	0.26 ± 0.14
156.00	134.33	σ_{p6n} (mb)		1.18 ± 0.28	1.67 ± 0.40
160.24	137.98	0.50 ± 0.15			1.77 ± 0.44
164.49	141.64	0.92 ± 0.23			2.12 ± 0.49
168.72	145.29	1.11 ± 0.28			1.62 ± 0.42
172.94	148.92	1.53 ± 0.36	σ_{p7n} (mb)		1.26 ± 0.33
177.21	152.60	1.77 ± 0.45	0.81 ± 0.25		

Table 4.10: Individual xn, αxn, and pxn ER cross-sections for the reaction $^{30}Si + ^{186}W$ (Run A) as a function of E_{lab} and $E_{c.m.}$.

E_{lab} (MeV)	$E_{c.m.}$ (MeV)	σ_{2n} (mb)	σ_{3n} (mb)	σ_{4n} (mb)	σ_{5n} (mb)
126.29	108.75	0.007 ± 0.01	0.06 ± 0.03	0.12 ± 0.06	
134.78	116.06	σ_{6n} (mb)	0.91 ± 0.23	7.88 ± 0.80	1.08 ± 0.11
143.27	123.37	1.76 ± 0.56		0.61 ± 0.03	13.91 ± 0.44
151.84	130.75	6.12 ± 0.58	σ_{7n} (mb)		5.99 ± 0.57
160.24	137.98	6.34 ± 0.48	0.16 ± 0.03		
168.72	145.29	1.02 ± 0.15	2.03 ± 0.43		
E_{lab} (MeV)	$E_{c.m.}$ (MeV)	$\sigma_{\alpha 2n}$ (mb)	$\sigma_{\alpha 3n}$ (mb)	$\sigma_{\alpha 4n}$ (mb)	$\sigma_{\alpha 5n}$ (mb)
126.29	108.75	0.02 ± 0.01	0.02 ± 0.02		
134.78	116.06		0.14 ± 0.09	0.69 ± 0.35	
143.27	123.37		0.03 ± 0.02	1.38 ± 0.15	0.3 ± 0.16
151.84	130.75	$\sigma_{\alpha 6n}$ (mb)		0.37 ± 0.10	1.43 ± 0.35
160.24	137.98	1.20 ± 0.37			3.59 ± 0.78
168.72	145.29	1.88 ± 0.41			2.51 ± 0.82
E_{lab} (MeV)	$E_{c.m.}$ (MeV)	σ_{p3n} (mb)	σ_{p4n} (mb)	σ_{p5n} (mb)	σ_{p6n} (mb)
126.29	108.75				
134.78	116.06		0.13 ± 0.07		
143.27	123.37	0.12 ± 0.03	1.41 ± 0.15		
151.84	130.75		0.85 ± 0.43	0.42 ± 0.22	
160.24	137.98			1.71 ± 0.46	0.32 ± 0.16
168.72	145.29			1.51 ± 0.14	0.40 ± 0.25

Table 4.11: Individual xn, αxn, and pxn ER cross-sections, for the reaction ^{30}Si + ^{186}W (Run B) as a function of E_{lab} and $E_{c.m.}$.

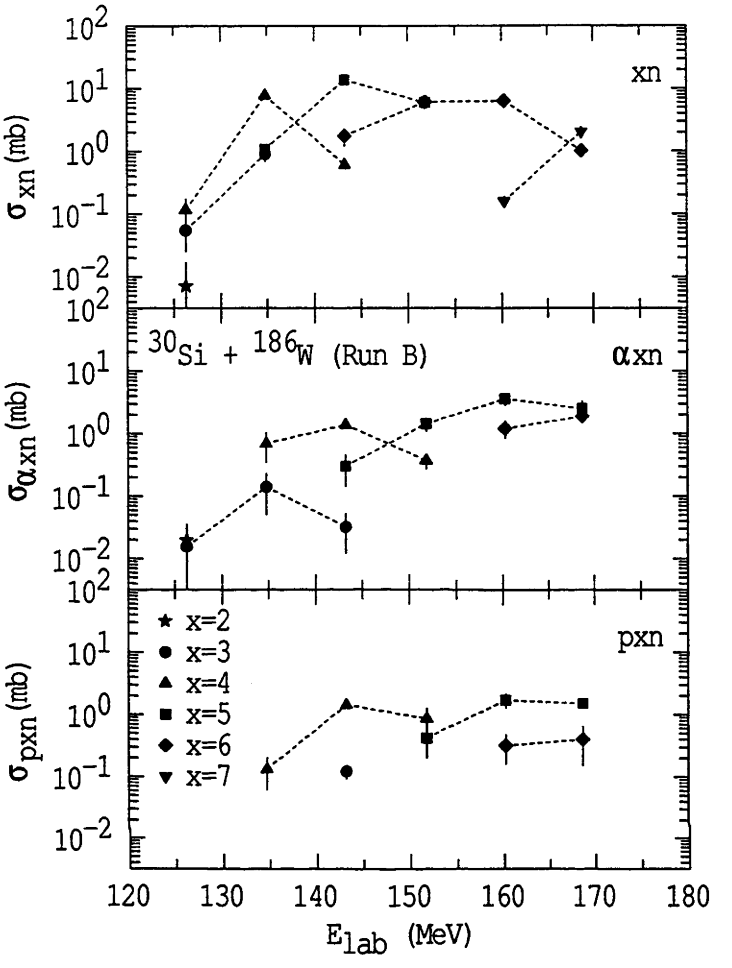

Figure 4.14: Individual xn, αxn, and pxn ER cross-sections for the reaction $^{30}Si + ^{186}W$ (Run B) as a function of E_{lab}. The lines guide the eye.

Summed xn, αxn, pxn and total ER cross-section are tabulated in Tables 4.12, 4.13 and 4.14. While the listed uncertainties for the individual cross-sections are purely statistical, the uncertainties for the total ER cross-sections have been set at a minimum of $\pm 5\%$ to reflect systematic uncertainties. These include uncertainties in target thickness, beam current uniformity over time, tabulated α-decay energies and branching ratios, background estimations and residual long-lifetime activity in targets used for several beam energies.

E_{lab} (MeV)	$E_{c.m.}$ (MeV)	σ_{xn} (mb)	$\sigma_{\alpha xn}$ (mb)	σ_{pxn} (mb)	σ_{ER} (mb)
59.80	56.48	15.4 ± 0.9	7.5 ± 6.2	0.05 ± 0.06	22.9 ± 6.2
63.66	60.12	114 ± 4	34.9 ± 4.6	0.18 ± 0.19	149 ± 7
67.52	63.77	174 ± 6	25.8 ± 5.8	0.42 ± 0.28	200 ± 10
71.39	67.42	200 ± 7	27.5 ± 3.5	4.00 ± 0.52	232 ± 12
75.25	71.07	203 ± 4	59 ± 10	8.7 ± 2.7	270 ± 14
79.11	74.72	183 ± 14	36 ± 8	19.6 ± 3.7	239 ± 17
82.98	78.37	150 ± 22	55 ± 6	26.3 ± 5.4	231 ± 23
86.84	82.02	115 ± 9	63 ± 19	14.3 ± 2.7	192 ± 21
90.70	85.66	92.4 ± 5.2	50 ± 5	21.3 ± 2.1	164 ± 8
94.56	89.31	76.2 ± 4.0	104 ± 8	31.2 ± 2.4	212 ± 11

Table 4.12: Summed xn, pxn, αxn, and total ER cross-sections for the reaction $^{12}C + ^{204}Pb$ as a function of E_{lab} and $E_{c.m.}$. The uncertainty in the total ER cross-sections was set at a minimum of ±5%.

E_{lab} (MeV)	$E_{c.m.}$ (MeV)	σ_{xn} (mb)	$\sigma_{\alpha xn}$ (mb)	σ_{pxn} (mb)	σ_{ER} (mb)
81.72	74.53	0.51 ± 0.23	0.05 ± 0.06	0.01 ± 0.01	0.57 ± 0.23
85.74	78.20	4.94 ± 0.51	1.30 ± 0.74	0.44 ± 0.15	6.68 ± 0.92
89.73	81.84	22.5 ± 2.0	4.3 ± 1.2	0.63 ± 0.15	27.4 ± 2.3
93.78	85.53	39.2 ± 3.3	9.3 ± 1.7	1.39 ± 0.26	49.9 ± 3.7
97.74	89.14	41.8 ± 3.1	11.3 ± 1.7	2.15 ± 0.42	55.3 ± 3.6
101.75	92.80	36.5 ± 2.9	7.5 ± 1.4	2.04 ± 0.39	46.0 ± 3.2
105.75	96.45	28.8 ± 2.1	9.6 ± 1.3	5.12 ± 0.81	43.5 ± 2.6
109.76	100.11	21.8 ± 1.9	15.5 ± 2.5	6.13 ± 0.85	43.4 ± 3.3
113.76	103.75	15.2 ± 3.3	14.4 ± 5.0	5.3 ± 2.1	34.9 ± 6.3
117.76	107.40	11.5 ± 1.0	17.9 ± 3.2	8.7 ± 1.3	38.2 ± 3.6
121.77	111.06	7.53 ± 0.57	16.6 ± 2.4	8.70 ± 0.96	32.9 ± 2.7
125.77	114.71	5.41 ± 0.47	12.9 ± 1.6	7.15 ± 0.87	25.4 ± 1.9
129.77	118.36	3.79 ± 0.52	12.0 ± 1.7	7.7 ± 1.0	23.5 ± 2.1
133.78	122.01	2.16 ± 0.37	15.3 ± 1.9	8.1 ± 1.0	25.6 ± 2.2

Table 4.13: Summed xn, pxn, αxn, and total ER cross-sections for the reaction $^{19}F + ^{197}Au$ as a function of E_{lab} and $E_{c.m.}$. The uncertainty in the total ER cross-sections was set at a minimum of ±5%.

E_{lab} (MeV)	$E_{c.m.}$ (MeV)	σ_{xn} (mb)	$\sigma_{\alpha xn}$ (mb)	σ_{pxn} (mb)	σ_{ER} (mb)
Run A					
130.55	112.42	4.74 ± 0.74	1.28 ± 0.45	0.23 ± 0.07	6.25 ± 0.87
134.79	116.07	9.25 ± 1.58	2.69 ± 0.61	1.35 ± 0.26	13.3 ± 1.7
139.03	119.72	15.8 ± 2.6	2.48 ± 0.52	4.01 ± 0.82	22.3 ± 2.7
143.28	123.38	15.8 ± 2.8	1.06 ± 0.27	3.54 ± 0.59	20.4 ± 3.0
147.52	127.03	15.1 ± 2.3	0.99 ± 0.24	2.97 ± 0.51	19.0 ± 2.3
151.78	130.70	13.4 ± 2.0	1.17 ± 0.53	2.26 ± 0.53	16.9 ± 2.2
156.00	134.33	8.63 ± 1.68	1.32 ± 0.43	2.85 ± 0.49	12.8 ± 1.8
160.24	137.98	7.50 ± 1.47	1.46 ± 0.51	2.27 ± 0.46	11.2 ± 1.6
164.49	141.64	5.07 ± 0.84	3.87 ± 0.77	3.04 ± 0.54	12.0 ± 1.3
168.72	145.29	2.95 ± 0.52	5.20 ± 1.00	2.73 ± 0.50	10.9 ± 1.2
172.94	148.92	2.63 ± 0.48	4.96 ± 0.89	2.79 ± 0.49	10.4 ± 1.1
177.21	152.60	1.38 ± 0.33	4.98 ± 1.04	2.58 ± 0.51	8.9 ± 1.2
Run B					
126.29	108.75	0.18 ± 0.07	0.04 ± 0.02		0.21 ± 0.07
134.78	116.06	9.87 ± 0.84	0.83 ± 0.36	0.13 ± 0.07	10.8 ± 0.9
143.27	123.37	16.3 ± 0.7	1.71 ± 0.22	1.53 ± 0.15	19.5 ± 1.0
151.84	130.75	12.1 ± 0.8	1.80 ± 0.36	1.27 ± 0.48	15.2 ± 1.0
160.24	137.98	6.50 ± 0.48	4.79 ± 0.86	2.03 ± 0.49	13.3 ± 1.1
168.72	145.29	3.05 ± 0.46	4.39 ± 0.92	1.91 ± 0.29	9.4 ± 1.1

Table 4.14: Summed xn, pxn, αxn, and total ER cross-sections for the reaction ^{30}Si + ^{186}W (Runs A and B) as a function of E_{lab} and $E_{c.m.}$. The uncertainty in the total ER cross-sections was set at a minimum of ±5%.

4.2.1.2 Evaporation Residue Channel Ratios

To investigate the reaction mechanisms resulting in ER formation, the individual ER channels for the three reactions are compared. The compound nucleus excitation energy at which the individual xn channels occur is consistent across the three reactions, as shown by the experimental ratios (points) in Figure 4.15. In the figure the coloured lines are statistical model calculations using the SM-SP option ($k_f = 0.75$). The parameters used in the statistical model calculations were chosen as they provided good fits to the experimental fission/xn decay probabilities and fission anisotropies. Although the statistical model calculations are discussed

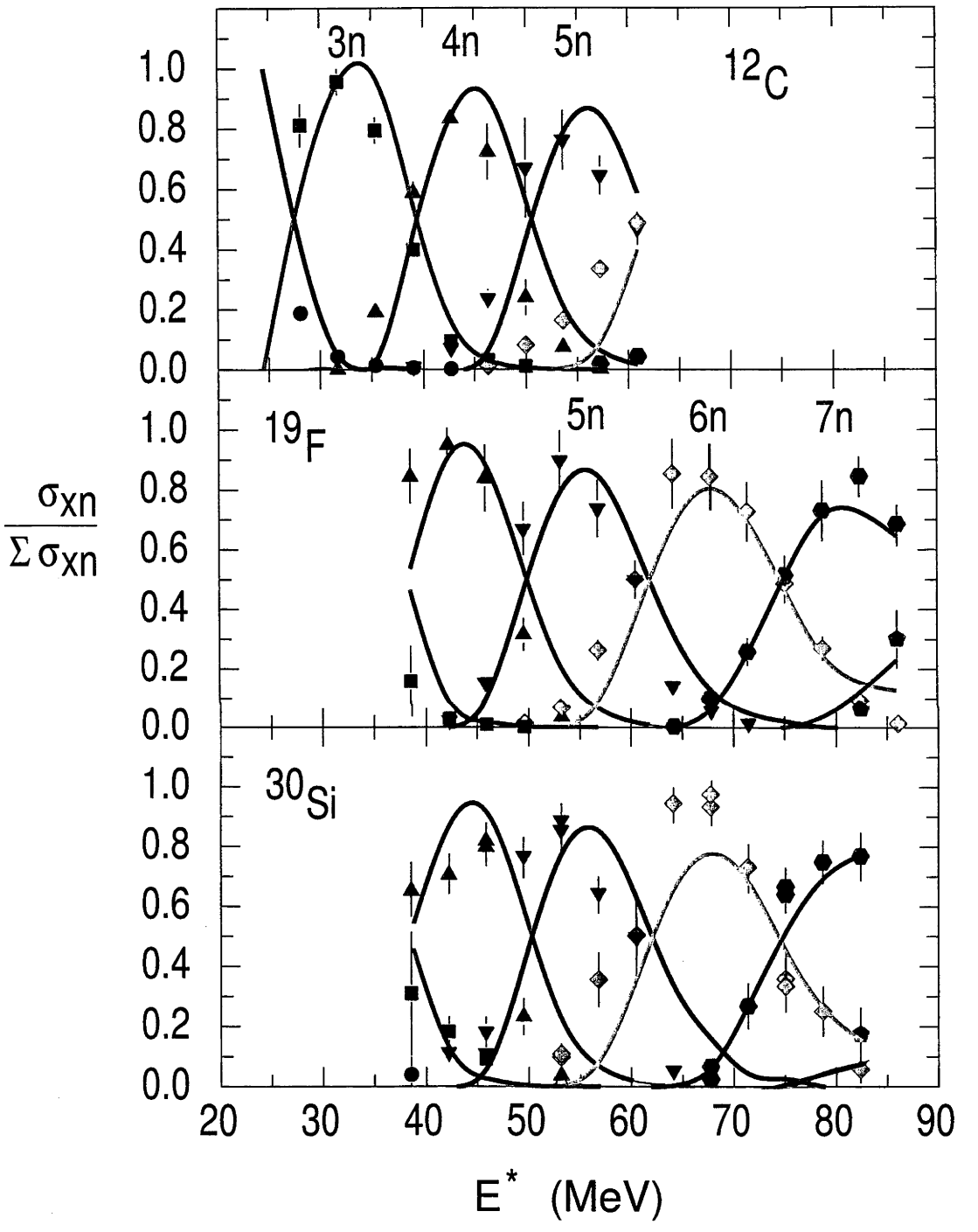

Figure 4.15: The proportion of individual xn ERs channels as a function of excitation energy, for the three reactions. The lines are statistical model calculations - see text.

in detail later in this chapter, it is worth noting a few observations. Reasonable agreement is achieved between the xn ER experimental results (points in Figure 4.15) and model calculation using level densities with shell and pairing corrections to the excitation energies (SM-SP option) (coloured lines). Although not shown, calculations based on FRLDM excitation energies (SM-FRLDM option) shift the position of each calculated xn channel to higher energies, indicating that the effective excitation energies in the calculations are too small. This is reasonable since the effect of shell and pairing is to lower the ground state energy, thus effectively increasing the excitation energy available for decay. Since neutron decay becomes more dominant at the lower compound nucleus excitation energies, where shell and pairing effects are most prominent, the extra energy due to shell and pairing should mainly be seen in the neutron evaporation multiplicity. For αxn and pxn ERs, the individual channel data were not precise enough to make conclusive comparisons between the three reactions.

The xn data show consistency between the three reactions. The peaks in the ER yields for each isotope occur at an excitation energy value essentially independent of the reaction, confirming that the actual energies of the ^{216}Ra nuclei formed in the three reactions are indeed the same.

In addition to comparing the individual xn ER channels, useful information on the reaction mechanisms can be gained by comparing the ratios of the total xn, αxn and pxn ER cross-sections. Figure 4.16 shows that the proportion of xn ERs is significantly lower for the $^{12}C + ^{204}Pb$ reaction than for the other two reactions. The fraction of pxn ER formation is small, and is relatively consistent for the three reactions. However, corresponding to the comparative decrease in xn ER formation for the $^{12}C + ^{204}Pb$ reaction, is an increase in αxn ER formation.

The green and red lines in Figure 4.16 are SM calculations based on the SM-FRLDM option ($k_f = 1.09$) and SM-SP option ($k_f = 0.75$) respectively. The latter are the same calculations as using in Figure 4.15. As with the individual xn ERs, the model calculations including shell and pairing effects give a better reproduction of the experimental results than do the SM-FRLDM calculations, agreeing quite closely with yields for the $^{30}Si + ^{186}W$ reaction.

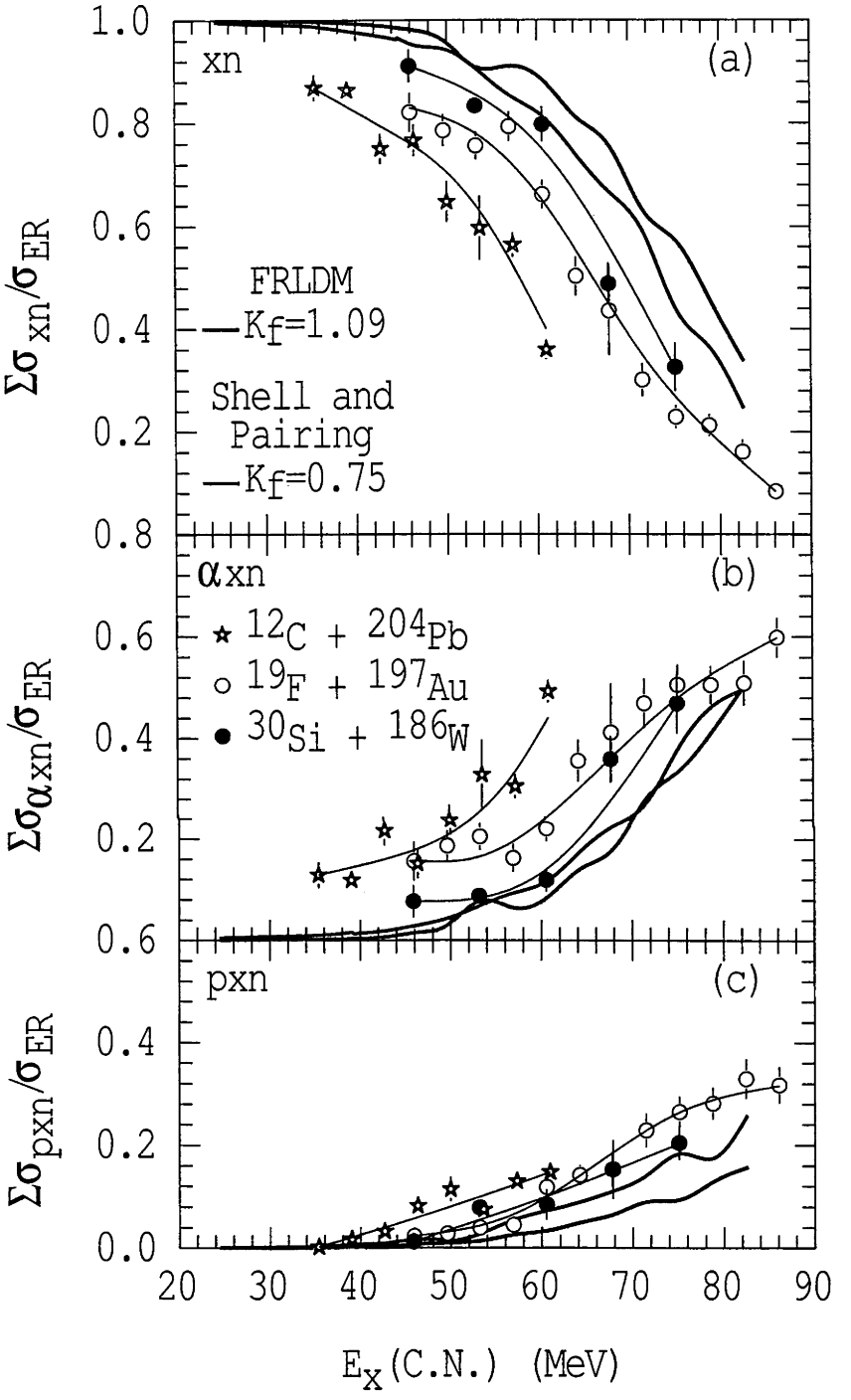

Figure 4.16: Distribution of evaporation residue cross-sections for the three reactions $^{12}C + ^{204}Pb$, $^{19}F + ^{197}Au$ and $^{30}Si + ^{186}W$ as a function of excitation energy. The frames show the fraction of ERs originating from (a) *xn* reaction, (b) *αxn* reactions and (c) *pxn* reactions. Of the two set of results for the $^{30}Si + ^{186}W$ reaction, only the higher statistic results from Run B are shown. The black lines show the trends of the experimental data. Also shown are SM calculations (green and red lines) as outlined in the text.

4.2.1.3 Projectile Breakup

The higher fraction of αxn ERs from the $^{12}C + ^{204}Pb$ reaction is consistent with a moderate amount of incomplete fusion from breakup of the ^{12}C projectile. While the measured individual channel ERs from this work are not sufficiently precise to determine exactly the extent of breakup, estimates from previously reported results are consistent with the results from this work, as described below.

The phenomenon of projectile breakup during capture reactions has been well documented for a number of loosely bound nuclei, such as $^{6,7,9,11}Li$ [Taka97, Petr97] and $^{9,10,11}Be$ [Sign98, Dasg99, Feko95, Yosh95], however breakup of the ^{12}C projectile has not been as extensively reported. Amongst others, studies by Vergani *et al.* [Verg93] of the $^{12}C + ^{197}Au$ fusion reaction, by Chakrabarty *et al.* [Chak00] of the $^{12}C + ^{169}Tm$ fusion reaction, and by Sakuragi *et al.* [Saku86] of elastic and inelastic ^{12}C scattering reactions, report a small but significant breakup of ^{12}C nuclei. The most favoured ^{12}C breakup channel by Q-value is $^{12}C \rightarrow ^{8}Be + \alpha$.

If the breakup of ^{12}C in the reaction $^{12}C + ^{197}Au$ studied by Vergani *et al.* [Verg93] is taken as a guide, then the extent of breakup in the $^{12}C + ^{204}Pb$ reaction can be estimated. As the mass and charge of the two targets are comparable, the interaction between the targets and the projectiles will be similar, and a direct comparison of ^{12}C breakup is reasonable. The red line in Figure 4.17 shows the ratio of Vergani's cross-sections for incomplete fusion ($^{8}Be + ^{197}Au$) to complete fusion (CF) as a function of excitation energy for the reaction $^{12}C + ^{197}Au$. It was assumed that, at the same excitation energy, there would be a similar ratio of incomplete fusion ($^{8}Be + ^{204}Pb$) to complete fusion for the reaction $^{12}C + ^{204}Pb$. The $^{12}C + ^{204}Pb$ measured xn and pxn ER cross-sections were assumed to originate fully from complete fusion. After subtracting the $^{8}Be + ^{204}Pb$ breakup fractions estimated above from the measured total $^{12}C + ^{204}Pb$ ER cross-section, the xn and pxn ER ratios shown in Figure 4.16 were scaled to give ratios to complete fusion (now excluding the incomplete fusion) as shown in Figure 4.17(a) and (c) by the dashed lines. Any complete fusion ER cross-section not from xn or pxn was then assigned to αxn complete fusion (Figure 4.17(b) dashed line). Based on the above analysis, up to 20% of the measured ER cross-sections for the $^{12}C + ^{204}Pb$ reaction may originate from the breakup-fusion reaction $^{8}Be + ^{204}Pb$. The scaled $^{12}C + ^{204}Pb$ values in Figure 4.17 are in much better agreement with the values from the

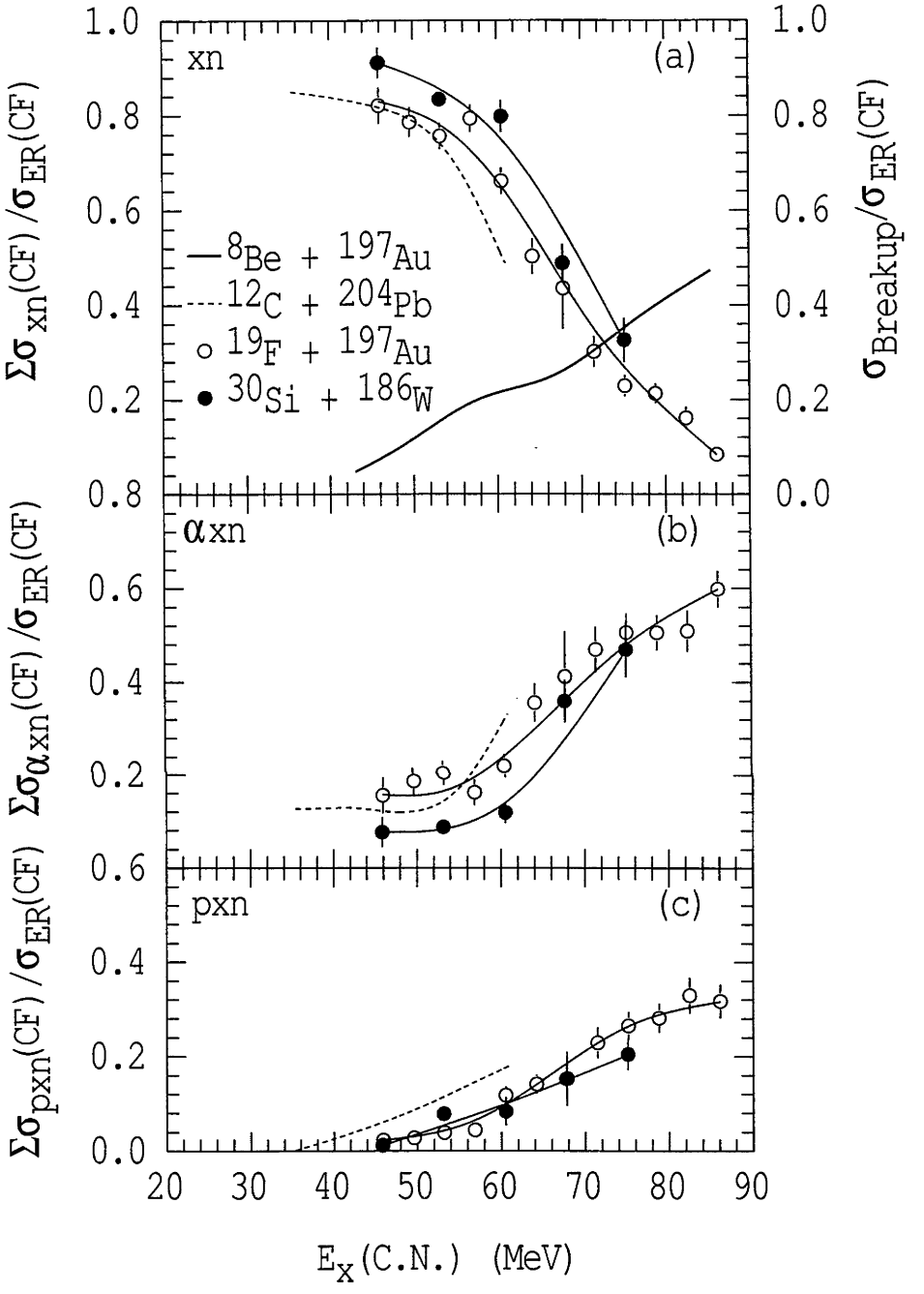

Figure 4.17: Scaled evaporation residue cross-sections taking into account ^{12}C projectile breakup: ^{12}C + ^{204}Pb (dashed line), ^{19}F + ^{197}Au and ^{30}Si + ^{186}W. The frames show the fraction of complete fusion (CF) ERs originating from (a) *xn* reaction, (b) *αxn* reactions and (c) *pxn* reactions. The ratio of breakup (^{8}Be + ^{197}Au) to complete fusion for the reaction ^{12}C + ^{197}Au [Verg93] is shown by the red line in frame (a).

$^{19}F + ^{197}Au$ and $^{30}Si + ^{186}W$ reaction data.

In addition to ^{12}C, breakup of ^{19}F has been noted in heavy-ion capture reactions [Rosn85, Park89, Terr89, Toma98, Luna99]. The extent of ^{19}F breakup is less than for ^{12}C. It can breakup into several channels, leading to α-particles, oxygen, nitrogen, carbon and boron fragments [Park89]. The observed difference in xn, αxn and pxn ER fraction between the two reactions $^{19}F + ^{197}Au$, and $^{30}Si + ^{186}W$ (Figure 4.16) is likely to be a reflection of ^{19}F breakup, and subsequent incomplete fusion of the fragments with the ^{197}Au target.

The effect of breakup on the angular momentum distribution for complete fusion is uncertain. It has been reported [Verg93, Chak00] that breakup reactions stemmed from high l collisions, which would compete principally with fission. The alternative view is that breakup reactions may occur over a larger range of l values and would therefore remove flux from both ER and fission decay. While the effect on angular momentum is of interest, its effect is expected to be small. A comprehensive debate on the subject is however outside the scope of this work.

To avoid problems that may be associated with projectile breakup, in this work emphasis has been placed on the xn ERs channels which can only be formed through complete fusion. Fission yields from compound nuclei formed in reactions with breakup fragments are expected to be negligible [Dasg99, Verg93]. This is due to the compound nuclei being formed with lower angular momentum and excitation energy, and having a higher fission barrier than in the corresponding complete fusion reactions. Our experimental fission data support this view (see Section 3.5.6).

4.2.2 Fission

Measurements of fission fragments, using the CUBE detector, provided data from which fission cross-sections, fission fragment anisotropies and fission mass-distributions were extracted. Measurements were made for all three reactions at beam energies which were in most cases identical to those for the ER measurements. Because of the difference in target thicknesses, the laboratory energies for the two types of measurements varied slightly. Great care was taken to obtain precise fission data, resulting in uncertainties which in most cases are less than $\pm 1\%$.

4.2.2.1 Fission Cross-Sections

Fission cross-sections were extracted from TSM fits to the fission differential cross-sections, in the same way as for the O + Pt reactions with K_0 as a free parameter. This was done initially with a single average angular momentum, and finally with a distribution of angular momenta obtained by fitting the capture cross-sections with coupled-channels calculations. Figure 4.18 shows the experimental

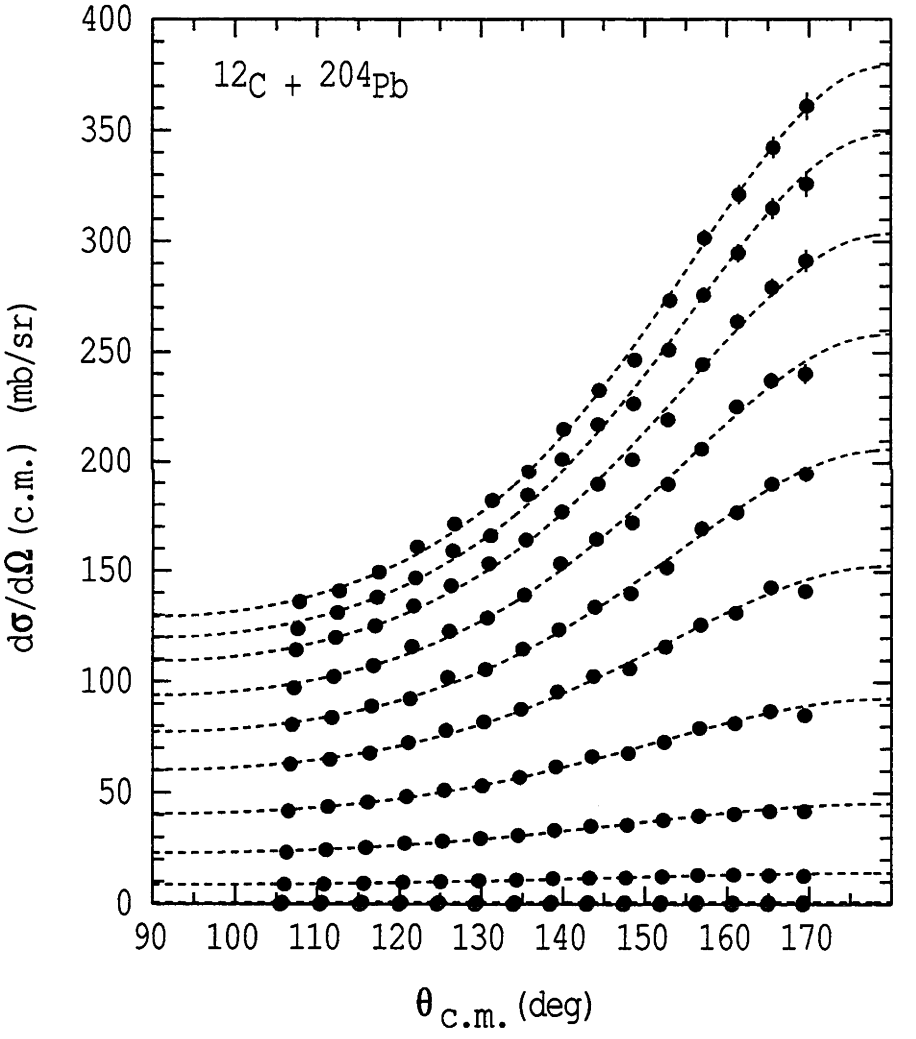

Figure 4.18: Fission differential cross-sections for the reaction $^{12}C + ^{204}Pb$ for eleven beam energies ranging from E_{lab} = 94.58 MeV, the top set of points, to E_{lab} = 55.96 and 59.82 MeV, overlapping at the bottom of the frame. Experimental uncertainties are typically smaller than the size of the points. The lines are TSM fits to the experimental data.

fission differential cross-sections for the ^{12}C + ^{204}Pb reaction. The fits using the calculated angular momentum distributions, shown by the dashed lines, reproduce well the experimental data. Similarly good fits to the fission differential cross-sections for the ^{19}F + ^{197}Au and ^{30}Si + ^{186}W reactions were obtained, allowing reliable determination of the anisotropies and cross-sections.

The final fission cross-sections are listed in Table 4.15. The fission cross-sections for the reaction ^{19}F + ^{197}Au from this work are shown in Figure 4.19, together with those from Ikezoe *et al.* [Ikez90]. The centre-of-mass energies of the Ikezoe points have been calculated taking into account energy losses in the target. The two sets of data are in good agreement at the higher energies, but disagree slightly as the energy decreases through the Coulomb barrier region.

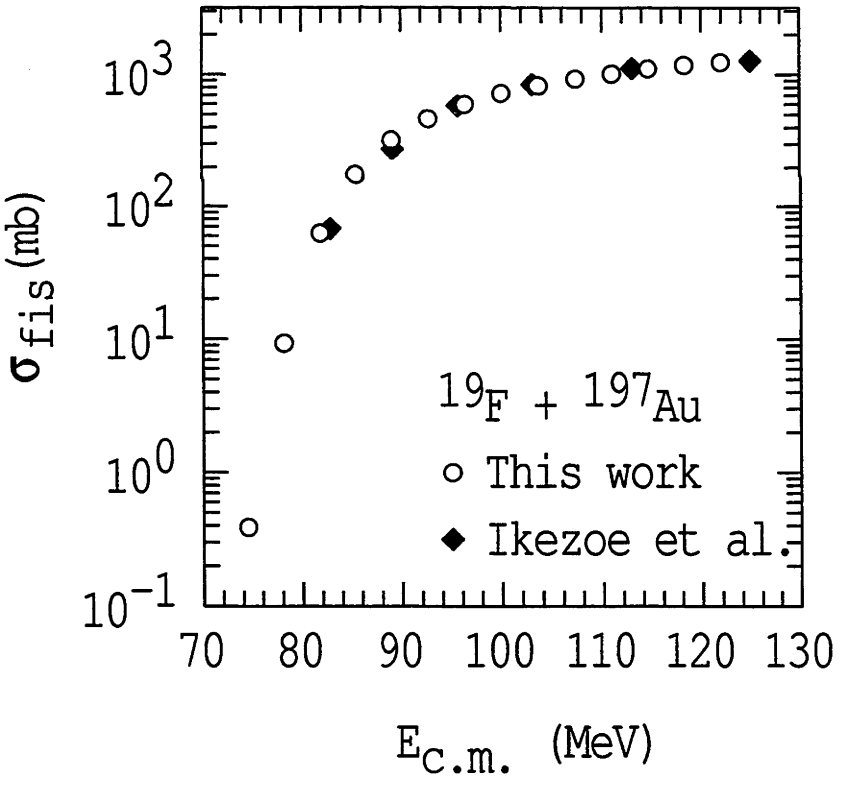

Figure 4.19: Fission cross-sections for the reaction ^{19}F + ^{197}Au as a function of centre-of-mass energy. Uncertainties are less than the size of the points.

$^{12}C + ^{204}Pb$

E_{lab}(MeV)	$E_{c.m.}$(MeV)	σ_{fis} (mb)
55.96	52.85	0.012 ± 0.001
59.82	56.50	5.01 ± 0.04
63.69	60.15	64.23 ± 0.32
67.55	63.80	180.6 ± 0.9
71.41	67.44	332.7 ± 1.7
75.31	71.13	509.3 ± 2.5
79.14	74.74	662.6 ± 3.3
83.00	78.39	810.4 ± 4.1
86.86	82.03	946.2 ± 4.7
90.72	85.68	1049 ± 5
94.58	89.33	1135 ± 6

$^{19}F + ^{197}Au$

E_{lab}(MeV)	$E_{c.m.}$(MeV)	σ_{fis} (mb)
81.66	74.48	0.388 ± 0.011
85.70	78.16	9.310 ± 0.067
89.67	81.78	62.67 ± 0.31
93.68	85.44	175.1 ± 0.9
97.68	89.09	318.2 ± 1.6
101.70	92.75	462.7 ± 2.3
105.69	96.39	593.8 ± 3.0
109.70	100.05	717.8 ± 3.6
113.70	103.70	820.8 ± 4.1
117.71	107.36	926.4 ± 4.6
121.71	111.00	1010 ± 5
125.72	114.66	1104 ± 6
129.72	118.31	1177 ± 6
133.73	121.97	1237 ± 6

$^{30}Si + ^{186}W$

E_{lab}(MeV)	$E_{c.m.}$(MeV)	σ_{fis} (mb)
126.56	108.98	0.59 ± 0.05
130.78	112.62	12.57 ± 0.11
135.21	116.43	54.16 ± 0.41
139.29	119.94	124.1 ± 0.8
143.51	123.58	222.4 ± 1.1
147.75	127.23	329.5 ± 1.6
152.00	130.89	434.4 ± 2.2
156.23	134.53	531.7 ± 2.7
160.47	138.18	615.8 ± 3.1
164.71	141.83	720.9 ± 3.6
168.94	145.48	802.2 ± 4.0
173.19	149.14	838.1 ± 4.2
177.47	152.82	917.3 ± 4.6

Table 4.15: Fission cross-sections for the reactions $^{12}C + ^{204}Pb$, $^{19}F + ^{197}Au$, and $^{30}Si + ^{186}W$.

4.2.2.2 Fission Fragment Anisotropies

Fission fragment anisotropies for the three reactions $^{12}C + ^{204}Pb$, $^{19}F + ^{197}Au$ and $^{30}Si + ^{186}W$ were extracted from the fission differential cross-sections over the range of centre-of-mass angles $110° \lesssim \theta_{c.m.} \lesssim 170°$, using the same TSM fits as were used to obtain the final fission cross-sections. The anisotropies for the three reactions are shown in Figure 4.20 as a function of excitation energy, and are listed in Table 4.16.

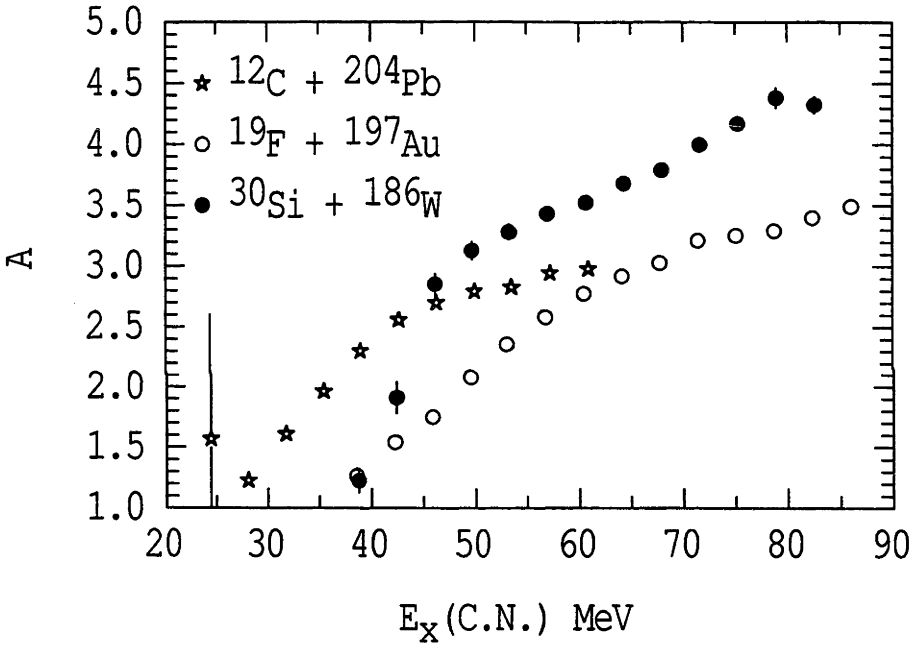

Figure 4.20: Fission fragment anisotropies for the three reactions $^{12}C + ^{204}Pb$, $^{19}F + ^{197}Au$ and $^{30}Si + ^{186}W$ as a function of excitation energy. Experimental uncertainties are typically smaller than the size of the points.

Fission anisotropies can prove to be a sensitive tool with which to measure the dynamics of the capture and fission processes. However, direct comparison of the anisotropies for the three reactions is not appropriate due to their dependence on both temperature and angular momentum. Therefore, the anisotropies are compared to TSM calculations in Section 4.2.5 using fission angular momentum and temperature distributions from SM calculations.

$^{12}C + ^{204}Pb$

$E_{c.m.}$ (MeV)	A
52.85	1.57 ± 1.04
56.48	1.23 ± 0.04
60.12	1.61 ± 0.02
63.79	1.96 ± 0.02
67.44	2.30 ± 0.02
71.13	2.56 ± 0.02
74.74	2.70 ± 0.03
78.39	2.79 ± 0.03
82.03	2.83 ± 0.03
85.68	2.95 ± 0.03
89.33	2.98 ± 0.03

$^{19}F + ^{197}Au$

$E_{c.m.}$ (MeV)	A
74.50	1.27 ± 0.07
78.16	1.54 ± 0.04
81.78	1.75 ± 0.02
85.44	2.08 ± 0.02
89.09	2.35 ± 0.03
92.75	2.58 ± 0.03
96.39	2.78 ± 0.03
100.05	2.92 ± 0.04
103.70	3.03 ± 0.03
107.36	3.21 ± 0.04
111.00	3.26 ± 0.04
114.66	3.29 ± 0.04
118.31	3.40 ± 0.04
121.97	3.49 ± 0.05

$^{30}Si + ^{186}W$

$E_{c.m.}$ (MeV)	A
108.98	1.23 ± 0.10
112.62	1.91 ± 0.13
116.43	2.85 ± 0.09
119.94	3.13 ± 0.08
123.58	3.28 ± 0.07
127.23	3.43 ± 0.05
130.89	3.53 ± 0.05
134.53	3.68 ± 0.05
138.18	3.79 ± 0.05
141.83	4.00 ± 0.06
145.48	4.17 ± 0.06
149.14	4.38 ± 0.09
152.82	4.33 ± 0.07

Table 4.16: Fission fragment anisotropies for the reactions $^{12}C + ^{204}Pb$, $^{19}F + ^{197}Au$, and $^{30}Si + ^{186}W$.

4.2.2.3 Fission Fragment Mass-Distributions

Fission mass-distributions have been extracted for the three reactions using the kinematic coincidence method [Hind96] and the deduced velocity vectors from the fission fragment coincident measurements (see Section 2.3.2). The variance of the normalised mass-distributions, for $\theta_{c.m.}$ cuts of $130° \lesssim \theta_{c.m.} \lesssim 165°$ for the ^{12}C, ^{19}F and ^{30}Si induced reaction, are shown as a function of excitation energy in Figure 4.21 and listed in Table 4.17. Also shown in Figure 4.21 are two points from previously

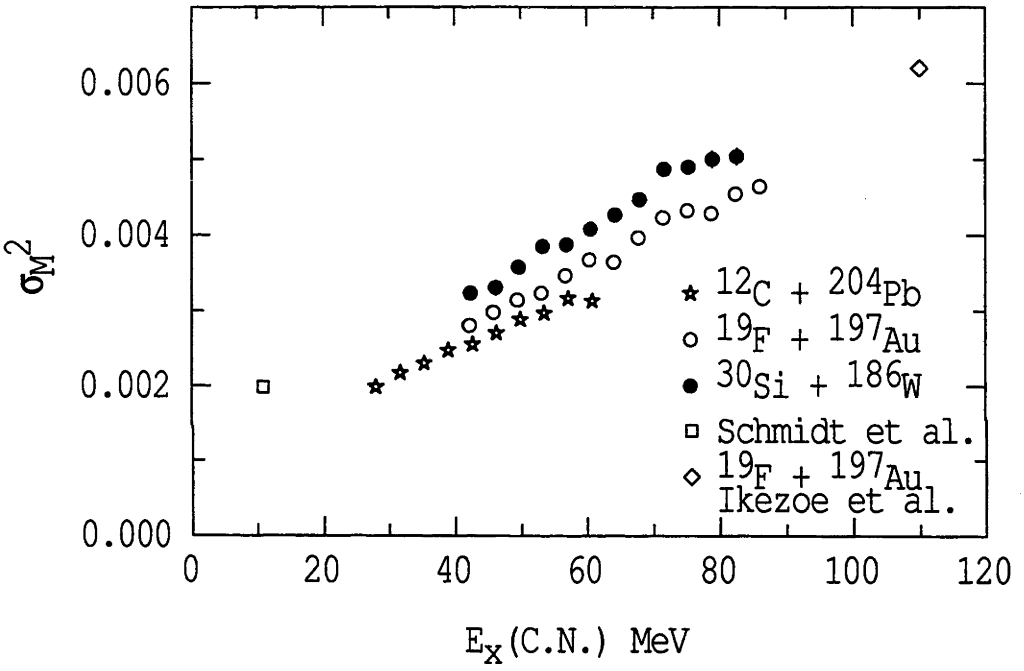

Figure 4.21: Fission fragment mass-distributions characterised by the mass-width, σ_M^2, as a function of excitation energy. See text for details. Experimental uncertainties are typically smaller than the size of the points.

published results. The highest energy point (open diamond) is from Ikezoe *et al.* [Ikez88], who measured fission from compound nuclei formed in the reaction ^{19}F + ^{197}Au, at E_{lab} = 160 MeV and $\theta_{c.m.}$ = 151°. The lowest energy point (open square) is from Schmidt *et al.* [Schm00] who measured the fission decay of ^{216}Ra at $E_x(C.N.) \approx 11$ MeV. The ^{216}Ra nuclei were produced by fragmentation of a ^{238}U beam. The mass-distribution in this case showed a component of mass-asymmetric fission which would increase the variance, and was not seen in the heavy-ion induced fission data.

$^{12}C + ^{204}Pb$

$E_{c.m.}$ (MeV)	σ_M^2
56.48	$1.984 \times 10^{-3} \pm 1.8 \times 10^{-5}$
60.12	$2.171 \times 10^{-3} \pm 1.6 \times 10^{-5}$
63.79	$2.296 \times 10^{-3} \pm 1.6 \times 10^{-5}$
67.44	$2.471 \times 10^{-3} \pm 2.2 \times 10^{-5}$
71.13	$2.551 \times 10^{-3} \pm 2.2 \times 10^{-5}$
74.74	$2.700 \times 10^{-3} \pm 2.2 \times 10^{-5}$
78.39	$2.878 \times 10^{-3} \pm 2.7 \times 10^{-5}$
82.03	$2.961 \times 10^{-3} \pm 2.7 \times 10^{-5}$
85.68	$3.156 \times 10^{-3} \pm 2.0 \times 10^{-5}$
89.33	$3.128 \times 10^{-3} \pm 2.0 \times 10^{-5}$

$^{19}F + ^{197}Au$

$E_{c.m.}$ (MeV)	σ_M^2
78.16	$2.801 \times 10^{-3} \pm 4.5 \times 10^{-5}$
81.78	$2.973 \times 10^{-3} \pm 1.8 \times 10^{-5}$
85.44	$3.133 \times 10^{-3} \pm 2.0 \times 10^{-5}$
89.09	$3.225 \times 10^{-3} \pm 2.0 \times 10^{-5}$
92.75	$3.460 \times 10^{-3} \pm 2.0 \times 10^{-5}$
96.39	$3.672 \times 10^{-3} \pm 2.0 \times 10^{-5}$
100.05	$3.641 \times 10^{-3} \pm 2.0 \times 10^{-5}$
103.70	$3.964 \times 10^{-3} \pm 2.2 \times 10^{-5}$
107.36	$4.230 \times 10^{-3} \pm 2.2 \times 10^{-5}$
111.00	$4.325 \times 10^{-3} \pm 2.2 \times 10^{-5}$
114.66	$4.286 \times 10^{-3} \pm 2.2 \times 10^{-5}$
118.31	$4.544 \times 10^{-3} \pm 2.2 \times 10^{-5}$
121.97	$4.643 \times 10^{-3} \pm 2.3 \times 10^{-5}$

$^{30}Si + ^{186}W$

$E_{c.m.}$ (MeV)	σ_M^2
112.62	$3.228 \times 10^{-3} \pm 9.5 \times 10^{-5}$
116.43	$3.302 \times 10^{-3} \pm 10.1 \times 10^{-5}$
119.94	$3.569 \times 10^{-3} \pm 9.3 \times 10^{-5}$
123.58	$3.842 \times 10^{-3} \pm 9.7 \times 10^{-5}$
127.23	$3.869 \times 10^{-3} \pm 8.1 \times 10^{-5}$
130.89	$4.078 \times 10^{-3} \pm 8.1 \times 10^{-5}$
134.53	$4.264 \times 10^{-3} \pm 8.3 \times 10^{-5}$
138.18	$4.471 \times 10^{-3} \pm 8.8 \times 10^{-5}$
141.83	$4.871 \times 10^{-3} \pm 9.5 \times 10^{-5}$
145.48	$4.900 \times 10^{-3} \pm 9.0 \times 10^{-5}$
149.14	$5.002 \times 10^{-3} \pm 11.5 \times 10^{-5}$
152.82	$5.038 \times 10^{-3} \pm 11.5 \times 10^{-5}$

Table 4.17: Fission fragment mass-distributions, characterised by the mass-width, σ_M^2, for the reactions $^{12}C + ^{204}Pb$, $^{19}F + ^{197}Au$, and $^{30}Si + ^{186}W$.

The results for the three reactions show a fission mass-split dependence on the entrance channel mass-asymmetry. The reaction with the highest projectile mass (^{30}Si), or lowest entrance channel mass-asymmetry, resulted in fission fragments with a wider average mass-split distribution than reactions with lighter projectiles.

This could in principle be attributed to different angular momenta introduced in the three reactions. This question is addressed in the next section.

4.2.3 Capture Reactions

The capture cross-sections and capture barrier distributions for the three reactions ^{12}C + ^{204}Pb, ^{19}F + ^{197}Au and ^{30}Si + ^{186}W have been determined from the summed cross-section data. They have been fitted with coupled-channels calculations. The resulting angular momentum distributions were used in SM/TSM calculations to model the capture and decay processes for these three reactions.

4.2.3.1 Capture Excitation Functions

The experimental capture cross-sections, σ, for each of the three reactions were determined by adding the ER and fission cross-sections at each energy. For the two reactions ^{12}C + ^{204}Pb (Table 4.18), and ^{19}F + ^{197}Au (Table 4.19), the energies at which the ER and fission data were measured, differed by only $\Delta E_{c.m.} \lesssim 50$ keV, and the ER and fission cross-sections were simply summed. The lowest energy ^{12}C + ^{204}Pb ER cross-section was extrapolated from the higher energy cross-sections, making use of the smooth trend of σ_{fis}/σ with energy. Capture cross-sections for the ^{30}Si + ^{186}W reaction (Table 4.20) are the sum of the fission cross-sections and interpolated ER cross-sections. The energy difference between the fission and ER data 160 keV $\leq \Delta E_{c.m.} \leq$ 370 keV was considered too large to just add the fission and ER data. The interpolated ER values come from a combination of ER data from both Runs A and B. Where repeat energies were measured, a weighted average for the two runs was used.

The capture cross-sections for the three reactions are shown in Figure 4.22 by the solid circles. The open squares represent the fission cross-sections, while the open diamonds show the ER cross-sections. For the ^{30}Si + ^{186}W reaction, the ER cross-sections are shown by the open diamonds for Run A and by the stars for Run

$E_{c.m.}$ (MeV)	σ_{fis} (mb)	σ_{ER} (mb)	σ (mb)
52.85	0.012 ± 0.001	0.076 ± 0.04 (*)	0.09 ± 0.04
56.48		22.9 ± 6.2	
56.50	5.01 ± 0.04		27.9 ± 6.2
60.12		149 ± 7	
60.15	64.23 ± 0.32		213 ± 7
63.77		200 ± 10	
63.80	180.6 ± 0.9		381 ± 10
67.42		232 ± 12	
67.44	332.7 ± 1.7		564 ± 12
71.07		270 ± 14	
71.13	509.3 ± 2.5		780 ± 14
74.72		239 ± 17	
74.74	662.6 ± 3.3		901 ± 17
78.37		231 ± 23	
78.39	810.4 ± 4.1		1042 ± 23
82.02		192 ± 21	
82.03	946.2 ± 4.7		1138 ± 22
85.66		164 ± 8	
85.68	1049 ± 5		1213 ± 10
89.31		212 ± 11	
89.33	1135 ± 6		1346 ± 12

Table 4.18: Fission, ER and capture cross-sections for the reaction ^{12}C + ^{204}Pb. (*) indicates extrapolated data.

$E_{c.m.}$ (MeV)	σ_{fis} (mb)	σ_{ER} (mb)	σ (mb)
74.48	0.388 ± 0.011		0.96 ± 0.23
74.53		0.57 ± 0.23	
78.16	9.310 ± 0.067		15.99 ± 0.92
78.20		6.68 ± 0.92	
81.78	62.67 ± 0.31		90.1 ± 2.3
81.84		27.4 ± 2.3	
85.44	175.1 ± 0.9		225.0 ± 3.8
85.53		49.9 ± 3.7	
89.09	318.2 ± 1.6		373.5 ± 3.9
89.14		55.3 ± 3.6	
92.75	462.7 ± 2.3		508.7 ± 4.0
92.80		46.0 ± 3.2	
96.39	593.8 ± 3.0		637.2 ± 3.9
96.45		43.5 ± 2.6	
100.05	717.8 ± 3.6		761.2 ± 4.9
100.11		43.4 ± 3.3	
103.70	820.8 ± 4.1		855.6 ± 7.6
103.75		34.9 ± 6.3	
107.36	926.4 ± 4.6		964.6 ± 5.8
107.40		38.2 ± 3.6	
111.00	1010 ± 5		1043 ± 6
111.06		32.9 ± 2.7	
114.66	1104 ± 6		1130 ± 6
114.71		25.4 ± 1.9	
118.31	1177 ± 6		1200 ± 6
118.36		23.5 ± 2.1	
121.97	1237 ± 6		1263 ± 7
122.01		25.6 ± 2.2	

Table 4.19: Fission, ER and capture cross-sections for the reaction $^{19}F + ^{197}Au$.

$E_{c.m.}$ (MeV)	σ_{fis} (mb)	σ_{ER} (mb)	Run	σ_{ER} Interpolated (mb)	σ (mb)
108.75		0.21 ± 0.07	B		
108.98	0.59 ± 0.05			0.45 ± 0.20	1.04 ± 0.21
112.42		6.25 ± 0.87	A		
112.62	12.57 ± 0.11			6.50 ± 0.87	19.07 ± 0.88
116.06		11.2 ± 0.8	w.a.		
116.43	54.16 ± 0.41			12.4 ± 0.8	66.60 ± 0.93
119.72		22.3 ± 2.7	A		
119.94	124.1 ± 0.8			22.5 ± 3.4	146.6 ± 3.5
123.37		19.6 ± 0.9	w.a.		
123.58	222.4 ± 1.1			19.4 ± 0.9	241.8 ± 1.5
127.03		19.0 ± 2.3	A		
127.23	329.5 ± 1.6			19.0 ± 4.8	348.5 ± 5.0
130.73		15.4 ± 1.0	w.a.		
130.89	434.4 ± 2.2			15.3 ± 1.4	449.7 ± 2.6
134.33		12.8 ± 1.8	A		
134.53	531.7 ± 2.7			12.8 ± 3.0	544.5 ± 4.0
137.98		12.8 ± 0.9	w.a.		
138.18	615.8 ± 3.1			12.7 ± 1.4	628.5 ± 3.4
141.64		12.0 ± 1.3	A		
141.83	720.9 ± 3.6			12.0 ± 2.5	732.9 ± 4.4
145.29		9.8 ± 0.9	w.a.		
145.48	802.2 ± 4.0			9.8 ± 1.4	811.9 ± 4.2
148.92		10.4 ± 1.1	A		
149.14	838.1 ± 4.2			10.4 ± 2.5	848.5 ± 4.9
152.60		8.9 ± 1.2	A		
152.82	917.3 ± 4.6			8.9 ± 2.5	926.2 ± 5.2

Table 4.20: Fission, ER and capture cross-sections for the reaction ^{30}Si + ^{186}W. (w.a. denotes the weighted average of the total ER cross-sections from runs A and B

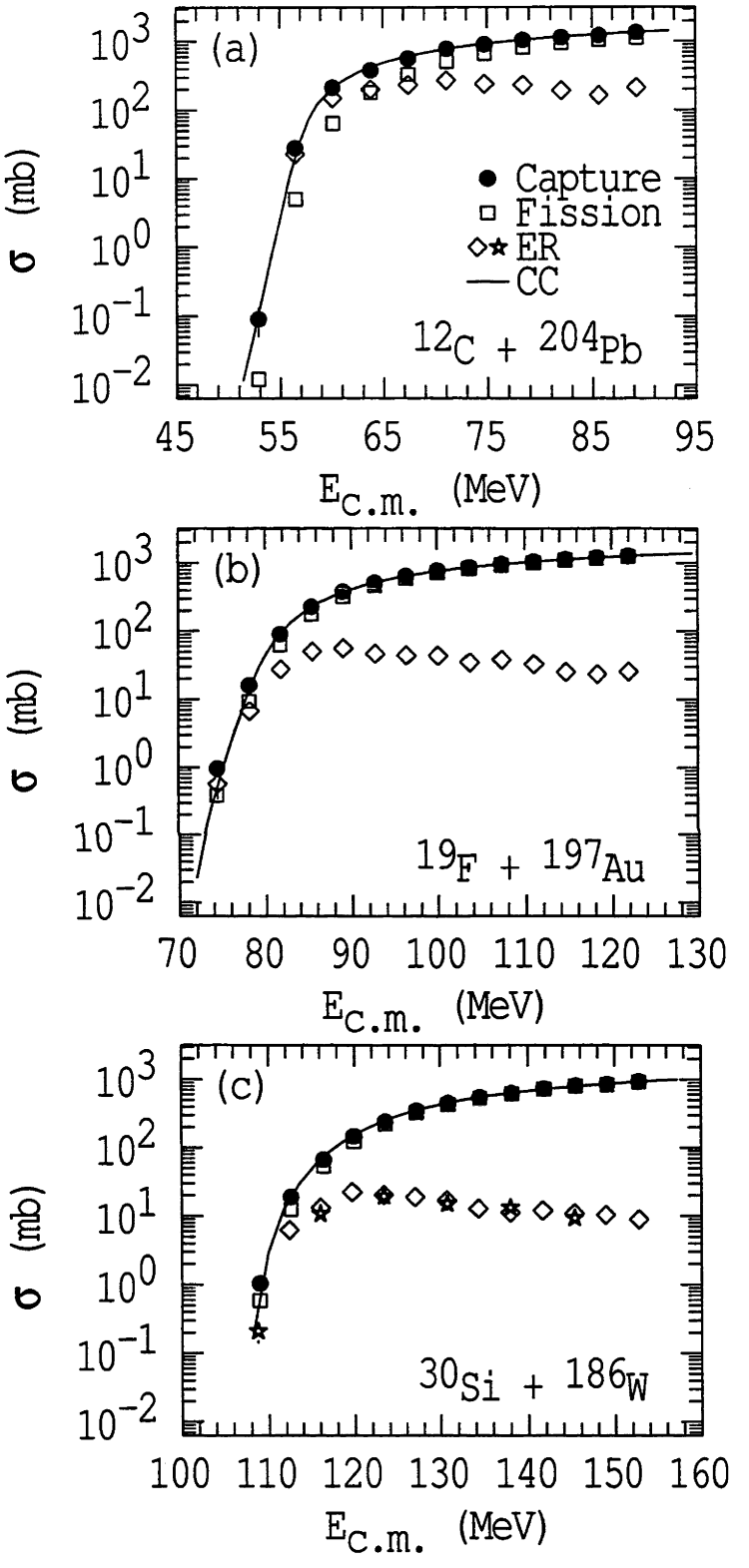

Figure 4.22: Cross-sections as a function of centre-of-mass energy. Experimental uncertainties are typically smaller than the size of the points. The lines are coupled-channels calculations.

B. The lines are the coupled-channels calculated capture cross-sections as described in Section 4.2.3.3.

It can be seen that as the beam energy increases there is an exponential rise in the fission probabilities. This results from the projectile bringing in higher angular momentum and the fission barrier height falling as l^2. Statistical decay simulations show that the fission probability exceeds 98% at $l = 30$, and ER survival is restricted to low angular momentum values.

4.2.3.2 Capture Barrier Distribution

The experimental capture barrier distributions, defined as $d^2(E\sigma)/dE^2$ (see Section 2.1.4), were calculated using equation 2.26, with uncertainties calculated using equation 2.27. Since the experimental data were taken at intervals of $\Delta E_{c.m.} \approx 3.7$ MeV, this value was used as the energy step ΔE in these equations. To gain fine detail in the capture barrier distributions, experiments are often taken with smaller energy steps of approximately $E_{c.m.} = 1$ to 2 MeV [Dasg98]. Because the energy step in this work was relatively large in comparison, the capture barrier distributions are smoothed and only gross features are distinguishable.

4.2.3.3 Coupled-Channels Calculations

The experimental capture excitation functions and capture barrier distributions for the three reactions were fitted with coupled-channels calculations, in order to obtain angular momentum distributions. The first stage in fitting the data was to match the capture cross-sections at energies above the Coulomb barrier region with the one-dimensional barrier penetration model. This was done using a bare potential with a Woods-Saxon form of the nuclear potential with potential depth, V_0, surface diffuseness parameter, a_0, and nuclear radius parameter, r_N (as described in Section 4.1.2), consistent with many other reactions. The parameters used in the bare potential are shown for each reaction in Table 4.21. For the two reactions ^{12}C + ^{204}Pb and ^{19}F + ^{197}Au the potential depths were fixed according to the relation $V_0 = V_{Coulomb}(r = 0) - Q_{GS}$. However, for the reaction ^{30}Si + ^{186}W in order for both the coupled-channels codes CCFULL and CCMPH to operate correctly, a greater potential depth was required. The other parameters a_0 and r_N were then varied to achieve the best fits (the lowest χ^2 values) to the capture cross-sections above the

	$^{12}C + ^{204}Pb$	$^{19}F + ^{197}Au$			$^{30}Si + ^{186}W$	
Bare Potential						
V_0 (MeV)	79.91	114.89			290.00	
a_0 (fm)	0.921	1.038			1.240	
r_N (fm)	1.092	1.043			0.880	
Target Static Deformation						
β_2	-	-			0.28	
β_4	-	-			-0.061	
Target Vib. Couplings						
No. Phonons	1	1			1	
β_2	0.0410	0.11			-	
E_{β_2} (MeV)	0.899	0.400			-	
β_3	0.100	0.125			0.081	
E_{β_3} (MeV)	2.6180	1.433			1.045	
Projectile Vib. Couplings						
No. Phonons	-	1	2		1	2
β_2	-	0.4	0.5657		0.316	0.447
E_{β_2} (MeV)	-	0.8785	1.7570		2.235	4.470
Transfer Couplings						
Q_t (MeV)	-	7.470	5.0	3.0	-	
S_t	-	0.4	0.4	0.2	-	

Table 4.21: Parameters used in coupled-channels calculations for the three reactions leading to ^{216}Ra. Shown are the bare potential parameters utilised in the Woods-Saxon form of the nuclear potential (potential depth, V_0, surface diffuseness parameter, a_0, and nuclear radius parameter, r_N); quadrupole, β_2, and hexadecapole, β_4 static target deformations [Rama87, NDS]; vibrational coupling strengths, β_2 and β_3, and energies, E_{β_2} and E_{β_3}, of respectively quadrupole and octupole state couplings in the targets and projectiles [Rama87, NDS, Spea89]; and transfer reaction Q-values, Q_t, and coupling strengths, S_t.

Coulomb barrier region.

It proved possible to reproduce simultaneously the experimental capture cross-sections and capture barrier distributions with coupled-channels calculations performed using the code CCMPH, with coupling parameters from known properties of collective modes in each nucleus, as outlined in Table 4.21.

For the reaction $^{12}C + ^{204}Pb$ the calculations included quadrupole and octupole vibrational couplings in the ^{204}Pb target. No projectile vibrational couplings were included in the calculations, as the CCPMH code was unable to handle properly the high energy first excited states of ^{12}C nucleus. However, it has been shown [Taki94, Hagi97] that couplings to states with high excitation energy only leads to potential renormalisation (i.e. a shift in energy of the barrier distribution) without affecting the shape of the barrier distribution. The effect of these excitations are therefore already included in the bare potential, which is obtained by a fit to the high energy cross-sections. No transfer couplings were included due to a lack of significant positive Q-value transfer reactions.

The calculations for the reactions $^{19}F + ^{197}Au$ included vibrational couplings for both the target and projectile. The maximum Q_t transfer coupling for the $^{19}F + ^{197}Au$ reaction corresponds to one proton transfer from the projectile to the target. The other transfer couplings represent qualitatively transfer to excited states. The couplings used should not be taken to indicate that these are the precise channels which affect the capture process, but rather they are realistic simulations of the real situation.

For the reaction $^{30}Si + ^{186}W$, the projectile and target can both be considered deformed, but only the target is a good rotor. To handle this complex situation, calculations were performed using the exact coupled-channels code CCFULL [Hagi97, Hagi99]. This code is able to perform realistic calculations including rotational states in both the target and projectile. The resulting capture cross-sections, capture barrier distributions and angular momentum distributions from CCFULL were very similar to those using the CCMPH code and the couplings in Table 4.21. Given that the results were similar, and that the determination of the exact coupling are not within the scope of this work, the CCMPH results were used to provide model consistency across the three reactions. When using the CCMPH code, the ^{186}W target was treated as a classically deformed nucleus. While octupole vibra-

tional coupling were included for the target, they only produce a slight difference in the calculated quantities. No single- or two-particle positive Q-value transfer reactions are present, so no transfer couplings were included in the calculations.

The CCMPH calculated capture excitation functions and capture barrier distribution in the barrier region are shown in Figure 4.23. For the capture barrier distributions, an energy step of $\Delta E = 3.7$ MeV was used to correspond with the experimental energy step. Good agreement was achieved between the experimental results and the coupled-channels calculations, with the experimental capture cross-sections for the three reactions being typically reproduced by the calculations to within 2%.

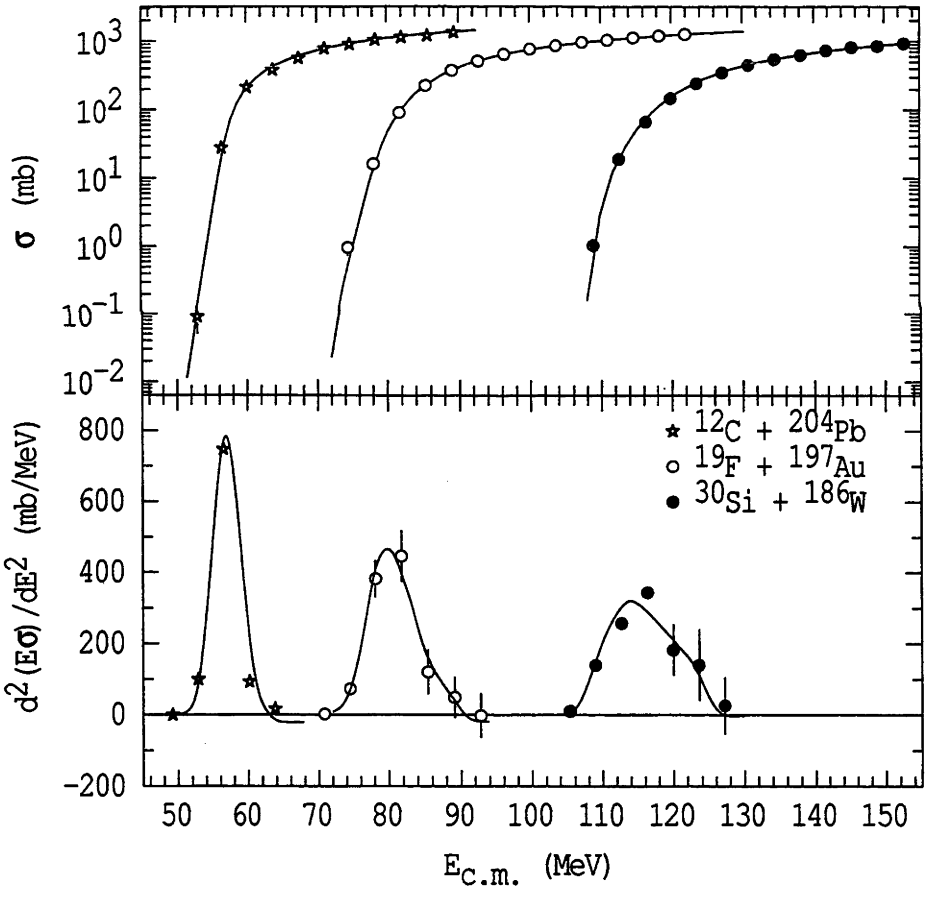

Figure 4.23: (a) Capture excitation functions, and (b) capture barrier distributions, as a function of centre-of-mass energy. The points represent experimental results with uncertainties typically smaller than the size of the points, and the lines are coupled-channels calculations using the parameters in Table 4.21

4.2.3.4 Angular Momentum Distributions

From the coupled-channels calculations, capture angular momentum distributions were obtained. The calculated capture mean squared angular momenta are shown in Figure 4.24 as a function of excitation energy, for the three reactions.

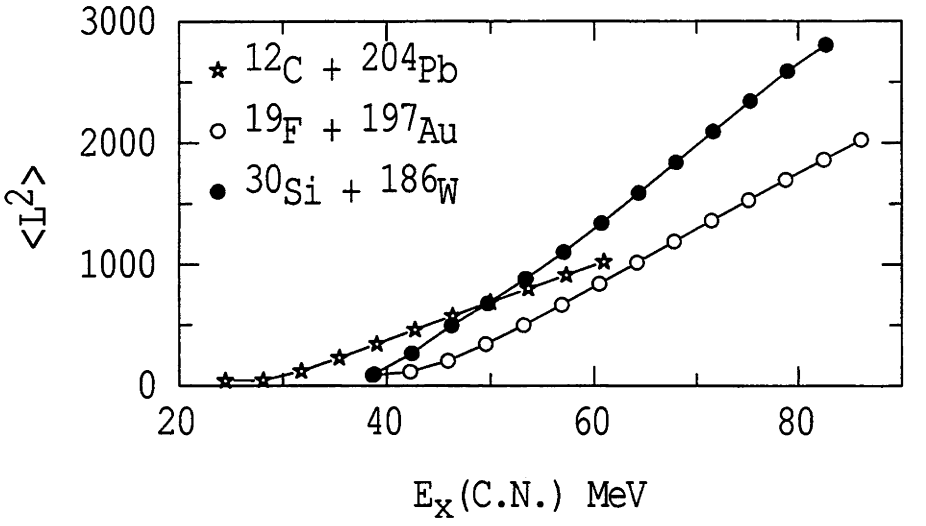

Figure 4.24: Calculated capture mean squared angular momenta for the three reactions as a function of excitation energy. Experimental uncertainties are typically smaller than the size of the points. The lines guide the eye.

The $\langle l^2 \rangle$ of compound nuclei formed in the ^{12}C induced reaction approaches that for the ^{19}F reaction at the highest energy. At an excitation energy of $E_x(C.N.) \approx 50$ MeV the $\langle l^2 \rangle$ for the two reactions ^{12}C + ^{204}Pb and ^{30}Si + ^{186}W are the same. Qualitatively this must occur, as the heavier projectiles have a higher threshold excitation energy for capture, but carry more angular momentum than ^{12}C. If the decay of the compound nucleus is independent of entrance channel, it is expected that the observed decay of the compound nuclei from the ^{12}C and ^{30}Si induced reactions, at $E_x(C.N.) \approx 50$ MeV, should also be the same. However, the variance of the fission mass-distributions for the three reactions (Figure 4.21) do not match at any energy, but rather show a systematic dependence on projectile mass, as well as the expected increase with excitation energy.

4.2.4 Reduced Evaporation Residue Cross-Sections

Using the partial wave representation of capture (equation 2.6), the reduced cross-sections (equation 2.7) can be compared for the three reactions in a way that does not rely on the capture angular momentum distributions being similar. The experimental reduced ER cross-sections, $\overline{\sigma}_{ER}$, were derived using;

$$\overline{\sigma}_{ER} = \frac{2\mu E}{\pi\hbar^2}\sigma_{ER} \tag{4.2}$$

The xn ER cross-sections, $\overline{\sigma}_{xn}$, were similarly derived.

If the limiting particle evaporation angular momentum, l_{lim}^{ER}, is the same for all three reactions, then the reduced cross-sections $\overline{\sigma}_{ER}$ should saturate at the same values. Similarly, the xn ER reduced cross-sections $\overline{\sigma}_{xn}$, should also be independent of entrance channel.

When the experimental reduced cross-sections are compared (Figure 4.25), they saturate as expected for all the reactions. However the reduced cross-sections for

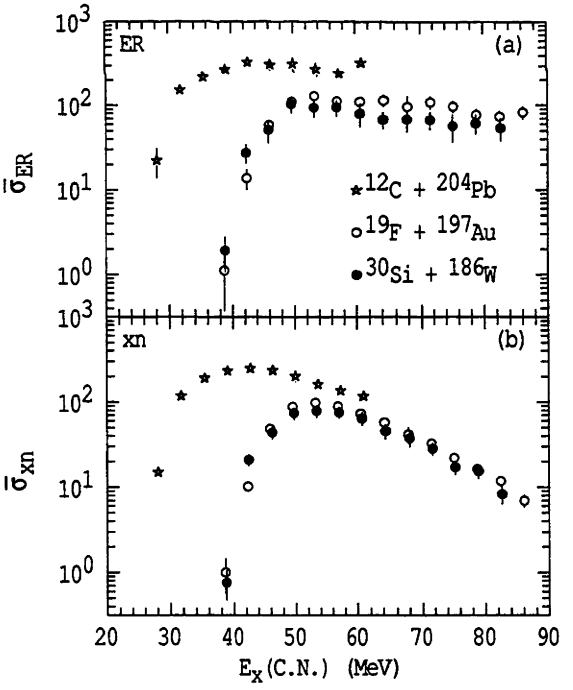

Figure 4.25: Reduced cross-sections as a function of excitation energy, for (a) total ERs and (b) sum of xn ERs. The points for the reaction $^{30}Si + ^{186}W$ are the weighted average of Runs A and B. Uncertainties are in several cases smaller than the size of the points.

the $^{12}C + ^{204}Pb$ reaction are larger than those for the $^{19}F + ^{197}Au$ reaction, which in turn are larger than those for the $^{30}Si + ^{186}W$ reaction. This is the case for both the reduced ER and xn ER cross-sections.

This discrepancy in reduced cross-sections cannot be attributed to the breakup of ^{12}C in the $^{12}C + ^{204}Pb$ reaction. As outlined in section 4.2.1.3, only up to 20% of the measured ER cross-section for the $^{12}C + ^{204}Pb$ reaction may originate from the breakup reaction $^{8}Be + ^{204}Pb$, while the reduced ER cross-sections (Figure 4.25(a)), vary between the three reactions by up to 300%. In addition, any breakup would result in a smaller xn cross-sections for the $^{12}C + ^{204}Pb$ reaction, not a larger σ_{xn}, as reflected in the reduced xn cross-sections (Figure 4.25(b)).

The differences in the reduced ER cross-sections are explored in the next section.

4.2.5 Statistical Model and Transition State Model Calculations

To model the decay of the ^{216}Ra compound nucleus, the SM was used in conjunction with the TSM, using the same procedure as was used for the O + Pt reactions. The calculations were compared to measured decay from the three reactions $^{12}C + ^{204}Pb$, $^{19}F + ^{197}Au$ and $^{30}Si + ^{186}W$. As some charged particle ERs may be attributable to incomplete fusion with projectile breakup fragments, the fission to xn ER cross-section ratios were used as a more sensitive tool than the fission probabilities when comparing the calculations with the data.

Figure 4.26 shows experimental results (points) together with SM/TSM calculations (lines). Frames (a), (b) and (c) in Figure 4.26 show the ratio of the fission to xn ER cross-sections individually for the three reactions, while frames (d), (e) and (f) show the fission fragment anisotropies, A. The final two frames, (g) and (h), show the reduced ER and xn ER cross-sections. Although the reduced ER and xn ER cross-sections are presented here, the model calculations were also compared to the measured ER and xn ER cross-sections. Either comparison gave the same quantitative results.

The fission/xn ratios and anisotropies for the three reactions cannot be directly compared, but the reduced cross-sections can be. They show a reduction in $\overline{\sigma}_{ER}$ and $\overline{\sigma}_{xn}$ with increasing projectile mass. This occurs even for the same excitation energy, and in the case of the reactions $^{12}C + ^{204}Pb$ and $^{30}Si + ^{186}W$, the same $\langle l \rangle^2$ at $E_x(C.N.) \approx 50$ MeV. Indeed the $\overline{\sigma}_{xn}$ show a strong dependence on projectile

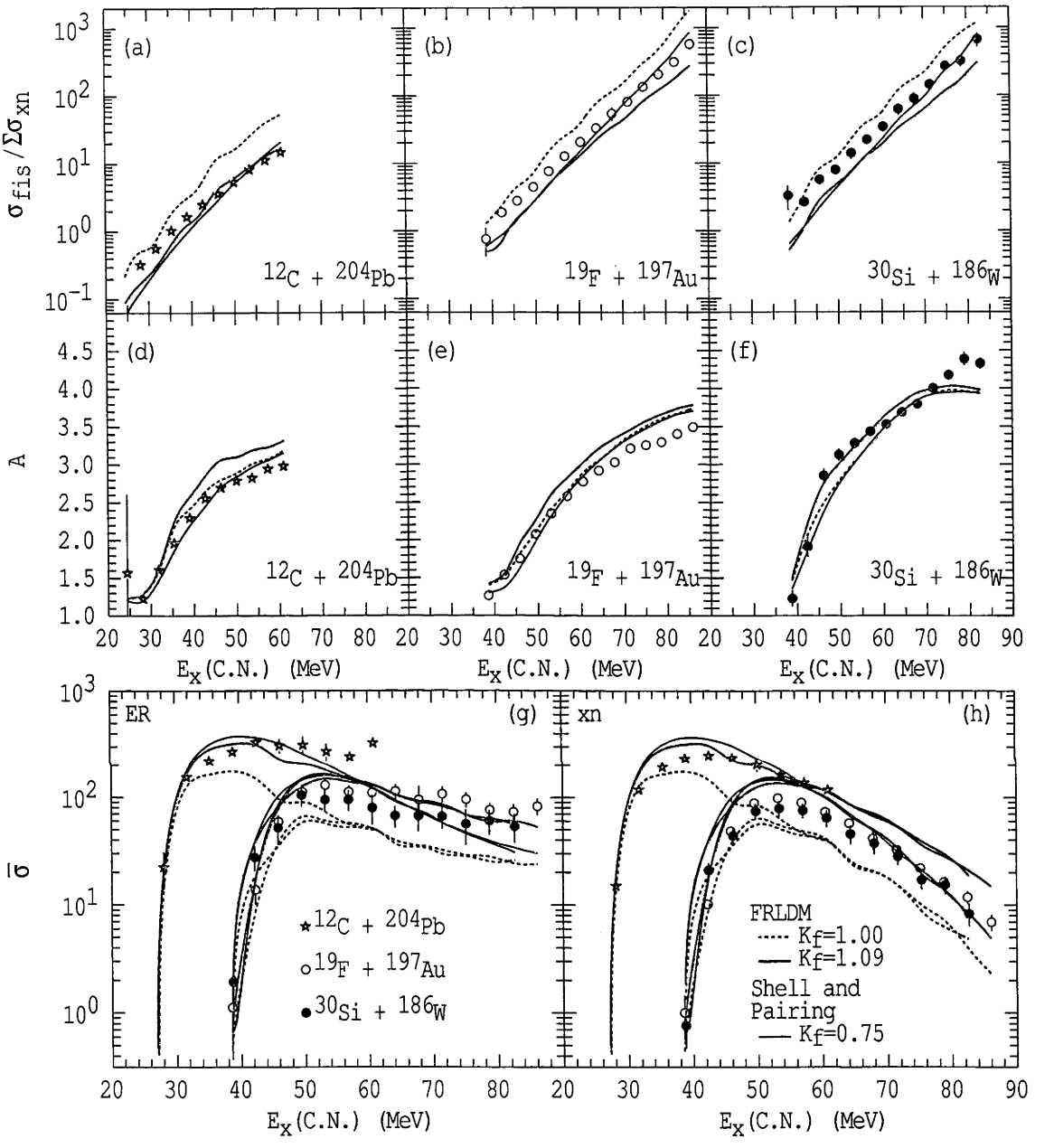

Figure 4.26: Model calculations in comparison to experimental results as a function of excitation energy. (a), (b) and (c) fission to xn ER cross-section ratios, (d), (e) and (f) fission fragment anisotropies, (g) reduced ER cross-sections, and (h) reduced xn ER cross-sections. SM/TSM calculations are shown for three model inputs. The green dashed and solid lines correspond to the SM-FRLDM option with fission barrier scaling factors of $k_f = 1.00$ and $k_f = 1.09$ respectively. The red lines correspond to the SM-SP option with $k_f = 0.75$. Experimental uncertainties are typically smaller than the size of the points.

mass, with those for ^{19}F and ^{30}Si induced reactions being respectively 0.64 ± 0.09 and 0.57 ± 0.08 of those for ^{12}C induced reaction at the two highest energies. No similar entrance channel dependence is observed in the SM calculation (lines in frames 4.26(g) and 4.26(h)).

Statistical model calculations were performed using the JO_SHELL code, utilising capture l-distributions from the coupled-channels calculations. As the three reactions form the same compound nucleus, common sets of inputs were used in the SM calculations. For all calculations the level density parameters for the equilibrium and the saddle-point deformations were taken from Tōke and Swiatecki [Tōke81], the fission transient delay time was set to $\tau_f = 20 \times 10^{-21}$ sec, and the Kramers factor was set at $K_r = 1$.

The three calculations in Figure 4.26 use level densities based on the excitation energy above either the FRLDM ground-state (SM-FRLDM option) with fission barrier scaling factors of $k_f = 1.00$ (green dashed lines) or $k_f = 1.09$ (green solid lines), or using shell and pairing enhancements (SM-SP option) and $k_f = 0.75$ (red lines). The parameters for the solid green and red lines were chosen to provide the best fits to the ^{12}C + ^{204}Pb fission to xn ER cross-section ratios. The calculations with $k_f = 1.00$ (green dashed lines) are shown for comparison. Because of the observed entrance channel dependence in the experimental reduced cross-sections, the model calculations were chosen to best fit the decay from the ^{12}C + ^{204}Pb reaction, as any unusual features are expected to be at a minimum for this reaction.

Evaluated first is a comparison of model calculations to the measured decay from compound nuclei formed in the ^{12}C + ^{204}Pb reaction. In addition to producing a good fit to the ^{12}C + ^{204}Pb fission to xn ER cross-section ratios (frame 4.26(a)), the calculations with the SM-FRLDM option and $k_f = 1.09$ gave good descriptions of the reduced xn ER cross-sections (frame 4.26(g)) and reduced xn ER cross-sections (frame 4.26(h)). The calculations using the SM-SP option and $k_f = 0.75$ gave a equally good fit to the ^{12}C + ^{204}Pb fission/xn cross-section ratios but a better reproductions of the ^{12}C + ^{204}Pb anisotropies (frames 4.26(d)).

A feature of all the SM calculations is that although a reasonable agreement can be achieved between the ^{12}C + ^{204}Pb calculated and experimental fission/xn cross-section ratios (solid green and red lines in frame 4.26(a)), the calculations fail to fit the slope of the data as a function of energy, instead increasing at a greater

rate than for the data. This is a common feature for all the calculations both for these three reactions and for the O + Pt reactions. It is discussed further in the last chapter.

Looking at the fission to xn ER cross-sections (Figure 4.26(a), (b) and (c)) the three model calculations give a consistent picture across the three reactions. With increasing projectile mass, there is a strengthening in the experimental fission competition when compared to the calculations with a given set of parameters.

Similarly a comparison of experimental and TSM calculated anisotropies, (Figure 4.26(d), (e) and (f)) show the calculations mostly overestimated the experimental anisotropies for the $^{12}C + ^{204}Pb$ reaction, while mostly underestimating the data from the $^{30}Si + ^{186}W$ reaction.

To check the model calculations, the angular momentum dependent variables used in the SM code were examined closely. Figure 4.27 shows variables at an excitation energy of $E_x(C.N.) \approx 57$ MeV, which is above the average Coulomb barrier energy for all of these reactions. Frame 4.27(a) shows the capture probabilities as calculated by the coupled-channels code, and used as an input to the SM code. The fission probabilities from the SM code approach unity for $l \gtrsim 30$, as shown in frame 4.27(b). The oscillations are the results of statistical fluctuations, even though 90,000 cascades were used in this case. The last frame shows the ER reduced cross-sections for each l-value.

The calculated l dependent variables in Figure 4.27, and the calculated quantities in Figure 4.26, indicate no unexpected reaction-dependent feature that would explain the observed differences between the model calculation and the experimental data. The difference in $\overline{\sigma}_{ER}$ and $\overline{\sigma}_{xn}$ in Figure 4.26 cannot be explained by low $\mathcal{T}_l(E)$, as the measured capture cross-sections for all three reaction can only be reproduced with $\mathcal{T}_l(E)$ values close to unity at low l. The $\overline{\sigma}_{ER}(l)$ (frame 4.27(c)) demonstrates that the calculated limiting angular momentum, l_{lim}^{ER}, leads to the same level of saturation of SM ER cross-sections. The fission probabilities (frame 4.27(b)) also reflect this l_{lim}^{ER}.

The observed trends in the experimental results from the three reactions cannot be explained using just the SM and TSM calculations. However, a consistent picture has emerged from this comparison as to the entrance channel effects of capture-fission and fusion-ER reactions.

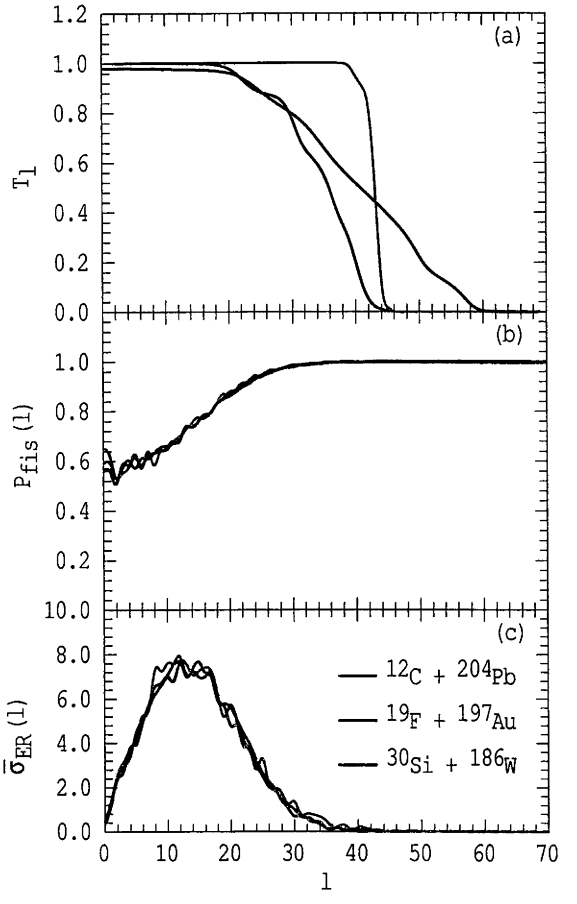

Figure 4.27: Angular momentum dependent variables for $E_x(C.N.) \approx 57$ MeV. (a) experimental capture probabilities derived from the coupled-channels calculations (b) SM fission probabilities, and (c) SM ER reduced cross-sections. Frames (b) and (c) used SM calculations with the SM-FRLDM option and $k_f = 1.09$.

4.2.6 Entrance Channel Effects on Capture-Decay Dynamics

From the experimental data and model calculations several features are observed.

There is evidence of breakup of the ^{12}C projectile in the $^{12}C + ^{204}Pb$ reaction. The experimental ER channel ratios for the three reactions show a relatively larger αxn component for this reactions than for the other two reactions at the same excitation energies. However the presence of ^{12}C breakup alone does not explain the observed entrance channel effects on the capture-decay dynamics

The fission mass-distributions from the experimental data show a consistently wider mass-split with increasing projectile mass (smaller mass-asymmetry), and do

not match even at the same $E_x(C.N.)$ and $\langle l^2 \rangle$.

The reduced cross-sections for all ER, and xn ER, from the experimental data show a decrease in ER formation with increasing projectile mass. This was not reproduced by the SM calculations, which gave ER and xn ER reduced cross-sections which saturate at the same level for all three reaction, as would be expected.

The SM fission to ER ratios for the $^{30}Si + ^{186}W$ and $^{19}F + ^{197}Au$ reactions were consistently below the data, whilst the calculations for the $^{12}C + ^{204}Pb$ reaction agree with the data. Using the SM calculations as a benchmark, the fission probabilities from the experimental data are progressively higher with increasing projectile mass.

The TSM anisotropies consistently underestimated the data for the $^{30}Si + ^{186}W$ reaction in comparison to the other reactions. Again, using the SM calculations as a benchmark, the anisotropies from the experimental data are progressively higher with increasing projectile mass.

These observations lead to the conclusion that there is a mass-asymmetry (ie projectile mass) dependence of the decay of ^{216}Ra formed in the reactions $^{12}C + ^{204}Pb$, $^{19}F + ^{197}Au$ and $^{30}Si + ^{186}W$. Why this may occur is discussed in the next chapter.

CHAPTER 5

Entrance Channel Effects in the Decay of Compound Nuclei

In the previous chapter experimental results and model calculations were presented that showed that the decay of the ^{216}Ra compound nucleus, formed in the three reactions ^{12}C + ^{204}Pb, ^{19}F + ^{197}Au and ^{30}Si + ^{186}W, was entrance channel dependent. This chapter discusses the significance of these results and interpretation of the physics involved. The threshold for entrance channel effects on heavy-ion capture-fission reactions is investigated, together with its implications for other reactions.

The model independent quantities of the fission fragment mass-distributions and reduced ER cross-sections both showed a clear correlation with entrance channel. With increasing projectile mass, but the same excitation energy, the fission mass-distributions become wider, and the reduced ER cross-sections decrease. Correspondingly, in comparisons with SM/TSM calculations, for increasing projectile mass, the ER cross-sections decrease, while both the fission probabilities and the fission fragment anisotropies increase.

While the differences in decay can be linked to the different projectile and target combination, the question arises as to what is the difference in the dynamics of these reactions that leads to the differences in their decay. During the capture process, properties of the nuclei, such as deformation and surface vibrations have a dramatic role to play. These properties and their effect on the capture barrier and angular momentum distributions have been extensively studied [Dasg98], and coupled-channels models are now able to reproduce precisely (1%) capture cross-sections for a wide range of reactions [Hagi99]. It is therefore concluded that it is not

the capture process which is leading to the differences between the three reactions, but the subsequent evolution of the compound nuclei.

Consider the difference in orbital angular momenta, $l\hbar$, imparted by the different reactions. While the fission properties and the model calculations are strongly influenced by the angular momentum distribution, the survival of the nucleus against fission is much less sensitive to this quantity. The orbital angular momentum of the compound nucleus, $l\hbar$, differs only slightly from the orbital angular momentum, $J\hbar$, of the ER or fissioning system. The difference is the angular momentum lost or gained with the evaporation of light particles, and typically is one or two units of $\hbar$.

Using the partial wave representation,

$$\sigma_{ER}(E) = \frac{\pi\hbar^2}{2\mu E}\sum_{l=0}^{\infty}(2l+1)\mathcal{T}_l(E)(1-P_{fis}(E,l)) \tag{5.1}$$

once the capture probabilities, $\mathcal{T}_l(E)$, all become unity for low angular momenta below the limiting angular momentum for ER formation, l_{lim}^{ER}, where $P_{fis}(E,l) \sim 1$, the number of partial waves leading to survival ceases to increase. The result is that the ER cross-sections, $\sigma_{ER}(E)$, are insensitive to the angular momentum distribution above a critical energy (being that which produces angular momentum distributions with $\mathcal{T}_l(E) = 1$ for $l \leq l_{lim}^{ER}$). Although the coupled-channels model calculations performed here for these reactions at the higher energies predict $\mathcal{T}_l(E) \approx 1$ at low angular momentum ($l_{lim}^{ER} \lesssim 30$), all other such models also predict that at beam energies sufficiently high above the Coulomb barrier $\mathcal{T}_l(E) \approx 1$ for all l which lead to ERs. The difference in reduced ER and xn ER cross-sections cannot therefore be explained in terms of different angular momentum distributions for the three reactions. Rather, the same angular momenta are leading to different ER yields for the different reactions.

The fall in the reduced ER cross-sections with increasing projectile mass indicates that not all partial waves are contributing equally to ER formation for the three reactions. Possibilities are that the limiting angular momentum, l_{lim}^{ER}, is decreasing with increasing projectile mass, or the fission probability $P_{fis}(E,l)$ is increased at lower l values, or a combination of both. The fact that $\sigma_{fis}/\Sigma\sigma_{xn}$ (see Figure 4.26) shows very similar slopes for the three reactions is not consistent with increased fission at low l, but rather supports a reduction of l_{lim}^{ER} with projectile mass.

Both the fission probabilities and the fission fragment angular distributions are sensitive to the angular momentum, $J\hbar$, of the fissioning system, as the rotational energy of the compound nucleus is dependent on the angular momentum and the nuclear shape. It is therefore appropriate to look at the anisotropies, A. The anisotropies are approximately given by equation 2.70 (repeated here as equation 5.2):

$$A = \frac{W(180°)}{W(90°)} \approx 1 + \frac{\langle J^2 \rangle \hbar^2}{4\mathcal{J}_{eff}T} = 1 + \frac{\langle J^2 \rangle}{4K_0^2} \tag{5.2}$$

It shows that A is sensitive to the mean squared angular momentum $\langle J^2 \rangle$, as well as the variance K_0^2 of the Gaussian distribution of K about $K = 0$ (where K_0^2 in the TSM is the product of the fission saddle-point temperature T and the effective moment of inertia $\mathcal{J}_{eff}$ at the saddle-point shape).

Using accurate angular momentum distributions from precise coupled-channels calculations, it has been shown [Mort95B, Dasg98, Hind99B] that the TSM can reproduce the experimental anisotropies for fusion-fission reactions near the Coulomb barrier, where there is no quasi-fission. Great care was taken in this work to obtain accurate l-distributions for the three reactions, using coupled-channels fits to the capture cross-sections and capture barrier distributions. The $\langle l^2 \rangle$ from capture for the two reactions $^{12}C + ^{204}Pb$ and $^{30}Si + ^{186}W$ are the same at $E_x(C.N.) \approx 50$ MeV. Using equation 5.2, if $\langle J^2 \rangle$ are very similar, but the anisotropies are quite different then the two reactions must have different K_0^2. The decrease in ER reduced cross-sections with increasing projectile mass, either due to a lowering of the threshold l_{lim}^{ER}, or to an increase in $P_{fis}(E, l)$ at low l, will cause the fission $\langle J^2 \rangle$ to be smaller for the heavier projectile. This then enhances the difference in K_0^2 as a function of projectile mass.

A decrease in K_0^2 resulting in an increase in anisotropy, has been found to be a signature of quasi-fission [Back85, Tōke85, Hind95A, Hind95B, Back96, Hind99A]. An increase in the width of the fission fragment mass-distributions has also been identified as a signature of quasi-fission [Back96]. Therefore, an examination of quasi-fission in relation to the results from this work is warranted.

5.1 Quasi-Fission

In capture reactions the projectile and target surmount the Coulomb barrier and the kinetic energy of the projectile is translated into the excitation energy of the combined system. This combined system initially has a di-nuclear shape. In fusion-fission reactions, the combined system evolves into a compact equilibrated shape from which it can subsequently evaporate light particles, and then form an evaporation residue, or elongate and fission. In the quasi-fission process, the di-nuclear system fissions before a compact shape is achieved [Back85, Hind95B, Hind96, Hind99A]. The fission fragments retain some memory of the projectile and target, resulting in wider distributions of fission fragment masses. Fission from the di-nuclear system restricts the distribution of K quantum numbers, and results in a lower K_0^2 [Hind99B].

Quasi-fission has been reported to compete with fusion-fission for reactions which include deformed actinide target nuclei (e.g. [Hind96, Mein97]) or a large projectile ($A \geq 24$) incident on a heavy nuclei target such as Pb (e.g. [Mort95A, Back96, Hind99A]). Given these observations, the presence of quasi-fission for the ^{30}Si induced reaction could be expected. This would explain the broader fission mass-distributions, and larger fission anisotropies observed for the ^{30}Si + ^{186}W reaction than for the other two reactions. Although the ^{186}W nuclei are deformed, the anisotropies from this reaction lack the characteristic anisotropies of reactions involving deformed actinide nuclei, which increase as the energy falls through the Coulomb barrier region. The negative hexadecapole deformation of ^{186}W may play a significant role in determining quasi-fission anisotropies. In contrast with ^{232}Th and ^{235}U, which have positive hexadecapole moments giving rise to only tip collisions occurring at the lowest beam energies, collisions at these lowest energies with the ^{186}W nuclei occur over a wider range of symmetry axis angles with respect to the beam axis. For ^{186}W this results in a greater range of K values during quasi-fission, and may result in lower anisotropies than for an equivalent nucleus with a positive β_4.

In comparing target nuclei deformation, ^{204}Pb is essentially spherical and the small oblate deformation of ^{197}Au result in contact shapes up to 2% longer than average. The larger prolate deformation of ^{186}W can result in shapes over 7% longer than average. The largest change in the effect of deformation is thus between ^{197}Au

and ^{186}W, whereas the largest change in ER yields is between ^{197}Au and ^{204}Pb. Hence target nuclei deformation is unlikely to be the main reason for the observed suppression of fusion and presence of quasi-fission.

Of surprise is the apparent presence of quasi-fission in the ^{19}F + ^{197}Au reaction at energies near the Coulomb barrier, with mass-distributions and anisotropies lying between those of the other two reactions. Ikezoe *et. al* [Ikez90] claimed evidence for non-equilibrium fission for ^{19}F + ^{197}Au at high beam energies from mass distributions. However, this is the first indication of quasi-fission near the Coulomb barrier in a reaction with a target lighter than Th and a projectile with mass $A < 24$. The data suggest that although quasi-fission is present, it is not as significant as for the ^{30}Si + ^{186}W reaction, as might be expected.

The competition between quasi-fission and fusion-fission is able to explain the observed differences in fission fragment mass-distribution and anisotropy data for the three reactions. However, in order to explain the observed ER cross-sections, it is necessary to conclude that quasi-fission is also competing with the formation of ERs at low angular momenta. This new finding suggests that quasi-fission competes with fusion-fission and fusion-ER formation over a wider range of angular momenta than previously believed.

Given these findings, the question arises as to what is the threshold for quasi-fission, the answer to which may lie in the potential energy of the evolving system.

5.2 The Threshold for Quasi-Fission

5.2.1 Businaro-Gallone Criterion

Although for capture reactions the time from nuclear contact to thermal equilibration of the combined system is of the order of only 10^{-22} seconds [Schr84], the estimated time scale for quasi-fission from contact to scission is of the order of 10^{-20} seconds [Davi85]. An adiabatic approach to modelling the reaction dynamics over a liquid drop potential energy landscape should be appropriate. Models describing certain aspects of this process have been developed, calculating trajectories over three-dimensional potential energy surfaces. However, none has predicted fusion inhibition for asymmetric reactions like ^{19}F + ^{197}Au.

Fusion and quasi-fission has previously been discussed qualitatively in terms

of the dependence of the calculated height of the mass-asymmetric fission barriers [Tōke85, Rama90, Ravi96]. These have qualitative similarities to the actual potential energy landscape determining the evolution of the system after capture, for which detailed calculations are not available.

The liquid drop model saddle-point potential energies of the combined system have been calculated by Davies and Sierk [Davi85] as a function of fissility and mass-asymmetry (see Section 2.6.3). Figure 5.1 shows Davies and Sierk's calculated Businaro-Gallone saddle-point potential maxima in Figure 2.20 (small solid points), plotted as a function of mass-asymmetry and fissility. The line is a cubic spline fit to the Businaro-Gallone maxima and is the Businaro-Gallone ridge. The relationship between the entrance channel mass-asymmetry and the Businaro-Gallone ridge has been cited as an explanation for classes of fission other than fusion-fission [Rama90, Liu95, Liu96].

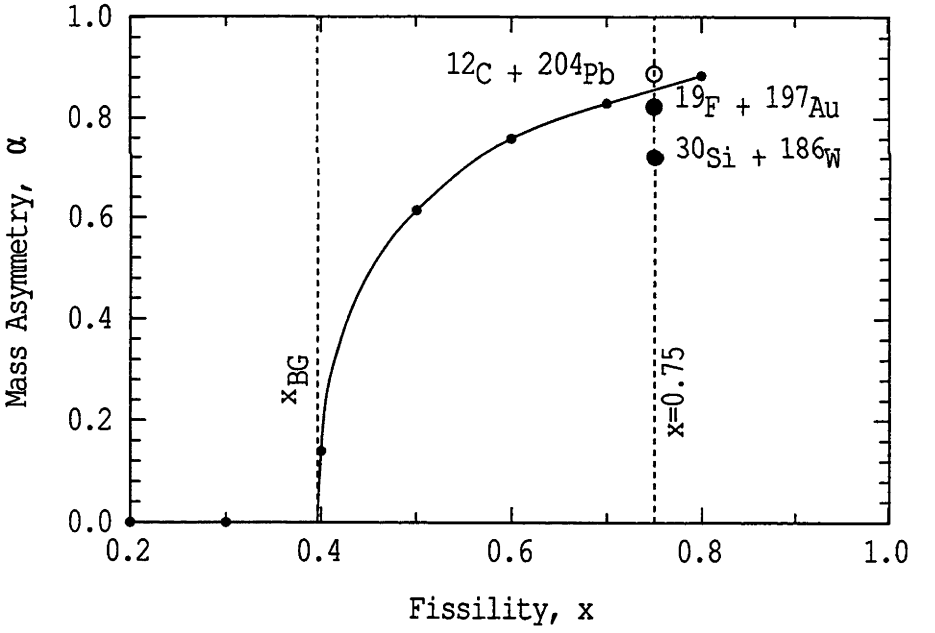

Figure 5.1: The Businaro-Gallone saddle-point potential energy maxima, as a function of fissility and mass-asymmetry. The small solid points were calculated by Davies and Sierk [Davi85] and are the same as the solid points in Figure 2.20. The cubic spline fit to the Businaro-Gallone maxima is the Businaro-Gallone ridge. The vertical dashed line (x=0.75) corresponds to the fissility for the ^{216}Ra nucleus. The three points on the dashed line show the mass-asymmetry for the reactions ^{12}C + ^{204}Pb, ^{19}F + ^{197}Au, and ^{30}Si + ^{186}W. Also shown is the Businaro-Gallone value, $x_{BG} = 0.396$ [Sobo84].

The vertical line ($x = 0.75$) in Figure 5.1 corresponds to the fissility for the ^{216}Ra nucleus, and the large points indicate the initial mass-asymmetry for the three reactions ^{12}C + ^{204}Pb, ^{19}F + ^{197}Au, and ^{30}Si + ^{186}W just after energy equilibration.

The mass-asymmetry for the combined system resulting from capture of the ^{12}C projectile by ^{204}Pb, lies on the side of the Businaro-Gallone ridge where it is energetically favourable for the nucleus to evolve into a more asymmetric configuration. This is the same picture of fusion that is expected for lighter systems below the Businaro-Gallone value $x < x_{BG}$. For the reaction ^{30}Si + ^{186}W the combined system lies on the other side of the Businaro-Gallone ridge. On this side it is energetically favourable for the nucleus to evolve into a more symmetric configuration, more reminiscent of the fission saddle-point configuration. From the symmetric configuration, fission can occur without a compact shape ever being achieved. Such a process leads to quasi-fission, and would not lead to a configuration that could form an ER. The initial mass-asymmetry for combined nuclei formed in the ^{19}F + ^{197}Au reaction lie between those for the other two reactions and on the same side of the Businaro-Gallone ridge as that for the ^{30}Si + ^{186}W reaction. Since ^{19}F + ^{197}Au lies close to the ridge the presence of some quasi-fission for this reaction could be expected.

To test the validity of the potential energy picture in combined nucleus evolution, and the significance of the Businaro-Gallone ridge to quasi-fission, it is worth looking at other reactions involving non-actinide heavy nuclei targets. Figure 5.2 shows studied reactions as a function of their mass-asymmetry and fissility. The solid line is the Businaro-Gallone ridge. Those reactions shown by solid points are documented as displaying quasi-fission (or non-equilibrium fission). The open points are the remaining reactions where quasi-fission has not been reported or where fusion-fission has been assumed.

All the reactions where quasi-fission has been identified are located below the Businaro-Gallone ridge (less mass-asymmetric). The majority of the remaining reactions are either above or close to the ridge. Given the limitations of the calculated Businaro-Gallone ridge, most notably the exclusion of angular momentum, it provides a remarkably good divide separating reactions identified as displaying quasi-fission and those that have been considered as proceeding through the fusion-fission mechanism exclusively.

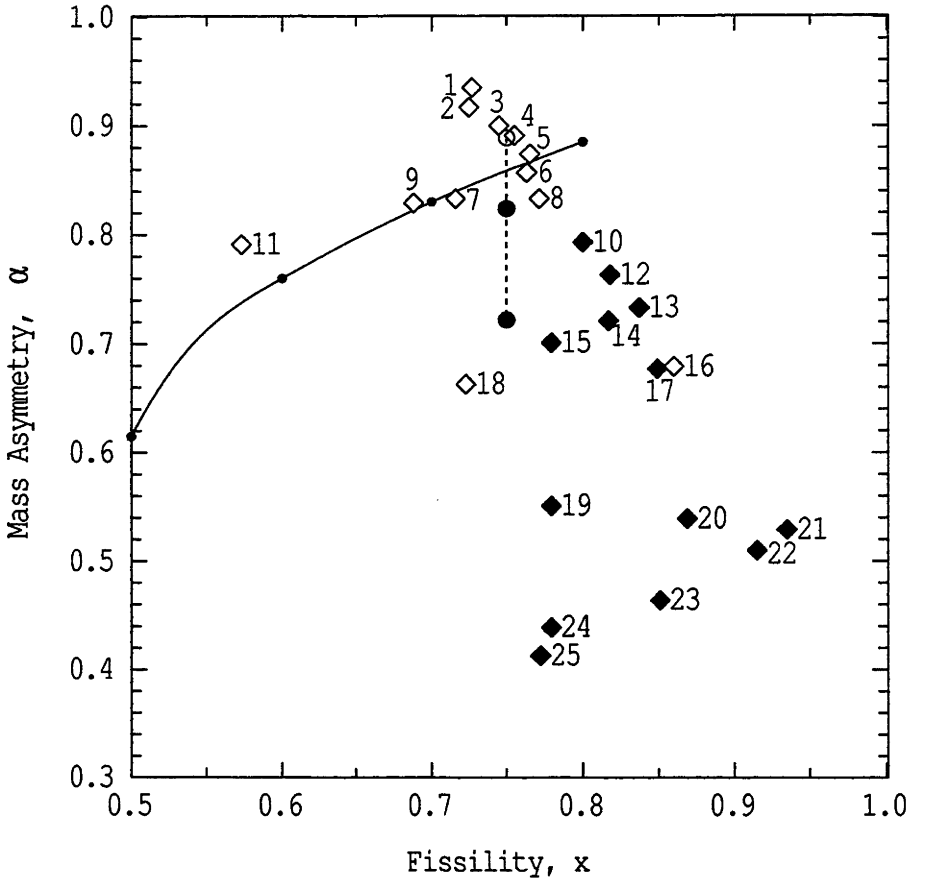

Figure 5.2: Reaction mass-asymmetry and fissility in comparison to the Businaro-Gallone ridge (solid line). Reactions are:

(1) ^{7}Li + ^{209}Bi [Dasg00],
(2) ^{9}Be + ^{208}Pb [Dasg99],
(3) ^{11}B + ^{209}Bi [Ravi98],
(4) ^{12}C + ^{209}Bi [Ravi98],
(5) ^{14}N + ^{209}Bi [Ravi98],
(6) ^{16}O + ^{208}Pb [Back85, Mort95B],
(7) ^{18}O + ^{197}Au [Hind92],
(8) ^{19}F + ^{208}Pb [Back85, Hind99B],
(9) ^{18}O + ^{192}Os [Lest99],
(10) ^{24}Mg + ^{208}Pb [Back85],
(11) ^{18}O + ^{154}Sm [Hind92],
(12) ^{28}Si + ^{208}Pb [Mort95A],
(13) ^{32}S + ^{208}Pb [Back85, Hind96],
(14) ^{32}S + ^{197}Au [Back85],
(15) ^{32}S + ^{182}W [Back96, Nish99],
(16) ^{40}Ar + ^{209}Bi [Rive88],
(17) ^{40}Ar + ^{208}Pb [Hind92],
(18) ^{34}S + ^{168}Er [Mort00],
(19) ^{48}Ti + ^{166}Er [Back96],
(20) ^{56}Fe + ^{187}Re [Rive88],
(21) ^{64}Ni + ^{208}Pb [Hind92],
(22) ^{64}Ni + ^{197}Au [Hind92],
(23) ^{64}Ni + ^{175}Lu [Hind92],
(24) ^{60}Ni + ^{154}Sm [Back96],
(25) ^{64}Ni + ^{154}Sm [Hind92].

Solid points correspond to those where where quasi-fission or non-equilibrium fission has been reported. The three un-numbered circles correspond the the three reactions ^{12}C + ^{204}Pb, ^{19}F + ^{197}Au, and ^{30}Si + ^{186}W from this work, and are repeated from Figure 5.1. The dashed line at x=0.75 corresponds to the fissility of ^{216}Ra.

There are a few exception to the above generalisation. An obvious exception is reaction #16, ^{40}Ar + ^{209}Bi. Mass-distributions for this reaction were measured in comparison to reaction #20 ^{56}Fe + ^{187}Re [Rive88]. Quasi-fission was identified in the latter reaction, and a comparison of the two led to the conclusion that there was no quasi-fission for the reactions ^{40}Ar + ^{209}Bi. However, the data presented in the paper show asymmetric fission fragment mass-distributions for both reactions, a signature of quasi-fission [Back96, Hind96]. A second obvious exception is reaction #18, ^{34}S + ^{168}Er [Mort00], which shows large anisotropies at energies below the average Coulomb barrier, suggestive of quasi-fission, but not yet proven to be such.

Looking closer to the Businaro-Gallone ridge, four reactions are located just beneath the ridge: #6 ^{16}O + ^{208}Pb, #7 ^{18}O + ^{197}Au, #8 ^{19}F + ^{208}Pb and the reaction ^{19}F + ^{197}Au (top solid circle) from this work. Taken in isolation each of these reactions may not display obvious evidence of quasi-fission. However, as demonstrated by the three reactions in this work, by systematically comparing reactions leading to the same compound nucleus, subtle effects can be identified. Only by comparison with the ^{12}C + ^{204}Pb data was quasi-fission identified in the ^{19}F + ^{197}Au reaction. Using the Businaro-Gallone ridge as a threshold for quasi-fission, and the presence of quasi-fission in the reaction ^{19}F + ^{197}Au, gives the interesting result that quasi-fission may be expected in the reaction ^{19}F + ^{208}Pb (#8).

5.2.2 Deformation of the Combined System

The picture outlined above is a simplified version of the total potential energy landscape. Nevertheless, it explains how entrance channel mass-asymmetry could contribute to combined nucleus shape evolution leading to quasi-fission. It does not address the effect of angular momenta, fluctuations in the combined system's shape due to its excited state, or the elongation of the combined system. The latter variable should be very important, and is discussed below.

Important elements of the potential energy surface of the combined system with fissility $x = 0.75$ are illustrated in Figure 5.3, in terms of mass-asymmetry, α. The saddle-point energies for constrained mass-asymmetry are shown in Frame (a) in units of the surface energy for a spherical nucleus, $E_s^{(0)}$. The data have been extrapolated from Davies and Sierk [Davi85]. The initial mass-asymmetry for the three reactions is shown by the arrows. The elongation of the combined system is

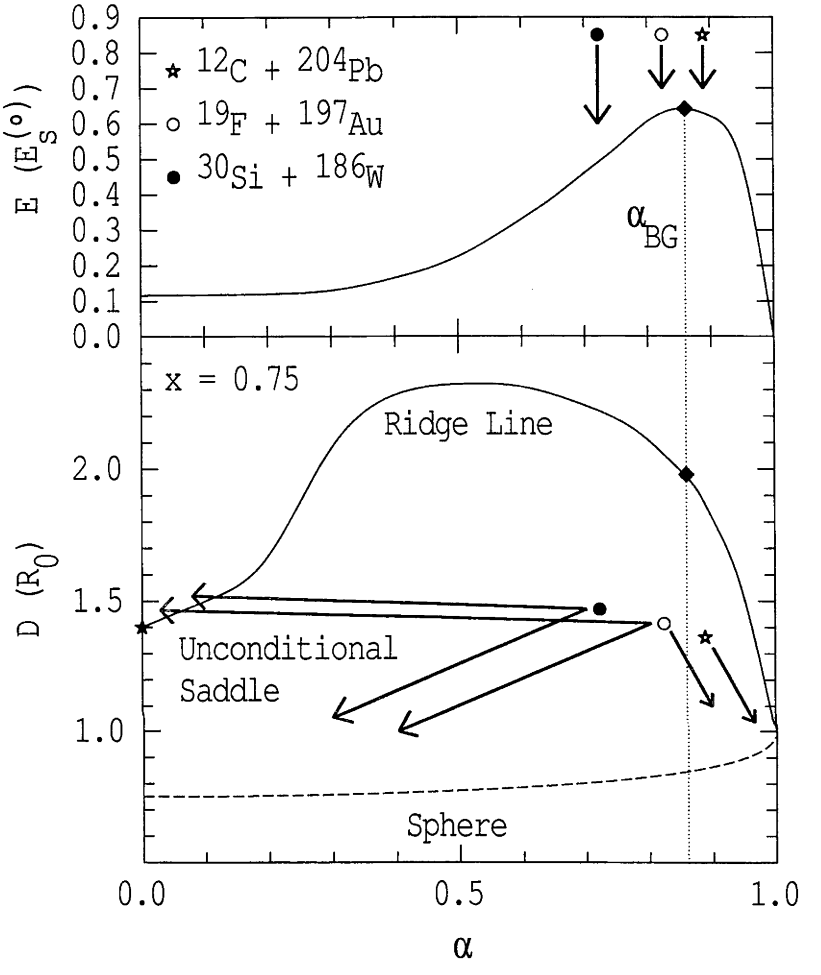

Figure 5.3: Elements of the potential energy surface in units of $E_s^{(0)}$, for the compound nucleus ^{216}Ra as a function of the mass-asymmetry α. The points α_{BG} correspond to the Businaro-Gallone potential energy maximum. (a) Saddle-point energies. The arrows indicate the initial mass-asymmetry for the three systems. (b) Centre-of-mass separation D. The points represent the initial configuration of the dinuclear systems from the three reactions leading to ^{216}Ra. The spherical configuration and the estimated position of the conditional fission saddle ridge line are shown. Possible trajectories are sketched from the points leading to quasi-fission (red arrows) and fusion-fission (blue arrows).

represented in Frame (b) by the separation, D, of the centres of mass of the two partial nuclear masses to the right and left of a plane passing through the neck of the dinuclear system, defined in units of the radius of the spherical configuration (R_0) [Davi85]. For fusion-fission to occur the system must reach the equilibrium configuration, which should be close to the dashed line corresponding to a sphere. The ridge line represents the locus of configurations of the conditional (α-fixed) saddle-points for the fissility $x = 0.75$ (^{216}Ra), and is extrapolated from Davies and Sierk [Davi85] using the methodology of Hinde *et al.* [Hind95A, Hind96]. If D is larger than the ridge line, the potential energy surface forces the system to fission. The points represent the initial configuration of the dinuclear systems from the three reactions leading to ^{216}Ra. The diamond $\alpha_{BG} \approx 0.86$ on the ridge line is where the potential energy is at a maximum, as shown in Frame (a).

The solid star represents the unconditional (fission) saddle-point from this LDM calculation. It is worth noting that equivalent (more realistic) finite range model (FRLDM) calculations give more compact unconditional saddle-point shapes.

Possible trajectories for the three reactions are shown by the red and blue arrows. The red arrows represent paths that lead to a crossing of the ridge and quasi-fission, and blue paths lead to formation of a fully equilibrated compound nucleus. The trajectories will depend on the details of the potential energy surface and the inertia and viscosity tensors. However, experimental evidence [Tōke85] shows that the mass-asymmetry degree of freedom equilibrates more rapidly than does the elongation.

The injection point for the ^{12}C + ^{204}Pb reaction (star) is not only more mass-asymmetric than α_{BG}, it is a more compact shape than the unconditional saddle-point. Thus, qualitatively, trajectories from this point will proceed to complete fusion, mostly by becoming more mass-asymmetric and compact. For the reaction ^{30}Si + ^{186}W which is both less mass-asymmetric than α_{BG} and less compact that the unconditional saddle-point, trajectories will proceed primarily to less mass-asymmetric shapes, and may proceed to either complete fusion or quasi-fission. The combined effect of the larger effective moment of inertia compared to that of the unconditional saddle-point at $\alpha = 0.0$, and the fact that K equilibrium [Rama85] may not occur, will result in a larger anisotropy. It will also result in a wider mass-distribution of fission fragments. The injection point for the reaction ^{19}F + ^{197}Au is

slightly less mass-asymmetric than α_{BG}, but about as compact as the unconditional saddle-point. From this point most trajectories will proceed to complete fusion, but a small fraction will proceed to quasi-fission, possibly at a less symmetric shape than for the ^{30}Si + ^{186}W reaction, leading to anisotropies and mass-distributions somewhere between those from the other two reactions.

As the fissility increases, the unconditional saddle-point moves to more compact shapes, increasing the probability of quasi-fission, whilst for lower fissility, the opposite occurs. Thus Figure 5.3 needs to be interpreted taking this fact into account.

As mentioned in Section 5.2.1, studies have been undertaken of the potential energy surface for reactions that lead to quasi-fission. A simple modelling by Ravi Prasad and Ramamurthy [Ravi96] of entrance channel dynamics showed that by solving the Langevin equations of motion separately for the elongation and mass-asymmetry degrees of freedom, they could reproduce the fission fragment mass yield for the capture reaction ^{12}C + ^{232}Th, including both quasi-fission and compound nucleus fission components. Their analysis also indicated that quasi-fission was occurring in the early stages of the reaction dynamics before compound nucleus formation.

5.2.3 Determining Quasi-Fission

With increasing entrance channel mass-asymmetry, the difficulty becomes not only whether quasi-fission is present, but how can the presence of quasi-fission be determined. What can be used as a benchmark with which to compare the experimental data? In this work it has been shown that the comparison of experimental data for different reactions forming the same compound nucleus, can provide a relative measure for the presence of quasi-fission. This can provide evidence of quasi-fission in the more mass-symmetric reactions, but cannot exclude the presence of quasi-fission in the most asymmetric reaction on which the comparison is based. On this basis, the possibility of some quasi-fission in the reaction ^{12}C + ^{204}Pb cannot be entirely discounted.

Other experiments have studied entrance channel effect on capture-decay reactions using several reactions which lead to the same compound nucleus.

Thoennessen *et al.* [Thoe93] and Charity *et al.* [Char97] reported on entrance channel effects for the two reactions ^{16}O + ^{148}Sm and ^{64}Ni + ^{100}Mo, which following

fusion both lead to the compound nucleus ^{164}Yb. Differences were observed at $E_x(C.N.) = 49$ MeV, in the spectral shape of gamma rays from decay from the giant dipole resonance[Thoe93]. Only the spectrum from the ^{16}O + ^{148}Sm reaction could be described by statistical model calculations. The spectra of α-particles in coincidence with ER production from ^{164}Yb at $E_x(C.N.) = 170$ MeV, was also enhanced at lower kinetic energies for the more mass-symmetric reaction [Char97].

Liang *et al.* [Lian97] measured light charged particle decay in coincidence with ERs from the ^{156}Er compound nucleus, populated by ^{12}C + ^{144}Sm and ^{60}Ni + ^{96}Zr at the same excitation energy. Steeper slopes of the high energy tail were observed in the case of the more symmetric reaction. It was suggested that this was due to a longer formation time in the ^{60}Ni-induced reaction.

Measurements of ER cross-sections and entry state γ-ray fold distributions were reported by Barreto *et al.* [Barr95] for decay from the compound nucleus ^{160}Er at $E_x(C.N.) = 54$ MeV, employing the reactions ^{16}O + ^{144}Nd and ^{64}Ni + ^{96}Zr. An entrance channel dependence of γ-ray fold distributions of the xn products was observed. Although it was described in terms of angular momentum distributions, it was noted that entrance channel effects due to early reactions dynamics may still remain.

The reactions cited above, leading to the compound nuclei ^{160}Er, ^{156}Er and ^{164}Yb, all involve two reactions which lie on either side of the Businaro-Gallone ridge. Decay from these compound nuclei suggest an entrance channel effect on compound nucleus decay. However, they are not in a region where fission competes significantly with ER formation. As a consequence the presence of quasi-fission cannot be determined through looking at the saturation of the reduced ER cross-sections or the fission fragment mass-distributions. To observe these results, heavier compound nuclei need to be studied.

The two reactions ^{48}Ca + ^{172}Yb and ^{124}Sn + ^{96}Zr lead to the compound nucleus ^{220}Th. Evaporation residues from these reactions have been measured by Sahm *et al.* [Sahm85]. The saturation level for the reduced xn ER cross-sections is smaller for the more mass-symmetric reaction, when compared at the same excitation energies. However, both these reactions lie on the mass-symmetric side of the Businaro-Gallone ridge, and quasi-fission could be expected for both these reactions. The reaction ^{16}O + ^{204}Pb, also leads to the compound nucleus ^{220}Th, and lies on the

other side of the Businaro-Gallone ridge. Measurement and comparison of ERs from this reaction would prove an excellent opportunity to explore the quasi-fission threshold.

Few measurements are currently available of ER cross-sections for reactions lying on either side of the Businaro-Gallone ridge, producing the same heavy compound nuclei in the Pb to U range. Comparison of ERs from the compound nuclei ^{200}Pb, ^{198}Pb and ^{192}Pb, while not conclusive, suggest higher reduced ER cross-sections for more mass-asymmetric reactions. Data for the compound nucleus ^{200}Pb formed in the reactions ^{16}O + ^{184}W [Bemi87], ^{19}F + ^{181}Ta [Hind82] and ^{30}Si + ^{170}Er [Hind82, Hind83] appear to have larger reduced ER cross-sections for the ^{16}O + ^{184}W reaction, but the energy is not sufficiently high as to ensure ER saturation. Evaporation residue data from the reactions ^{16}O + ^{182}W [Bemi87] and ^{28}Si + ^{170}Er [Hind83] leading to ^{198}Pb, while only having a small overlap in excitation energy, may show a mass-symmetry relationship. For ^{192}Pb, formed in the reactions ^{28}Si + ^{164}Er [Hind83] and ^{100}Mo + ^{92}Zr [Quin93] the reduced ER cross-sections saturate at a lower level for the ^{100}Mo + ^{92}Zr reaction, but the data is only available for a limited energy range.

Further experiments on these or similar systems could be used to positively identify the presence of quasi-fission. Both fission and ER data are required for a thorough treatment of the threshold of quasi-fission.

In a lot of cases, it is not possible to undertake convenient comparative reactions. In the absence of comparative reactions, disagreement with the TSM remains the main tool in determining the presence of quasi-fission. Due to the number and range of parameters available, the TSM itself is not without uncertainties. However, the requirement to simultaneously reproduce the fission and ER cross-sections, and the use of accurate angular momentum distributions, constrains the parameters available, providing confidence in the modelling process of fusion-fission dynamics.

CHAPTER 6

Summary and Conclusion

This chapter summarises the results, analysis and interpretations presented in the previous chapters, highlighting the main points arising from the present work. It has been broken into six categories:

1. Breakup of the ^{12}C and ^{19}F projectiles in the ^{12}C + ^{204}Pb and ^{19}F + ^{197}Au reactions.

2. The statistical model (SM) description of compound nucleus decay. This includes a discussion of the SM code, JO_SHELL, used in this work, its applicability, strengths and limitations.

3. Investigating the claimed presence of a local shell effects at $N = 126$ by studying fission decay of radon compound nuclei across the $N = 126$ closed shell.

4. Entrance channel dependent decay of the ^{216}Ra compound nucleus, and the threshold of quasi-fission.

5. Production of super-heavy elements.

6. Conclusion.

6.1 Projectile Breakup

Comparison of the evaporation residue cross-sections from compound nuclei formed in the three reactions ^{12}C + ^{204}Pb, ^{19}F + ^{197}Au and ^{30}Si + ^{186}W, indicates that there is relatively more αxn ER (radon) production from the ^{12}C +

^{204}Pb reaction, than from the ^{19}F + ^{197}Au reaction, which in turn has a higher production than the ^{30}Si + ^{186}W reaction. This is attributed to breakup of the ^{12}C and ^{19}F projectiles as they approach the targets.

The most favourable ^{12}C breakup channel by Q value is $^{12}C \rightarrow {}^{8}Be + \alpha$. The incomplete fusion reaction ^{8}Be + ^{204}Pb predominantly leads to the production of radon ERs. The same Rn nuclei are also produced directly as αxn ERs from the complete fusion reaction ^{12}C + ^{204}Pb. The combination of complete and incomplete fusion, results in a larger proportion of Rn nuclei than expected from solely complete fusion. As well as the reaction ^{8}Be + ^{204}Pb, the incomplete fusion reaction α + ^{204}Pb can form Po ERs. The half-lives of these nuclei are in the order of hours to years. The measurements taken in this work were not configured to determine precise cross-sections for Po ERs. Of course the capture of both breakup fragments by the target cannot be distinguished experimentally from complete fusion.

For both the reactions ^{12}C + ^{204}Pb and ^{12}C + ^{197}Au [Verg93], there is expected to be a similar amount of ^{12}C breakup. Indeed the amount of ^{12}C breakup observed in this work, appears consistent with observations by Vergani *et al.* [Verg93] of about 17% ^{12}C breakup.

Breakup of ^{19}F is less prominent than for ^{12}C. The ^{19}F projectile can breakup through several channels, which can produce α, O, N, C, and also B fragments [Park89]. Incomplete fusion of O and N fragments with the ^{197}Au target would lead to Fr and Rn compound nuclei, which are also produced as pxn and αxn ERs in the complete fusion reaction ^{19}F + ^{197}Au.

Incomplete fusion reactions are not only of interest in nuclear reactions. Such reactions involving breakup have been used successfully in gamma-ray spectroscopy research [Drac97] as a tool for forming heavy nuclei near to stability. The principal advantages of using fusion with breakup fragments are, access to relatively neutron-rich nuclei and gaining higher spin input than is achievable with beams equivalent to the breakup fragment mass.

6.2 The Statistical Model

A new statistical model (SM) code has been written which incorporates several different elements with which to explore the dynamics of capture-fission and fusion-

ER reactions. This code named JO_SHELL is a Monte Carlo type code based on the code JOANNE of Lestone [Lest90, Lest91, Lest93].

The principle feature is the inclusion of microscopic shell and pairing effects on the excitation energy used to calculate the level densities. It has often been assumed that nuclei produced in heavy-ion capture reactions, have excitation energies high enough to destroy shell and pairing effects. Is this assumption entirely valid, and at what energy are these effects washed out? For nuclei near the closed shell, can these properties affect the decay of compound nuclei, particularly for last chance fission or the last neutron evaporation? To model these effects, the code JO_SHELL has the option to calculate level densities either by using the excitation energy above the FRLDM ground-state energy (SM-FRLDM option) or a modified excitation energy above the true ground-state [Möll95, Jung98] (SM-SP option). With the latter option, at high excitation energies the shell and pairing effects are washed out, while they approach their maximum as the excitation energy approaches zero.

Other features of the JO_SHELL code include individually calculated average pairing energies (equation 2.60) for each of the initial and subsequent compound nuclei through the decay process. The average pairing gaps, Δ, of the compound nucleus equilibrium deformation and saddle-point configuration [Möll95] are also calculated for each nucleus. Level density parameters can be automatically calculated based on the equations of Tōke and Swiatecki [Tōke81], or entered manually. True ground-state energies and FRLDM ground-state energies [Möll95] are read in from data files.

The result of these changes is a code which has improved functionality, while providing the opportunity for automatic computation of most standard parameters. However, of much more importance is how it performs in the reproduction of experimental data. Comparison of model calculations and experimental results are useful for the six O + Pt reactions and the reaction $^{12}C + ^{204}Pb$. The presence of quasi-fission in the experimental results from the two reactions $^{19}F + ^{197}Au$ and $^{30}Si + ^{186}W$, restricts their usefulness in comparing different model calculations.

The new code, JO_SHELL must, and does, remain consistent with the assumption of the SM that decay is independent of formation (in accordance with Bohr's hypothesis). Therefore, even though it does not reproducing exactly the data from the reactions in this work, the calculations can be used to compare results from

reactions leading to the same or similar compound nuclei.

The SM-FRLDM and SM-SP options both give good reproductions of the experimental fission probabilities, for certain fission barrier scaling factors, k_f. In the case of the SM-FRLDM option, the required range of factors $0.98 \leq k_f \leq 1.09$ is consistent with expectations of $k_f \approx 1$. However for the SM-SP option very low values were required, $k_f \approx 0.75$. For both options, the model calculations slightly over-predict the increase in fission probabilities with increasing energy.

The fission fragment anisotropies were calculated using the Transition State Model (TSM) and results of the SM calculations above. For the SM-FRLDM option and $0.98 \leq k_f \leq 1.09$ the calculations in general over-predicted the anisotropies for the O + Pt and ^{12}C + ^{204}Pb reactions. In contrast the SM-SP calculations using $k_f \approx 0.75$ under-predicted the O + Pt anisotropies but provided a good prediction of the ^{12}C + ^{204}Pb anisotropies. As with the fission probabilities, both model calculations predict an increase in anisotropy with increasing energy which is greater than that observed.

Looking at the experimental evaporation residue channels from the three reactions leading to ^{216}Ra, even considering projectile breakup, the model calculations including shell and pairing gave a better prediction of the different relative xn channels probabilities, than did the SM-FRLDM option calculations. As the xn ERs undergo their last evaporation at very low energy, ground state shell and pairing effects are more likely to be evident in ER decay than for fission decay.

It is not at first apparent from the model calculations presented in this work, that the inclusion or exclusion of shell and pairing effects in the level density calculations provides a better reproduction of the experimental results. It is clear however that the inclusion of these effects does not lead to any striking features in the fission probabilities or anisotropies as a function of compound nucleus energy or neutron number. Nevertheless, the requirement for such a low fission barrier scaling factor indicates that the SM-SP option does not give a complete description of compound nucleus decay, and that other effects may also be influencing the level densities.

Junghans *et al.* [Jung98, Jung99], reported on a large number of nuclei produced in fragmentation reactions. Calculations using only shell and pairing over-predicted the survival probabilities for actinide nuclei produced with $N \approx 126$ from the fragmentation of ^{238}U. Calculations disregarding these effects, which were considered

unrealistic, described the date quite well. It was concluded that collective enhancements (rotational and vibrational degrees of freedom) must be present in the level densities, at least in the energy range where shell effects were present. Model calculations including shell and pairing effects and collective enhancements in the level densities, were also able to reproduce the experimental results. The influence of the shell/pairing and collective enhancements in the level density canceled each other, so that the level densities behaved like those for macroscopic nuclei. Nuclei which were expected to have negligible fission, e.g. those from the fission of ^{208}Pb [Jong98], could however be described with the inclusion of only shell and pairing effects.

This is consistent with the results of the present work, where calculations using JO_SHELL option SM-SP and realistic values of k_f under-estimated the fission probabilities, but that calculations based on the SM-FRLDM option gave a better description of the data. It also may explain why the shell and pairing effects improved the prediction of the ERs channel probabilities, where fission does not have a significant influence.

As stated earlier, the SM calculations used in this work over-predicted the increase in fission probabilities and anisotropies with increasing energy. A possible explanation for this trend was reported by Lestone [Lest99], who reported that the standard SM does not incorporate correctly rotational degrees of freedom of compound nuclei rotating in three dimensions. By taking into account the K-dependence of the fission barrier height, Lestone achieved improved reproductions of experimental data from O-induced reactions. Preliminary calculations conducted by Hinde [Hind00] show that inclusion of rotational degrees of freedom in SM calculations, as outlined by Lestone [Lest99], are able to provide better reproduction of both fission probabilities and anisotropies for the reactions studied in this work.

6.3 Decay Across the $N = 126$ Closed Shell

Fission fragment measurements were made for the six reactions ^{16}O + ^{192,194,196,198}Pt and ^{18}O + ^{196,198}Pt, which lead to the compound nuclei, ^{208,210,212,214,216}Rn (N = 122, 124, 126, 128 and 130). Although the compound nuclei span the $N = 126$ closed shell, no localised influences of the $N = 126$ closed shell were observed in the fission fragment anisotropies. Calculated anisotropies,

either with or without shell and pairing, also showed no evidence of local features that could be attributed to the $N = 126$ closed shell.

This finding contradicts that of Shrivastava *et al.* [Shri99] who reported that fission fragment anisotropies for the reaction $^{12}C + ^{198}Pt \rightarrow ^{210}Po$ ($N = 126$) were larger than SM calculations, while anisotropies for the reaction $^{12}C + ^{194}Pt \rightarrow ^{206}Po$ ($N = 122$) were in agreement with SM calculations. Shrivastava *et al.* suggested that this was due to a significant shell effect in the anisotropies of fission fragments emitted from ^{210}Po.

The reaction $^{18}O + ^{192}Os \rightarrow ^{210}Po$ forms the same compound nucleus as the reaction $^{12}C + ^{198}Pt$ used by Shrivastava *et al.*. Analysis of decay from the $^{18}O + ^{192}Os$ reaction by Lestone [Lest99] shows that SM calculations, including rotational degrees of freedom but not shell effects, were able to reproduce ER cross-sections, fission cross-sections and pre-scission neutron multiplicities from this reaction. This suggests that, perhaps through fortuitous cancellation, the closed shell does not significantly affect the observable quantities in decay of the ^{210}Po compound nucleus.

The lack of a closed shell effect found in this work has been observed in other experiments. Junghans *et al.* [Jung98, Jung99], in their measurements of fission probabilities for a large number of nuclei with low excitation energies, found no suppression of fission for neutron-deficient actinides near the magic number $N = 126$.

The lack of empirical evidence for stabilisation against fission by the $N = 126$ closed shell lends weight to the simple assumption previously used that such effects are washed out by the high excitation energy and high angular momentum which usually apply in heavy-ion induced fission. Fission decay occurs at angular momenta and excitation energies higher than those for ER formation. As a result any shell effects would be less likely to be seen in capture-fission reaction than fusion-ER reactions. Further detailed calculations, including shell effects and collective enhancement to level densities would be valuable, though out of the scope of this study.

6.4 Entrance Channel Dependent Decay of the ^{216}Ra Compound Nucleus

To investigate the effect of entrance channel on compound nucleus formation and decay, detailed measurements were made for the three reactions ^{12}C + ^{204}Pb, ^{19}F + ^{197}Au and ^{30}Si + ^{186}W, which following fusion all lead to the compound nucleus ^{216}Ra. Fission cross-sections, fission fragment anisotropies and fission fragment mass-distributions were measured for these reactions, together with the identity and cross-sections of evaporation residues, determined through their α-decay. To avoid results where breakup was present, emphasis was placed on using xn ER yields, which can only be formed through complete fusion. Projectile breakup and incomplete fusion were shown to not significantly influence the comparison of results from these three reactions

Entrance channel effects were observed in the experimental data as a function of mass-asymmetry for the reactions ^{12}C + ^{204}Pb, ^{19}F + ^{197}Au and ^{30}Si + ^{186}W. For decreasing mass-asymmetry (heavier projectiles) there was a decrease in yield of ERs, both for total ERs and xn ERs, and an increase in fission fragment anisotropies and in the width of fission fragment mass-distributions. This has been interpreted in terms of the inhibition of fully equilibrated compound nucleus formation for the heavier projectiles, and an increasing contribution from quasi-fission. For quasi-fission reactions no ERs are produced and full mass-equilibrium does not occur. This is the first experimental data that shows convincingly that quasi-fission competes not only with fusion-fission reactions, but also competes at low angular momenta with ER production.

The presence of quasi-fission in the reaction ^{19}F + ^{197}Au is surprising. For reactions involving heavy-ion non-actinide targets, this is the lightest projectile for which quasi-fission has been observed at energies near the Coulomb barrier.

The entrance channel threshold for quasi-fission may be interpreted in terms of the potential energy of the conditional fission saddle-points as a function of mass-asymmetry. For combined systems formed in the ^{12}C + ^{204}Pb reaction, the potential energy favours shape evolution towards a more mass-asymmetric system, which in turn leads to a mass-equilibrated compound nucleus. However, for the ^{19}F + ^{197}Au reaction, and to a greater extent the ^{30}Si + ^{186}W reaction, the potential en-

ergy favours evolution into a more mass-symmetric system. From this position it may approach an unstable shape leading to quasi-fission, or contract into a mass-equilibrated compound nucleus. The peak of the potential energy curve as a function of mass-asymmetry and fissility, known as the Businaro-Gallone ridge, marks the threshold for quasi-fission. To date all reactions where quasi-fission has been observed lie on the more mass-symmetric side of the Businaro-Gallone ridge. From this work, the three reactions $^{12}C + ^{204}Pb$, $^{19}F + ^{197}Au$ and $^{30}Si + ^{186}W$ encompass the Businaro-Gallone ridge, with only the first reaction on the side favouring formation of a fully equilibrated compound nucleus. This is consistent with the experimental results which show increasing quasi-fission competition for the reactions $^{19}F + ^{197}Au$ and $^{30}Si + ^{186}W$.

6.5 Production of Super-Heavy Elements

In this study of entrance channel effects in capture-decay reactions, features have emerged that will have consequences for production of super-heavy elements. In capture reactions which lead to super-heavy compound nuclei, there will be a substantial component of quasi-fission inhibiting the production of fully equilibrated nuclei. For those fully equilibrated nuclei that are formed, a lack of the expected shell stability against fission would further inhibit the formation of ERs. Further theoretical studies will be required to understand the complex multi-dimensional fusion dynamics after capture including the effects of mass-asymmetry, deformation of the symmetric fission barrier and elongation of the system at contact [Hind96]. The findings of this work will provide a quantitative test for new models (such as diffusion models [Abe96]) being developed. Access to the super-heavy island of stability nuclei will therefore be a challenging task, however, an understanding of the inhibition of fusion caused by quasi-fission may hold the key to forming super-heavy nuclei.

6.6 Conclusion

In this work, a study has been made of entrance channel effects in capture-fission (fusion-fission and quasi-fission) and fusion-ER reactions. Measurements were made

of decay from compound nuclei formed in nine different reactions. In addition a new statistical model code was developed and used to compare calculations with experimental data.

Six of these reactions, ^{16}O + $^{192,194,196,198}Pt$ and ^{18}O + $^{196,198}Pt$, lead to the compound nuclei, $^{208,210,212,214,216}Rn$ which span the $N = 126$ closed shell. No localised effects of the $N = 126$ closed shell were observed in the decay of these compound nuclei.

The remaining three reactions, ^{12}C + ^{204}Pb, ^{19}F + ^{197}Au, and ^{30}Si + ^{186}W, showed decay to be dependent on the mass-asymmetry of the entrance channel.

The most significant results of this work are the unexpected inhibition of fusion and presence of quasi-fission, even at low angular momentum values, in the ^{19}F + ^{197}Au reaction, and the comprehensive data set showing a correlation between reaction mass-asymmetry and the onset and extent of quasi-fission. This data set provides a quantitative test of models explaining reaction dynamics, especially the boundary between Bohr's simple fusion process [Bohr36] and the complex, dynamical process of quasi-fission.

Bibliography

[Abe96] Y. Abe, S. Ayik, P.-G. Reinhard and E. Suraud, *On stochastic approaches of nuclear dynamics*, Phys. Rep. **275**, 49 (1996)

[Ande79] G. Andersson, M. Areskoug, H.-Å. Gustafsson, G. Hyltén, B. Schrøder and E. Hagebø, *Medium energy proton induced fission in Tb, La and Ag*, Z. Phys. **A293**, 241 (1979)

[Back85] B.B. Back, R.R. Betts, J.E. Gindler, B.D. Wilkins, S. Saini, M.B. Tsang, C.K. Gelbke, W.G. Lynch, M.A. McMahan and P.A. Baisdan, *Angular distributions in heavy-ion-induced fission*, Phys. Rev. **C32**, 195 (1985)

[Back96] B.B. Back, P.B. Fernandez, B.G. Glagola, D. Henderson, S. Kaufman, J.G. Keller, S.J. Sanders, F. Videbæk, T.F. Wang and B.D. Wilkins, *Entrance-channel effects in quasifission reactions*, Phys. Rev. **C53**, 1734 (1996)

[Bala96] A.B. Balantekin, A.J. DeWeerd and S. Kuyucak, *Relations between fusion cross sections and average angular momenta*, Phys. Rev. **C54**, 1853 (1996)

[Ball75] J.B. Ball, C.B. Fulmer, E.E. Gross, M.L. Halbert, D.C. Hensley, C.A. Ludemann, M.J. Saltmarsh and G.R. Satchler, *Heavy ion elastic scattering survey (I). ^{208}Pb Target*, Nucl. Phys. **A252**, 208 (1975)

[Barr95] J.L. Barreto, N.G. Nicolis, D.G. Sarantites, R.J. Charity, L.G. Sobotka, D.W. Stracener, D.C. Hensley, J.R. Beene, C. Baktash, M.L. Halbert

and M. Thoennessen, *Decay of* $^{160}Er^*$ *in* $^{16}O + ^{144}Nd$ *and* $^{64}Ni + ^{96}Zr$ *fusion reactions*, Phys. Rev. **C51**, 2584 (1995)

[Bass80] R. Bass, *Nuclear Reactions with Heavy Ions*, Springer-Verlag (1980)

[Becc83] F.D. Becchetti, H.H. Hicks, C.A. Fields, R.J. Peterson, R.S. Raymond, R.A. Ristinen, J.L. Ullmann and C.S. Zaidins, ^{3}*He-induced fission of nuclei* $159 < A$, Phys. Rev. **C28**, 1217 (1983)

[Beck78] M. Beckerman and M. Blann, *Statistical-model analyses of heavy-ion-induced fusion reaction products*, Phys. Rev. **C17**, 1615 (1978)

[Beck88] M. Beckerman, *Sub-barrier fusion of two nuclei*, Rep. Prog. Phys. **51**, 1047 (1988) and references therein

[Bemi87] C.E. Bemis Jr., T.C. Awes, J.R. Beene, R.L. Ferguson, H.J. Kim, F.K. McGowan, F.E. Obenshain, F. Plasil, P. Jacobs, Z. Frankel, U. Smilansky and I. Tserruya, *Fusion of* ^{16}O *with* $^{182,184,186}W$ *at subbarrier energies*, ORNL, Physics Division, Progress Report of period ending Sept 1986, ORNL-6326 (1987)

[Bimb72] R. Bimbot, D. Gardes and M.K. Rivert, *Recoil study of transfer reactions: evidence for alpha and* ^8Be *transfers in* ^{12}C *reactions with heavy nuclei (Au, Bi)*, Nucl. Phys, **A189**, 193 (1972)

[Birk79] J.R. Birkelund, L.E. Tubbs, J.R. Huizenga, J.N. De and D. Sperber, *Heavy-ion fusion: comparison of experimental data with classical trajectory models*, Phys. Rep. **56**, 107 (1979)

[Blan66] M. Blann, *Evidence for the influence of shell structure on level densities in the continuum*, Nucl. Phys. **80**, 223 (1966)

[Blan72] M. Blann and F. Plasil, *Limits on angular momentum in heavy-ion compound-nucleus reactions*, Phys. Rev. Lett. **29**, 303 (1972)

[Blan82A] M. Blann and T.T. Komoto, *Statistical fission parameters for nuclei at high excitation and angular momenta*, Phys. Rev. **C26**, 472 (1982)

[Blan82B] M. Blann, F. Plasil, R.L. Ferguson, R.L. Hahn, F.E. Obenshain, F. Pleasonton, G.R. Young, *Comment on 'Fission barrier of ^{153}Tb'*, Phys. Rev. Lett. **49**, 505 (1982)

[Bohr36] N. Bohr, *Neutron Capture and Nuclear Constitution*, Nature **137**, 344 (1936)

[Bohr39] N. Bohr and J.A. Wheeler, *The mechanism of nuclear fission*, Phys. Rev. **56**, 426 (1939)

[Bohr56] A. Bohr, *Proceedings of the United Nations International Conference on the Peaceful Uses of Atomic Energy, Geneva, Switzerland, 1955*, (United Nations, New York, 1956), Vol 2, p151 (1956)

[Bohr69] A. Bohr and B.R. Mottelson, *Nuclear Structure*, Benjamin, New York, Vol I, p. 152 (1969)

[Brog81] R.A. Broglia and A. Winther, *Heavy Ion Reactions Lecture Notes, Volume I: Elastic and Inelastic Reactions*, (Benjamin/Cummings, Reading) p 105 (1981)

[Busi55A] U.L. Businaro and S. Gallone, *On the Interpretation of Fission Asymmetry According to the Liquid Drop Nuclear Model*, Nuovo Cimento, **1**, 629 (1955)

[Busi55B] U.L. Businaro and S. Gallone, *Saddle Shapes, Threshold Energies and Fission Asymmetry on the Liquid Drop Model*, Nuovo Cimento, **1**, 1277 (1955)

[Chak00] S. Chakrabarty, B.S. Tomar, A. Goswami, G.K. Gubbi, S.B. Manohar, A. Sharma, B. Bindukumar, S. Mukherjee, *Complete and incomplete fusion reactions in the ^{12}C + ^{169}Tm*, Nucl. Phys. **A678**, 355 (2000)

[Char86] R.J. Charity, J.R. Leigh, J.J.M. Bokhorst, A. Chatterjee, G.S. Foote, D.J. Hinde, J.O. Newton, S.Ogaza and D. Ward, *Heavy-ion induced fusion-fission systematics and the effect of the compound-nucleus spin distribution on fission-barrier determination*, Nucl. Phy. **A457**, 441 (1986)

[Char97] R.J. Charity, M. Korolija, D.G. Sarantites and L.G. Sobotka, *Charged-particle evaporation from hot ^{164}Yb compound nuclei and the role of ^{5}He emission*, Phys. Rev. **C56**, 873 (1997)

[Cott88] P.D. Cottle, K.A. Stuckey and K.W. Kemper, *Fragmentation of octupole strength in even-A Pt isotopes*, Phys. Rev. **C38**, 2843 (1988)

[Dasg92] M. Dasgupta, A. Navin, Y.K. Agarwal, C.V.K. Baba, H.C. Jain, M.L. Jhingan and A. Roy, *Fusion of $^{28}Si + ^{68}Zn$, $^{32}S + ^{64}Ni$, $^{37}Cl + ^{59}Co$ and $^{45}Sc + ^{51}V$ in the vicinity of the Coulomb barrier*, Nucl. Phy. **A539**, 351 (1992)

[Dasg97] M. Dasgupta, *The Simplified Couple Channel Codes*, Internal Report, ANU-P/1333 (1997)

[Dasg98] M. Dasgupta, D.J. Hinde, N. Rowley and A.M. Stefanini, *Measuring Barriers to Fusion*, Annu. Rev. Nucl. Part. Sci. **48**, 401(1998), and references therein

[Dasg99] M. Dasgupta, D.J. Hinde, R.D. Butt, R.M. Anjos, A.C. Berriman, N. Carlin, P.R.S. Gomes, C.R. Morton, J.O. Newton, A. Szanto de Toledo and K. Hagino, *Fusion versus Breakup: Observation of Large Fusion Suppression for $^{9}Be + ^{208}Pb$*, Phys. Rev. Lett. **82**, 1395 (1999)

[Dasg00] M. Dasgupta, P.R.S. Gomes, *Effect of Projectile Breakup on the Fusion of $^{6,7}Li + ^{209}Bi$*, Department of Nuclear Physics, ANU, Annual Report 1999, ANU-P/1420 (2000)

[Dass83A] C.H. Dasso, S. Landowne and A. Winther, *A study of Q-value effects on barrier penetration*, Nucl. Phys. **A407**, 221 (1983)

[Dass83B] C.H. Dasso, S. Landowne and A. Winther, *Channel-coupling effects in heavy-ion fusion reactions*, Nucl. Phys. **A405**, 381 (1983)

[Dass87] C.H. Dasso and S. Landowne, *CCFUS-a simplified coupled-channel code for calculation of fusion cross sections in heavy-ion reactions*, Comp. Phys. Comm. **46**, 187 (1987)

[Davi85] K.T.R. Davies and A.J. Sierk, *Conditional saddle-point configurations*, Phys. Rev. **C31**, 915 (1985)

[Dela77] H. Delagrange, A. Fleury and J.M. Alexander, *Fission probability calculations for heavy-ion induced reactions*, Phys. Rev. **C16**, 706 (1977)

[Drac97] G.D. Dracoulis, A.P. Byrne, T. Kibédi, T.R. McGoram and S.M. Mullins, *Incomplete fusion as a spectroscopic tool*, J. Phys. G **23**, 1191 (1997)

[Feko95] V. Fekou-Youmbi, J. L. Sida, N. Alamanos, F. Auger, D. Bazin, C. Borcea, C. Cabot, A. Cunsolo, A. Foti, A. Gillibert, A. Lépine, M. Lewitowicz, R. Liguori-Neto, W. Mittig, E. Pollacco, P. Roussel-Chomaz, C. Volant and Y. Yong Feng *Sub-Coulomb fusion with halo nuclei*, Nucl. Phys. **A583**, 811c (1995)

[Fern89] J. Fernández-Niello, C.H. Dasso and S. Landowne, *CCDEF-a simplified coupled-channel code for fusion cross sections including static nuclear deformations*, Comp. Phys. Comm. **54**, 409, (1989)

[Fire96] R.B. Firestone, *Table of Isotopes 8th Edition Vol II*, John Wiley & Sons Inc, (1996)

[Gavr80] A. Gavron, *Statistical model calculations in heavy ion reactions*, Phys. Rev. **C21**, 230 (1980)

[Gran80] P. Grange and H.A. Weidenmuller, *Fission probability and the nuclear friction constant*, Phys. Lett. **96B**, 26 (1980)

[Gran86] P. Grange, S. Hassani, H.A. Weidenmuller, A. Gavron, J.R. Nix and A.J. Sierk, *Effect of nuclear dissipation on neutron emission prior to fission*, Phys. Rev. **C34**, 209 (1986)

[Gree54] A.E.S. Green, *Coulomb radius constant from nuclear masses*, Phys. Rev. **95**, 1006 (1954)

[Hagi97] K. Hagino, N. Takigawa, M. Dasgupta, D.J. Hinde and J.R. Leigh, *Adiabatic Quantum Tunneling in Heavy-Ion Sub-barrier Fusion*, Phys. Rev. Lett. **79**, 2014 (1997)

[Hagi99] K. Hagino, N. Rowley and A.T. Kruppa, *A program for coupled-channel calculations with all order couplings for heavy-ion fusion reactions*, Comp. Phys. Comm. **123**, 143 (1999)

[Halp58] I. Halpern and V.M. Strutinsky, *Proceeding of the Second United Nations International Conference on the Peaceful Uses of Atomic Energy, Geneva, Switzerland, 1957*, (United Nations, Geneva, Switzerland, 1958), p 408 (1957)

[Hill53] D.L. Hill and J.A. Wheeler, *Nuclear constitution and the interpretation of fission phenomena*, Phys. Rev. **89**, 1102 (1953)

[Hind82] D.J. Hinde, J.R. Leigh, J.O. Newton, W. Galster and S. Sie, *Fission and Evaporation Competition in ^{200}Pb*, Nucl. Phys. **A385**, 109 (1982)

[Hind83] D.J. Hinde, J.O. Newton, J.R. Leigh and R.J. Charity, *Fission Barriers of Pb Nuclei at High Angular Momentum*, Nucl. Phys. **A398**, 308 (1983)

[Hind86] D.J. Hinde, R.J. Charity, G.S. Foote, J.R. Leigh, J.O. Newton, S. Ogaza and A. Chatterjee, *Neutron multiplicities in heavy-ion-induced fission: Timescale of fusion-fission*, Nucl. Phys. **A452**, 550 (1986)

[Hind92] D.J. Hinde, D. Hilscher and H. Rossner, *Dynamics of Fission and Quasi-fission Revealed by Pre-Scission Neutron Evaporation*, Nucl Phys. **A538**, 243c (1992)

[Hind95A] D.J. Hinde, M. Dasgupta, J.R. Leigh, J.P. Lestone, J.C. Mein, C.R. Morton, J.O. Newton and H. Timmers, *Fusion-Fission versus Quasi-fission: Effect of Nuclear Orientation*, Phys. Rev. Lett. **74**, 1295 (1995)

[Hind95B] D.J. Hinde, C.R. Morton, M. Dasgupta, J.R. Leigh, J.C. Mein and H. Timmers, *Competition between Fusion-Fission and Quasi-fission in the Reaction $^{28}Si + ^{208}Pb$*, Nucl. Phys. **A592**, 271 (1995)

[Hind96] D.J. Hinde, M. Dasgupta, J.R. Leigh, J.C. Mein, C.R. Morton, J.O. Newton and H. Timmers, *Conclusive Evidence for the Influence of Nuclear Orientation on Quasi-Fission*, Phys. Rev. **C53**, 1290 (1996)

[Hind99A] D.J. Hinde, M. Dasgupta, C.R. Morton, A.C. Berriman, R.D. Butt and J.O. Newton, *Interplay of fusion and fission dynamics*, Proceedings of the Second International Conference on Fission and Neutron-Rich Nuclei Conference, June 28-July 2 1999, St Andrews, Scotland, World Scientific 345 (ANU-P/1408), (1999)

[Hind99B] D.J. Hinde, A.C. Berriman, M. Dasgupta, J.R. Leigh, J.C. Mein, C.R. Morton and J.O. Newton, *Limiting Angular Momentum for Statistical Model Description of Fission*, Phys. Rev. **C60**, 054602 (1999)

[Hind00] D.J. Hinde, *private communication*, (2000)

[Huiz62] J.R. Huizenga and G. Igo, *Theoretical reaction cross sections for alpha particles with an optical model*, Nucl. Phys. **29**, 462 (1962)

[Igna75] A.V. Ignatyuk, M.G. Itkis, V.N. Okolovich, G.N. Smirenkin and A.S. Tishin, *Fission of pre-actinide nuclei. Excitation functions for the (alpha, f) reaction*, Yad. Fiz. **21**, 1185 (1975), (Sov. J. Nucl. Phys. **21**, 612 (1975))

[Ikez88] H. Ikezoe, N. Shikazono, Y. Tomita, Y. Sugiyama, K. Ideno, W. Yokota, Y. Nagame, S.M. Lee, M. Ogihara, S.C. Jeong, H. Fujiwara and D.J. Hinde, *Mass Distribution of fission fragments in the* $^{19}F + ^{197}Au$ *reaction*, Z. Phys. **A330**, 289 (1988)

[Ikez90] H. Ikezoe, N. Shikazono, Y. Nagame, Y. Sugiyama, Y. Tomita, K. Ideno, A.Iwamoto and T. Ohtsuki, *Pre-scission* ^{4}He *multiplicity in the* $^{19}F + ^{197}Au$ *reaction*, Phys. Rev. **C42**, 342 (1990)

[Jong98] M. de Jong, K.-H. Schmidt, B. Blank, C. Boeckstiegel, T. Brohm, H.-G. Clerc, S. Czajkowski, M. Dornik, H. Geissel, A. Grewe, E. Hanelt, A. Heinz, H. Irnich, A.R. Junghans, A. Magel, G. Muenzenberg, F. Nickel, M. Pfuetzner, A. Piechaczek, C. Schneidenberger, W. Schwab, S. Steinhaeuser, K. Suemmer, W. Trinder, B. Voss and C. Ziegler, *Fragmentation cross sections of relativistic* ^{208}Pb *projectiles*, Nucl. Phys. **A628**, 479 (1998)

[Jung98] A.R. Junghans, M. de Jong, H.-G. Clerc, A.V. Ignatyuk, G.A. Kudyaev and K.-H. Schmidt, *Projectile-fragment yields as a probe for the collective enhancement in the nuclear level density*, Nucl. Phy. **A629**, 635 (1998)

[Jung99] A.R. Junghans, A. Heinz, K.-H. Schmidt, and A.V. Ignatyuk, *Collective enhancement in hot nuclei - Up to what excitation energy do they persist?*, Nucl. Phy. **A649**, 214c (1999)

[Jung00] A.R. Junghans, *private communication*, (2000)

[Kram40] H.A. Kramers, *Brownian motion in a field of force and the diffusion model of chemical reactions*, Physica **7**, 284 (1940)

[Lars72] J.S. Larsen, J.L.C. Ford Jr., R.M. Gaedke, K.S. Toth, J.B. Ball and R.L. Hahn, *Investigation of the ^{208}Pb (^{12}C, ^{11}B) ^{209}Bi and ^{208}Pb (^{12}C, ^{13}C) ^{207}Pb reactions at high bombarding energies. (Levels population)*, Phys. Lett. **42B**, 205 (1972)

[Leig82] J.R. Leigh, D.J. Hinde, J.O. Newton, W. Galster and S.H. Sie, *Fission-Imposed Limits to the Angular Momentum Carried by Evaporation Residues from the Compound Nucleus ^{200}Pb*, Phys. Rev. Lett. **48**, 527 (1982)

[Lest90] J.P. Lestone, *Light Charged Particle Production in Heavy-Ion Induced Fusion-Fission Reactions*, PhD Thesis, ANU, (1990)

[Lest91] J.P. Lestone, *The statistical model code 'JOANNE'*, Internal Report, ANU/P-1084 (unpublished) (1991)

[Lest93] J.P. Lestone, J.R. Leigh, J.O. Newton, D.J. Hinde, J.X. Wei, J.X. Chen, S. Elfström and M. Zielinska-Pfabè, *Pre-Scission Charged Particle Multiplicities following the Reactions $^{164,167,170}Er$ + ^{28}Si*, Nucl. Phys. **A559**, 277 (1993)

[Lest95] J.P. Lestone, *Fast method for obtaining finite range corrected potential energy surfaces*, Phys. Rev. **C51**, 580 (1995)

[Lest97] J.P. Lestone, A.A. Sonzogni, M.P. Kelly and R. Vandenbosch, *Near- and sub-barrier fission fragment anisotropies and the failure of the statistical theory of fission decay rates*, J. Phys. G: Nucl. Part. Phys. **23**, 1349 (1997)

[Lest99] J.P. Lestone, *Calculating fission rates at high spin: Incorporation of rotational degrees of freedom in thermodynamically fluctuating axially symmetric systems*, Phys. Rev. **C59**, 1540 (1999)

[Lian97] J.F. Liang, J.D. Bierman, M.P. Kelly, A.A. Sonzogni, R. Vandenbosch and J.P.S. van Schegen, *Entrance Channel Dependent Light Charged Particle Emission from the ^{156}Er Compound Nucleus*, Phys. Rev. Lett. **78**, 3074 (1997)

[Liu95] Z.H. Liu, H.G. Zhang, J.C. Xu, Y.Qiao and C.J. Lin, *Pre-equilibrium fission for low angular momentum*, Phys. Lett. **B353**, 173 (1995)

[Liu96] Zuhua Liu, Huanqiao Zhang, Jincheng Xu, Yu Qiao, Xing Qian and Chengjian Lin, *Fission before K equilibration*, Phys. Rev **C54**, 761 (1996)

[Luna99] M. Lunardon, C. Merigliano, G. Viesti, D. Fabris, G. Nebbia, M. Cinausero, G. de Angelis, E. Farnea, E. Fioretto, G. Prete, A. Brondi, G. La Rana, R. Moro, A. Principe, E. Vardaci, N. Gelli, F. Lucarelli, P. Pavan, D.R. Napoli and G. Vedovato, *Alpha particle emission, incomplete fusion and population of high-spin states in the reaction 120 MeV ^{19}F + ^{181}Ta.* Nucl. Phys. **A652**, 3 (1999)

[LUND] Lund Nuclear Data WWW Service,
web site: nucleardata.nuclear.lu.se/nucleardata
Mass data from the *Table of Isotopes* at the Korean Atomic Energy Research Institute (KAERI) (2000)

[Mein97] J.C. Mein, D.J. Hinde, M. Dasgupta, J.R. Leigh, J.O. Newton and H. Timmers, *Precise Fission Fragment Anisotropies for the ^{12}C + ^{232}Th Reaction: Supporting the Nuclear Orientation Dependence of Quasifission*, Phys. Rev. **C55**, R995 (1997)

[Möll95] P. Möller, J.R. Nix, W.D. Myers and W.J. Swiatecki, *Nuclear Ground-State Masses and Deformations*, Atomic Data and Nuclear Data Tables **59**, 185 (1995)

[Mort94] C.R. Morton, M. Dasgupta, D.J. Hinde, J.R. Leigh, R.C. Lemmon, J.P. Lestone, J.C. Mein, J.O. Newton, H. Timmers, N. Rowley and A.T. Kruppa, *Clear Signatures of Specific Inelastic and Transfer Channels in the Distribution of Fusion Barriers*, Phys. Rev. Lett. **72**, 4074 (1994)

[Mort95A] C.R. Morton, *Fusion Barrier Distributions and Fission Fragment Anisotropies in Heavy Ion Fusion Reactions*, PhD Thesis, ANU (1995)

[Mort95B] C.R. Morton, D.J. Hinde, J.R. Leigh, J.P Lestone, M. Dasgupta, J.C. Mein, J.O. Newton and H. Timmers, *Resolution of the Anomalous Fission Fragment Anisotropies for the* $^{16}O + ^{208}Pb$ *Reaction*, Phys. Rev. **C52**, 243 (1995)

[Mort00] C.R. Morton, *Evidence for the influence of target nucleus deformation on the fission anisotropy*, Department of Nuclear Physics, ANU, Annual Report 1999, ANU-P/1420 (2000)

[Mura86] T. Murakami, C.-C. Sahm, R. Vandenbosch, D.D. Leach, A. Ray and M.J. Murphy, *Fission probes of sub-barrier fusion cross section enhancements and spin distribution broadening*, Phys. Rev. **C34**, 1353 (1986)

[Myer66] W.D. Myers and W.J. Swiatecki, *Nuclear masses and deformations*, Nucl. Phys. **81**, 1 (1966)

[Myer67] W.D. Myers and W.J. Swiatecki, *Anomalies in nuclear masses*, Ark. Fys. **36**, 343 (1967)

[NDS] Nuclear Data Sheets **60**, 527 (1990); **74**, 259 (1995); **79**, 277 (1996); **83**, 145 (1998); and **84**, 717 (1998)

[Newt88] J.O. Newton, D.J. Hinde, R.J. Charity, J.R. Leigh, J.J.M. Bokhorst, A. Chatterjee, G.S. Foote and S. Ogaza, *Measurement and statistical model analysis of pre-fission neutron multiplicities*, Nucl. Phys. **A483**, 126 (1988)

[Nino99] V. Ninov, K.E. Gregorich, W. Loveland, A. Ghiorso, D.C. Hoffman, D.M. Lee, H. Nitsche, W.J. Swiatecki, U.W. Kirbach, C.A. Laue, J.L. Adams, J.B. Patin, D.A. Shaughnessy, D.A. Strellis, P.A. Wilk, *Observation of superheavy nuclei produced in the reaction of* ^{86}Kr *with* ^{208}Pb, Phys. Rev. Lett. **83**, 1104 (1999)

[Nish99] K. Nishio, H. Ikezoe, S. Mitsuoka and J. Lu, *Preequilibrium fission following fusion of* $^{32}S + ^{182}W$, JAERI Tandum and V.D.G. Annual Report 1998, JAERI-Review 99-028 (1999)

[Oert80] W. von Oertzen, H Fuchs, A. Gamp, H. Homeyer, U. Jahnke and J.C. Jacmart, *Evaporation residue cross sections from the fusion of* $^{52}Cr + ^{110}Pd$, Z. Phys **A298**, 207 (1980)

[Ogan99A] Yu.Ts. Oganessian, A.V. Yeremin, A.G. Popeko, S.L. Bogomolou, G.V. Buklanov, M.L. Chelnokov, V.I. Chepigin, B.N. Gikal, V.A. Gorshkov, G.G. Gulbekian, M.G. Itkis, M.L. Kabachenko, A.Yu. Lavrentevu, O.N. Malyshev, J. Rohac, R.N. Sagaidak, S. Hofmann, S. Saro, G. Giardina, K. Morital, *Synthesis of nuclei of the superheavy element 114 in reactions induced by* ^{48}Ca, Nature **400**, 242 (1999)

[Ogan99B] Yu.Ts. Oganessian, V.K. Utyonkov, Yu.V. Lobanov, F.Sh. Abdullin, A.N. Polyakov, I.V. Shirokovsky, Yu.S. Tsyganov, G.G. Gulbekian, S.L. Bogomolov, B.N. Gikal, A.N. Mezentsev, S. Iliev, V.G. Subbotin, A.M. Sukhov, G.V. Buklanov, K. Subotic, M.G. Itkis, K.J. Moody, J.F. Wild, N.J. Stoyer, M.A. Stoyer, R.W. Lougheed, *Synthesis of superheavy nuclei in the* $^{48}Ca + ^{244}Pu$ *reaction*, Phys. Rev. Lett. **83**, 3154 (1999)

[Ogan00] Yu.Ts. Oganessian, V.K. Utyonkov, Yu.V. Lobanov, F.S. Abdullin, A.N. Polyakov, I.V. Shirokovsky, Y.S. Tsyganov, G.G. Gulbekian, S.L. Bogomolov, B.N. Gikal, A.N. Mezentsev, S. Iliev, V.G. Subbotin, A.M. Sukhov, O.V. Ivanov, G.V. Buklanov, K. Subotic, M.G. Itkis, K.J. Moody, J.F. Wild, N.J. Stoyer, M.A. Stoyer, R.W. Lougheed, *Synthesis of superheavy nuclei in the* $^{48}Ca + ^{244}Pu$ *reaction:* $^{288}114$, Phys. Rev. **C62**, 041604 (2000)

[Ogan01] Yu.Ts. Oganessian, V.K. Utyonkov, Yu.V. Lobanov, F.Sh. Abdullin, A.N. Polyakov, I.V. Shirokovsky, Yu.S. Tsyganov, G.G. Gulbekian, S.L. Bogomolov, B.N. Gikal, A.N. Mezentsev, S. Iliev, V.G. Subbotin, A.M. Sukhov, O.V. Ivanov, G.V. Buklanov, K. Subotic, M.G. Itkis, K.J. Moody, J.F. Wild, N.J. Stoyer, M.A. Stoyer, R.W. Lougheed, C.A. Laue, Ye.A. Karelin , A.N. Tatarinov, *Observation of the decay of* ^{292}*116*, Phys. Rev. **C63**, 011301R (2001)

[Park89] D.J. Parker, J.J. Hogan, J. Asher, *Complete and incomplete fusion of 6 MeV/nucleon light heavy ion on* ^{51}*V*, Phys. Rev **C39**, 2256 (1989)

[Park91] D.J. Parker, P.Vergani, E. Gadioli, J.J. Hogan, F. Vettore, E. Gadioli Erba, E. Fabrici and M. Galmarini, *Recoil range study of complete and incomplete fusion of C with Au at 10 MeV/nucleon*, Phys. Rev **C44**, 1528 (1991)

[Pere76] C.M. Perey and F.G. Perey, *Compilation of phenomenological optical-model parameters 1954-1975*, At. Data Nucl. Data Tables **17**, 1 (1976)

[Petr97] M. Petrascu, I. Tanihata, T. Kobayashi, A. Isbasescu, H. Petrascu, A. Korsheninnokov, E. Nikolski, S. Fukuda, H. Kumagai, S. Momota, A. Ozawa, K. Yoshida, C. Bordeanu, I. David, I. Lazar, I. Mihai, G. Vaman and M.Giurgiu, *Neutron pre-emission at the fusion of* ^{11}*Li halo nuclei with Si targets*, Phys. Rev. **B405**, 224 (1997)

[Plas78] F. Plasil, *Deexcitation of compound nuclei with high angular momenta*, Phys. Rev. **C17**, 823 (1978)

[Plas80] F. Plasil, R.L. Ferguson, R.L. Hahn, F.E. Obenshain, F. Pleasonton and G.R Young, *Fission barrier of* ^{153}*Tb*, Phys. Rev. Lett. **45**, 333 (1980)

[Plas84] F. Plasil, T.C. Awes, B. Cheynis, D. Drain, R.L. Fergusson, F.E. Obenshain, A.J. Sierk, S.G. Steadman and G.R Young, *Angular-momentum-dependent fission barriers in the rare-earth region*, Phys. Rev. **C29**, 1145 (1984)

[Plic83] J. van der Plicht, H.C. Britt, M.M. Fowler, Z. Fraenkel, A. Gavron, J.B. Wilhelmy, F. Plasil, T.C. Awes and G.R. Young, *Fission of polonium, osmium, and erbium composite systems*, Phys. Rev. **C28**, 2022 (1983)

[Pühl77] F. Pühlhofer, *On the interpretation of evaporation residue mass distributions in heavy-ion induced fusion reactions*, Nucl. Phys. **A280**, 267 (1977)

[Quin93] A.B. Quint, W. Reisdorf, K-H. Schmidt, P. Armbruster, F.P. Hessberger, S. Hofmann, J. Keller, G. Munzenberg, H. Stelzer, H-G. Clerc, W. Morawek and C-C. Sahm, *Investigation of the fusion of heavy nearly symmetric systems*, Z. Phys. **A346**, 119 (1993)

[Rama85] V.S. Ramamurthy and S.S. Kapoor, *Interpretation of fission-fragment angular distributions in heavy-ion fusion reactions*, Phys. Rev. Lett. **54**, 178 (1985)

[Rama87] S. Raman, C.H. Malarkey, W.T. Milner, C.W. Nestor Jr., and P.H. Stelson, *Transition probability, B(E2), from the ground to the first-excited 2+ state of even-even nuclides*, Atomic Data and Nuclear Data Tables **36**, 1 (1987)

[Rama90] V.S. Ramamurthy, S.S. Kapoor, R.K. Choudhury, A. Saxena, D.M. Nadkarni, A.K. Mohanty, B.K. Nayak, S.V. Sastry, S. Kailas, A. Chatterjee, P. Singh and A. Navin, *Entrance-Channel Dependence of Fission-Fragment Anisotropies: A Direct Experimental Signature of Fission before Equilibration*, Phys. Rev. Lett. **65**, 25 (1990)

[Ravi96] G.V. Ravi Prasad and V.S. Ramamurthy, *Light fragment emission during mass asymmetry relaxation in heavy-ion induced fission*, Phys. Rev. **C54**, 815 (1996)

[Ravi98] G.V. Ravi Prasad, A.M. Samant, A.Shrivastava, A. Navin, A. Chatterjee, P. Singh, S. Kailas and V.S. Ramamurthy, *Fission fragment angular distribution at near-barrier energies in* ^{11}B, ^{12}C, ^{14}N + ^{209}Bi, Phys. Rev. **C57**, 971 (1998)

[Rive88] M.F. Rivet, R. Alami, B. Borderie, H. Fuchs, D. Gardes and H. Gauvin, *Fusion-fission of heavy systems. Influence of the entrance channel mass asymmetry*, Z. Phys. **A330**, 295 (1988)

[Rosn85] G. Rosner, J. Pochodzalla, B. Heck, G. Hlawatsch, A. Miczaika, H.J. Rabe, R. Butsch, B. Kolb and B. Sedelmeyer, *Complete and incomplete fusion in* $^{19}F + ^{40}Ca$ *and* $^{32}S + ^{27}Al$, Phys. Lett. **150B**, 87 (1985)

[Rowl89] N. Rowley, A. Kabir and R. Lindsay, *Scaling of heavy-ion fusion cross sections and other entrance-channel properties*, J. Phys. **G15**, L269 (1989)

[Rowl91] N. Rowley, G.R. Satchler and P.H. Stelson, *On the 'distribution of barriers' interpretation of heavy-ion fusion*, Phys. Lett. **B254**, 25 (1991)

[Rowl93] N. Rowley, J.R. Leigh, J.X. Wei and R. Lindsay, *Obtaining average angular momenta from fusion excitation functions near the Coulomb barrier*, Phys. Lett. **B314**, 179 (1993)

[Rusa97] A.Y. Rusanov, M.G. Itkis and V.N. Okolovich, *Features of mass distributions of hot rotating nuclei*, Physics of Atomic Nuclei **60**, 683 (1997)

[Sahm85] C.-C. Sahm, H.-G. Clerc, K.-H. Schmidt, W. Reisdorf, P. Armbruster, F.P. Hessberger, J.G. Keller, G. Münzenberg and D. Vermeulen, *Fusion probability of symmetric heavy, nuclear systems determined from evaporation-residue cross sections*, Nuc. Phys. **A441**, 316 (1985)

[Saku86] Y. Sakuragi, M. Yahiro and M. Kamimura, *Microscopic Coupled-Channels Study of Scattering and Breakup of Light Heavy-Ions*, Prog. of Theor. Phys. Supplement **89**, 136 (1986)

[Scar95] F. Scarlassara, S. Beghini, G. Montagnoli,L. Müller, G.F. Segato, D. Ackermann, P. Bednarczyk, He Jian-Hua and A.M. Stefanini, *Nuclear deformation of* ^{194}Pt *probed with sub-barrier fusion reactions*, Istituto Nazionale di Fisica Nucleare, Laboratori Nazionale de Legnaro, Annual Report 1994, LNL-INFN(Rep)-095/95 (1995)

[Scar99] F. Scarlassara, *private communication*, (1999)

[Schm00] K.-H. Schmidt, S. Steinhäuser, C. Böckstiegel, A. Grewe, A. Heinz, A.R. Junghans, J. Benlliure, H.-G. Clerc, M. de Jong, J. Müller, M. Pfützner, B. Voss, *Relativistic Radioactive Beams: A New Access to Nuclear-Fission Studies*, Nucl. Phys. **A665**, 221 (2000)

[Schr84] W.U. Schroder and J.R. Huizenga, in *Treatise in Heavy-Ion Science*, edited by D.A. Bromley, Plenum, New York, Vol 2, p. 115 (1984)

[Shri99] A. Shrivastava, S. Kailas, A. Chatterjee, A.M. Samant, A. Navin, P. Singh and B.S. Tomar, *Shell Effects in Fission Fragment Anisotropies for* $^{12}C + ^{194,198}Pt$ *Systems*, Phys. Rev. Lett. **82**, 699 (1999)

[Sier86] A.J. Sierk, *Macroscopic model of rotating nuclei*, Phys. Rev. **C33**, 2039 (1986)

[Sign97] C. Signorini, *Fusion and breakup at the barrier with unstable nuclei*, Nucl. Phys. **A616**, 262c (1997)

[Sign98] C. Signorini, Z.H. Liu, Z.C. Li, K.E.G. Löbner, L. Müller, M. Ruan, K. Rudolph, F. Soramel, C. Zotti, A. Andrighetto, L. Stroe, A. Vitturi and H.Q. Zhang, *Does break-up affect* $^{9}Be + ^{209}Bi$ *fusion at the barrier?*, Eur. Phys. J. **A2**, 227 (1998)

[Siko82] B. Sikora, W. Scobel, M. Beckerman, J. Bisplinghoff and M. Blann, *Measurement and statistical analyses of fission and fusion excitation functions for* ^{35}Cl *on* ^{62}Ni, ^{116}Sn *and* ^{141}Pr *up to* $E_{lab} = 215$ *MeV*, Phys. Rev. **C25**, 1446 (1982)

[Sobo84] L.G. Sobotka, M.A. McMahan, R.J. McDonald, C. Signarbieux, G.J. Wozniak, M.L. Padgett, J.H. Gu, Z.H. Liu, Z.Q. Yao and L.G. Moretto, *Compound-Nucleus Decay along the Mass-Asymmetry Coordinate and the Role of the Businaro-Gallone Point*, Phys. Rev. Lett. **53**, 2004 (1984)

[Sonz98] A.A. Sonzogni, R. Vandenbosch, A.L. Caraley, J.P. Lestone, *Is quasi-fission responsible for anomalous fission fragment anisotropies?*, Phys. Rev. **C58**, R1873 (1998)

[Spea77] R.H. Spear, D.C. Kean, M.T. Esat, A.M.R. Joye and M.P. Fewell, *Energy calibration of the ANU 14UD Pelletron accelerator*, Nucl. Instr. Meth. **147**, 455 (1977)

[Spea89] R.H. Spear, *Reduced electric-octupole transition probabilities, B(E3;01+ → 31-), for even-even nuclides throughout the periodic table*, Atomic Data and Nuclear Data Tables **42**, 55 (1989)

[Stea86] S.G. Steadman, M.J. Rhoades-Brown, *Sub-Barrier Fusion Reactions*, Annu. Rev. Nucl. Part. Sci. **36**, 649 (1986) and references therein

[Stel88] P.H. Stelson, *Neutron flow between nuclei as the principal enhancement mechanism in heavy-ion subbarrier fusion*, Phys. Lett. **B205**, 190 (1988)

[Stok78] R.G. Stokstad, Y. Eisen, S. Kaplanis, D. Pelte, U. Smilansky and I. Tserruya, *Effect of nuclear deformation on heavy-ion fusion*, Phys. Rev. Lett **41**, 465 (1978)

[Stru67] V.M. Strutinsky, *Shell effects in nuclear masses and deformation energies*, Nucl. Phys. **A95**, 420 (1967)

[Stru68] V.M. Strutinsky, *"Shells" in deformed nuclei*, Nucl. Phys. **A122**, 1 (1968)

[Taka97] J. Takahashi, M. Munhoz, E.M. Szanto, N. Carlin, N. Added, A.A.P. Suaide, M.M. de Moura, R. Liguori Neto, A. Szanto de Toledo and L.F. Canto, *Is fusion inhibited for weakly bound nuclei?*, Phys. Rev. Lett. **78**, 30 (1997)

[Taki94] N. Takigawa, K. Hagino, M. Abe and A.B. Balantekin, *Role of mass renormalization in adiabatic quantum tunneling*, Phys. Rev. **C49**, 2630 (1994)

[Terr89] F. Terrasi, A. Brondi, G. La Rana, G. De Angelis, A. D'Onofrio, R. Moro, E. Perillo, M. Romano, *Dissipative mechanisms in the 120 MeV $^{19}F + ^{64}Ni$ reaction*, Phys. Rev. **C40**, 742 (1989)

[Thoe93] M. Thoennessen, J.R. Beene, F.E. Bertrand, C. Baktash, M.L. Halbert, D.J. Horen, D.G. Sarantites, W. Spang and D.W. Stracener, *Evidence for Long Formation Times of Near-Barrier Fusion Reactions*, Phys. Rev. Lett. **70**, 4055 (1993)

[Thom64] T.D. Thomas, *The analysis of nuclear evaporation spectra*, Nucl. Phys. **53**, 558 (1964)

[Tōke81] J. Tōke and W.J. Swiatecki, *Surface-Layer Corrections to the Level-Density Formula for a Diffuse Fermi Gas*, Nucl. Phys. **A372**, 141 (1981)

[Tōke85] J. Tōke, R. Bock, G.X. Dai, A. Gobbi, S. Gralla, K.D. Hildenbrand, J. Kuzminski, W.F.J. Müller, A. Olmi, H. Stelzer, B.B. Back and S. Bjørnholm, *Quasi-fission - the mass-drift mode in heavy-ion reactions*, Nucl. Phys. **A440**, 327 (1985)

[Toma98] B.S. Tomar, A. Goswami, G.K. Gubbi, A.V.R. Reddy, S.B. Manohar, B. John and S.K. Kataria, *Incomplete fusion in the $^{19}F + ^{93}Nb$ reaction*, Phys. Rev. **C58**, 3478 (1998)

[Vand73] R. Vandenbosch and J.R. Huizenga, *Nuclear Fission*, Academic Press, New York (1973)

[Vand92] R. Vandenbosch, *Angular momentum distributions in subbarrier fusion reactions*, Annu. Rev. Nucl. Part. Sci. **42**, 447, (1992)

[Verg93] P. Vergani, E. Gadioli, E. Vaciago, E. Fabrici, E. Gadioli Erba, M. Galmarini, G. Ciavola and C. Marchetta, *Complete and incomplete fusion and emission of preequilibrium nucleons in the interaction of ^{12}C with ^{197}Au below 10MeV/nucleon*, Phys. Rev. **C48**, 1815 (1993)

[Viol85] V.E. Viola, K. Kwiatkowski and M. Walker, *Systematics of fission fragment total kinetic energy release*, Phys. Rev. **C31**, 1550 (1985)

[Vork95] D. Vorkapic and B. Ivanisevic, *Anomalous anisotropies of fission fragments for sub-barrier fusion-fission reactions*, Phys. Rev. **C52**, 1980(1995)

[Ward83] D. Ward, R.J. Charity, D.J. Hinde, J.R. Leigh and J.O. Newton, *Measurement of pre-fission neutrons from ^{200}Pb; further limits to the statistical fission parameters*, Nucl. Phys. **A403**, 189 (1983)

[Wei91] J.W. Wei, J.R. Leigh, D.J. Hinde, J.O. Newton, R.C. Lemmon, S. Elfstrom, J.X. Chen and N. Rowley , *Experimental determination of the fusion-barrier distribution for the $^{154}Sm + ^{16}O$ reaction*, Phys. Rev. Lett. **67**, 3368 (1991)

[Weis88] D.C. Weisser and M.D. Malev, *Gridded buncher - far field extension using carbon coated teflon sleeves*, Nucl. Instr. Meth. Phys. Res. **A268**, 488, (1988)

[Wong73] C.Y. Wong, *Interaction barrier in charged-particle nuclear reactions*, Phys. Rev. Lett. **31**, 766 (1973)

[Yosh95] A. Yoshida, N. Aoi, T. Fukuda, M. Hirai, M. Ishihara, H. Kobinata, Y. Mizoi, L. Mueller, Y. Nagashima, J. Nakano, T. Nomura, Y.H. Pu, F. Scarlassala, C. Signorini and Y. Watanabe, *A Measurement of fusion cross section with neutron halo nuclei*, Nucl. Phys. **A588**, 109c (1995)

[Zebe74] A.M. Zebelman, L. Kowalski, J. Miller, K. Beg, Y. Eyal, G. Jaffe, A. Kandil and D. Logan, *Fission and complete-fusion probabilities as a function of angular momentum for ^{170}Y compound nuclei excited to 107 MeV*, Phys. Rev. **C10**, 200 (1974)

[Zieg80] J.F. Ziegler, *Handbook of Stopping Powers and Ranges in all Elements*, Vol **5**, Pergamon Press, New York (1980)